Nanoscale Heat Conduction with Applications in Nanoelectronics and Thermoelectrics

by

Ronggui Yang

M.S., Mechanical Engineering (2001)
University of California at Los Angeles

M.S., Engineering Thermophysics (1999)
Tsinghua University, Beijing, China

B.S., Thermal Engineering (1996)
Xi'an Jiaotong University, Xi'an, China

Submitted to the Department of Mechanical Engineering
in Partial Fulfillment of the Requirements for the Degree of
Doctor of Philosophy in Mechanical Engineering

at the
Massachusetts Institute of Technology
February 2006

Signature of Author..
Department of Mechanical Engineering
December 20, 2005

Certified by..
Gang Chen
Professor of Mechanical Engineering
Thesis Supervisor

Accepted by..
Lallit Anand
Chairman, Department Committee on Graduate Students

Nanoscale Heat Conduction with Applications in Nanoelectronics and Thermoelectrics

by

Ronggui Yang

Submitted to the Department of Mechanical Engineering on December 20, 2005
in Partial Fulfillment of the Requirements for the Degree of
Doctor of Philosophy in Mechanical Engineering

ABSTRACT

When the device or structure characteristic length scales are comparable to the mean free path and wavelength of energy carriers (electrons, photons, phonons, and molecules) or the time of interest is on the same order as the carrier relaxation time, conventional heat transfer theory is no longer valid. Tremendous progress has been made in the past two decades to understand and characterize heat transfer in nanostructures. However most work in the last decade has focused on heat transfer in simple nanostructures, such as thin films, superlattices and nanowires. In reality, there is a demand to study transport process in complex nanostructures for engineering applications, such as heat transfer in nanoelectronic devices and the thermal conductivity in nanocomposites which consists of nanowires or nanoparticles embedded in a matrix material. Another class of problems which are rich in physics and might be explored for better design of both nanoelectronic devices and energy conversion materials and devices are coupled electron and phonon transport. Experimentally, most past work has been focused on thermal conductivity characterization of various nanostructures and very little has been done on the fundamental transport properties of energy carriers.

This thesis work contributes to the following aspects of heat transfer, nanoelectronics, and thermoelectrics. 1) Simulation tools are developed for transient phonon transport in multidimensional nanostructures and used to predict the size effect on the temperature rise surrounding a nanoscale heat source, which mimics the heating issue in nano-MOSFETs. 2) Semiconductor nanocomposites are proposed for highly efficient thermoelectric materials development where low thermal conductivity is a blessing for efficiency enhancement. Both the deterministic solution and Monte Carlo simulation of the phonon Boltzmann equation are established to study the size effect on the thermal conductivity of nanocomposites where nanoparticles and nanowires are embedded in a host material. 3) Explored the possibility of creating nonequilibrium conditions between electrons and phonons in thermoelectric materials using high energy flux coupling to electrons through surface plasmons, and thus to develop highly efficient thermoelectric devices. 4) Established a sub-pico second optical pump-probe measurement system where a femtosecond laser is employed and explored the possibility of extracting phonon reflectivity at interfaces and the phonon relaxation time in a material, which are the two most fundamental phonon properties for nanoscale energy transport from the pump-probe measurements.

Thesis Supervisor: Gang Chen
Title: Professor of Mechanical Engineering

Acknowledgements

I am deeply indebted to my advisor, Professor Gang Chen, for his forceful encouragement and his constructive criticism during the course of my study towards a Ph.D degree. His advice and support extended far beyond the technical realm. It has been a pleasure and a privilege to work with someone of his vision, intuition, ability, and outstanding background. His inquisitive ideas and probing questions as well as his contagious enthusiasm and relentless energy and spirit will be an inspiration for my professional career.

I am deeply grateful to my thesis committee members, Professor Mildred S. Dresselhaus, Professor John H. Lienhard, and Professor Bora Mikic, for their time reading my papers and thesis and examining my progress, for their support and constructive criticisms of my investigations, and for their efforts moving me ahead for my professional career.

I would like to acknowledge the contributions to this thesis from past and present members of Prof. Gang Chen's group: Dr. Xiaoyuan Chen, Dr. Ming-Shan Jeng, Mr. Aaron Schmidt, Ms. Marine Laroche, and Mr. Arvind Narayanaswamy. Dr. Xiaoyuan Chen taught me everything on lasers and optics after we decided to build the pump and probe measurement system. He is a very knowledgeable scientist with great patience and creativity. I enjoyed the time working and discussing with him, and in particular, around 500 cups of coffee we brought back across the street.

Essential for the completion of my graduate study was the collaboration with different research groups and the help from them. I thank all my collaborators during my stay at UCLA and MIT. Those who need special thanks are: Professors M.S. & G. Dresselhaus and some of her group members, Dr. Yu-Ming Lin and Mr. Ming Tang, Professor Zhifeng Ren and his group at Boston College, Dr. G. Jeffrey Snyder and Dr. Jean-Pierre Fleurial at JPL/Caltech, Professor Xiang Zhang at UC-Berkeley and his student Dr. Nicholas Fang now an assistant professor at UIUC, Professor Jonathan Freund and his student Mr. Hong Zhao at UIUC, Dr. Sebastian Volz at Ecole Centrale Paris in France, Professor Yuan Taur at UCSD, Dr. Robert M. Crone and Dr. Cynthia

Hipwell at Seagate Technologies.

I would like to thank all other ex- and current members of Professor Gang Chen's group for their friendship, support, encouragement, and many useful discussions and debates: Dr. Weili Liu, Dr. Taofang Zeng, Dr. Theodore Borca-Tasciuc, Dr. Diana Borca-Tasciuc, Dr. Bao Yang, Dr. D.K. Qing, Dr. Jinbo Wang, Dr. David Song, Dr. Ravi Kumar, Dr. Koji Miyazaki, Dr. Alexander Jacquote, Dr. Da-Jeng Yao, Dr. Min Chen, Dr Min Gao, Dr. Jing Liu, Dr. Yi Shi, Dr. Fardad Hashemi, Mr. Chris Dames, Mr. Lu Hu, Mr. Zony Chen, Mr. Qing Hao, Mr. Hohyun Lee, Mr. Ase Henry, Mr. Jianping Fu, Mr. Sheng Shen, Mr. James Cybulski, Mr. Ashish Shah, Mr. Mr. M. Takashiri, Mr. Vincent Berube, Mr. Shinichiro Nakamura, Mr. Jivtesh Garg, Mr. Gregg Arthur Radtke, Mr. Jack Ma, Mr. Andy Muto, and all the others. I would also like to thank many of my friends who I have spent almost all my time with when I was not in my lab and in the bed during the graduate study, especially Mr. Yujie Wei, Dr. Yuetao Zhang, Dr. Gang Tan, and Dr. Feng Zhang, and their wives, Mr. Yong Li, and Dr. Cheng Su, for their friendship and support. I wish them good luck with their research endeavor and good fortune in their life.

I am grateful to the financial support by DARPA HERETIC projects, DOE BES, NSF, NASA, DOD MURI on Metamaterials, DOD MURI on Thermoelectrics, Intel Corporation, and Seagate Technologies.

Finally, I am grateful to my wife Qunying Zheng, my son Kevin Yang, our parents, our brothers and sisters, for their love, continuous support, and blessings.

Ronggui Yang
Cambridge, MA 02139

Vita

Ronggui Yang is an adjunct assistant professor of mechanical engineering at the University of Colorado at Boulder from July 2005 and will formally join as an assistant professor immediately after he successfully defends his Ph.D thesis at MIT. Prior to MIT, he had a master's degree in MEMS from UCLA in 2001, a master's degree in Engineering Thermophysics from Tsinghua University in Beijing in 1999, and a Bachelor's degree in Thermal Engineering from Xi'an Jiaotong University in 1996. His research interests are on nanoscale and ultrafast thermal sciences, and their applications in energy and information technologies and biomedical engineering. He is the winner of the Best Paper Award in Research category of ASME InterPACK 2005, the 2005 Goldsmid Award for Research Excellence in Thermoelectrics from the International Thermoelectric Society, and a recipient of the NASA Tech Brief Award for a Technical Innovation in 2004. He is an active member of ASME, IEEE, MRS, APS, and Sigma Xi. He serves as a referee for a dozen of prestigious academic journals including Physical Review Letters, Physical Review B, Nano Letters, Applied Physics Letters, ASME Journal of Heat Transfer, International Journal of Heat and Mass transfer, and IEEE Transactions, and has been invited to serve as a co-Guest Editor for a special issue on "Nanoscale Heat Transfer" in the Journal of Computational and Theoretical Nanoscience and a book proposal reviewer for John Wiley & Sons. He currently holds two pending patents on thermoelectric energy conversion and has published a number of journal and conference papers on nanoscale heat transfer and thermoelectrics.

Contents

Abstract **3**

Acknowledgements **4**

Vita **6**

List of Figures **11**

List of Tables **22**

1. Introduction **23**
  - **1.1 Introduction** 23
  - **1.2 Fundamentals of Nanoscale Heat Conduction** 23
    - **1.2.1 Characteristic Length Scales** 24
    - **1.2.2 Wave. Vs. Particle Transport** 27
    - **1.2.3 Nanoscale Heat Honduction Phenomena** 28
      - Phonon Rarefaction Effect 29
      - Nonequilibrium Electron-Phonon Transport 31
    - **1.2.4 Characterization of Nanoscale Heat Transfer** 31
  - **1.3 Applications of Nanoscale Heat Transfer in Nanoelectronics** 33
  - **1.4 Thermoelectric Energy Conversion** 34
  - **1.5 The Scope and Organization of this Work** 37
  - **1.6 References** 41

2. Numerical Solution of Multidimensional Transient Ballistic-Diffusive Equations and Phonon Boltzmann Equation: Application to Heating in

Nanoscale MOSFETs 45
2.1 Introduction 45
2.2 Boltzmann Equation and Equation of Phonon Radiative Transport 47
  Phonon Gray Medium Aproximation 50
2.3 Ballistic-Diffusive Equations and Numerical Solution 55
  2.3.1 Boundary Conditions for BDE and comments 60
  2.3.2 Numerical Calculation Scheme 62
2.4 Two-Dimensional Transient Phonon BTE Solver 67
2.5 Results and Discussions 73
  CASE I: Emitted Temperature Boundary Condition 73
  CASE II: Equivalent equilibrium Temperature Boundary Condition 75
  CASE III: Nanoscale Volumetric Heat Generation 77
2.6 Conclusions 78
2.7 References 80

3. Thermal Conductivity of Two-Dimensional Nanocomposites 83
3.1 Introduction 83
3.2 Theoretical Model 87
  3.2.1 Unit Cell and Periodic Transport 87
  3.2.2 Transport across the wire direction 91
    Boundary Conditions 92
    Interface Conditions 94
    Numerical Simulation and Effective Thermal Conductivity 95
  3.2.3 Transport along the Wire Direction 96
3.3 Results and Discussions 101
  3.3.1 Transport across the Wire Direction 101
    Nonequilibrium Temperature and Heat Flux Distribution 101
    Effect of Wire Dimension 105
    Effect of Atomic Percentage 105
    Comparison with EMA 108
  3.3.2 Transport along the Wire Direction 111

3.4 Conclusions 114
3.5 References 116

4. Monte Carlo Simulation for Phonon Transport and Thermal Conductivity in Nanoparticle Composites 119
4.1 Introduction 119
4.2 Monte Carlo Simulation 121
    4.2.1 Computational Domain and Boundary Conditions 122
    4.2.2 Phonon Scattering 125
    4.2.3 Process Flow 127
    4.2.4 Convergence and Accuracy 129
4.3 Results and Discussions 129
    4.3.1 Code Validation - Bulk and 2-D Simulation 131
    4.3.2 Three Dimensional Periodic Structures 134
    4.3.3 Effects of Randomness 141
    4.3.4 Interfacial Area per Unit Volume (Interface Density) 143
    4.3.5 Temperature Dependence (Comparison with Experiments) 144
4.4 Conclusions 145
4.5 References 148

5. Surface-Plasmon Enabled Nonequilibrium Thermoelectric Refrigerators and Power Generators 149
5.1 Introduction 149
5.2 Theoretical Model 151
    5.2.1 Surface-plasmon Energy Transport Model 153
    5.2.2 Surface-Plasmon Coupled Nonequilibrium Thermoelectric Devices 157
    5.2.3 Material Property Selection 164
5.3 Results and Discussion 167
    5.3.1 Refrigerator 167
    5.3.2 Power Generators 174

5.4 Conclusions 177
5.5 References 178

6. Sub-picosecond Pump-and-Probe Characterization of Thermal Transport at Nanoscale 181
6.1 Introduction 182
6.2 Pump-Probe Experimental Setup and Data Acquisition 186
6.3 Model Development 192
6.4 Preliminary Experimental Results and Discussions 203
6.5 Summary and Future Work 209
6.6 References 210

7. Summary and Recommendations 213
7.1 Summary and Conclusions 213
7.2 Recommendations for Future Directions 215
7.3 References 217

List of Figures

1-1. (a). Phonon mean free path in silicon estimated on the basis of Eq. (1-2) and Eq. (1-3), using the reported data on the specific heat and the speed of sound. (b) The temperature dependent phonon mean free path for Si and Ge using Eq. (1-3). 25

1-2. Thermal wavelengths for representative energy carriers. At room temperature, the wavelength is around 10 Å for phonons. 26

1-3. Heat conduction between two spheres to mimic the heat transport process surrounding a heat generating spherical region embedded inside a semi-infinite medium and thus to illustrate the phonon rarefaction effect. 29

1-4. (a) A MOSFET made by IBM. MOSFET is the workhorse of today's IC industry. (b) The Monte Carlo simulation of electron transport at IBM shows that heat is mostly generated over a lateral dimension of ~10 nm on the drain side of the MOSFET. 34

1-5. Schematic demonstration of thermoelectric device configurations for (a) refigeration and (b) power generation. (arrows indicate carrier transport direction) 36

2-1. The phonon dispersion relation for Si and Ge, which related the phonon energy to its momentum. Reprinted from references [30, 31]. 52

2-2. In deriving the ballistic-diffusive heat-conduction equations, the local carrier distribution function f is divided into two parts: f_b which originates from the boundary f_w and experiences outgoing scattering only, and f_m which originates from the inside domain and is directed into the indicated direction either through scattering or through phonon emission by the medium. 55

2-3. Schematic drawing of device geometry simulated in this calculation: a) a confined surface heating at y=0, where T_1 and T_0 represent the emitted temperature in case I and the equivalent equilibrium temperature in case II. b) Case III: a nanoscale heat source embedded in the substrate, which is similar to the heat generation and transport in a MOSFET device. 63

2-4. Geometry and notation for the calculation of the ballistic component coming from the

boundary. 64
2-5. Numerical solution scheme of the ballistic-diffusive equations. 68
2-6. Local coordinate used in phonon Boltzmann transport simulation. 69
2-7. Directions of phonon transport in two-dimensional planes as given by different combinations of the direction cosines and the corresponding differencing schemes used for the BTE solver. 72
2-8. Comparison of the transient temperature and heat flux in the y direction at the centerline of the geometry for Kn = 10 based on the emitted temperature condition: (a) temperature, and (b) heat flux q_y^*. 74
2-9. (a) Comparison of the steady state temperature distribution at the centerline using the Fourier theory, the Boltzmann transport equation (BTE), and the ballistic-diffusive equations (BDE) for different Knudsen numbers. (b) Comparison of the heat flux q_y^* at the centerline for Kn= 0.1 at t^*=100. 75
2-10. Comparison of transient temperature and heat flux distribution at the centerline using the Fourier theory, the Boltzmann equation, and the ballistic-diffusive equations based on thermalized temperature boundary conditions: (a) and (b) heat flux q_y^*, (c) temperature. 76
2-11. The ballistic and diffusive component contributions to the total temperature and heat flux at the centerline: (a) temperature, and (b) heat flux q_y^*. 79
2-12. Comparison of the two dimensional temperature rise distribution after the device is operated for 10 ps. (a) the Boltzmann transport equation (BTE), (b) the Ballistic-diffusive equations (BDE), and (c) the Fourier law. 79
2-13. (a) Comparison of the heat flux distribution obtained by the Boltzmann transport equation (BTE), the ballistic-diffusive equations (BDE), and the Fourier law (Fourier) at the centerline (b) Comparison of the peak temperature rise inside the device obtained by the Boltzmann equation, the Ballistic-diffusive equations and the Fourier law. 80

3-1. There are two forms of nanocomposites: (a) nano-particles or nanowires embedded in a host matrix material,or (b) mixtures of two different kinds of nanoparticles. (c) This thesis focuses on periodic nanocomposites where nanoparticles or nanowires are embedded periodically in a matrix material. The periodic nanocomposite can be viewed as a periodic stack of unit cells, shown as red squares. 88

3-2. (a) Heat flow across a periodic 2-D composite with silicon wires embedded in the germanium host, (b) the unit cell to be simulated, (c) local coordinates used in the phonon Boltzmann equation simulation, (d) heat flow across a 1-D Si-Ge layered structure (superlattice). 92

3-3. (a). A periodic two dimensional nanocomposite (composite with tubular nanowire inclusions), (b) cross-sectional view of a unit cell: a square unit cell cross-section is approximated as a circular cross-section of equal area, (c) by the approximation in (b), the transport in nanocomposites becomes phonon transport in core-shell cylindrical structures, (d) periodic silicon nanowire composites, (e) cylindrical nanoporous silicon material. 98

3-4. Phonon transport in cylindrical coordinates. 99

3-5. Effective temperature (T-T_{ref}) distribution in the unit cell of $Si_{0.2}$-$Ge_{0.8}$ composites with $T(0,y) - T(L_{Ge},y) = 1$ K applied for different wire dimensions: (a) temperature contour for L_{Si} =268nm, (b) the temperature distribution along x^* at $y^* = 0.5$, $y^* = 0.7$ and $y^* = 0.85$ for L_{Si} =268nm, (c) temperature contour for L_{Si} =10nm, (d) the temperature distribution along x^* at $y^* = 0.5$, $y^* = 0.7$ and $y^* = 0.85$ for a L_{Si} =10 nm. The temperature discontinuity at the interface is clearly shown. The temperature distribution in a L_{Si} =10 nm nanocomposite is very different from macroscale composites due to ballistic phonon transport at the nanoscale and these effects cannot be captured by Fourier heat conduction theory. 103

3-6. The dimensionless heat flux distribution in the x-direction q_x^*: (a) L_{Si} =268nm composite, and (b) L_{Si} =10 nm composite. These results show that the x-directional heat flux is always positive even in the localized negative temperature gradient region shown in Fig. 3-5. 104

3-7. (a) Illustration to show the mechanisms of negative temperature gradient in the localized regions using the thermal radiation analogy. (b) the temperature distribution along x^* at $y^* = 0.5$, $y^* = 0.7$ and $y^* = 0.85$ for L_{Si} =10 nm over three periods. 104

3-8. The dimensionless average temperature distribution along the x direction in a $Si_{0.2}$-$Ge_{0.8}$ composite with a silicon wire dimension of L_{Si}=268 nm and L_{Si}=10 nm, respectively. 106

3-9. The thermal conductivity of $Si_{0.2}$-$Ge_{0.8}$ composites as a function of the silicon wire dimension or layer thickness. The smaller the characteristic length of silicon (the silicon wire dimension in composites and the thickness of the silicon layer in superlattices), the smaller is the thermal conductivity. 106

3-10. The thermal conductivity of Si_{1-x}-Ge_x composites as a function of atomic percentage x of germanium. For a fixed silicon wire dimension, the lower the atomic percentage of germanium, the lower is the thermal conductivity of the nanocomposites. The result is very different from the bulk material due to the ballistic nature of phonon transport at the nanoscale and the interface effect. 108

3-11. Illustration to show that phonons experience less cross-interface scattering in periodic 2-D composites (b) than that in 1-D layered structures (a) but they experience additional scattering parallel to the interface. The efficiency of cross-interface scattering to reduce the thermal conductivity is around 5 times as effective as scattering parallel to the interface. 109

3-12. Comparison of the thermal conductivity of nanowire composites in the direction perpendicular to wire axial direction obtained from a phonon Boltzmann equation simulation and from the effective medium approximation (EMA) based on the Fourier law and the thermal boundary resistance, demonstrating that the EMA underpredicts size effects. 110

3-13. Thermal conductivity of the silicon-germanium nanocomposite which comprises of a germanium matrix with silicon wire inclusions as a function of the silicon wire radius and the volumetric ratio. 112

3-14. Thermal conductivity of porous silicon along the cylindrical pore direction as a function of the pore radius and porosity. 113

3-15. The effect of the silicon core layer thickness and the pore size of tubular silicon wire inclusions on the effective thermal conductivity of the nanocomposites: (a) 50nm pore radius, (b) 10nm pore radius. 115

3-16. The solid thermal conductivity of the composites decreases as the pore radius increases due to the increasing surface scattering per unit volume. 116

4-1. (a) Periodic nanocomposite with cubic silicon nanoparticles dispersed periodically in a germanium matrix. (b) With the periodic boundary condition dictated in section 4.2.1, the Monte Carlo simulation of phonon transport in the computational domain (unit cell) represents phonon transport in the whole structure shown in Fig. 4-1(a). The unit cell (computational domain) is further divided into subcells. 123

4-2. The schematic process flow of the Monte Carlo simulation algorithm. The Monte Carlo simulation starts with the initialization step. After the initialization step, phonons experience moving (transport) and scattering in each time step. 128

4-3. Typical variation of the thermal conductivity values with respect to the calculation time. The case shown is a 2D nanocomposite with 10nm Si nanowires embedded in a Ge host. The result converges after 10ns of simulation, corresponding to 10000 time steps, with a variation of less than 0.1% afterward. 130

4-4. Comparison of the thermal conductivity value from the gray-medium Monte-Carlo simulation conducted in this work with the experimental thermal conductivity value of a bulk germanium sample. The experimental Ge value is taken from Ref. [35]. The circular symbols indicate the results of simulating a solid bulk material without any particle inside. The triangle symbol represents the simulation of a "pseudo composite", when both the particle and the host material are Ge. When the two sides of the interface both have transmissivity values of one, the simulation should equal that of a solid bulk material without any particles. This pseudo composite simulation served to validate the Monte Carlo coding. 132

4-5. Comparison of the temperature (energy density) distributions inside a nanowire composite obtained, respectively, by the deterministic solution of the phonon Boltzmann transport equation and Monte Carlo method. (a) Geometric dimensions of the unit cell for a $Si_{0.2}$-$Ge_{0.8}$ nanowire composite with a 10nmx10nm nanowire inclusion with z along the wire direction, (b) temperature distribution along the x direction at various y positions assuming heat flows in the x-direction. 133

4-6. Comparison of thermal conductivity values for the 2D nanowire composites obtained by a Monte Carlo simulation and by a deterministic solution of the Boltzmann transport equation. The relative percentage deviation is less than 8%. 134

4-7. Sketch of nanoparticle composites with silicon cubic nanoparticles distributed in an aligned pattern (a), in a staggered pattern (b), and randomly (c) in a germanium matrix for Monte Carlo simulation conducted in this work. Even in (c) the cubic nanoparticles are aligned in parallel to each other. The thermal conductivity values calculated in this work are all in the direction normal to the cubic nanoparticles. 135

4-8. Temperature distribution inside an aligned periodic nanoparticle composite in the middle plane in the z-direction. The dimension of the nanoparticle is 10nm X 10nm X 10nm. The volume fraction of Si particles is 3.7%, corresponding to a $Si_{0.04}$-$Ge_{0.96}$ atomic composition.

.... 136

4-9. Comparison of the heat flux at the hot (x=0) and cold ($x=L_x$) x boundaries in: (a) A periodic aligned nanoparticle composite, i.e., with one 10nm cubic particle inside a 14nm cubic unit cell; and (b) A random nanoparticle composite, i.e, with 10 nanoparticles, each of which is a 10nm cube randomly distributed inside a 40nmx40nmx40nm unit cell. The comparison demonstrates the periodicity of local heat flux in the x direction. 137

4-10. The effects of silicon nanoparticle size and distribution on the thermal conductivity of nanoparticle composites: (a) Comparison of the thermal conductivity of composites with 10nm and 50nm silicon cubic particles distributed in a simple periodic pattern in a germanium host and that of a Si-Ge alloy as a function of atomic composition. (b) The effect of the distribution pattern on the thermal conductivity of composites with 10nm silicon particle inclusions. Also shown in Fig. 4-10(b) is the thermal conductivity of a Si-Ge alloy. 139

4-11. Thermal conductivity of nanoparticle composites predicted by the Monte Carlo simulation (MC) conducted in this work and that predicted by the effective medium approximation (EMA) proposed by Nan et al. in Ref. [14]. . The EMA based on incorporating the thermal boundary resistance into the solutions of the Fourier heat conduction law underpredicts the size effects. 141

4-12. Comparison of the thermal conductivity of a periodically aligned nanocomposite with 50nm cubic silicon particles distributed in a germanium matrix and that of a random composite with silicon nanoparticles having a size range from 10 to 100nm distributed randomly in a germanium matrix as a function of germanium atomic composition. 143

4-13. The thermal conductivity of nanoparticle composites as a function of the interfacial area per unit volume (interface density). The thermal conductivity data of nanoparticle composites falls on to a single curve nicely as a function of interfacial area per unit volume. The randomness either in particle size or position distribution causes slight fluctuations. However, these fluctuations are not a dominant factor for the reduction in the thermal conductivity. The effective thermal conductivity of 2-D nanowire composites is lower than that of 3-D nanoparticle composites for the same interface area per unit volume, since the effectiveness of interface scattering on the thermal conductivity reduction is different when the interface is perpendicular to the applied temperature difference direction and when the interface is parallel to the applied temperature difference direction. 146

4-14. (a) The temperature-dependent thermal conductivity of nanoparticle composites. (b) Comparison of the simulated thermal conductivity with recent experimental results from Jet Propulsion Laboratory [16]. 147

5-1. Schematic drawing of surface-plasmon coupled nonequilibrium thermoelectric devices: (a) refrigerator, and (b) power generator. A nanoscale vacuum gap is used to avoid the direct contact of the heat source or the cooling target with the thermoelectric device, and thus cut-off the heat flow through phonons between the heat source or the cooling target and the thermoelectric device. 152

5-2. (a) Schematic of half-spaces of InSb separated by a vacuum gap of thickness d, (b) thermal resistance network of the surface-plasmon coupled nonequilibrium devices. 155

5-3. Spectral "absorptivity" of a 10 nm film of InSb separated from a InSb half space (emitter) by a 10 nm layer of vacuum. "Absorptivity" is defined as the ratio $(q_{inc}-q_{exit})/q_{inc}$. This figure shows that only 10 nm of InSb is necessary to absorb all the surface plasmon energy flux. It confirms that our approximation of treating the thermoelectric device as two half-spaces of InSb separated by a 10 nm layer of vacuum is valid. 156

5-4. Spectral flux between two half-spaces of InSb separated by a vacuum gap of thickness d = 10 nm and d = 100 nm. The plasma frequency is assumed to be 0.18 eV. The smaller peak corresponds to resonance due to surface phonon polaritons and the bigger peak corresponds to resonance due to surface plasmon polaritons. 156

5-5. Total energy transfer between two half-spaces of InSb. The hotter half-space is maintained at T_1 and the temperature of the colder half-space is varied. The x-axis is the temperature difference between the hot and cold bodies. The blackbody energy transfer, with the hotter half-space maintained at 500 K, corresponds to the y-axis on the left. The other curves correspond to the y-axis on the right. 157

5-6. The temperature drop in the surface plasmon supporting layer with a thin metal layer underneath under a cooling heat flux of q=50W/cm^2: (a) the electron (T_e-T_m) and phonon (T_p-T_m) temperature drop inside the surface plasmon supporting material layer, and (b) the temperature drop at the plasmon material surface as a function of the thickness of the surface-plasmon material. 168

5-7. Typical temperature and COP change as a function of the applied current under a cooling load. T_{0e} and T_{0p} are the electron and phonon temperatures at the cold end of the thermoelectric element (i.e., the interface between the vacuum gap and the thermoelectric device) respectively, and T_l is the cooling target temperature. Comparing to the minimum temperature T=250 K to that which the conventional refrigerator can reach at such a cooling load at its optimum current density $j_{conv.opt.}$, the surface-plasmon coupled nonequilibrium thermoelectric refrigerator can reach a much lower temperature. 169

5-8. (a) The minimum cooling temperature of the surface-plasmon coupled nonequilibrium thermoelectric refrigerator as a function of thermoelectric element length for various G values. The shorter the thermoelectric element length and the smaller the coupling constant G, the lower the minimum temperature can be reached. (b) the minimum temperature as a function of $\frac{GL^2}{k}$ for various k_e/k. 170

5-9. The temperature distribution inside a 50 μm surface-plasmon coupled nonequilibrium thermoelectric refrigerator when the minimum cold end temperature is reached (dashed lines – electron temperature, solid lines – phonon temperature). The smaller is the electron phonon coupling constant G, the larger is the temperature difference between electrons and phonons. 171

5-10. (a) The cooling target temperature changes with thermoelectric element length and the electron-phonon coupling constant under a load of q=50W/cm^2. (b) the COP of surface-plasmon coupled nonequilibrium thermoelectric refrigerator as a function of thermoelectric element length and electron-phonon coupling constant with the cooling target temperature at 250K. For low G value, the COP of surface-plamson coupled nonequilibrium thermoelectric refrigerator can be much higher than the maximum of the conventional thermoelectric refrigerator. 173

5-11. The cooling target temperature with and without consideration of the reverse energy flow due to surface phonon polaritons (dashed lines with symbols – without, solid lines with symbols – with) under a cooling load of 50W/cm^2. Though the surface phonon polariton degrades the cooling performance, the surface-plasmon coupled nonequilibrium devices have much better performance than conventional devices. 173

5-12. Typical change of the output power density and the energy conversion efficiency with the ratio of the external and internal thermal resistances $\mu = R_L / R_{TE}$. Compared to a conventional thermoelectric power generator, the surface-plasmon coupled nonequilbrium thermoelectric power generator has a much higher energy conversion efficiency over a wide range of $\mu = R_L / R_{TE}$ 174

5-13. (a) the optimum energy conversion efficiency as a function of thermoelectric element length for different electron-phonon coupling constant with k_e/k=0.10 and Z=0.002K^{-1} operating at T_1=500K and T_2=300K, (b) the corresponding electron temperature at the hot end of the thermoelectric element. (c) the electron (dashed lines) and phonon (solid lines) temperature distributions in a 50 μm surface-plasmon coupled nonequilibrium thermoelectric power generator when the heat source is maintained at 500K. 176

5-14. The energy conversion efficiency changes as a function of thermoelectric element length for different k_e/k. 177

6-1. Typical sample configurations for the ultrafast pump-probe method: (a) to measure the interface thermal resistance and the thermal conductivity of the substrate. (b) to measure the thermal conductivity of thin film and superlattice nanostructures. 185

6-2. A schematic diagram of the pump-and-probe experimental setup constructed in the W.M. Rohsenow Heat and Mass Transfer Lab. 187

6-3. Photos of the sub-picoseconds pump-and-probe experimental system housing in the Rohsenow Heat and Mass Transfer Lab. 188

6-4. The signal detection mechanisms of the sub-ps pump-and-probe measurement. 191

6-5. A typical temporal measurement curve which is constructed by moving the stage a small step and then measuring the amplitude and phase of the sine wave at that point, as described in Fig. 6-4. 192

6-6. The fundamental transport process across a metal-semiconductor interface and the idea of the newly proposed model is to extract the interface phonon reflectivity and phonon relaxation time (□) by fitting the experimental data of the pump-probe measurement rather than fitting the interface thermal resistance and the thermal conductivity of the substrate. ·193

6-7. Model hierarchy for the description of the energy transport processes for ultrafast laser-material interactions. The conventional two temperature model which assumes that the electrons and phonons are in nonequilibrium and the phonon/lattice thermal transport is diffusive. This model is often used to fit the nonequilibrium electron-phonon coupling factor G from experiments. The other set of models that is often used to fit the interface thermal resistance and the thermal conductivity of the layer underneath the metal layer assumes that the metal layer is a lumped thermal mass. Both the conventional heat diffusion models are subsets of the newly proposed electron Fourier heat conduction and phonon Boltzmann transport model. 197

6-8. The electron and phonon temperatures rise after femtoscond laser heating. For the nonequilibrium models, the temperature shown is the front surface temperature. Tm is the lumped average temperature of the metal layer for the lumped model often used for the thermal interface resistance measurement. (a) The electrons and phonons are in nonequilbrium conditions at a short time scale, ~ tens of ps, but the difference of the nonequilibrium Fourier model and the nonequilbrium BTE model is negligible. (b)&(c), the difference between the electron and phonon temperatures at the front surface at large timescales is negligible. The difference between the nonequilibrium Fourier model and the nonequilbrium BTE model clearly shows a much slower phonon ballistic transport process. 200

6-9. The normalized temporal cooling curve. (a) The normalized temperature decay curve is different for the heat diffusion model and the nonequilibrium BTE model from 50ps to 2000ps, which is often the range of the pump-probe experiment. The temperature decays much more slowly for the phonon BTE model which would result in a much smaller thermal conductivity and a larger thermal interface resistance if one is trying to fit the phonon BTE results with the Fourier results. (b) If one fits the results with normalization to 1 ns and uses a much longer decay curve, say 10ns, one would find that the nonequilibrium Fourier results agrees very well with the nonequilibrium BTE results. 202

6-10. (a) The distributions of the temperature rise close to the interface region at various transients. (b) The distributions of the normalized temperature distribution close to the interface regime. This figure shows the relative contribution of the thermal resistance in the metal layer and the interface thermal resistance to the overall thermal resistance for the energy relaxation from the metal surface deeply into the semiconductor interface. 203

6-11. Raw experimental signals at different laser pumping intensities: (a) amplitude at a long time scale, ~ns, shows a fast peak in the beginning and a slow decaying process later, (b) The fast peak is an indication of the electron-phonon energy exchange that occurs during the ~10 ps time scale, (c) the raw phase signal. 205

6-12. The transient amplitude signal normalized to the amplitude of the signal at 50ps: (a) the fast peak is an indication of the electron-phonon energy exchange that occurs during the ~10 ps time scale, (b) the slow decaying process due to the energy transport through the interface and the substrate. 206

6-13. (a) Time evolution of the reflectivity change measured in the experiment. Time t=0 refers to the absorption of the first pump pulse after the laser is turned on. The time axis is in units of the time between pump pulses. The measured signal is a superposition of many pump pulses. (b) A comparison of the single pulse signal and the measured signal when we normalized both signals to their own maxima. 207

6-14. Comparison of single pulse modeling results with the experimental signal by changing (a) the phonon transmissivity at the interface and (b) the phonon relaxation time. None of the reasonable data input would be able to capture the fast decaying measured signal. This plot clearly demonstrates the importance of the multi-pulse effect. 208

List of Tables

5-1. Experimental data of the energy relaxation time (after Reference [29]). 166

Chapter 1. Introduction

1.1 Introduction

Heat transfer at the nanoscale may differ significantly from that in macro and microscales. With device or structure characteristic length scales becoming comparable to the mean free path and wavelength of heat carriers (electrons, photons, phonons, and molecules) or the time of interest is on the same order as the heat carrier relaxation time, classical laws are no longer valid and size effects become important [1-4]. Well-known examples are the failure of the Fourier law to predict the thermal conductivity of composite nanostructures such as superlattices, which is a simple periodic stack of alternate nanometer material layers [5, 6] and the failure of the Stefan-Boltzmann law in predicting radiation heat transfer across small gaps [7, 8]. Although much has been done in this area recently, there is still an immediate need for a better understanding of thermal phenomena in nanostructures. There are typically two types of problems. One is the management of heat generated in nanoscale devices to maintain the functionality and reliability of these devices. Examples are the heating issues in integrated circuits [9] and in semiconductor lasers [10]. The other is to utilize nanostructures to manipulate heat flow and energy conversion. Examples include nanostructures for thermoelectric and thermionic energy conversion [11, 12], for data storage [13] and for nano-diagnostics [14]. This thesis deals with both types of problems.

This chapter provides necessary background and gives an overview for this thesis. Section 1.2 discusses the fundamentals of nanoscale heat conduction including the characteristic length of phonon carriers and the particularities of nanoscale heat transfer, especially rarefied phonon heat conduction and nonequilibrium effects between energy carriers. Section 1.3 briefly discusses the importance of nanoscale heat transfer in nanoelectronics and section 1.4 provides the necessary background for thermoelectric energy conversion. Section 1.5 outlines the scope and the organization of this thesis.

1.2 Fundamentals of Nanoscale Heat Conduction

At the macroscale, heat conduction is predicted by the Fourier law,

$$q = -k\nabla T \qquad (1\text{-}1)$$

where k is the thermal conductivity, q is the heat flux, and ∇T is the temperature gradient. The Fourier law is a diffusion equation and the thermal conductivity is a materials property, which may depend on the detailed microstructure of the material but is independent of the size of the material.

At the nanoscale, the conduction of heat by energy carriers can be a ballistic process that is similar to photon transport in thermal radiation. Thermal conductivity is no longer only a materials property. Heat conduction in dielectric materials and most semiconductors is dominated by phonons. Size effects appear if the structure characteristic length is comparable to or smaller than the phonon characteristic lengths. Two kinds of size effects can exist: the classical size effect, when phonons can be treated as particles, and the wave effect, when the phonon wave phase information becomes important. Distinctions between these two regimes depend on several characteristic lengths, which we discuss below [3].

1.2.1 Characteristic Lengths

The important characteristic lengths of phonon heat conduction are the mean free path, the phonon wavelength, and the phase coherence length [3]. The mean free path is the average distance that phonons travel between successive collisions. The corresponding average time between successive collisions is the collision-free time, which is often referred to as microstate relaxation time. Direct calculation of the mean free path is generally difficult, particularly for electron and phonon transport in solid. The kinetic theories and experimental conductivity data are often used to estimate the mean free path according to

$$k = \frac{1}{3} C v^2 \tau = \frac{1}{3} C v \Lambda \qquad (1\text{-}2)$$

$$k = \frac{1}{3} \int_0^{\omega_{\max}} C_\omega v_\omega{}^2 \tau_\omega d\omega = \frac{\Lambda}{3} \int_0^{\omega_{\max}} C_\omega v_\omega d\omega \qquad (1\text{-}3)$$

where C is the volumetric specific heat, i.e. the specific heat per unit volume, τ the relaxation time, v the velocity of carriers. The integration in Eq. (1-3) is over all the phonon frequency and correspondingly, C_ω , v_ω , and τ_ω are the volumetric specific heat, the velocity, and the relaxation time at each frequency, respectively. If Eq. (1-2) is used to estimate the phonon mean free path with the measured specific heat and the speed of sound, the mean free path can be an order of magnitude lower than that based on Eq (1-3) [15-17]. The consideration of the frequency dependence is necessary because phonons are highly dispersive. In Fig. 1-1(a), we show the phonon mean free path in silicon which is estimated based on Eq. (1-2) and Eq. (1-3), using the reported data on the specific heat and the speed of sound.

Energy carriers have particle-wave duality. The phase and the frequency/wavelength are the two most important characteristics of carrier waves. The phase of a wave can be destroyed during collision, which is typically the case in inelastic scattering processes, such as the electron-phonon collision and phonon-phonon collision. An inelastic scattering process is the one that involves the energy exchange between carriers. If the phase destroying scattering process occurs frequently inside the medium, the wave characteristic of carriers can be ignored and the transport falls into the particle diffusion regime. Not all the scattering processes, however, destroy the phase. Elastic scattering processes such as scattering of photons by particulates and the scattering of electrons by impurities do not destroy phase. Thus, the phase coherence length is usually longer than the mean free path, but it is not much longer, particularly at room temperature for the electrons and phonons. Therefore we can treat them as having the same order of magnitude.

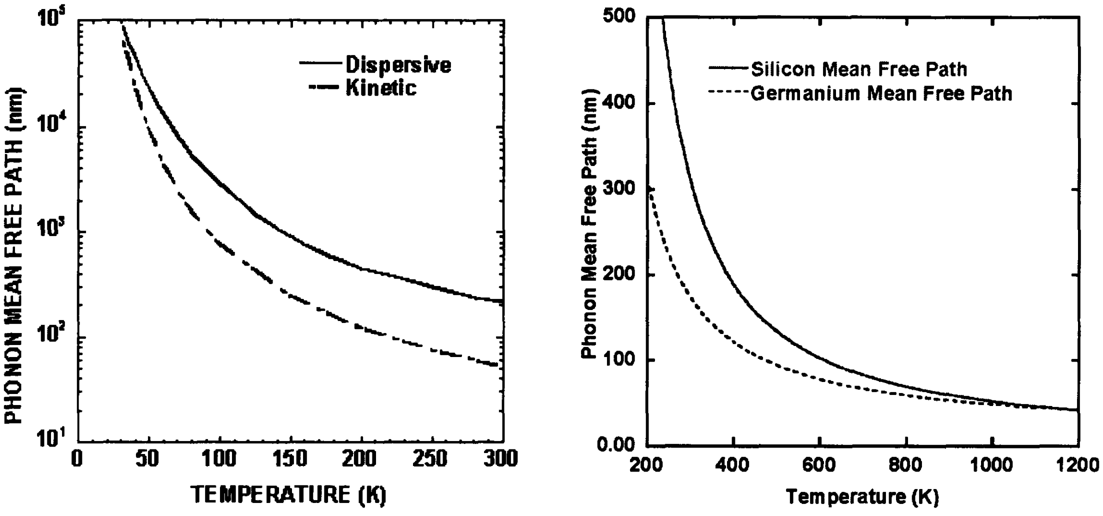

(a) (b)

Figure 1-1. (a). Phonon mean free path in silicon estimated on the basis of Eq. (1-2) and Eq. (1-3), using the reported data on the specific heat and the speed of sound. (b) The temperature dependent phonon mean free path for Si and Ge using Eq. (1-3).

The phonon wavelength in a crystal spans a wide range. Long wavelength phonons have a wavelength that is comparable to the crystal size. The shortest phonon wavelength is just twice of the lattice constant. However, not all the phonons in the wide range of wavelengths contribute equally to thermal transport. The actual probability of excitation for a specific quantum mechanical state depends on the energy of the state and the temperature of the object as governed by the Fermi-Dirac distribution for electrons and the Bose-Einstein distribution for phonons and photons. We can estimate the order of magnitude of the average wavelength of the energy carriers, λ_t , by assuming the average energy of one quantum state is κ_B T/2, where κ_B(=1.38x10^{-23} J/K) is the Boltzmann constant and calculating the corresponding wavelength from the Planck relation E=hν for phonons and photons, where h (=6.6x10^{-34} J·s) is the Planck constant, p the momentum and ν the frequency. This leads to,

$$\lambda_t = \frac{2\text{hv}}{\kappa_B T} \tag{1-4}$$

where v is the speed of carriers. Fig. 1-2 shows the phonon wavelength in silicon. At room temperature, the wavelength is around 10 Å for phonons.

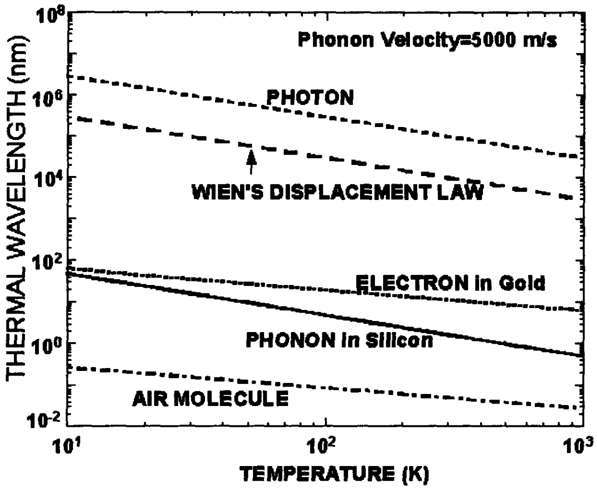

Figure 1-2. Thermal wavelengths for representative energy carriers. At room temperature, the wavelength is around 10 Å for phonons.

Size effects appear if the structure characteristic length is comparable to or smaller than the phonon characteristic lengths, i.e. mean free path, wavelength and phase coherence length of energy carriers.

1.2.2 Wave vs. Particle Size Effects

A key question in understanding phonon transport is whether one should treat phonons as waves or as particles. When treating them as waves, the phase information carried by waves should be included. The superposition of waves leads to interference, diffraction, and tunneling phenomena that also exist in other types of waves. Using the three characteristic lengths discussed above, we make the following qualitative observations.

One necessary condition for the inclusion of wave effects is that the mean free path (phase coherence length) should be comparable or longer than the structure characteristic length, such as the thickness of a film or the diameter of a wire, so that the phase of the wave can possibly be conserved. This condition, however, is not sufficient for actually observing the wave effects because of three additional factors: (1) interface scattering processes, (2) the wavelength of the carriers, and (3) the spectrum of the carriers, as explained below.

When a wave meets an interface, it will be scattered. The most familiar example is the reflection and refraction of optical waves [18]. Phonon waves show similar processes. For a flat interface, the phases and directions of the refracted and reflected waves are fixed relative to the incident waves. Thus, these processes do not destroy phase. Periodic interface corrugations are another example for which the incident and outgoing waves have clear fixed phase relations. Rough interfaces, however, are more complicated. If the detailed interface roughness structures are known and if the interface interaction is elastic, the directions of the reflected and refracted waves can be determined in principle. In reality, this is rarely possible and rough interface scattering is often assumed to be diffusive, i.e., the reflected and transmitted waves are isotropically distributed into all directions. Usually, the accompanying assumption is that the relationship between the phases of the reflected, transmitted and incident wave is lost, i.e., the scattering is phase randomizing. Such an assumption cannot be justified easily but appears to be true in many transport processes, particularly for phonons. In addition to elastic scattering, the inelastic scattering can be also strong at the interfaces and such scattering processes are phase breaking. Thus, interface scattering can be approximated as phase breaking if the interface is rough, and as phase preserving if it is smooth. Whether an interface is rough or smooth depends on the average roughness, δ, compared to the wavelength λ. We can approximately take [19]

$$\frac{\delta}{\lambda}\begin{cases} >> 0.1 & (Rough) \\ << 0.1 & (Smooth) \end{cases} \tag{1-5}$$

Thus, if interface scattering is diffuse, the wave aspects of energy carriers can be neglected and size effects, which appear when the characteristic dimension of the structure is comparable or larger than the mean free path, fall into the classical regime. The short phonon thermal wavelength suggests that the particle picture and classical size effects dominate except at very low temperatures when both the mean free path and thermal wavelength are long.

1.2.3 Nanoscale Heat Conduction Phenomena

Even when the phone transport falls in the particle picture or classical size effect regime, there are a range of unique heat conduction phenomena that are important at the nanoscale. The most distinguishable examples are thermal boundary resistance at interfaces and thermal conductivity reduction for simple nanostructures, including nanowires, thin films, and superlattice. For heat conduction perpendicular to an interface, phonon reflection implies that the energy carried by heat carriers will be reduced compared to the case when there is no interface, or equivalently, a resistance for heat flow exists at the interface. This phenomenon, called Kapitza resistance or thermal boundary resistance, has been known since the pioneering work of Kapitza for the liquid helium-solid interface and Little for the solid-solid interface [20, 21], and extensive experimental and theoretical studies have been carried out on these topics in the past. For two solids in perfect contact, the thermal boundary resistance is on the order of 10^{-8}-10^{-9} m^2K/W. Such a thermal boundary resistance corresponds to the thermal resistance of a solid layer of thickness 1 nm - 1 μm with a bulk thermal conductivity of 1-100 W/m-K. When dealing with films of comparable thickness or smaller, the interface thermal resistance contributes significantly to the total thermal resistance.

The most intensive research in nanoscale heat transfer is the measurement and the modeling of the thermal conductivity of thin films, superlattices, and more recently nanowires, due to their importance for nanoelectronics, photonic and thermoelectric devices. Reviews can be found in Ref. [22, 23]. Experimentally, it has been observed that the thermal conductivity of these low-dimensional nanostructures can be one or two orders of magnitude lower than the thermal conductivity values calculated based on the Fourier law, using the properties of their parent materials [24-30].

Here I present in particular two slightly not well-known phenomena, which are closely related to my thesis work: the phonon rarefaction effect and nonequilibrium heat conduction processes between different heat carriers.

Phonon Rarefaction Effect. Although the thermal conduction reduction in thin films and nanowires is a well-known phenomenon, the size effects outside for heat conduction external to nanostructures have not received much attention. Heat generated inside nanoscale regions or nanostructures eventually will be conducted to the surroundings. When the heat generation region or the size of the nanostructure is smaller than the mean free path of the heat carriers in the surrounding medium, the temperature rise of the nanostructure can be much higher than that predicted by the Fourier law [31]. To see why this occurs, we consider the heat conduction surrounding a heat generating spherical region embedded inside a semi-infinite medium, as shown in Fig. 1-3. The Fourier law leads to the following relation between heat transfer rate, Q, and the temperature rise at the surface of the sphere, T_s,

$$\mathrm{Q(Fourier)} = 4k\pi r\left(T_s - T_\infty\right) = \frac{4\pi}{3} rCv\Lambda\left(T_s - T_\infty\right) \qquad (1\text{-}6)$$

where T_∞ is the temperature of the medium away from the sphere and r is the radius of the sphere, and we have used the kinetic expression, Eq. (1-2), for the thermal conductivity. When the diameter of the nanosphere is much smaller than the mean free path of the heat carrier in its surroundings, however, we can neglect the scattering and treat the heat transfer between the region and its surroundings as a radiation process. This approach leads to the following solution for the heat transfer,

$$\mathrm{Q(radiation)} = \pi r^2 Cv(T_{s,e} - T_\infty) \approx 2\pi r^2 Cv\left(T_s - T_\infty\right) \qquad (1\text{-}7)$$

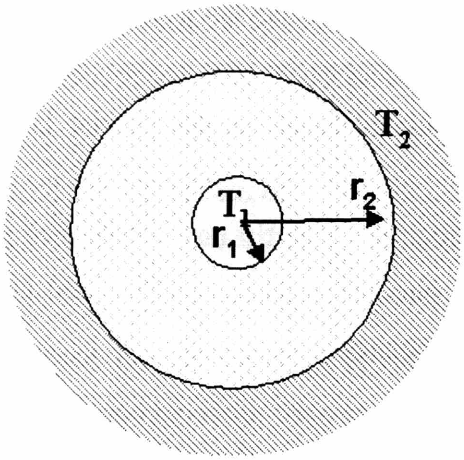

Figure 1-3. Heat conduction between two spheres to mimic the heat transport process surrounding a heat generating spherical region embedded inside a semi-infinite medium and thus to illustrate the phonon rarefaction effect.

where we have used $T_{s,e}$ to represent the temperatures of the phonons coming out of the nanoparticle or the emitted phonon temperatures. If there is no reflection at the interface, the surface temperature, as used in the Fourier law, is related to the emitted phonon temperature through, $T_s=0.5\cdot(T_{s,e}+T_\infty)$, which leads to the second equality of Eq.(1-7). Comparing Eq. (1-7) with Eq. (1-6), we can see that

$$\frac{Q(\text{Fourier})}{Q(\text{Radiation})}=\frac{2\Lambda}{3r} \tag{1-8}$$

Thus, in the limit where the mean free path is much larger than the sphere radius, the Fourier law over-predicts the heat transfer rate. This is because the Fourier law is only applicable when there is not a large temperature gradient within one mean free path. For the above example, the application of the Fourier law to a region much smaller than the mean free path (surrounding the sphere where the temperature varies significantly) inherently implies that there is strong scattering in this region, which is only true when the mean free path is much smaller than the region, while in reality, the mean free path corresponding to the bulk thermal conductivity is much larger.

Nonequilibrium between Energy Carriers. In dealing with nanoscale heat transfer, it is important to identify where and how heat is generated and how heat is exchanged between different groups of heat carriers. For example, the electric field in some devices such as a MOSFET easily reaches 10^6 V/m (1Volt across 1 micron). Depending on the electron-phonon heat exchange rate, the electrons can be heated to a much higher temperature than the phonons. Such hot electron effects occur when the electric fields become higher as the feature size shrinks. The temperature difference between the electrons and phonons would be $\sim 10^4 - 10^5$ K for a typical mobility of 10^2 cm^2/V s. Apparently the conventional assumption that the electrons and phonons are under local equilibrium in modeling transport phenomena, is no longer valid. This hot electron phenomena, nonequilibrium between electrons and phonons, also happens in the case of laser-materials interactions where the electrons can be thrown out of equilibrium with the lattice due to excitation by an ultra-short laser pulse [32].

In addition, different group of phonons have very different characteristics and they can be out of equilibrium with each other. For example, electrons interact more readily with optical phonons, particularly polar optical phonons as in GaAs [33, 34]. The optical phonons, however, do not carry heat as efficiently as acoustic phonons. Consequently, depending on the energy exchange rate between optical phonons and acoustic phonons, hot optical phonons under some circumstances can be generated. Due to the large dispersion of acoustic phonons, it is also possible that acoustic phonons are significantly out of equilibrium with each other.

Along the same line of reasoning, the coupled electron-phonon transport is the basis for solid-state energy conversion such as thermoelectric and thermionic cooling and power generation. Taking thermoelectric cooling as an example, electrons take energy away from phonons at a metal-semiconductor interface, carrying the energy to the hot side, and rejecting it to phonons. Although macroscopic thermoelectric phenomenon is well understood [35], some questions remain, such as what happens at the interface and how phonons are cooled and heated by electron systems.

1.2.4 Characterization of Nanoscale Heat Transfer

There are two key experimental directions in studying nanoscale heat transfer phenomena. One is the thermophysical property measurements of nanostructures such as thin films and nanowires. The other is the temperature measurements and particularly, temperature mapping surrounding nanoscale devices. During the last decade, remarkable progress has been made in the area of microscale thermometry, which can now allow temperature measurements at length and time scales comparable to the mean free paths and relaxation times of energy carriers in solids. As reviewed in [36], the two most renowned techniques are: (1) scanning thermal microscopy for high spatial resolution thermal imaging; and (2) scanning optical thermometry that combines high spatial and temporal resolution measurements.

Measuring thermophysical properties is always a challenging task, even at the macroscale. The thermophysical property characterization of nanostructures and microstructures is even more challenging. A variety of measurement techniques, using electrical, optical, and the hybrid sensing methods have been developed [3, 36, 37]. The two most successful methods for measuring the thermal conductivity of thin films and superlattice are the 3 ω method and the transient thermoreflectance method (TTR), which is also called the sub-picoseconds pump-probe method since this method utilizes an ultrafast (subpicosecond) laser. The 3 ω method, initially developed for measuring the thermal conductivity of bulk materials [38], is currently the most popular method for measuring the thermal conductivity of thin films where the thermal conductivity of thin films down to 20 nanometers in thickness has been measured [39, 40]. More recently, the method has been extended to study the thermal conductivity of nanowires and carbon nanotubes [41, 42].

In the optical pump- probe method, sub-picosecond time resolution is made possible by splitting the ultrafast laser output into an intense heating pulse, i.e. "pump" beam, and a weaker "probe" beam, and controlling the optical path length difference between the pump and probe beam through a mechanical delay stage [43]. The details will be described in chapter 6. The optical path length difference results in variable time delay between the pump and the probe beams. The pump beam is used to generate a temperature change at the sample surface. The decay of the temperature rise is measured by the reflected energy of the probe pulse series, where the probe takes a snapshot of the reflectance at a specific experimental time delay relative to the pump. The temporal resolution of the optical pump-probe method is on the order of the probe pulse duration. By localizing the energy deposition spatially and temporally, it is possible to monitor thermal changes in both the electron and phonon lattice systems with very high resolution, thus allowing for observation of electron–phonon relaxation dynamics, interface thermal resistance, and thermal conductivity of nanostructures, especially for superlattices and thin films [36, 44, 45]. Understanding the energy deposition and transport process in the material after ultrafast laser illumination is of significant importance for the pump- probe method. Whether the sub-picosecond pump-probe optical measurement can be used to study the fundamentals of phonons, such as the phonon reflectivity at an interface and the phonon relaxation time, like it does for electrons, needs further exploration.

1.3 Applications of Nanoscale Heat Transfer in Nanoelectronics.

The thermal management of microelectronics has already become a challenging issue. Commercial integrated circuits are currently available with transistors whose smallest lateral feature size is around 65 nm and the thinnest material films are below 2 nm, or only a few atomic layers thick. Such miniaturization has led to tremendous integration levels, with more and more transistors assembled together on a smaller area, together with more functionality. The technology advance is likely to follow the current miniaturization trend as summarized by Moore's law in the coming years. However as the gate length continues to decrease, it is also predicted that the operating voltage cannot be correspondingly reduced for maintaining a low leakage current and thus the device operating power cannot be reduced below a certain level [46]. The "power problem," i.e., the heat generation and chip temperatures reaching a level that will prevent the reliable operation of the integrated circuits. The chip-level power densities are currently on the order of 100 W/cm^2. How to avoid the hot spots on the chip where higher temperatures occur at a localized millimeter functional region is a hot topic today for chip and integrated circuit designers. While much of the attention has been focused on chip level packaging, nanoscale heat transfer effects including the thermal conductivity reduction of thin films and the phonon rarefaction effect discussed above may further complicate the problem in the performance and design at the device level. For example, figure 1-4(a) shows an SEM picture of a nanoscale MOSFET and figure 1-4(b) shows that heat is mostly generated on the drain side over a lateral dimension of ~10 nm in MOSFETs through the Monte Carlo simulation of electron transport. The rarefied phonon heat conduction effect discussed above means that the device temperature rise can be much higher than the prediction employing the Fourier law. In addition, nonequilibrum between optical and acoustic phonons can further increase the local temperature rise [46]. Microelectronic devices are pushing to tens of gigahertz clock frequency with a much shorter transient time. Energy transduction mechanisms at such short time scales can differ significantly from that at the macroscale. Understanding how the heat is generated and transported at the nanoscale has significant implications for the reliability of nanoelectronic devices.

1.4 Thermoelectric Energy Conversion

Energy conversion is a field that may greatly benefit from nanoscale energy transport phenomena. An example is thermoelectric cooling and power generation based on the Peltier effect and the Seebeck effect, respectively [47].

Thermoelectricity investigates the direct conversion of thermal energy into electric energy and vice versa. The fundamental physical reason for thermoelectric phenomena is the fact that the electrical carriers are also heat carriers at the same time. Therefore, the electron movement can be driven not only by the electrical potential, but also by a thermal potential. The basic physical effects in thermoelectricity are the Seebeck effect and the Peltier effect, named after the early investigators of these effects. The Seebeck effect is defined as how much of an electromotive force, or voltage, arises when the two ends of a material are maintained with a temperature difference between them. When a current passes through a thermocouple, the heat is transferred from one junction to the other; and thus the temperature of one junction increases and the other decreases. This phenomenon is called the Peltier effect. The magnitude of this heat transfer rate is proportional to the electrical current and the ratio is called the Peltier coefficient.

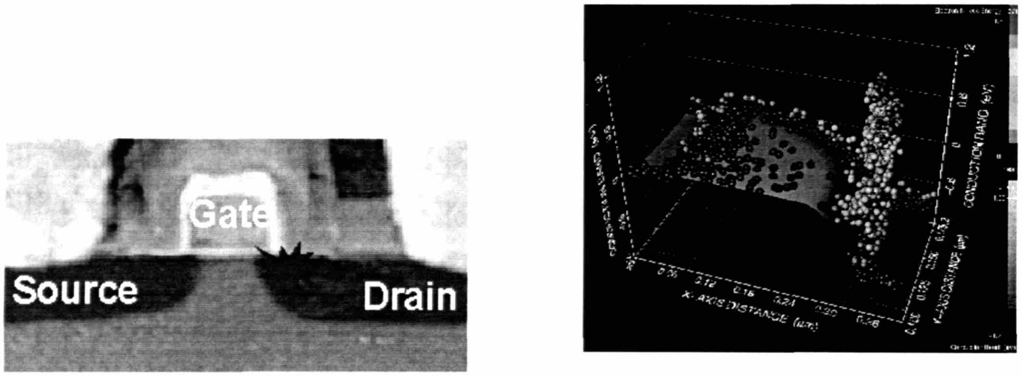

(a) (b)

Figure 1-4. (a) A MOSFET made by IBM. MOSFET is the workhorse of today's IC industry. (b) The Monte Carlo simulation of electron transport at IBM shows that heat is mostly generated over a lateral dimension of ~10 nm on the drain side of the MOSFET.

As an approach to realize direct energy conversion, thermoelectricity can be used for both cooling and power generation, depending on whether the work is taken from or put into the system. Figures 1-5(a) and (b) are schematic diagrams showing typical thermoelectric refrigeration and power generation devices. The basic thermoelectric device is a thermocouple composed of one n-type leg and one p-type leg. When used for cooling, an electrical potential is supplied to the device, as shown in Fig.1-5(a). The electrical potential will drive electrons and holes to flow in n-type leg and p-type legs respectively. Since the flow directions of electrons and holes are opposite to each other, the heat carried by both carriers in the two legs is always transported from the low temperature heat source to the high temperature heat sink. When used for power generation, the device is put in between a high temperature heat source and a low temperature heat sink, as shown in Fig.1-5(b). Electrons and holes are driven by the temperature gradient to diffuse from the hot to the cold side, which creates an electromotive force in the n-type and p-type legs, respectively. Since the electromotive forces are of opposite signs between the two legs, they add up and can be used to supply power to the external load.

The efficiency of a thermoelectric device is determined by the thermoelectric figure-of-merit of the material $ZT = \sigma S^2T/k$, where S is the Seebeck coefficient, σ is electrical conductivity, k is the thermal conductivity and T is the absolute temperature. The central issue in thermoelectrics research is to increase the thermoelectric figure of merit ZT. The best thermoelectric materials were succinctly summarized as "phonon-glass electron-crystal" material (or PGEC in short), which means that the materials should have a low lattice thermal conductivity as in a glass, and a high electrical conductivity as in crystals [48]. The best thermoelectric materials are found in heavily doped semiconductors. Insulators have poor electrical conductivity and metals have a low Seebeck coefficient. In semiconductors, the thermal conductivity has contributions from both electrons (k_e) and phonons (k_p), with the majority usually coming from phonons. The phonon thermal conductivity can in some cases be reduced without causing too much reduction in the electrical conductivity. A proven approach to reduce the phonon thermal conductivity is through alloying proposed in the late 1950's [49]. The mass difference scattering in an alloy reduces the lattice thermal conductivity significantly without much degradation to the electrical conductivity. The commercial state-of-the-art thermoelectric cooling materials are based on alloys of Bi_2Te_3 with Sb_2Te_3 (such as $Bi_{0.5}Sb_{1.5}Te_3$, p-type) and Bi_2Te_3 with Bi_2Se_3 (such as $Bi_2Te_{2.7}Se_{0.3}$, n-type), each having a ZT at room temperature approximately equal to one [50]. As shown in Figure 1, the progress since 1960s in improving ZT had been very slow before the 1990s. The value of the maximum ZT had essentially remained around one. The landscape in thermoelectrics research changed quite significantly in the 1990s due to several new conceptual developments leading to a renewed interest from several US research funding agencies. Low-dimensional materials, such as quantum wells, superlattices, quantum wires, and quantum dots offer new ways to manipulate the electron and phonon properties of a given material [51] after the groundbreaking work by Hicks and Dresselhaus [52,53,54,55]. Most significant enhancements of the thermoelectric figure-of-merit were reported in Bi_2Te_3/Sb_2Se_3 superlattices along the cross-plane direction [56] and PbTe/PbTeSe quantum-dot superlattices along the film-plane direction [57].

Although superlattice-based materials are the best systems for proof of principle studies and they have the highest reported ZT values today, superlattice-based materials are likely to be very expensive and difficult to scale up for large scale applications [58]. The difficulty in making high performance devices from superlattices and in characterizing their ZT also shows one major challenge in using these materials for example for making thermoelectric coolers. Thin film or superlattice-based thermoelectric devices which are around 1 – 10 micron thick suffer seriously from various losses and additional electrical and thermal resistances [59]. How to scale up the physics responsible for reported high ZT in superlattices into mass-producible cost-effective bulk thermoelectric materials and devices is a challenge for thermoelectricians today. This thesis will investigate the potential of nanocomposite materials for thermoelectrics applications.

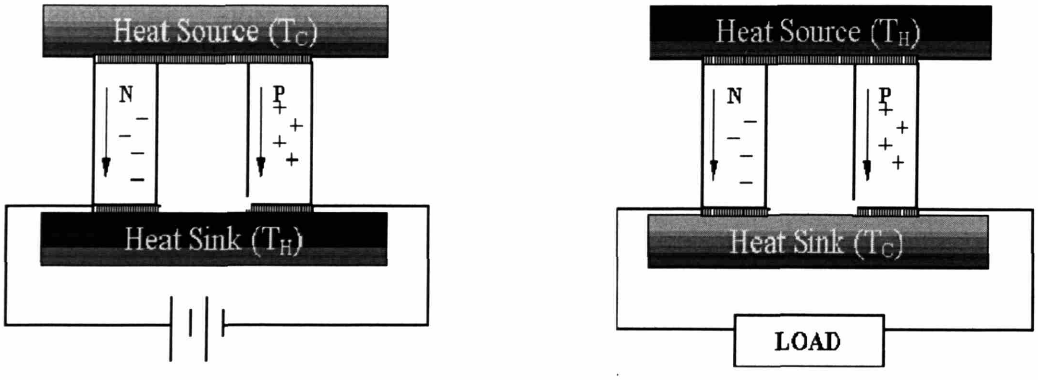

(a) (b)

Figure 1-5. Schematic demonstration of thermoelectric device configurations for (a) refigeration and (b) power generation. (arrows indicate carrier transport direction)

1.5 The Scope and Organization of this Work

The research on the size effect of heat transfer dates back to Casimir's pioneering work in the 1930's [60] and the resurgence of the effort starts around early 90's due to progress in micro and nano fabrication. However, most research has focused on heat transfer in simple nanostructures, for example, the theoretical prediction and experimental demonstration of thermal conductivity reduction of thin films, superlattices, and nanowires. In reality, there is also a large demand to study phonon transport in complex nanostructures. Examples are how heat generated in nanoelectronic device, where the heated region is often much smaller than the phonon mean free path, will be transported out, and how the thermal conductivity in nanocomposites which consists of nanowires or nanoparticles embedded in a matrix material, is different from that of macroscale composites. Often such kinds of problems are multiscale problems. Another class of problems, which are rich in physics and might be explored for better design of both nanoelectronic devices and energy conversion materials and devices, are coupled electron and phonon transport problems. Experimentally, most of the past work has been focused on the thermal conductivity characterization of various nanostructures and very little has been done on the fundamental properties of phonon transport, for example the phonon reflectivity at the interfaces and the phonon relaxation time in the bulk material.

This thesis work has been focused to contribute to the following aspects of heat transfer, nanoelectronics and thermoelectrics: 1) Developing simulation tools for transient phonon transport in multidimensional nanostructures and studying the predicted size effect on heat transfer surrounding a nanoscale heat generating region, i.e., the temperature rise in nanoelectronic devices, where heating is becoming a limiting factor for further scaling for electronic devices according to the semiconductor roadmap. 2) Proposing semiconductor nanocomposites for highly efficient thermoelectric materials development where the reduction of thermal conductivity is a blessing for efficiency enhancement. Both deterministic solution of the phonon Boltzmann equation and Monte Carlo simulations are established to study the size effect on thermal conductivity of nanocomposites where nanoparticles and nanowires are embedded in a host material. 3) Exploring the possibility of creating nonequilibrium conditions between electrons and phonons in thermoelectric material using the high energy flux coupling to electrons through surface plasmons, and thus to develop highly efficient thermoelectric devices. 4)

Establishing a sub-pico second optical pump-probe measurement system where a femtosecond laser is employed and exploring the possibility of extracting phonon reflectivity at the interfaces and phonon relaxation time in a material, which are the two most fundamental properties for nanoscale energy transport from pump-probe measurements. To this end, this thesis is organized as following.

It has been demonstrated in the last decade that the Boltzmannn transport equation (BTE) is a valid and useful tool for studying the classical size effect of phonon transport at the nanoscale. However, the solution of the phonon BTE has been limited to a few simple geometrical configurations, such as thin films, superlattices and nanowires. The inherent difficulties associated with the solution of the phonon BTE have significantly limited the consideration of the size and transient effects in multidimensional real engineering problems. Fewer studies have gone beyond non-planar and multidimensional geometries [61-63]. One of the objectives of chapter 2 is to develop numerical solution strategies for solving the transient phonon BTE in multidimensional structures. Modeling the multidimensional heat conduction processes in most devices involving multiple length scale devices from nanoscale to macroscale is very challenging. Direct numerical solution of the phonon BTE is preferred, but it is usually slow to implement such solutions. Approximate methods that are capable of capturing the major size effects but easier to implement are thus desirable. A ballistic-diffusive approximation was proposed, which essentially splits the carriers inside the medium into two groups - a ballistic component and a diffusive component [64, 65]. Chapter 2 extends the ballistic-diffusive equations to multidimensional space with a nanoscale heat source term and numerical implementations were performed on the transient ballistic-diffusive equations. The so-developed numerical simulation tools were applied to study the heating issue in a nanoscale MOSFET structure. Simulation results of heat conduction in nanoscale heat generation regions show that the localized nanoscale heating can have a several times larger temperature rise than that predicted by the Fourier law. This has significant implications for the reliability of MOSFET devices. This work also demonstrates that the ballistic-diffusive equations and the numerical calculation strategies can be promising for incorporating into commercial device simulators.

Nanostructure-based materials such as Bi_2Te_3/Sb_2Te_3 superlattices and PbTe/PbSeTe quantum dot superlattices have shown significant increases in *ZT* values compared to their bulk counterparts due to mainly the reduced phonon thermal conductivity of these structures [56, 57].

Nanocomposites may realize a similar thermal conductivity reduction and provide a pathway to scale-up the nanoscale effects observed in superlattices to thermoelectric materials in bulk form [58]. There are not many theoretical studies on the thermal conductivity of nanocomposites, despite their importance for practical applications such as for thermoelectrics and thermal interface materials. In chapter 3 the deterministic solution of the phonon Boltzmann equation is used to study the thermal conductivity of 2-D nanocomposites where silicon nanowires are periodically aligned in a germanium matrix both along and across the nanowire directions. Though very much doable, extending the 2-D BTE simulation to phonon transport in complex three-dimensional (3-D) spatial coordinates is very tedious, owing to the complexity in tracking the phonon transport deterministically. Chapter 4 presents an algorithm for studying phonon transport in nanoparticle composites using Monte Carlo simulations with special attention paid to the implementation of periodic boundary conditions. The size effects of phonon transport in nanoparticle composites were thus studied and the results showed that the thermal conductivity of nanoparticle composites can be lower than their alloy value. The calculations also show that the interfacial area per unit volume (interface density) is a useful parameter to correlate the size effect of the thermal conductivity in nanocomposites. Results of this study can be used to direct the development of both high efficiency thermoelectric materials and thermal interface materials containing high thermal conductivity particle or wire inclusions.

In addition to the materials development, there are also new opportunities to create novel thermoelectric devices that can potentially outperform conventional thermoelectric devices. Different device configurations have been explored in the past. Past studies include the investigation of thermoelectric effects in pn junctions and minority carrier effects [66,67], multistage thermoelectric devices [68], and transient effects [69].

In thermoelectric devices it is the electrons that do the useful energy conversion work and the electron temperature that matters for energy conversion efficiency. Following the rationale of reducing the phonon thermal conductivity, if there is a way to impart energy to electrons only (by cutting off the energy transport through phonons between the heat source or the cooling target and the thermoelectric element) while minimizing the energy coupling between electrons and phonons, it is possible to obtain better performance for thermoelectric devices. It has been long recognized that the nonequilbrium between electrons and phonons in a thermoelectric element can be exploited to improve the thermoelectric energy conversion efficiency [70-74], but there exist no easy ways to create such nonequilibrium states between electrons and phonons to benefit from hot electrons for power generation or to benefit from the cold electrons for refrigeration. Recent work on phonon-polariton coupling in the near-field shows that a heat flux as high as 10's or 100's W/cm^2 can be obtained when two half-spaces of a polar semiconductor (such as silicon carbide or boron nitride) are separated by a nanoscale vacuum gap for a temperature difference of 10's K between the two surfaces [75]. In Chapter 5, we conceptualize and investigate surface-plasmon coupled nonequilibrium thermoelectric devices. These devices use surface-plasmon coupling to limit the energy exchange between the heating source (or cooling target) and the thermoelectric element to electrons alone, while eliminating direct energy exchange between phonons. Models for refrigeration and power generation devices based on this concept are established, together with simplified criteria to guide the device design and materials selection. Our simulations show that these devices can lead to significant improvements in efficiency over conventional thermoelectric devices.

As shown in all the current theoretical modeling and simulation work, it is extremely important to have a correct phonon relaxation time or phonon mean free path as input parameters for any Monte Carlo or Boltzmann transport equation-based simulations for nanoscale heat conduction problems. Phonon reflectivity at interfaces and phonon relaxation time are clearly the most fundamental energy carrier properties for nanoscale heat conduction. Unfortunately no work has been done so far for phonon dynamics to extract these phonon properties. The closest studies are those using the optical pump-probe measurements to study thermal diffusivity and the interface thermal resistance. Almost all pump-probe measurements use the heat diffusion equation to fit the cooling curve thermal conductivity and interface resistance. However, for the heat diffusion equation to be valid, this cooling time scale should be many times longer than the phonon relaxation time. So the fit would result in fundamental errors if the cooling delay time is not long enough. For example, the phonon relaxation time is around 100 ps, and the experimental delay time is often around several hundred picoseconds or 1 nanosecond. During this thesis work, we set up the sub-picosecond pump-probe optical measurement facilities employing a Ti:sapphire femtosecond laser which have a output pulse width of ~100 fs. Chapter 6 studies the fundamentals of ultrafast laser material interaction and the possibilities of using the phonon Boltzmann equation to fit the experimental data and to extract the phonon reflectivity and relaxation time using the optical pump and probe measurement.

Finally, Chapter 7 summarizes the contribution of this thesis and presents some possible future directions for these studies.

1.6 References

1. C.-L. Tien, A. Majumdar and F. M. Gerner, Microscale Energy Transport, (Taylor & Francis, Washington, 1998).
2. G. Chen, Nanoscale Energy Transport and Conversion, (Oxford University Press, New York, 2005).
3. G. Chen, D. Borca-Tasciuc, and R.G. Yang, in Encyclopedia of Nanoscience and Nanotechnology, Eds. H.S. Nalwa, Vol. **7**, pp.429-459, (American Scientific Publishers, Stevenson Ranch, CA, 2004).
4. D. G. Cahill, W. K. Ford, K. E. Goodson, G. D. Mahan, A. Majumdar, H. J. Maris, and R. Merlin, J. Appl. Phys. **93**, 743 (2003).
5. G.Chen, Phys. Rev. B **57**, 14958 (1998).
6. B. Yang, and G. Chen, Phys. Rev. B **67**, 195311 (2003).
7. G. A. Domoto, R. F. Boehm, and C. L. Tien, Trans. ASME, J. Heat Transf. **92**, 412 (1972).
8. D. Polder and M.Von Hove, Phys. Rev. **4**, 3303 (1971).
9. K. E. Goodson and Y. S. Ju, Annu. Rev. Mater. Sci. **29**, 261 (1999).
10. G. Chen, Annu. Rev. Heat Transf. **7**, 69 (1996).
11. T. Tritt, Semiconductors and Semimetals **69-71**, (Academic Press, San Diego, 2001).
12. G. Chen and A. Shakouri, Trans. ASME, J. Heat Transf. **124**, 242 (2002).
13. G. Binning, M. Despont, U. Drechsler, W. Häberle, M. Lutwyche, P. Vettiger, H. J. Mamin, B. W. Choi, and T. W. Kenny, Appl. Phys. Lett. **74**, 1329 (1999).
14. K. Hamad-Schifferli, J.J. Schwartz, A.T. Santos, S. Zhang, and J.M. Jacobson, Nature **415**, 152 (2002).
15. P. Hyldgaard and G.D. Mahan, Thermal Conductivity, (Technomic, Lancaster, UK, 1996).
16. G. Chen, Trans. ASME, J. Heat Transf. **119**, 220 (1997).
17. Y. S. Ju and K. E. Goodson, Appl. Phys. Lett. **74**, 3005 (1999).
18. M. Born, and E. Wolf, Principles of Optics, 6th ed, (Pergamon Press, Oxford, 1980).
19. J.M. Ziman, Electrons and Phonons, (Clarendon Press, Oxford, 1960).

20. P. L. Kapitza, Zh. Eksp. Teor. Fiz. **11**, 1 (1941); [J. Phys. (USSR) **4**, 181 (1941)]; in Collected Papers of P. L. Kapitza, edited by D. der Haar, Vol. **2**, p. 581, (Pergamon, Oxford,1965).
21. W. A. Little, Can. J. Phys. **37**, 334 (1959).
22. S.T. Huxtable, A. R. Abramson, and A. Majumdar, in Heat and Fluid Flow in Microscale and Nanoscale Structures, Ed. M. Faghri and B. Sunden, (WIT Press, 2005).
23. B. Yang, and G. Chen, in Thermal Conductivity, Ed. T. Tritt, (Springer, 2004)
24. T. Yao, Appl. Phys. Lett. **51**, 1298 (1987).
25. W.S. Capinski, H.J. Maris, T. Ruf, M. Cardona, K. Ploog, and D. S. Katzer, Phys. Rev. B **59**, 8105 (1999).
26. T. Borca-Tasciuc, D. W. Song, J. R. Meyer, I. Vurgaftman, M-J. Yang, B. Z. Nosho, L. J. Whitman, H. Lee, R. U. Martinelli, G. W. Turner, M. J. Manfra, and G. Chen, J. Appl. Phys. **92**, 4994 (2002).
27. B. Yang, J. L. Liu, K. L. Wang and G. Chen, Appl. Phys. Lett. **80**, 1758 (2002).
28. W. L. Liu, T. Borca-Tasciuc, G. Chen, J. L. Liu, and K. L. Wang, K.L., J. Nanosci. Nanotechol. **1**, 39 (2001).
29. R. Venkatasubramanian, Phys. Rev. B **61**, 3091 (2000).
30. W.L. Liu, T. Borca-Tasciuc, G. Chen, J.L. Liu, and K.L. Wang, J. Nanosci. Nanotechnol. **1**, 39 (2001).
31. G. Chen, Trans.ASME, J. Heat Transf. 118, 539 (1996).
32. L. M. Phinney and C.L. Tien, Trans. ASME, J. Heat Transf. 3, 751 (1998).
33. A. Majumdar, K. Fushinobu, and K. Hijikata, J. Appl. Phys. 77, 6686 (1995).
34. E. Pop, K. Banerjee, P. Sverdrup, R. Dutton, and K. Goodson, International Electron Devices Meeting. Technical Digest, IEEE (2001) Piscataway, NJ, Vol. 951, p. 31.1.1.
35. H.J. Goldsmid, Thermoelectric Rrefrigeration, Plenum Press, New York (1964).
36 D.G. Cahill, K. Goodson, and A. Majumdar, ASME J. Heat Transf. **124,** 223 (2002). Costescu, R.M., Wall, M,A., and Cahill, D.G., Phys. Rev. B **67**, 054302 (2003).
37 G. Chen, Semiconductors and Semimetals **71**, 2003 (2001).
38. D. G. Cahil, Rev. Sci. Instrum. 61, 802 (1990).
39 W.Liu and M. Asheghi, Appl. Phys. Lett. **84,** 3819 (2004).

40. T. Borca-Tasciuc, J. L. Liu, T. Zeng, W. L. Liu, D. W. Song, C. D. Moore, G. Chen, K. L. Wang, M. S. Goorsky, T. Radetic, and R. Gronsky, Proceedings of the ASME Heat Transfer Division 1999, L. C. Witte, P. Ed., American Society of Mechanical Engineers, New York (1999) Vol. 364, p.117.
41. T.Y. Choi, D. Poulikakos, J. Tharian, and U. Sennhauser, Appl. Phys. Lett. **87,** 013108 (2005)
42. L. Lu, W. Yi, and D.L. Zhang, Rev. Sci. Instrum. **72**, 2996 (2001)
43. C.K. Sun, H.K. Choi, C.A. Wang, J.G. Fujimoto, Appl. Phys. Lett. **62**, 747 (1993). C.A. Paddock, and G.L. Eesley, J. Appl.. Phys. **60**, 285 (1986).
44. W.S. Capinski, and H.J. Maris, Rev. Sci. Instrumentation **67**, 2720 (1996). W.S. Capinski, and H.J. Maris, T.Ruf, M. Cardona, K.Ploog, and D.S. Katzer, Phys. Rev. B **59**, 8105 (1999)
45. P.M. Norris, A.P. Caffrey, R.J. Stevenson, J.M. Klopf, J.T. Mcleskey, A.N. Smith, Rev. Sci. Instrum. **74**, 400 (2003).
46. Y. Taur, C. H. Wann, and D. J. Frank, in International Electron Devices Meeting 1998. Technical Digest, Vol. **1080**, p. 789 (IEEE, Piscataway, NJ, 1998)..
47. H. J. Goldsmid, Applications of thermoelectricity, (Wiley, New York, 1960).
48. G. Slack, in CRC Handbook of Thermoelectrics (Ed: D.M. Rowe), pp.407-440, CRC Press (1995).
49. A.F. Ioffe, Semiconductor Thermoelements and Thermoelectric Cooling, (Infosearch Ltd., 1957).
50. H.J. Goldsmid, Thermoelectronic Refrigeration, (Plenum Press, 1964).
51. T. Tritt, Semiconductors and Semimetals **69-71**, (Academic Press, San Diego, 2001).
52. L.D. Hicks, and M.S. Dresselhaus, Phys. Rev. B **47**, 12727 (1993)
53. L.D. Hicks, and M.S. Dresselhaus, Phys. Rev. B **47**, 16631 (1993)
54. L.D. Hicks, and M.S. Dresselhaus, Appl. Phys. Lett. **63**, 3230 (1993)
55. L.D. Hicks, T.C. Harman, X. Sun, and M.S. Dresselhaus, Phys. Rev. B **53**, 10493 (1996)
56. R. Venkatasubramanian, E. Silvona, T. Colpitts, and B. O'Quinn, Nature **413**, 597 (2001).
57. T. C. Harman, P.J. Taylor, M.P. Walsh, and B. E. LaForge, Science **297**, 2229 (2002).
58. R.G. Yang and G. Chen Materials Integration, to appear in Sep. 2005 issue.
59. G. Chen, Thermomechanical Phenomena in Electronic Systems – Proceedings og the Intersociety Conference, Vol. **1**, 8 (2004)
60. H. B. Casimir, Physica **5**, 495 (1938).

61. G. Chen, ASME J. Heat Transf. 118, 539 (1996).
62. P.G. Sverdrup, Y.S. Ju, and K.E. Goodson, ASME J. Heat Transf. **123**, 130 (2001).
63 . J.Y. Murthy, and S.R. Mathur, ASME J. Heat Trans. **125**, 904 (2003).
64. G.Chen, Phys. Rev. Lett. **86**, 2297 (2001).
65. G. Chen, ASME J. Heat Transf. **124**, 320 (2002).
66. J. Tauc, Photo and Thermoelectric Effects in Semiconductors (Pergamon Press, New York, 1962).
67. K. P. Pipe, R.J. Ram, and A. Shakouri, Phys. Rev. B **66**, 125316 (2002).
68. B.J. O'Brien, C.S. Wallace and K. Landecker, J. Appl. Phys. **27**, 820 (1956); P.W. Cowling and J.E. Sunderland, Energy Conversion **7**, 289 (1968); R.G. Yang, G. Chen, G.J. Snyder, and J.-P. Fleurial, J. Appl. Phys. **95**, 8226 (2004); and references therein.
69. G.J. Snyder, J.-P. Fleurial, T. Caillat, R.G. Yang, and G. Chen, J. Appl. Phys. **92**, 1564 (2002); R.G. Yang, G. Chen, A.R. Kumar, G.J. Snyder, and J.-P. Fleurial, Energy Conversion and Management **46**, 1407 (2005); and references therein.
70. V.S. Zakordonests and G.N. Logvinov, Semiconductors **31**, 265 (1997); Yu G. Gurevich and G.N. Logvinoz, Sov. Phys. Semicond. **26**, 1091 (1992).
71. Y.G. Gurevich, O.L. Mashkevich, Phys. Rep. (Rev. Sec. Phys. Lett.) **181**, 327 (1989).
72. L.P. Bulat and V.G. Yatsyuk, Sov. Phys.-Semicond. **18**, 383 (1984); L.I. Anatychuk, L.P. Bulat, D.D. Nikirsa, and V.G. Yatsyuk, Sov. Phys.-Semicond. **21**, 206 (1987).
73. L.P. Bullat, Thermoelectricity under large temperature gradients, J. Themoelect. **4**, 3 (1997).
74. G. Chen and T. Zeng, Microscale Thermophyis. Eng. **5**, 71 (2001).
75. A. Narayanaswamy and G. Chen, Appl. Phys. Lett. **83**, 3544 (2003).

Chapter 2. Numerical Solution of Multidimensional Transient Ballistic-Diffusive Equations and Phonon Boltzmann Equation: Application to Heating in Nanoscale MOSFETs

Heat conduction at the micro- and nanoscale and during ultra-fast processes may deviate from the predictions of the Fourier law, for several reasons, such as boundary and interface scattering, the ballistic nature of the transport, and the finite relaxation time of heat carriers. The Boltzmann transport equation (BTE) has proven to be a valid and useful tool for nanoscale and ultrafast heat transfer where the particle description of energy carriers is valid. Direct numerical solution of the phonon BTE is preferred, but it is usually slow. Approximate methods that are capable of capturing the major size effects but easier to implement are thus very much desirable. The transient ballistic-diffusive heat conduction equations (BDE) were developed by Chen[♣] as an approximation to the phonon Boltzmann equation (BTE) for nanoscale heat conduction problems. In this chapter, we further develop the BDE for multidimensional heat conduction, including with a nanoscale heat source term and different boundary conditions. The numerical simulation schemes were applied for several 2-D cases, including the heat transport surrounding a nanoscale heat source, which mimics the heat generation inside a nanoscale MOSFET. For comparison, the transient BTE is also solved in multidimensional Cartesian coordinates using the discrete ordinates method with two Gauss-Legendre quadratures. The results show that the BDE captures the characteristics of the phonon BTE with much shorter computational time.

2.1 Introduction

The feature size of electronic devices in current integrated circuits has become comparable to or even smaller than the phonon mean free path in the substrate on which the devices are built, and this size is projected to be much smaller in the next ten years. For example, the mean free path of the heat carrying phonons in silicon is ~40-300 nm depending on how it is estimated. The volumetric heat generation rate inside ultra-small semiconductor devices can be expected to be very high, since the device operating power cannot be reduced below a certain

---

[♣] Chen, G., "Ballistic-Diffusive Heat-Conduction Equations," Physical Review Letters, Vol. 86, pp. 2297-2301, 2001.

level [1]. All the heat generated in a nanoscale region close to the drain side of the devices must be transported out through the substrate and then to the packaging heat sink. Qualitatively, the device scaling results in a serious phonon rarefaction effect as described in section 1.2 and thus a much higher temperature rise is observed than that is predicted by the Fourier law. In addition, the switching transient of these devices are approaching the phonon relaxation time, which is on the order of 10-100 ps in silicon.

It is well recognized that heat conduction in micro- and nanoscale devices and in ultrafast processes may deviate significantly from the predictions of the Fourier law, due to the boundary and interface scattering and the finite relaxation time of heat carriers [2]. The phonon Boltzmann equation (BTE) and Monte Carlo simulations can be used for simulating heat conduction processes continuously from the nanoscale to the macroscale in the regime where the particle description of phonons is valid [3, 4]. For many nanostructures and heat transfer configurations, past solutions of the BTE for electron transport, neutron transport, and photon transport can be applied [5-7]. However, the solution of the phonon BTE has been limited to a few simple geometrical configurations such as thin films and superlattices [8,9]. The inherent difficulties associated with the solution of the phonon BTE have significantly limited consideration of the size and transient effects in multidimensional real engineering problems. Fewer studies have gone beyond non-planar and multidimensional geometries [10-13]. In this work, we developed numerical solution strategies for solving the transient phonon BTE in multidimensional structures where double Guassian-Legendre quardratures are used to replace the conventional discrete ordinate method and thus much smoother convergent results are achieved.

Heat conduction in most devices is multidimensional and involves length scales from the nanoscale to the macroscale. Modeling the heat conduction processes in such multiple length scale devices is very challenging. Direct numerical solution of the phonon BTE is preferred, but it is usually slow. Approximate methods that are capable of capturing the major size effects but easier to implement are thus desirable. Recently the transient ballistic-diffusive heat conduction equations (BDE) are derived from the phonon BTE under the relaxation time approximation [14, 15]. The comparison of transient heat conduction in thin films using the BDE and the phonon BTE shows that the BDE can capture both the time retardation and the nonlocal processes, and thus can be applied to fast heat conduction process and to small structures. In this chapter, we also generalize the BDE to study multidimensional nanoscale heat conduction including different kinds of boundary conditions and the nanoscale heat source term. The numerical solution strategies for the BDE are presented. In the last section of this chapter, numerical results obtained from the BDE are compared with the numerical solution of the transient phonon BTE and the Fourier heat conduction equation in selected 2-D cases.

2.2 Boltzmann Equation and Equation of Phonon Radiative Transport

In the macroscale, heat transfer is characterized by three basic modes, i.e., conduction, convection and thermal radiation, or their combinations. Although the governing constitutive equations for each mode in the macroscale are very different in form and the energy carriers can be varied, the transport phenomena obey the same fundamental particle transport theory, the Boltzmann transport equation. For example, heat conduction obeys the Fourier law and thermal radiation can be described by the photon radiative transfer equation. Based on the one-particle assumption, the Boltzmann transport equation is appropriate for all the energy carriers - dilute gas molecules, electrons, photons and phonons. Its generality is impressive, since macroscopic transport behavior for particles, such as the Fourier Law, Ohm's Law, Newton's shear stress law, Fick's Law, and the hyperbolic heat equation can all be derived from the Boltzmann equation in the macroscale limit with appropriate approximations. From the Boltzmann equation, we can also derive the familiar conservation equations for mass, momentum, and energy used widely in the mechanical engineering discipline and even electrohydrodynamics used in electrical engineering [2,16,3].

In its general form, the BTE can be written as

$$\frac{\partial f}{\partial t} + \mathbf{v} \bullet \nabla_{\mathbf{r}} f + \mathbf{F} \bullet \nabla_{\mathbf{p}} f = \left(\frac{\partial f}{\partial t} \right)_{\mathrm{c}} \tag{2-1}$$

where f is the statistical distribution function of an ensemble of carriers, which depends on time t, position vector $\mathbf{r}$, and momentum vector $\mathbf{p}$. Here $\mathbf{F}$ is the force vector applied to the particles. The key to the Boltzmann equation is the scattering term, which is the term that restores the system to equilibrium. Quantum mechanical principles are often used to deal with scattering. The perturbation treatment in quantum mechanics leads to the Fermi golden rule of calculating the scattering probability from one quantum state to another [17]. A general expression of the scattering integral can be formally written, based on the scattering probability and the distribution function. This leads to an integral-differential form of the Boltzmann equation, which is difficult to solve but has been often treated in thermal radiation transport in the form of equation of radiative transfer [18, 19].

In real crystals, phonons experience various type of scattering, limiting transport processes. The most basic scattering mechanism is due to the anharmonicity of the lattice potential, which permits phonon-phonon scattering, including normal phonon-phonon scattering and Umklapp phonon-phonon scattering. Other important scattering mechanisms are:

- Phonon scattering at impurities and defects
- Phonon scattering at grain boundaries or surfaces
- Phonon scattering with carriers

Different scattering mechanisms might dominate in different materials, structures and at different temperatures. In nanostructures, phonon-surface/interface scattering dominates the transport at room and higher temperatures, which happens very similarly at very low temperature in even bulk materials. Each of these scattering categories must be distinguished with respect to the type of phonons involved. A large body of literature describes different phenomena [20, 21, 22, 23]. The evaluation of scattering integrals for phonons is very difficult. Generally, the scattering term can be written as

$$\left(\frac{\partial f(\mathbf{p})}{\partial t}\right)_{\mathrm{c}}=\left(\frac{\partial f(\mathbf{p})}{\partial t}\right)_{\mathrm{g}}+\sum\left(\frac{\partial f(\mathbf{p})}{\partial t}\right)_{\mathrm{i}} \tag{2-2}$$

where $\left(\frac{\partial f(\mathbf{p})}{\partial t}\right)_{\mathrm{g}}$ is the net phonon generation rate from electron-phonon interaction or photon-phonon interaction. $\left(\frac{\partial f(\mathbf{p})}{\partial t}\right)_{\mathrm{i}}$ denotes the phonon number change due to the phonon-phonon scattering, phonon scattering by lattice defects, and phonon-boundary scattering. Often the relaxation time approximation is used

$$\left(\frac{\partial f(\mathbf{p})}{\partial t}\right)_{i}=\frac{f_0(\mathbf{p})-f(\mathbf{p})}{\tau_i(T(\mathbf{r}),\mathbf{p})} \tag{2-3}$$

where $f_0(\mathbf{p})$ is the Bose-Einstein distribution for phonons at equilibrium temperature T, and $\tau(T(\mathbf{r}),\mathbf{p})$ is the relaxation time as a function of temperature and momentum. Often the scattering processes are approximated as frequency-dependent rather than wavevector-dependent [24]. These assumptions leads to approximate eq (2-3) as

$$\left(\frac{\partial f(\omega)}{\partial t}\right)_i = \frac{f_0(\omega) - f(\omega)}{\tau_i(T(\mathbf{r}),\omega)}. \tag{2-4}$$

When estimating the effect of several types of scattering centers, each related to a specific relaxation time τ_i, the total time between independent scattering events can be estimated from Mathiessen's rule [20], since the collision term in the Boltzmann equation is proportional to rhe collision rate and is additive, as shown in Eq. (2-2)

$$\frac{1}{\tau} = \sum_i \frac{1}{\tau_i}. \tag{2-5}$$

Most of time, one needs to fit the experimental thermal conductivity data for the phonon relaxation time according to Eq. (1-3) or alternatives [25]. Although the boundary scattering is often grouped together with other scattering mechanisms according to the Mathiessen rule, this must be done with extreme care because unlike the phonon-phonon scattering and phonon-impurity scattering, which are volumetric processes, the phonon boundary scattering is a surface process.

In analogy to the equation of radiative transfer for photons, the equation of phonon radiative transfer has been derived by Majumdar [26] as

$$\frac{\partial I_\omega}{\partial t} + \mathbf{v}_\omega \cdot \nabla_{\mathbf{r}} I_\omega = \frac{I_{\omega,o} - I_\omega}{\tau_\omega} + S_\omega \tag{2-6}$$

where τ_ω is the phonon relaxation time, $I_\omega(t,\mathbf{r},\hat{\mathbf{\Omega}})$ is the phonon intensity, and $S_{g\omega}$ is due to the phonon generation through the scattering with other carriers, for example, electron-phonon scattering and photon-phonon scattering.

The phonon intensity in Eq. (6) is defined as

$$I_\omega(t,\mathbf{r},\hat{\mathbf{\Omega}}) = v_\omega \hbar\omega f(t,\mathbf{r},\hat{\mathbf{\Omega}}) D(\omega)/4\pi \tag{2-7}$$

where D(ω) is the phonon density of states per unit volume, which should be obtained from the phonon dispersion relation of the specific material.

Accordingly, the phonon energy source term can be written as

$$S_\omega = v_\omega \hbar\omega \left(\frac{\partial f(\omega)}{\partial t} \right)_{g} D(\omega)/4\pi \tag{2-8}$$

Indeed, the Boltzmann equation for phonons, Eq.(2-1), and the Equation of Phonon Radiative Transport, Eq. (2-6), has been used interchangeably by the nanoscale heat transfer community.

Phonon Gray Medium Approximation A rigorous phonon transport simulation should incorporate the frequency dependence of the phonon relaxation time and group velocity, and thus should account for interactions among the dispersive phonons of different frequencies. However, it requires solution of the phonon BTE for many different frequencies. Previous works show that an average MFP is a good approximation for thermal conductivity modeling across interfaces (cross-plane transport) [27]. For transport parallel to the interface, a frequency dependent relaxation time gives a better solution [28]. However, the existing theories for the frequency dependence of the relaxation time contain large uncertainties because they are based on many approximations and rely on the fitting parameters from experimental data [29]. Therefore, we will use a frequency independent phonon MFP and phonon group velocity for simplicity, i.e. a phonon gray medium approximation.

Often the phonon MFP Λ is estimated from the thermal conductivity, the specific heat, and the speed of sound, according to the standard kinetic theory expression,

$$k = \frac{1}{3} C v \Lambda \tag{2-9}$$

where C is the volumetric specific heat. This method, however, neglects the fact that the phonons are highly dispersive. Figure 2-1 shows the phonon dispersion for Si and Ge, which relate the phonon energy and its momentum [30,31]. The phonon dispersions along different crystallographic directions are generally different. Both Si and Ge have the diamond structure consisting of interpenetrating FCC (face center cubic) structures, with a two distinct atom basis, and there are thus a total of six branches in each directions. The upper three branches are called optical phonons and the lower three are called acoustic phonons, which are the dominant energy carriers. With the known phonon dispersion, the group velocity (v_ω) and phonon density of state $D(\omega)$, which is the number of normal modes between frequencies ω and $\omega + d\omega$, can be found [22, 32]. The group velocity is defined as

$$v_\omega = \frac{d\omega}{d\mathbf{k}} \tag{2-10}$$

which is simply the slope of the branch on the dispersion relation, where k is the phonon wave vector.. The phonon density of state $D(\omega)$ for each branch is given by,

$$D(\omega) = \frac{k^2}{2\pi^2} \frac{\partial k}{\partial \omega} \tag{2-11}$$

At room temperature most acoustic phonons are populated close to the zone boundary where the phonon group velocity is significantly smaller than the sound velocity. Furthermore, the optical phonons contribute a significant portion to the specific heat, but little to the thermal conductivity due to their near zero group velocity.

The gray media approach assumes that phonon properties are frequency-independent, i.e., by averaging the frequency-dependent phonon properties over the phonon population. The average phonon properties, which are dependent on temperature only, including average phonon frequency, ω_{avg} , average phonon group velocity, v_{avg}, can be calculated as: .

average frequency:

$$\omega_{avg} = \frac{\sum_{p=1}^{3} \int_{0}^{\omega_{mp}} \hbar\omega \langle n \rangle D(\omega) d\omega}{\hbar \cdot N} \tag{2-12}$$

average group velocity:

$$v_{avg} = \frac{1}{N} \sum_{p=1}^{3} \int_{0}^{\omega_{mp}} \frac{\partial \omega}{\partial k} \langle n \rangle D(\omega) d\omega \tag{2-13}$$

where the phonon number density is given by

$$N = \sum_{p=1}^{3} \int_{0}^{\omega_{mp}} \langle n \rangle D(\omega) d\omega \tag{2-14}$$

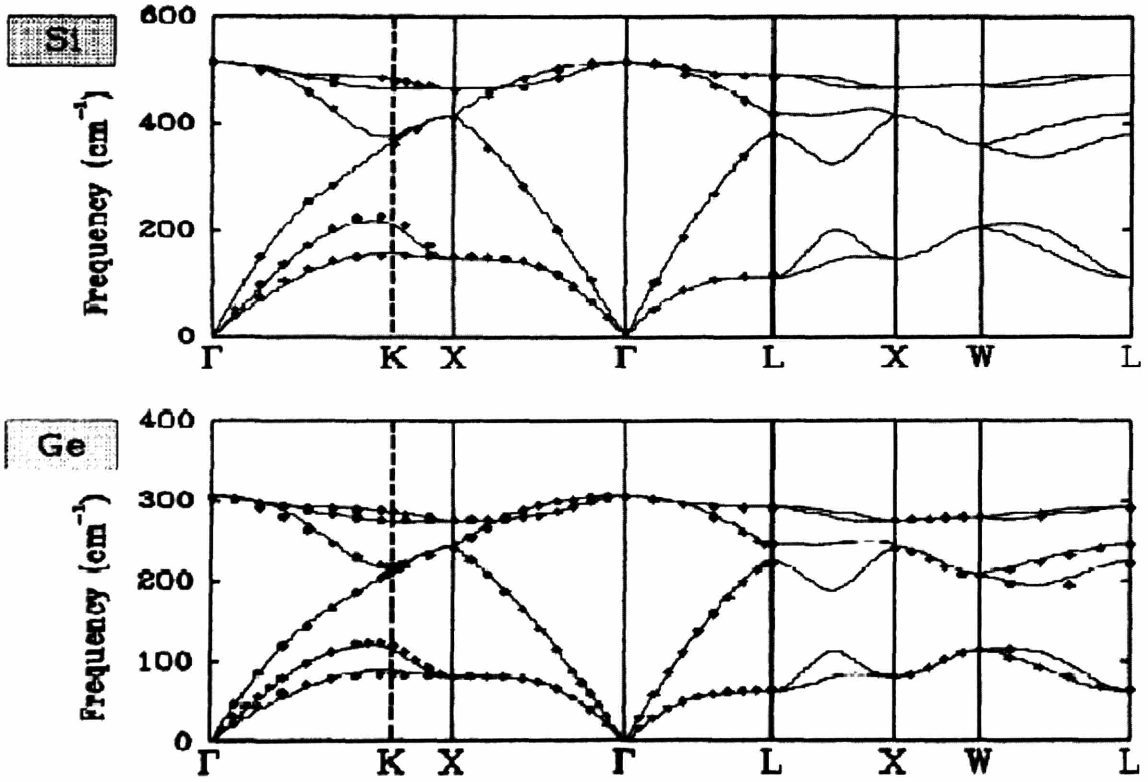

Figure 2-1. The phonon dispersion relation for Si and Ge, which related the phonon energy to its momentum. Reprinted from references [30, 31].

In the above expressions, the index p represents the specific branch of polarization, $\hbar = 1.05 \times 10^{-34}$ J·s is the Planck's constant divided by 2π, ω is the phonon frequency, ω_{mp} the maximum cut-off phonon frequency for each phonon branch, $k_B = 1.38 \times 10^{-23}$ J/K the Boltzmann constant, and <n> is the equilibrium distribution function for phonons, which follows from the Bose-Einstein statistics as:

$$\langle n \rangle = \frac{1}{\mathrm{Exp}\left(\frac{\hbar\omega}{k_B T}\right) - 1} \qquad (2\text{-}15).$$

In Eq. (2-12) through (2-14) the summation is only for three polarization branches, one longitudinal and two transverse acoustical phonon branches, since the contribution of optical phonons to the thermal conductivity is negligible due to their small group velocity [28]. As a simplification, the phonon dispersion relations are assumed to be isotropic and thus only the phonon dispersion in the [100] direction of Si and Ge in the literature is taken to calculate the phonon density of state in Eq. (2-11). The maximum wave vector, k_{max}, corresponding to the maximum phonon frequency is determined by $k_{max}=\pi/a$, where a is the equivalent atomic distance given by $\left(\pi \cdot \frac{V}{6N}\right)^{\frac{1}{3}}$. In this expression, V is the volume and N is the number of atoms in the volume.

The heat capacity due to the acoustic phonons can be written as

$$C_{ac} = \frac{\partial E}{\partial T} = \sum_{p=1}^{3} \int_0^{\omega_{mp}} \hbar\omega \frac{\partial \langle n \rangle}{\partial T} D(\omega) d\omega \qquad (2\text{-}16)$$

where E is the energy density of acoustic phonons and can be calculated as

$$E = \sum_{p=1}^{3} \int_0^{\omega_{mp}} \hbar\omega \langle n \rangle D(\omega) d\omega \qquad (2\text{-}17)$$

Using the average acoustic phonon properties and assuming the contribution from the optical phonons to the thermal conductivity to be negligible, the temperature-dependent phonon mean free path Λ can be calculated through the simple kinetic theory

$$\Lambda = \frac{3 \cdot k_{bulk}}{v_{avg} \cdot C_{ac}} \tag{2-18}$$

where k_{Bulk} is the thermal conductivity of the bulk material and is taken from experimental data in the literature [33]. The temperature dependent phonon mean free path for Si and Ge is shown in Fig. 1-1. We note that a similar but slightly different estimation of the phonon MFP and the group velocity was done by Chen [28], where he approximated the dispersion of the transverse and the longitudinal-acoustic phonons with simple sine functions. Both estimations of the phonon MFP taking the phonon dispersion into account leads to very close values for the phonon MFP. At room temperature, this estimation leads to phonon mean free path in silicon of the order of 250 nm to 300 nm, a much longer mean free path than using the simple kinetic theory expression $k = \frac{1}{3} C v \Lambda$. Experiments and modeling from Goodson's group also lead to similar values for the phonon MFP [8].

2.3 Ballistic-Diffusive Equations and Numerical Solution

Heat conduction in most devices is multidimensional and involves length scales from the nanoscale to the macroscale. Modeling the heat conduction processes in such multiple length scale devices is very challenging. Direct numerical solution of the phonon BTE is preferred, but it is usually slow. Approximate methods that are capable of capturing the major size effects but easier to implement are thus desirable. One such method, for example, is to focus on the interface region only by introducing appropriate boundary conditions, while away from the boundaries the usually diffusion or drift-diffusion equations are used, e.g. Ref [34].

Another approximation that provides further improvements compared to the introduction of special interface conditions is the ballistic-diffusive approximation [14, 15, 35, 36]. The essence of the ballistic-diffusive approximation is to divide the distribution function at any point into two parts, - a ballistic component and a diffusive component $f = f_b + f_m$ as shown in Fig.

2-2 [14, 15]. In this figure, f_b at an internal point along a specific direction originates from the boundaries or heat sources. In the course of traveling from the boundaries or sources to this point, some of the carriers are scattered and only those remaining are included in f_b. This part of carrier contribution is ballistic. The ballistic term can be further divided into the source term and the boundary emission term. The rest of the carrier contribution at this internal point is grouped into f_m. These are the carriers that are scattered or emitted into this direction from other internal points. The distribution of these carriers is more isotropic than the ballistic carriers from the boundary due to multiple scattering or nearly isotropic emission. The philosophy is then to treat this part of the heat carriers by the conventional diffusion approach. This approach has its origin in thermal radiation [35,19]. Recently the idea itself has been further explored to combine with the discrete ordinates method to reduce the ray effect in solving photon radiative transport equation (RTE) in optically thin media [37, 38]. The major difference of our method is that we consider the time dependence of heat conduction. The ballistic-diffusive equations we derive will facilitate the solution of complex engineering problems on the nanoscale and in ultrafast processes.

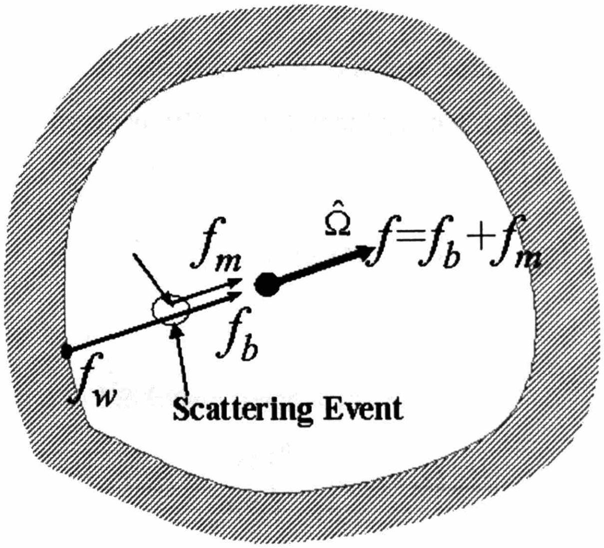

Figure 2-2. In deriving the ballistic-diffusive heat-conduction equations, the local carrier distribution function f is divided into two parts: f_b which originates from the boundary f_w and experiences outgoing scattering only, and f_m which originates from the inside domain and is directed into the indicated direction either through scattering or through phonon emission by the medium.

This work further develops the ballistic-diffusive equations for phonons [14,15] to include a nanoscale heat source term. Accordingly, the intensity at any point can be divided into two parts,

$$I_{\omega}(t,\mathbf{r}) = I_{b\omega}(t,\mathbf{r}) + I_{m\omega}(t,\mathbf{r}) \tag{2-19}$$

where $I_{b\omega}(t,\mathbf{r})$ represents carriers originating from the boundaries and/or the carrier generation source and experiencing out-scattering only.

Thus from Eq. (2-6), the governing equation for the ballistic part is

$$\frac{\partial I_{b\omega}}{\partial t} + \mathbf{v}_{\omega} \bullet \nabla_{\mathbf{r}} I_{b\omega} = -\frac{I_{b\omega}}{\tau_{\omega}} + S_{\omega} \tag{2-20}$$

We would like to note that in this splitting into two terms the carrier generation term is grouped into the ballistic component for studying the nanoscale heat source. In the ballistic-diffusive approximation approach, the ballistic term can be expressed explicitly in terms of the values at the boundaries, heat source and the initial distribution inside the system. A general solution for the ballistic part in its intensity form, Eq. (2-20), is given by Pomraning [39]

$$\begin{aligned} I_{b\omega}(t,\mathbf{r},\hat{\mathbf{\Omega}}) = & \int_{0}^{\infty} S_{\omega}(t - s/|\mathbf{v}|, r - s\hat{\mathbf{\Omega}}, \hat{\mathbf{\Omega}}) \bullet \exp[-\int_{0}^{s} \frac{ds'}{|\mathbf{v}|\tau}] ds \\ & + I_{w\omega\omega}(t - |\mathbf{r} - \mathbf{r}_{s}|/|\mathbf{v}|, \mathbf{r}_{s}, \hat{\mathbf{\Omega}}) \bullet \exp[-\int_{0}^{|\mathbf{r}-\mathbf{r}_{s}|} \frac{ds'}{|\mathbf{v}|\tau}] \bullet H(|\mathbf{v}|t - |\mathbf{r} - \mathbf{r}_{s}|) \\ & + I_{i\omega}(\mathbf{r} - |\mathbf{v}|t\hat{\mathbf{\Omega}}, \hat{\mathbf{\Omega}}) \bullet \exp[-\int_{0}^{!\mathbf{v}|t} \frac{ds'}{|\mathbf{v}|\tau}] \bullet H(|\mathbf{r} - \mathbf{r}_{s}| - |\mathbf{v}|t) \end{aligned} \tag{2-21}$$

where s is the distance along the direction of propagation, $I_{w\omega\omega}$ denotes the phonons entering the system through the boundary surface and $I_{i\omega}$ is due to the initial distribution condition inside the system. The Heaviside or unit step function $H(\xi)$ indicates that $I_{w\omega e}$ should be taken as zero for negative time and $I_{i\omega}$ should be taken as zero for points outside the system. The integral equation simply follows the fact that phonons of direction $\hat{\mathbf{\Omega}}$ which are at point $\mathbf{r}$ at time t must have originated at some point $\mathbf{r} - s\hat{\mathbf{\Omega}}$ at a time $t - s/|\mathbf{v}|$ due to the finite speed of the phonon, i.e., the time retardation. The exponential in the equation accounts for the out-scattering.

The other part $I_{m\omega}(t,\mathbf{r})$ in Eq. (2-19) represents those phonons originating from inside the medium due to the excitation and the boundary contributions converted into scattered or emitted phonons after absorption:

$$\frac{\partial I_{m\omega}}{\partial t} + \mathbf{v} \bullet \nabla I_{m\omega} = -\frac{I_{m\omega} - I_{o\omega}}{\tau_\omega} \tag{2-22}$$

For this part, we can use the diffusion approximation that is familiar in thermal radiation [36]. This can be derived from the spherical harmonic expansion of the intensity [35],

$$I_{m\omega}(t,\mathbf{r},\hat{\mathbf{\Omega}}) = J_{o\omega}(t,\mathbf{r}) + \mathbf{J}_{1\omega}(t,\mathbf{r}) \bullet \hat{\mathbf{\Omega}} \tag{2-23}$$

where $\mathbf{J}_{1\omega}$ is a vector. Substituting Eq. (2-23) into Eq. (2-22) yields

$$\frac{1}{|\mathbf{v}|}\frac{\partial J_{o\omega}}{\partial t} + \frac{1}{|\mathbf{v}|}\frac{\partial \mathbf{J}_{1\omega}}{\partial t} \bullet \hat{\mathbf{\Omega}} + \hat{\mathbf{\Omega}} \bullet \nabla J_{o\omega} + \hat{\mathbf{\Omega}} \bullet \left[\nabla \mathbf{J}_{1\omega} \bullet \hat{\mathbf{\Omega}}\right] = \frac{I_{o\omega} - J_{o\omega}}{\Lambda_\omega} - \frac{\mathbf{J}_{1\omega} \bullet \hat{\mathbf{\Omega}}}{\Lambda_\omega} \tag{2-24}$$

where $\Lambda_\omega \left(= |\mathbf{v}|\tau_\omega\right)$ is the heat carrier mean free path at frequency ω. Integrating the above equation over the solid angle of the whole space leads to,

$$\frac{4\pi}{|\mathbf{v}|}\frac{\partial \mathrm{J}_{o\omega}}{\partial t} + \frac{4\pi}{3}\nabla \bullet \mathbf{J}_{1\omega} = -\frac{4\pi}{\Lambda_\omega}\left(\mathrm{J}_{o\omega} - \mathrm{I}_{o\omega}\right). \tag{2-25}$$

Multiplying Eq. (2-25) by the unit vector $\hat{\Omega}$ and integrating the thus-obtained equation over the solid angle of the whole space gives [19]

$$\frac{1}{|\mathbf{v}|}\frac{\partial \mathbf{J}_{1\omega}}{\partial t} + \nabla J_{o\omega} = -\frac{\mathbf{J}_{l\omega}}{\Lambda_{\omega}} \tag{2-26}$$

Based on the decomposition of the phonon distribution (intensity), Eq. (2-19), the heat flux can be expressed as

$$\mathbf{q}(t,\mathbf{r}) = \int\left[\int I_{\omega}\cos\theta d\hat{\mathbf{\Omega}}\right]d\omega = \mathbf{q}_b + \mathbf{q}_m \qquad \text{(2-27)},$$

where the ballistic and diffusive heat flux contributions are defined as

$$\mathbf{q}_b(t,\mathbf{r}) = \int\left[\int I_{b\omega}(t,\mathbf{r})\cos\theta d\hat{\mathbf{\Omega}}\right]d\omega \tag{2-28}$$

and

$$\mathbf{q}_m(t,\mathbf{r}) = \frac{4\pi}{3}\int \mathbf{J}_{1\omega}d\omega. \tag{2-29}$$

The energy conservation equation gives

$$-\nabla \bullet \mathbf{q} + \dot{q}_e = \frac{\partial u}{\partial t} \tag{2-30}$$

where $\dot{q}_e$ is the heat generation per unit volume due to external heat sources, and u is the internal energy of the heat carriers per unit volume. Here u is found from $u = \int \hbar\omega f D(\omega) d\omega d\Omega / 4\pi$, which can be written as

$$u = \int\left[\int\left[\frac{I_{b\omega}}{|\mathbf{v}|}d\Omega\right]\right]d\omega + \int\frac{4\pi J_{o\omega}}{|\mathbf{v}|}d\omega = u_b + u_m \tag{2-31}$$

where u_b and u_m are the internal energy of the ballistic and the diffusive components, respectively. The total internal energy is related to the equivalent temperature through

$$\frac{\partial u}{\partial t} = C\frac{\partial T}{\partial t} = \frac{\partial u_m}{\partial t} + \frac{\partial u_b}{\partial t} \tag{2-32}$$

It should be noted that in the ballistic regime, the statistical distribution of heat carriers deviates far from equilibrium. The local temperature in this caseis best considered as a measure of the local internal energy.

Integrating Eq. (2-26) over frequency and solid angle, and utilizing Eq. (2-29), we have the following constitutive relation for the diffusive component,

$$\tau\frac{\partial \mathbf{q}_m}{\partial t} + \mathbf{q}_m = -\frac{k}{C}\nabla u_m \tag{2-33}$$

where k is the thermal conductivity,

$$k = \int C_\omega |\mathbf{v}_\omega| \Lambda_\omega d\omega / 3 \tag{2-34}$$

and τ is an average of the relaxation time that is spectrally weighed by the heat flux at each carrier frequency. Inclusion of the frequency-dependence of the relaxation time can be done through such an averaging procedure but is not the emphasis of this work. If we treat u_m/C as an effective temperature representing the local energy of the diffusive carriers, Eq. (2-32) is the familiar Cattaneo equation [40]. In the current model, however, q_m and u_m are only part of the heat flux and internal energy. From Eqs. (2-30) and (2-32), we have

$$-\nabla \bullet \mathbf{q}_m = \frac{\partial u_m}{\partial t} + \frac{\partial u_b}{\partial t} + \nabla \bullet \mathbf{q}_b . \tag{2-35}$$

Taking the divergence of Eq. (2-33) and utilizing Eq. (2-35) to eliminate q_m leads to

$$\tau\frac{\partial^2 u_m}{\partial t^2}+\frac{\partial u_m}{\partial t}=\nabla\left(\frac{k}{C}\nabla u_m\right)-\nabla \bullet \mathbf{q}_\mathrm{b}+\dot{q}_e \tag{2-36}$$

In deriving Eq. (2-36), we have used the following equation

$$\tau\frac{\partial u_b}{\partial t}+\nabla \bullet \mathbf{q}_\mathrm{b}=-u_b+\dot{q}_e \tag{2-37}$$

that can be derived from Eq. (2-20). Equation (2-36) differs from the hyperbolic heat conduction equation, derived on the basis of the Cattaneo constitutive relation, mainly because of the additional ballistic term $\nabla \bullet \mathbf{q}_b$. This additional term, together with the appropriate boundary conditions, however, makes a large difference in the final results, as will be seen later. We will call Eqs. (2-21) and (2-36) as the ballistic-diffusive heat conduction equations, or the ballistic-diffusive equations. Among the two equations, only the solution of Eq. (2-36) is mathematically involved. The ballistic term can be expressed explicitly in terms of the values at the boundaries, as in Eq. (2-21). Solving Eq. (2-36) is much simpler than solving the Boltzmann equation, which involves seven coordinates in the phase space (three spatial, three momentum, and one time), because Eq. (2-36) is averaged over the momentum space and thus involves only three spatial coordinates plus time, as in the Fourier equation. This equation can be solved using standard finite difference or finite volume methods and this is what is decribed in the following.

2.3.1 Boundary Conditions for BDE and comments

The formulation of the ballistic-diffusive equations implies that heat carriers originating from the boundaries be treated as the ballistic components. The boundary heat carriers may be emitted/transmitted from another medium or reflected from the same medium. The boundary does not contribute to the diffusive component, thus the diffusive heat flux at the boundary is

$$\mathbf{q}_m \bullet \mathbf{n}=-\int_{\hat{\Omega}\bullet\mathbf{n}<0} I_{m\omega}\hat{\mathbf{\Omega}}\bullet\mathbf{n}d\Omega \tag{2-38}$$

where **n** is the unit vector perpendicular to the boundary. Substituting Eqs. (2-23) and (2-29) into the above equation yields,

$$\mathbf{q}_m \bullet \mathbf{n} = -v u_m / 2 \qquad (2\text{-}39)$$

This is the Marshak boundary condition in the limit of black walls for thermal radiation or neutron diffusion. In the studies by Olfe [35], the boundaries are limited to the blackbody radiation. Several authors [36, 40] modified this boundary condition for nonblack surfaces by including the reflected components into the diffusive heat flux. We argue here, without substantial simulation results, that Eq. (2-49) can be applied to nonblack surfaces by grouping the reflected component into the ballistic part. This means that the boundary values in the ballistic components may be coupled to the diffusion components at the same location. Such a treatment will not increase the mathematical complexity significantly since only algebraic equations are involved for nonblack surfaces.

We can eliminate q_m in Eq. (2-39) based on the constitutive relation, Eq. (2-33), to obtain the following boundary conditions for the diffusion components,

$$\tau \frac{\partial u_m}{\partial t} + u_m = \frac{2\Lambda}{3} \nabla u_m \bullet \mathbf{n} . \qquad (2\text{-}40)$$

The Boltzmann transport equation is a first-order partial differential equation in spatial coordinates, and thus needs only part of the boundary conditions specified in the spatial coordinates. For example, the boundary condition is needed at one end and the other end can be left free in one-dimensional examples. However, this boundary condition must specify the intensity in all solid angle directions, including those entering the domain (leaving the boundary) and those leaving the domain (entering the boundary). In most of the literature, particularly for photon radiation transport, only the intensity distribution entering the domain is given. However, over all boundaries, which is equivalent to specifying the intensity distribution over all 4π solid angle directions on part of the boundary. In radiation heat transfer, the temperature representing the distribution of the photons entering the domain is specified as the temperature at the boundary. This is justified because most of these boundaries are solid boundaries and the temperature actually represents the local solid temperature. For phonons, a similar treatment will cause misinterpretation because the temperature representing phonons entering the domain covers only half of the solid-angle in space, and it is called the emitted phonon temperature [27]. Phonons entering the boundary, which cover the other half of the solid angle, may have a different characteristic temperature. The local energy density, and thus the corresponding temperature, which represents the sum of the phonons leaving and entering the boundary, is different from the emitted phonon temperature, and it is called the equivalent equilibrium temperature. Because the temperature distribution inside the calculation domain obtained from the phonon BTE or BDE represents the local energy phonon density, it is consistent only with the equivalent equilibrium temperature. If the emitted phonon temperature is used to represent the local temperature, an artificial temperature jump is developed at the boundaries for "black" surfaces that have no phonon reflection. The temperature concept used in the Fourier law is a local equilibrium quantity. It represents the local energy density. Thus a comparison between the Fourier law-based heat conduction equation with the phonon BTE or BDE would be meaningful only when the equivalent equilibrium temperature boundary conditions are used in the phonon BTE or BDE. The use of the consistent temperature definition, however, makes the simulation more demanding because the phonon characteristics entering a boundary are usually unknown, making iteration necessary.

2.3.2 Numerical Calculation Scheme

In this section, we studied the transient phonon transport in the 2-D geometry as shown in Fig. 2-3 (a) and 2-3(b). In Fig. 2-3(a), a heater is deposited on a substrate and the heater width can be varied to control the phonon Knudsen number, which is defined as $Kn = \frac{\Lambda}{L_h}$, where Λ is the phonon mean free path and L_H is the heater width. The substrate is initially at the ambient temperature T_0. At time $t = 0$, the heater is suddenly increased to temperature T_1, where T_1 and T_0, respectively, represent the emitted temperature in case I and the equivalent equilibrium temperature in case II. Case III investigates the size effect of a nanoscale heat source inside the medium as shown in Fig. 2-3(b).

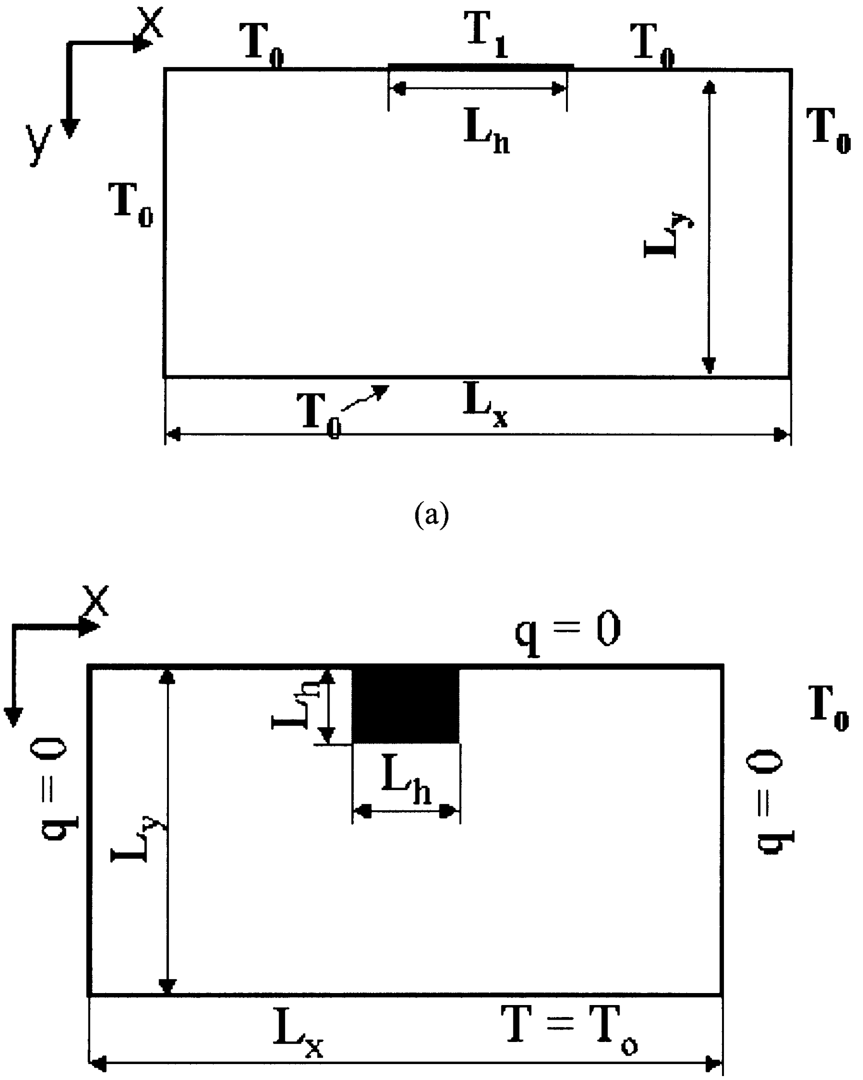

Figure 2-3. Schematic drawing of device geometry simulated in this calculation: a) a confined surface heating at y=0, where T_1 and T_0 represent the emitted temperature in case I and the equivalent equilibrium temperature in case II. b) Case III: a nanoscale heat source embedded in the substrate, which is similar to the heat generation and transport in a MOSFET device.

As an example, I show here how the numerical solution was conducted for the two-dimenionsional case I. From Fig. 2-4, the ballistic component of the temperature in the substrate can be expressed as:

$$
\begin{aligned}
T_b(x_0, y_0) &= \int_\Omega \frac{I_b}{Cv} d\Omega \\
&= \frac{\Delta T}{2\pi} \int_{\frac{L_x - L_h}{2}}^{\frac{L_x + L_h}{2}} \int_0^{\sqrt{(vt)^2 - (x-x_0)^2 - y_0^2}} \exp[-\frac{s}{\Lambda}] \bullet \frac{y_0}{s^3} dzdx
\end{aligned}
\qquad (2\text{-}41)
$$

in which $s = \sqrt{(x - x_0)^2 + y_0^{\,2} + z^2}$ is the length of the phonon path, v is the phonon velocity, and Λ is the phonon mean free path. Similarly we have the x component and y component of the ballistic heat flux as:

$$
q_{bx} = \frac{Cv\Delta T}{2\pi} \int_{\frac{L_x - L_h}{2}}^{\frac{L_x + L_h}{2}} \int_0^{\sqrt{(vt)^2 - (x-x_0)^2 - y_0^2}} \exp[-\frac{s}{\Lambda}] \bullet \frac{y_0 (x - x_0)}{s^4} dzdx \qquad (2\text{-}42)
$$

$$
q_{by} = \frac{Cv\Delta T}{2\pi} \int_{\frac{L_x - L_h}{2}}^{\frac{L_x + L_h}{2}} \int_0^{\sqrt{(vt)^2 - (x-x_0)^2 - y_0^2}} \exp[-\frac{s}{\Lambda}] \bullet \frac{y_0^{\,2}}{s^4} dzdx \qquad (2\text{-}43)
$$

in which C is the volumetric heat capacity.

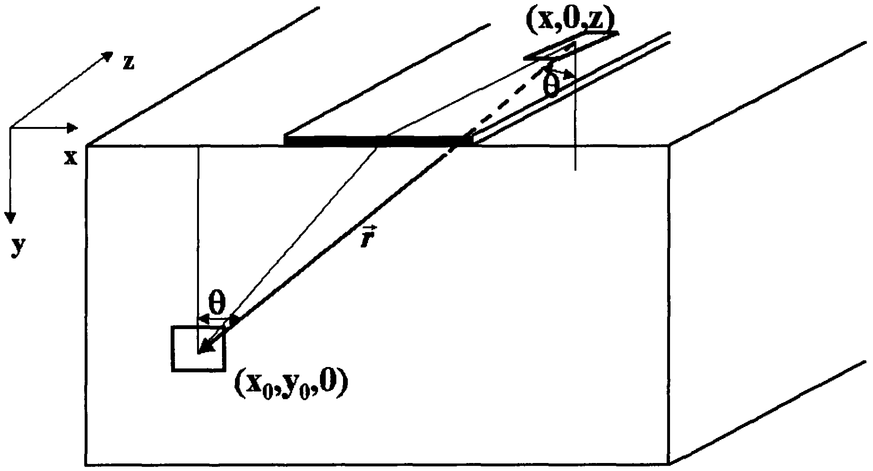

Figure 2-4. Geometry and notation for the calculation of the ballistic component coming from the boundary.

The following nondimensional parameters are introduced for our calculation:

$$\theta_m = \frac{T_m}{\Delta T} \qquad \theta_b = \frac{T_b}{\Delta T} \qquad \theta = \frac{T}{\Delta T}$$

$$\mathrm{q}_{\mathrm{m}}^{*} = \frac{\mathrm{q}_{\mathrm{m}}}{\mathrm{Cv}\Delta\mathrm{T}} \qquad \mathrm{q}_{\mathrm{b}}^{*} = \frac{\mathrm{q}_{\mathrm{b}}}{\mathrm{Cv}\Delta\mathrm{T}} \qquad \mathrm{q}^{*} = \frac{\mathrm{q}}{\mathrm{Cv}\Delta\mathrm{T}}$$

$$t^{*} = \frac{t}{\tau} \qquad k_n = \frac{\Lambda}{L_h} \qquad \eta = \frac{x}{L_x} \qquad \xi = \frac{y}{L_y}$$

$$\gamma_{xh} = \frac{L_x}{L_h} \qquad \gamma_{yh} = \frac{L_y}{L_h} \qquad \gamma_{zh} = \frac{L_z}{L_h} \tag{2-44}$$

Accordingly, Eq. (2-36) for the diffusive component can be written as:

$$\begin{aligned} &\frac{\partial^2 \theta_m}{\partial t^{2*}} + \frac{\partial \theta_m}{\partial t^{*}} = \frac{Kn^2}{3}\left(\frac{1}{\gamma_{xh}^2}\frac{\partial^2 \theta_m}{\partial \eta^2} + \frac{1}{\gamma_{yh}^2}\frac{\partial^2 \theta_m}{\partial \xi^2}\right) \\ &- Kn\left(\frac{\partial q_{bx}^{*}}{\partial \eta}\frac{1}{\gamma_{xh}} + \frac{\partial q_{by}^{*}}{\partial \xi}\frac{1}{\gamma_{yh}}\right) \end{aligned}, \tag{2-45}$$

and its associated initial and boundary conditions can be written as:

$$t^{*} = 0: \quad \theta(\eta,\xi,0) = 0, \quad \frac{\partial \theta(\eta,\xi,t^{*})}{\partial t^{*}}\Big|_{t^{*}=0} = 0 \tag{2-46}$$

$$\eta = 0,1: \left(\frac{\partial \theta_m}{\partial t^{*}} + \theta_m\right)\Big|_{\eta=0,1} = \vec{x} \bullet \frac{2Kn}{3\gamma_{xh}}\left(\frac{d\theta_m}{d\eta}\right)\Big|_{\eta=0,1} \tag{2-47}$$

$$\xi = 0,1: \left(\frac{\partial \theta_m}{\partial t^{*}} + \theta_m\right)\Big|_{\xi=0,1} = \vec{y} \bullet \frac{2Kn}{3\gamma_{yh}}\left(\frac{d\theta_m}{d\xi}\right)\Big|_{\xi=0,1} \tag{2-48}$$

Equation (2-33) can be written as:

$$\frac{\partial q_{mx}^{*}}{\partial t^{*}} + q_{mx}^{*} = -\frac{Kn}{3\gamma_{xh}} \frac{\partial \theta_m}{\partial \eta}, \tag{2-49}$$

and its associated initial and boundary conditions can be written as:

$$\frac{\partial q_{my}^{*}}{\partial t^{*}} + q_{my}^{*} = -\frac{Kn}{3\gamma_{xy}} \frac{\partial \theta_m}{\partial \xi} \tag{2-50}$$

$$\eta = 0,1: \quad \vec{x} \bullet q_{mx}^{*} = -\theta_m / 2 \tag{2-51}$$

$$\xi = 0,1: \quad \vec{y} \bullet q_{my}^{*} = -\theta_m / 2 \tag{2-52}$$

It is straightforward to construct a more complicated solution for Case II and case III. The parameters $\gamma_{xh} = \frac{L_X}{L_h} = 10$ and $\gamma_{yh} = \frac{L_Y}{L_h} = 5$ are set in case I and case II.

Case III investigates the size effect of a nanoscale heat source inside the medium as shown in Fig. 2-3(b). The heat source is similar to that generated in a MOSFET device as shown in Figure 1-5.

Nanoscale heat conduction problems often involve multiscale modeling. For example, heat is generated in a nanoscale source region and is eventually conducted to a much larger substrate. In order to accurately capture the physics of the transport phenomena and to minimize the calculation time, a non-uniform grid system is used in this work. Fine grids are used close to the heating region. In the x direction, the length underneath [refer to Fig. 2-3(a)] or inside [refer to Fig. 2-3(b)] the heating area L_h is divided uniformly into N_h grids. The grids outside the heater area are increased in size using a geometric series, with each consecutive the grid size increased by grid size ratio χ_x. For Fig. 2-3(b), the length inside the heating region is divided uniformly into N_h grids and the rest is divided non-uniformly with an increase in size by grid size ratio χ_y. The total grids in the x direction are $N_x - 2$ and the total grids in the y direction are $N_y - 2$. The total calculation points are $N_x \times N_y$ since the additional points with zero volume are added at all the boundaries. For Fig. 2-3(a), a simpler division in the y direction with a non-uniform division starting just underneath the heating region, has also been tested. The results presented in this work use the same set of grid system as that used for Fig. 2-3(b). The grid size dependence of the simulation results has been studied. The results presented in the work used $N_x = 151$, $N_y = 81$, $N_h = 31$, $\chi_x = 1.05$, and $\chi_y = 1.05$, which give convergent results for all the cases studied.

A general numerical calculation block diagram is shown in Fig. 2-5. From Eq. (2-21), it is not difficult to understand that the ballistic term can be subdivided into a source term, a boundary emission term and an initial condition term. At each time step, calculation of the ballistic component induced by the internal heat source and the initial conditions is straightforward since the internal heat generation and the initial conditions are known. The ballistic term from the boundaries depends on whether the emitted temperatures at the boundaries are known or not. In case I, the calculation is easier since the emitted temperatures at the boundaries are pre-defined. However, the emitted phonon temperatures at the boundaries are unknown for most practical engineering problems, e.g. case II and III. Thus we used an iteration scheme to obtain the emitted phonon temperatures at the boundaries in each time step. A Gauss-Legendre integration scheme is used to calculate the ballistic components, and the conventional finite-difference technique is used to solve the governing equation for the diffusive component. For comparison, the diffusion heat conduction equation based on the Fourier law is also solved using the finite difference method for an identical geometry and boundary conditions.

2.4 Two-Dimensional Transient Phonon BTE Solver

To validate the simulation results of BDE in multi-dimensions, the transient phonon BTE is also numerically solved in 2-D structures as shown in Fig. 2-3(a) and 2-3(b). To be rigorous, phonon transport simulations should incorporate the frequency dependence of the phonon relaxation time and group velocity, and thus account for interactions among phonons of different frequencies. This requires solution of the phonon BTE, i.e. Eq. (2-6), for many different frequencies, which has been performed previously for one-dimensional transport by several authors [28, 41]. The present study focuses on the complexity of two-dimensional transport. Thus for simplicity the frequency dependence of the phonon properties are neglected. Integrating Eq. (2-6) over frequency, we obtain the same form as in equation (2-6) but without the frequency as subscripts.

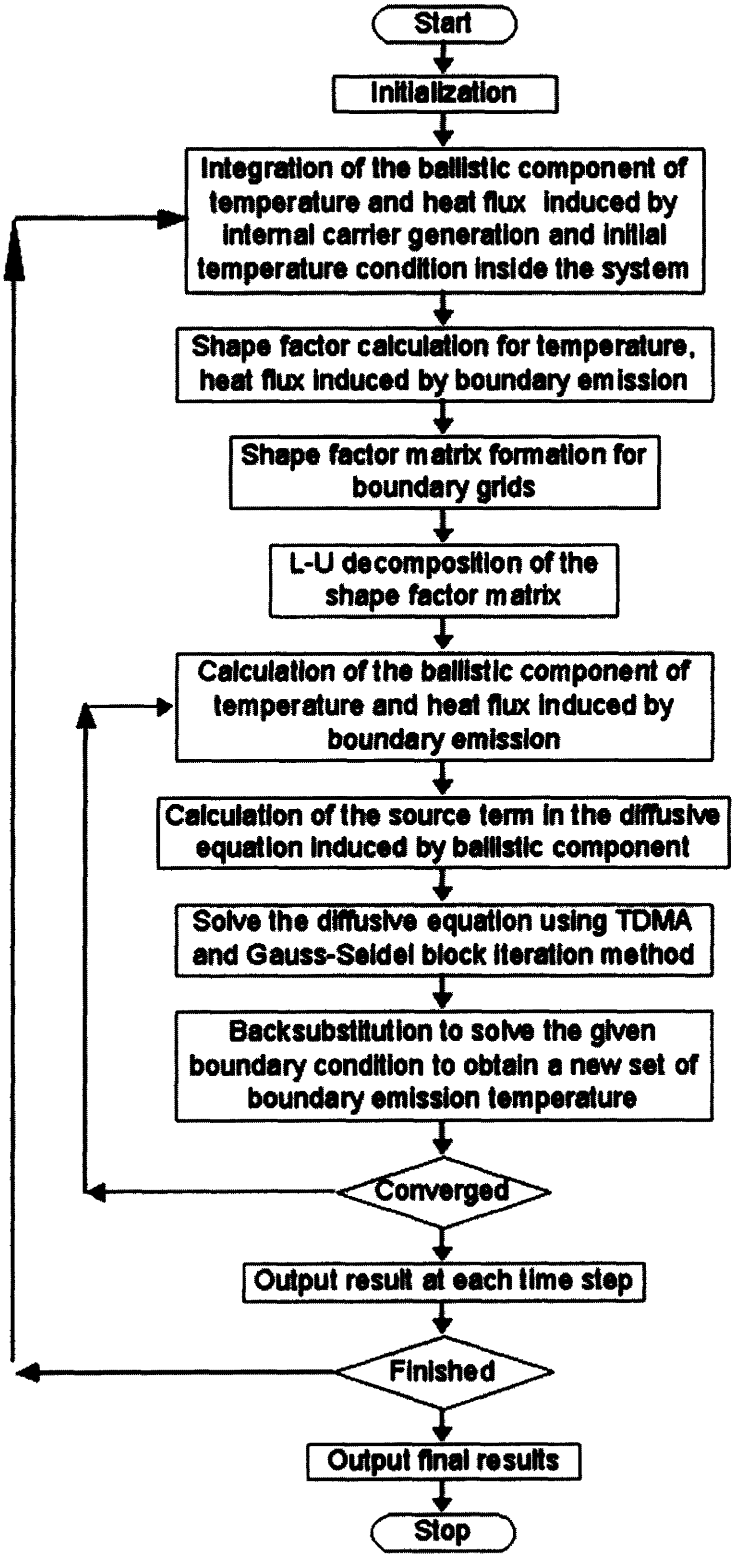

Figure 2-5. Numerical solution scheme of the ballistic-diffusive equations.

The 2-D phonon BTE under the single mode relaxation time approximation can be written as,

$$\sin\theta\cos\phi\frac{\partial I}{\partial y}+\cos\theta\frac{\partial I}{\partial x}=-\frac{I-I_o}{\Lambda} \qquad (2\text{-}53)$$

where θ and ϕ , as shown in Fig. 2-6 are the polar and the azimuthal angles, respectively, and Λ is the average phonon MFP.

In nanostructures, however, the local equilibrium cannot be established and thus the temperature obtained should not be treated as being the same, as in the case of local thermal equilibrium. From the first law of thermodynamics, we obtain the following expression for the equilibrium phonon intensity as [42]:

$$I_0(t,\mathbf{r})=\frac{1}{4\pi}\int_{4\pi}I(t,\mathbf{r},\hat{\mathbf{\Omega}})d\Omega\frac{1}{4\pi}\int_0^{2\pi}\int_0^{\pi}I_i(t,x,y,\theta,\varphi)\sin\theta d\theta d\varphi \qquad (2\text{-}54)$$

and the corresponding temperature obtained is a measure of the local energy density.

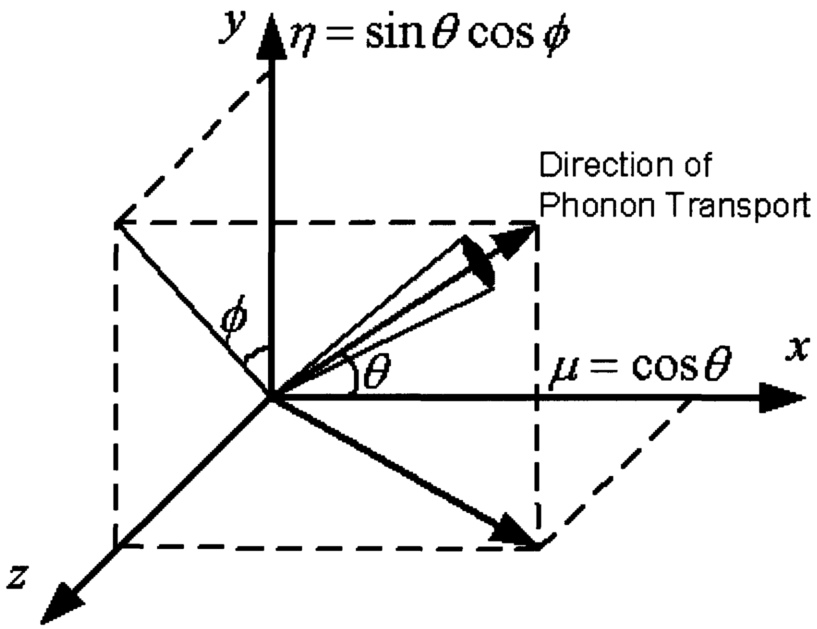

Figure 2-6. Local coordinate used in phonon Boltzmann transport simulation.

Equation (2-6) or (2-53) is similar to the photon radiative transport equation (RTE) [6,18]. The key is to solve $I(t,\mathbf{r},\hat{\mathbf{\Omega}})$. A variety of solution methods is available in the thermal radiative transfer literature [6, 18]. The discrete ordinates method (DOM) achieves a solution by solving RTE exactly for a set of discrete directions spanning the solid angle 4π. The discrete ordinates method has received considerable attention and development in the last decade because of its ability to solve many radiative transport problems with relatively good accuracy and moderate computing resources. Different sets of directions and weights have been tabulated and may result in considerably different accuracy [43, 44]. The most serious drawback of the method is that it does not ensure conservation of radiative energy [45]. The finite volume method (FVM) was first proposed by Briggs et. al [46] in 1975 using an exact integration to evaluate the solid angle integrals. The method is fully conservative in radiative energy and recently reviewed by Raithby [45]. However, both methods suffer from two shortcomings: ray effects and false scattering effects. Ray effects are related to the angular discretization, while false scattering effects are related to the spatial discretization. Several proposals to overcome these numerical inaccuracies have been proposed [37,38, 47-49]

We focused our solution method on the discrete ordinates method. Similar to the solution of the BDE, the non-uniform grid system has been used. The grid size dependence of the simulation results has been studied with a combination of the choice of the discrete directions. The results presented in the work used $N_x = 121$, $N_y = 71$, $N_h = 21$, $\chi_x = 1.05$, and $\chi_y = 1.05$, which give convergent results for all the cases studied. Figure 3 shows the direction cosines projecting the path of the phonon transport onto the x-y plane using the polar and azimuthal angles, θ and φ. For the angular discretization, the conventional S_{12} quadrature [50] has also been examined. The "ray effect" is found to be very serious for the Kn=10 (the acoustic thin limit) case though the method gives enough accuracy for small Knudsen number (the acoustic thick limit). We therefore used two Gauss-Legendre quadratures to increase the discretized direction points: One to discretize the cosine μ into N_μ points from -1 to 1 and the other to discretize φ into N_ϕ points for $0\sim\pi$ (not $0\sim2\pi$ due to symmetry). Thus we present only the results using two Gauss-Legendre quadratures in the rest of this work. We have tested the dependence of the simulation results with the number of discrete directions. For the spatial grids presented in this work, the change of the simulated results is negligible when N_μ >100 and N_ϕ >12. For example, the maximum relative difference in the temperature distribution for using N_μ =100 and N_ϕ =12 discrete directions and using N_μ =160 and N_ϕ =16 discrete directions is less than 0.02%. The reported simulation results in this work used N_μ =120 and N_ϕ =16. Fewer points can be used for fast calculation. Then equation (2-54) can be written as

$$I_0(t,x,y)=\frac{2}{4\pi}\sum_n\sum_m I(t,x,y,\mu_n,\varphi_m)w_n w'_m \qquad \text{(2-55),}$$

the factor 2 in the denominator is due to the symmetry. The weights satisfy $\sum_n\sum_m \mathrm{w}_n \mathrm{w}'_m = 2\pi$.

The diamond scheme and the step scheme are the two most popular schemes for spatial discretization [51]. The step scheme is the counterpart of the upwind in computational fluid dynamics, and it is well known that it tends to smooth out steep gradients yielding the so-called false diffusion effect, i.e., false scattering effect. The diamond scheme reduces false scattering effect, but it may yield unphysical results. Following the recommendation by Chai et. al [51], the step scheme has been used for spatial discretization in this work. As shown in Fig. 2-7, spatial differencing depends on the directions of phonon transport in the two-dimensional plane. As an example, we show here the discretized equation for the case η>0 and μ>0. For a given direction (μ_n, φ_m), we have:

$$\frac{I^{k+1}_{i,j,n,m}-I^{k}_{i,j,n,m}}{\Delta t}+|v|\mu\frac{I^{k+1}_{i,j,n,m}-I^{k+1}_{i-1,j,n,m}}{\Delta x}+|v|\eta\frac{I^{k+1}_{i,j,n,m}-I^{k+1}_{i,j-1,n,m}}{\Delta y}=-\frac{I^{k+1}_{i,j,n,m}-\frac{1}{4\pi}\sum_n\sum_m I^{k+1}_{i,j,n,m}w_n w'_m}{\tau}+S_\omega \qquad \text{(2-56)}$$

with k in the subscript is the time index, i the index in the x direction and j the index in the y direction. As shown in Eq. (2-56), the transient equation is solved using an implicit scheme in time marching. The equation is solved by iteration on the value of the equilibrium intensity $\mathrm{I}_0(\mathrm{t},\mathrm{x},\mathrm{y})=\frac{1}{2\pi}\sum_m\sum_n \mathrm{I}(\mathrm{t},\mathrm{x},\mathrm{y},\mu_n,\varphi_m)\mathrm{w}_n\mathrm{w}'_m$. At each time step, the initial value of the equilibrium intensity is guessed by setting it equal to the value of the previous time step and then the field of the intensity inside the medium for every direction is calculated. The iteration advances by taking the values of intensity $I^{k+1}_{i,j,n,m}$ in $\sum_{n}\sum_{m} I^{k+1}_{i,j,n,m} w_n w'_m$ equal to its previous iteration to calculate the equilibrium intensity I_0. We would like to note that although an implicit scheme has been used for the transient calculation, the nature of the BTE equation involves the iteration for the I_0 term. Thus the so-called implicit scheme is not a "full" implicit scheme. The time step for a stable calculation should be $\Delta t < min(\frac{\Delta x}{|\mathbf{v}|}, \frac{\Delta y}{|\mathbf{v}|})$. For transient simulations, one needs to consider the change of value in each time step when a convergence criterion is selected. In our calculation, the maximum relative error of the equilibrium intensity between two iteration steps is selected to be $2\text{x}10^{-6}$. That is, when the relative error of the calculated value of the equilibrium intensity between two iteration steps is less than 2×10^{-6}, the calculation advances to the next time step. This convergence criterion gives convergent transient results for all the cases presented in this work although it might be too strict for some cases and it might consume longer computational time than necessary. For equivalent equilibrium temperature cases, the relative error for the iterations of the nondimensional emitted temperature at the boundaries is also controlled to be less than 2×10^{-6}.

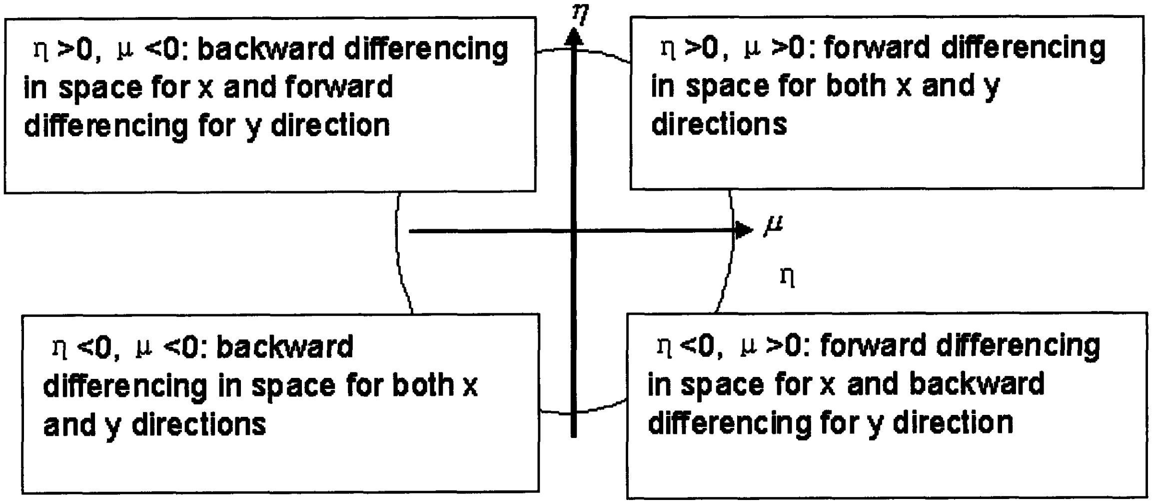

Figure 2-7. Directions of phonon transport in two-dimensional planes as given by different combinations of the direction cosines and the corresponding differencing schemes used for the BTE solver.

Although the temperature cannot be defined as a measure of equilibrium when the system is at the nanoscale, we can still use the effective temperature to reflect the local energy density inside the medium. Assuming a constant specific heat over a wide temperature range, we can write an equation for determining the temperature:

$$T(t,x,y)=\frac{4\pi I_0(t,x,y)}{C|\vec{v}|}=\frac{1}{C|\vec{v}|}\sum_n\sum_m I(t,x,y,\mu_n,\varphi_m)w_n w'_m\,. \qquad (2\text{-}57)$$

The heat flux can be accordingly written as:

$$q_x(t,x,y)=\sum_m\sum_n I(t,x,y,\mu_n,\varphi_m)\,\mu_n w_n w'_m \qquad (2\text{-}58)$$

$$q_y(t,x,y)=\sum_m\sum_n I(t,x,y,\mu_n,\varphi_m)\sqrt{1-\mu_n{}^2}\cos\varphi_m\cdot w_n w'_m \qquad (2\text{-}59)$$

2.5 Results and Discussions

Several two-dimensional cases have been simulated. In case I, the boundary conditions are specified as the emitted phonon temperature boundary conditions in Fig. 2-3(a) to compare the simulation results of the Boltzmann transport equation (BTE) and the ballistic-diffusive equations (BDE). Case II assumes the equivalent equilibrium temperature boundary condition to compare the BTE results with those of the BDE and the Fourier law. Case III investigates the size effect of a nanoscale heat source inside a medium as shown in Fig. 2-3(b)

CASE I: Emitted Temperature Boundary Condition

To compare the simulation results of the phonon BTE and BDE, the emitted phonon temperatures are assumed at the boundaries of the simulation geometry shown in Fig. 2-3(a).

Figure 2-8 shows a comparison of the transient temperature and the heat flux in the y direction at the centerline of the geometry for Kn=10. It shows that the BDE can capture the characteristics of the phonon BTE in the multi-dimensional case. However, it takes an Intel P4 800MHz PC only around 20-minute calculation time to reach the steady state for the BDE compared to 100 minutes for the phonon BTE. For small Knudsen numbers, i.e., the acoustic thick limit, the calculation time of the BTE solver can be much longer, but the calculation time of the BDE does not change much.

Very often, the results of the phonon BTE are compared with those obtained from the Fourier heat conduction theory. From the discussion above, it is clear that the comparison might not be meaningful without consistent use of the temperature concept. But the comparison gives a sense of how heat conduction based on the Fourier law and the BTE might differ. Figure 2-9(a) shows a comparison of the steady state temperature distribution at the centerline using the Fourier theory, the phonon BTE, and the BDE for different Knudsen numbers. As we can see, the BDE agrees well with the phonon BTE for all the Knudsen numbers. When the Knudsen number is small, both the BDE and the phonon BTE results become very close to those of the Fourier theory. Figure 2-9(b) show the heat flux comparison at the centerline for Kn=0.1 at nondimensional time t*=100, i.e., after a time elapse of 100 times of the phonon relaxation time. Apparently, BDE agree well with the phonon BTE. There is again a slight difference between the Fourier theory and the phonon BTE even in the small Knudsen number limit (acoustic thick limit). The underlying physics is due to the subtle difference in boundary conditions.

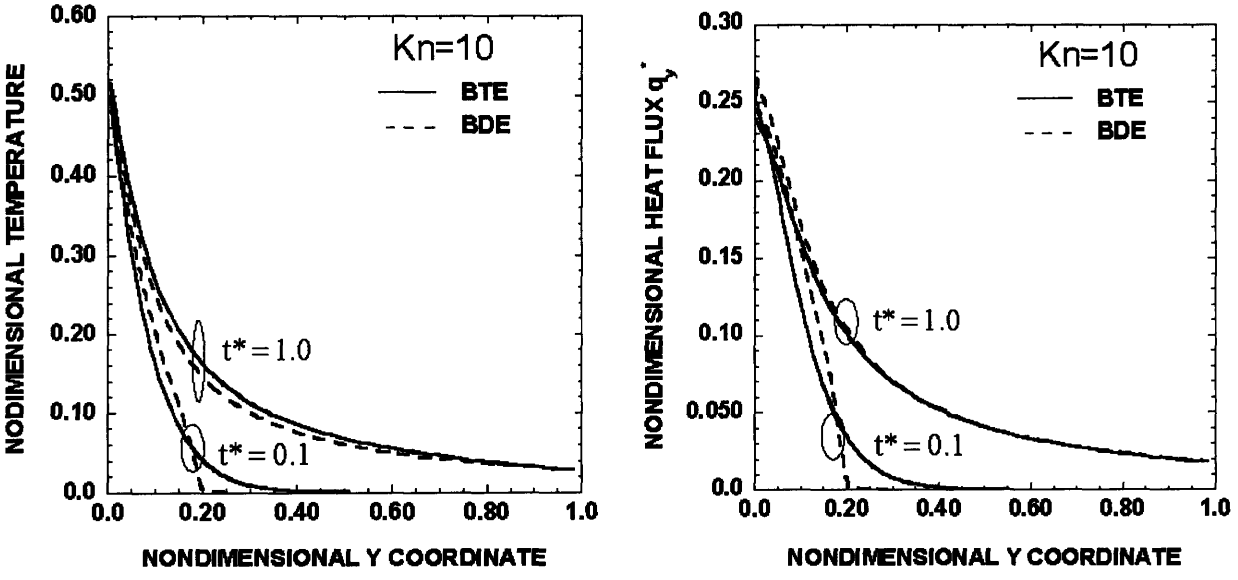

(a) (b)

Figure 2-8. Comparison of the transient temperature and heat flux in the y direction at the centerline of the geometry for Kn = 10 based on the emitted temperature condition: (a) temperature, and (b) heat flux q_y^*.

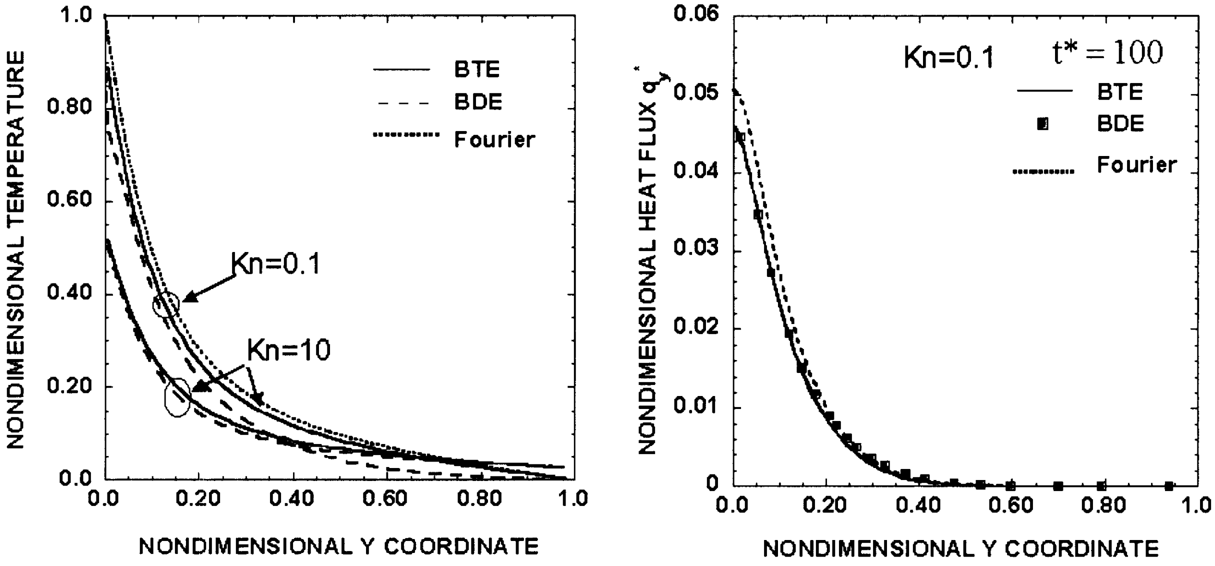

(a) (b)

Figure 2-9. (a) Comparison of the steady state temperature distribution at the centerline using the Fourier theory, the Boltzmann transport equation (BTE), and the ballistic-diffusive equations (BDE) for different Knudsen numbers. (b) Comparison of the heat flux q_y^* at the centerline for Kn= 0.1 at t^*=100.

CASE II: Equivalent equilibrium Temperature Boundary Condition

As explained before, the emitted phonon temperatures in Case I do not represent the local energy density at the boundaries. To compare with results obtained from the diffusion heat conduction equation based on the Fourier law, the boundaries in Fig. 2-3(a) are set as an equivalent equilibrium temperature in Case II. Though the results are presented in temperature, it should be properly interpreted as an energy density. As discussed before, iteration is needed to obtain the transient emitted phonon temperatures at the boundaries from given equivalent equilibrium temperature boundary conditions. The calculation time for both the BTE and the BDE can be 4-5 times longer than the corresponding calculation time using the emitted temperature boundary conditions.

Figure 2-10(a) and (b) compares the transient nondimensional heat flux in the y direction calculated using the phonon BTE, BDE and the Fourier law. The BDE gives very good agreement with the phonon BTE. However, the Fourier law overpredicts the heat flux by several times compared to the prediction by the phonon BTE. These results indicate that the suppressed heat conduction in nanostructures will lead to a larger temperature rise than that obtained from the Fourier law if a heat flux is specified at the boundary. Figure 2-10(c) shows the comparison of the transient temperature distribution along the centerline. Compared to case I, no temperature jump is observed at the boundary because of the consistent use of equivalent equilibrium temperature at the boundaries. Both the phonon BTE and BDE show time retardation due to the finite propagation speed of the phonons that cannot be predicted by the Fourier law. The temperature distribution predicted by Fourier heat conduction theory is very close together for $t^* = 0.1$ and $t^* = 1.0$ as shown in Fig. 2-10(b).

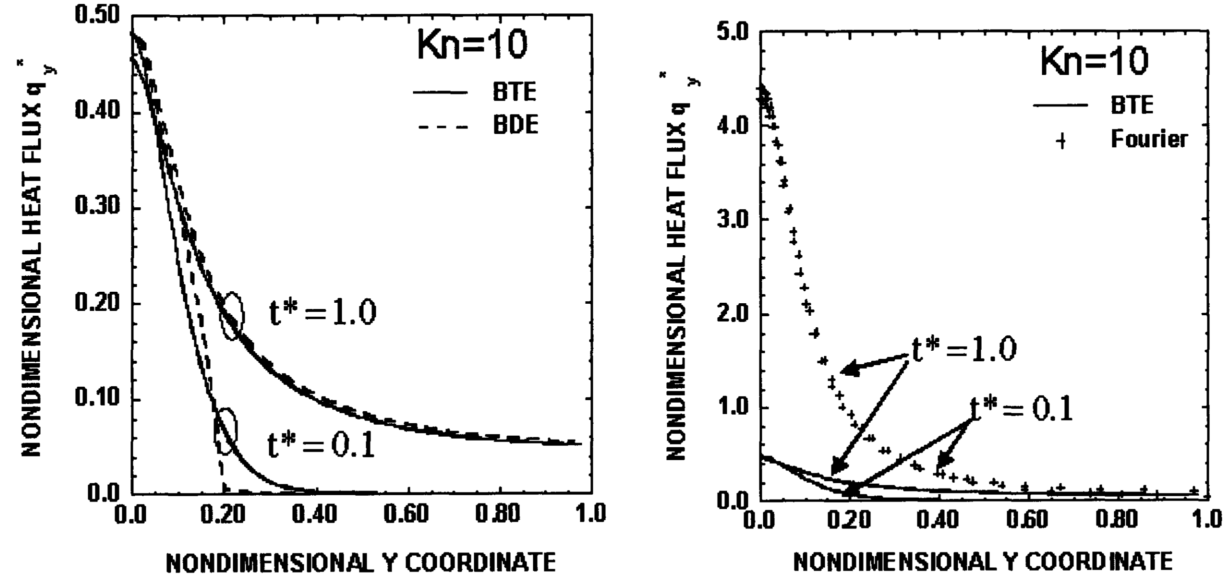

(a) (b)

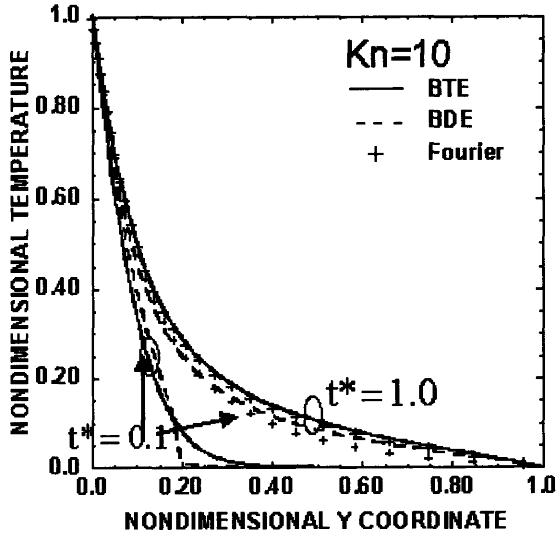

(c)

Figure 2-10. Comparison of transient temperature and heat flux distribution at the centerline using the Fourier theory, the Boltzmann equation, and the ballistic-diffusive equations based on thermalized temperature boundary conditions: (a)&(b) heat flux q_y^*, (c) temperature.

CASE III: Nanoscale Volumetric Heat Generation

In case III, we investigate the size effect of a nanoscale heat source inside the medium, as shown in Fig. 2-3(b). The heat source is similar to that generated in a metal oxide semiconductor field effect transistor (MOSFET), which is the backbone of microelectronics. A 10nm x 10 nm x 1 μm hot strip is embedded in the silicon substrate. The power generation rate is 1 X 10^{19} W/m^3, typically for a period of 10 ps [1]. We are interested in finding out the temperature rise ~10 ps after the device is turned on. With the given input properties stated in the second section, we can model the problem as a two dimensional nanoscale heat conduction problem because 1 μm in the length direction (z) is much longer than the phonon traveling length 30 nm in 10 ps. We know that the geometric parameters L_x and L_y will not much affect the results obtained by the phonon BTE and the BDE when the surrounding length is larger than 30 nm, thus $L_x = 10L_h$ and $L_y = 5L_h$ is used in the calculation.

Figure 2-11 shows the source, boundary emission and the diffusive component contribution to the total temperature and the heat flux in the y direction at the centerline. The region close to the heater is dominated by the ballistic part. The ballistic component of the temperature rise induced by the heat source reaches a maximum while the ballistic component of the heat flux induced by the heat source is zero at the center of the heat source because the heat carrier is propagating in both directions. The ballistic component induced by the boundary emission decays exponentially from the boundary. The region far away from the heater is dominated by the diffusive part. There is bending for the diffusive component in both the temperature and heat flux profiles because the heat carriers are treated as a ballistic component out of the boundary once they are diffused into the boundary. A small wave front is also observed where the boundary emission component decays to zero. This wavefront is believed to be artificial since it does not appear in solution of the Boltzmann equation.

Figure 2-12 shows a comparison of the temperature distribution obtained by the phonon BTE, BDE and the Fourier law. The peak temperature predicted by the Fourier law is much smaller than that predicted by the phonon BTE and BDE. However, the Fourier law predicts a broader temperature-affected region because the Fourier law assumes a very large thermal conductivity and an infinite phonon propagation speed. The heat flux distribution shown in Fig. 2-13(a) explains the difference in Fig. 2-12. The Fourier law overpredicts the heat flux by many times especially in the short time scale when compared to those obtained by the phonon BTE.

Localized nanoscale heating is clearly shown in the results and the phonon BTE and BDE captures such an effect fairy well. Figure 2-13(b) shows the peak temperature rise in the device as a function of time. A saturation of temperature rise after 10 ps is predicted by all the methods although the magnitudes are different. From the cases studied, we also would like to note that the relative difference between the BDE and the phonon BTE is case specific. Without a heat source inside the medium, the relative difference between the BDE and the phonon BTE is negligible. The difference between the phonon BTE and the BDE are larger when an internal heat source exists but the results from the BDE are still significantly better than those from the Fourier law. For example, the relative errors are 25% and 85% for the BDE and the Fourier's law when compared to the phonon BTE in case III.

2.6 Conclusions

In this chapter, we further developed the BDE for multidimensional heat conduction problems including a nanoscale heat source term and different boundary conditions. The numerical solution strategies for multidimensional nano-scale heat conduction using the BDE are presented. The transient Boltzmann equation is solved using the discrete ordinates method with the two Gauss-Legendre quadratures. Several 2-D cases are simulated to compare the results of the transient phonon BTE, BDE, and the Fourier law. Special attention has been paid to the boundary conditions. Compared to the cases without internal heat generation, the differences between the BTE and BDE are larger for the case studied with internal heat generation due to the nature of the ballistic-diffusive approximation, but the results from the BDE are still significantly better than those from the Fourier law. Overall, the BDE captures the characteristics of the phonon BTE with much shorter computational time.

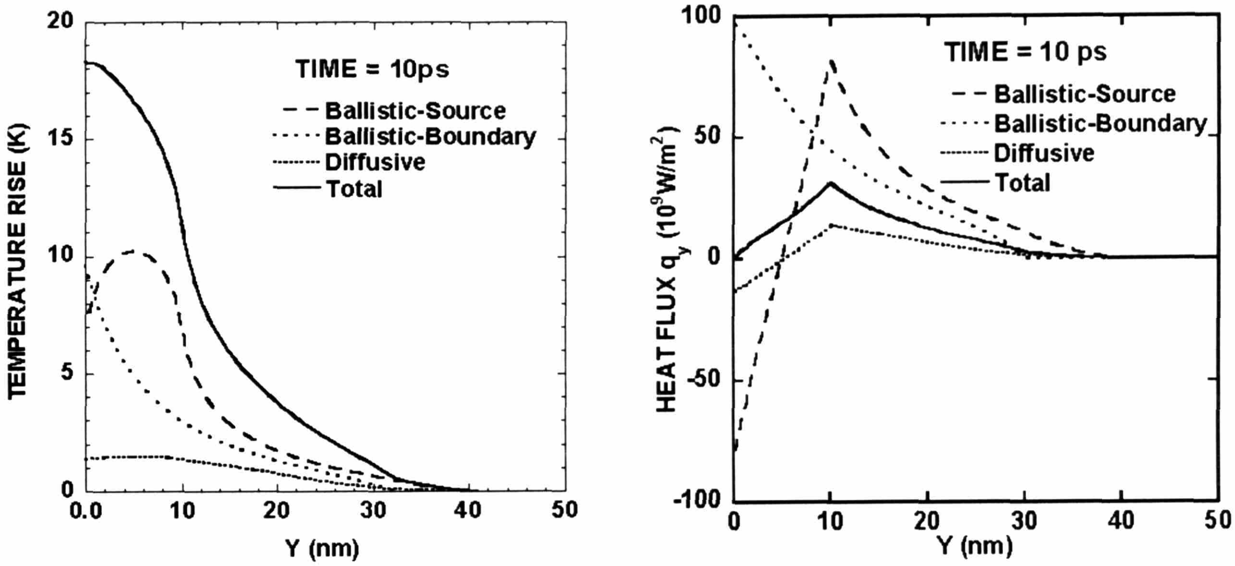

(a) (b)

Figure 2-11. The ballistic and diffusive component contributions to the total temperature and heat flux at the centerline: (a) temperature, and (b) heat flux q_y^*.

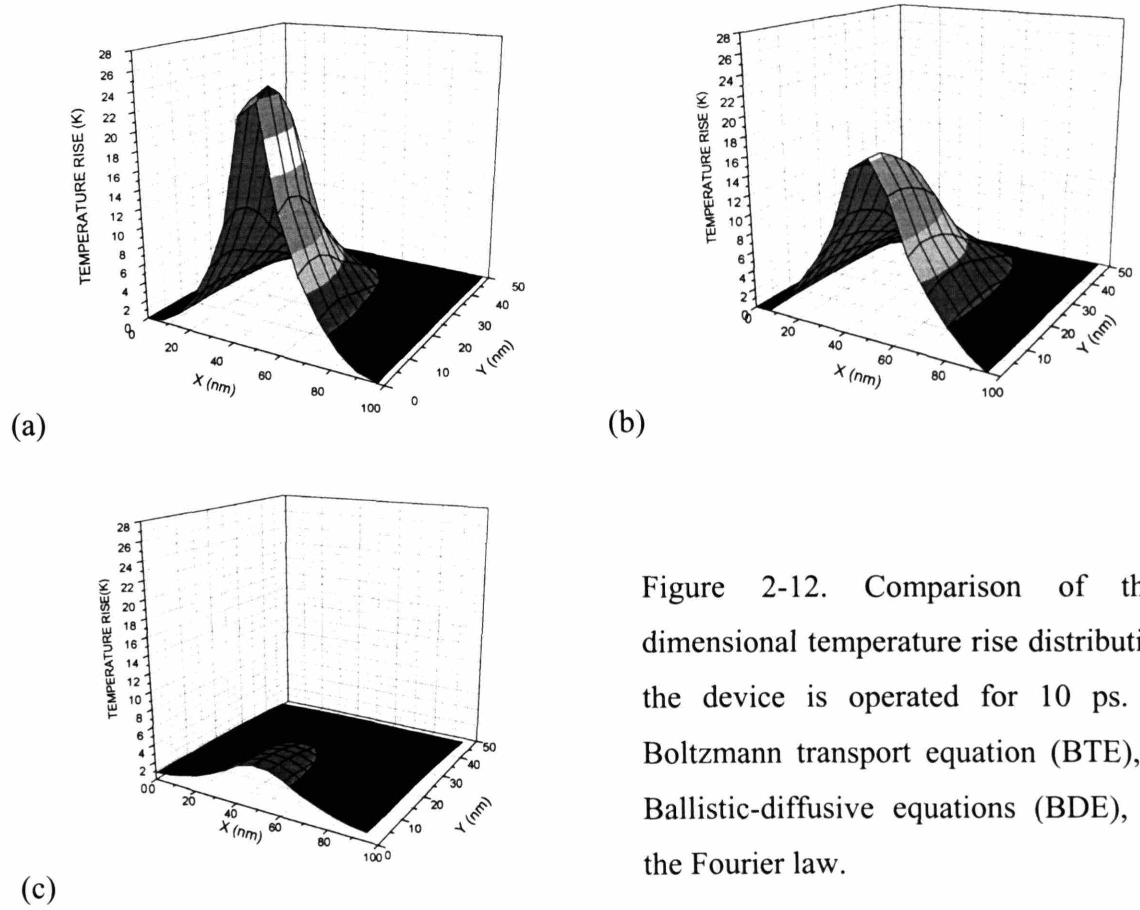

(a) (b)

(c)

Figure 2-12. Comparison of the two dimensional temperature rise distribution after the device is operated for 10 ps. (a) the Boltzmann transport equation (BTE), (b) the Ballistic-diffusive equations (BDE), and (c) the Fourier law.

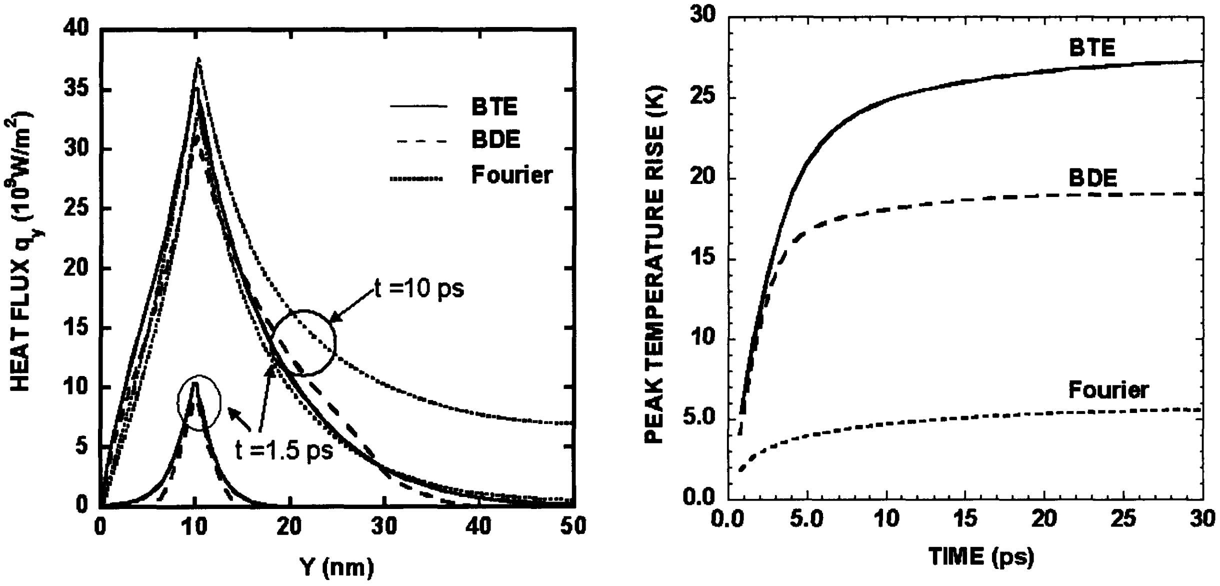

(a) (b)

Figure 2-13. (a) Comparison of the heat flux distribution obtained by the Boltzmann transport equation (BTE), the ballistic-diffusive equations (BDE), and the Fourier law (Fourier) at the centerline (b) Comparison of the peak temperature rise inside the device obtained by the Boltzmann equation, the Ballistic-diffusive equations and the Fourier law.

2.7 References

1. Y. Taur, IEDM Technical Digest, pp. 789-793 (1998).
2. C.L. Tien, A. Majumdar, and F.M. Gerner, Microscale Energy Transport, (Taylor & Francis, Washington, DC, 1998).
3. G. Chen, Nanoscale Energy Transport and Conversion, (Oxford University Press, New York, 2005)
4. G. Chen, D. Borca-Tasciuc, and R.G. Yang, in Encyclopedia of Nanoscience and Nanotechnology, Eds. H.S. Nalwa, Vol. **7**, pp.429-459, (American Scientific Publishers, Stevenson Ranch, CA, 2004)
5. E. Lewis, Computational Methods of Neutron Transport, (John Wiley & Sons, Inc., New York, 1984).
6. M.F. Modest, Radiative Heat Transfer, 2nd ed., (Academic Press, New York, 2003).
7. C.R. Tellier, and A.J. Tosser, Size Effects in Thin Films, (Elsevier, Amsterdam, 1982).

8. K.E. Goodson, and Y.S. Ju, Annual Review in Material Science **29**, 261 (1999).

9. G. Chen, Semiconductors and Semimetals **71**, 203 (2000).

10. G. Chen, ASME Journal of Heat Transfer **118**, 539 (1996).

11. P.G. Sverdrup, Y.S. Ju, and K.E. Goodson, ASME Journal of Heat Transfer **123**, 130 (2001).

12. J.Y. Murthy, and S.R. Mathur, ASME Journal of Heat Transfer **125**, 904 (2003).

13. S.V.J. Narumanchi, J.Y. Murthy, J.Y., and C.H. Amon, ASME Journal of Heat Transfer **125**, 896 (2003).

14. G.Chen, Physics Review Letters **86**, 2297 (2003).

15. G. Chen, ASME Journal of Heat Transfer **124**, 320 (2002).

16. C. Cercignani, The Boltzmann Equation and its Applications, (Spring-Verlag, New York, 1988).

17. B.K. Ridley, Quantum Processes in Semiconductors, 4th ed, (Oxford University Press, 1999).

18. R. Siegel, and J.R. Howell, Thermal Radiation Heat Transfer, 4th ed, (Taylor & Francis, Washington DC, 2001)

19. M. F. Modest, Radiative Heat Transfer, (McGraw-Hill, Inc., New York, 1993)..

20. J. M. Ziman, Electrons and Phonons, (Oxford University Press, 2001).

21. L.J. Challis, V.W. Rampton, and A.F.G. Watt, Phonon Scattering in Solids, (Plenum Press, New York, 1975).

22. G.P. Srivastava, Physics of Phonons, (Adam Hilger, New York, 1990)

23. R. Berman, Thermal Conductivity in Solids, (Clarendon Press, Oxford, UK, 1976)

24. D.K. Ferry, Semiconductors, (McMillan, New York, 1991)

25. J. Callaway, Physical Review **113**, 1046 (1959).

26. A. Majumdar, ASME Journal of Heat Transfer **115**, 7 (1993)

27. G. Chen, Physical Review B **57**, 14958 (1998).

28. G. Chen, ASME Journal of Heat Transfer **119**, 220 (1997)

29. P.G. Klemens, Solid-State Physics **7**, 1 (1958).

30. B. N. Brockhouse, Physical Review Letters **2**, 256 (1959).

31. G. Nilsson and G. Nelin, Physical Review B **3**, 364 (1971).

32. N.W. Ashcroft, and N.D. Mermin, Solid State Physics, (Brooks Cole, 1976).

33. The temperature dependent thermal conductivity of bulk Si and Ge is available at http://www.ioffe.rssi.ru/SVA/NSM/Semicond/

34. G. Chen, Applied Physics Letters **82**, 991 (2003).

35. D.B. Olfe, AIAA Journal 5, 638-643 (1967).

36. M.F. Modest, Journal of Thermophysics and Heat Transfer **3**, 283 (1989).

37. M. Ramankutty, and A. Crosbie, Journal of Quantitative Spectroscopy and Radiative Transfer **57**, 107 (1997).

38. M. Sakami, and A. Charette, Journal of Quantitative Spectroscopy and Radiative Transfer **64**, 275 (2000).

39. G.C. Pomraning, The Equation of Radiation Hydrodynamics, (Pergamon, New York., 1973).

40. C.Y. Wu, Journal of Thermophysics **1**, 296 (1987).

41. K.E. Goodson, ASME Journal of Heat Transfer **118**, 279 (1996).

42. A.A. Joshi, and A. Majumdar, Journal of Applied Physics **74**, 31 (1993).

43. W.A. Fiveland, ASME Journal of Heat transfer **109**, 809 (1987).

44 J.S. Truelove, ASME Journal of Heat transfer **109**, 1048 (1987).

45. G.D. Raithby, Numerical Heat Transfer – Part B: Fundamentals **35**, 389 (1994).

46. L.L. Briggs, W.F. Miller, and E.E. Lewis, Nuclear Science and Engineering **57**, 205 (1975).

47. J.C. Chai, H.S. Lee, and S.V. Patankar S,V, Numerical Heat Transfer Part B: Fundamentals **24**, 373 (1993).

48. P. Coelho, Journal of Quantitative Spectroscopy and Radiative Transfer **73**, 231 (2002).

49. J. Murthy, and S. Mathur, Journal of Thermophysics and Heat Transfer **12**, 313 (1998).

50. W.A. Fiveland, in Fundamentals of Radiation Heat Transfer, HTD-Vol. 160, pp. 89-96 (1991).

51. J.C. Chai, S.V. Patankar, and H.S. Lee, Journal of Thermophysics and Heat Transfer **8**, 140 (1994).

Chapter 3. Thermal Conductivity of Two-Dimensional Nanocomposites

In this chapter, the deterministic solution of the phonon Boltzmann equation is established to study the phonon thermal conductivity of nanocomposites with nanowires embedded in a host semiconductor material, both along and across the wire directions. Special attention has been paid to cell-cell interaction using periodic boundary conditions. The general approach is applied to study silicon wire / germanium matrix nanocomposites. We predict the thermal conductivity dependence on the size of the nanowires and the volumetric fraction of the constituent materials. At constant volumetric fraction, the smaller the wire diameter, the smaller is the thermal conductivity of periodic two-dimensional nanocomposites. For fixed silicon wire dimension, the lower the atomic percentage of germanium, the lower the thermal conductivity of the nanocomposites. Comparison is also made with the thermal conductivity of superlattices, alloys, and conventional model. The simulation shows that the temperature profiles in nanocomposites when the temperature gradient is applied across the nanowire direction are very different from those in conventional composites, due to ballistic phonon transport at the nanoscale. Such temperature profiles cannot be captured by existing models in the literature. The results of this study can be used to direct the development of high efficiency thermoelectric materials.

3.1 Introduction

The efficiency and energy density of thermoelectric devices are determined by the dimensionless thermoelectric figure of merit $ZT = \frac{S^2 \sigma T}{k}$, where S is the Seebeck coefficient, σ is the electrical conductivity, k is the thermal conductivity, and T is the absolute temperature [1]. Significant advances for increasing ZT have been made, based on new ideas about how to engineer electron and phonon transport [2]. One particularly fruitful and exciting approach has been the use of nanostructures, so that the electronic performance can be improved or maintained concurrently with a reduction of the phonon thermal conductivity [3-5]. Nanostructure-based materials, such as Bi_2Te_3/Sb_2Te_3 superlattices and PbTe/PbSeTe quantum dot superlattices, have shown significant increases in ZT values compared to their bulk counterparts due mainly to the reduced phonon thermal conductivity of these structures [6,7]. Nanocomposites may realize a similar thermal conductivity reduction and may provide a pathway to scale-up the nanoscale effects that are observed in superlattices to nanocompsite thermoelectric materials in bulk form [8]. A recent report on high ZT bulk thermoelectric materials indeed contains nanostructure constituents [9]. With a simple hot pressing procedure, Zhao et al. showed that the effective thermal conductivity of a Bi_2Te_3 nanocomposite with tubular Bi_2Te_3 nanowire inclusions is reduced, leading to a 25% increase in ZT compared to homogenous bulk materials [10].

Most previous studies on thermal transport in nanostructures have focused on thin films, semiconductor superlattices and nanowires. One key question in modeling of the thermal conductivity in nanostructures, especially such as superlattices and nanocomposites where the structures are periodic, is when the wave effect, i.e., the phonon dispersion change, should be considered [11, 12]. For example, models for phonon transport in superlattices generally fall into two groups. One group ("wave models") assumes that phonons form superlattice bands and then calculates the modified phonon dispersion using lattice dynamics or other methods [13-16]. The other group of models ("particle models") assumes that the major reason for the thermal conductivity reduction is the sequential scattering of phonons at interfaces [17-20]. In these models, phonon transport falls into the totally incoherent regime, and superlattices are treated as inhomogeneous multilayer structures. Diffuse interface scattering is usually incorporated into the Boltzmann equation (BE) as a boundary condition. These models succeeded in fitting experimental values for several superlattice systems in the thick period range. However, because the wave nature of phonons is ignored, these models fail to explain the thermal conductivity recovery in the short period limit that is observed in some superlattices. More recently, models [12,21] and direct simulations [22] combining the above two pictures have been presented. These models and simulations further confirm the importance of diffuse interface scattering for thermal conductivity reduction. The diffuse interface scattering can not only reduce the phonon MFP but also can destroy the coherence of phonons. Due to the loss of coherence, the phonon dispersion change in nanostructures predicted by the ideal lattice dynamics approximation cannot be realized. Previous studies of the thermal conductivity of superlattices demonstrated that classical size effect models are expected to be applicable to a wide range of nanostructures. This has been further confirmed by a recent study on developing the classical size effect model for phonon transport in nanowires and superlattice nanowires [23]. The model, assuming gray and diffuse phonon scattering at interfaces and side walls, has successfully explained the thermal conductivity reduction effect measured from nanowires. Based on all these previous studies, we believe that the reduced thermal conductivity in superlattices comes from the sequential interface scattering of phonons, i.e., classical size effect, rather than the coherent superposition of phonon waves. This conclusion leads naturally to the idea of using nanocomposites as potentially an economical alternative to superlattices in the quest for high ZT materials [24,25]. Thus we will apply in this chapter and in chapter 4 the phonon Boltzmann equation and Monte Carlo simulation method to study the classical size effect on the thermal conductivity of nanocomposites.

Another field of related research is effective thermal conductivity of composites. The effective thermal conductivity of composites at the macroscale has been studied since Maxwell (for a review, see Milton [26]), and a variety of methods have been proposed to estimate physical properties of heterogeneous media. In most of these research works, the interfaces between two hetero-media are treated as non-resistive to heat flow. The interface thermal resistance, or Kapitza resistance [27] has been considered only recently. The first two theoretical analyses that include the interface thermal resistance were conducted by Hasselman and Johnson [28], and by Benvensite [29], respectively. Hasselman and Johnson extended the classical work of Maxwell and Rayleigh to derive a Maxwell-Garnett type effective medium approximation (EMA) for calculating the effective thermal conductivity of simple spherical particle and cylindrical fiber reinforced matrix composites in which interface effects and particle size effect are included. Benvensite and Miloh [29] developed a general framework incorporating thermal boundary resistance by averaging all pertinent variables like heat flux and intensity over the composite medium, viewed as a continuum consisting of a matrix with inclusions. Every et al [30] refined the effective medium theory and presented an asymmetric Bruggeman type EMA, corrected for Kapitza resistance, as a simple solution for a high volumetric fraction of an inclusion, based on Bruggeman's integration-embedding principle. A noticeable work was by Nan et al., [31] who adopted the multiple scattering theory [32] to develop a more general EMA formulation for the effective thermal conductivity of arbitrary particulate composites with interfacial thermal resistance. They considered the properties of the matrix and reinforcement, particle size and particle size distribution, volume fraction, interface resistance and the effect of shape. Other models have also been proposed including the bounding model [33,34] and the thermal resistance network theory. Numerical simulation of the thermal conductivity of composites can also be found in the literature [35-38]. However these macroscopic models are developed based on Fourier heat conduction theory, and this theory is not valid at the nanoscale due to ballistic phonon transport.

So far, there are not many theoretical studies on the thermal conductivity of nanocomposites, despite their importance in both thermoelectrics and thermal management of electronics (especially the development of thermal interface materials). Closely related works have been done by Khitun et al. [39] and Balandin and Lazarenkova [40] to explain the *ZT* enhancement of Ge quantum dot structures (where Ge quantum dots are ~4nm and can be thought of as nanoparticles). The model by Khitun et al. is to calculate the reduced thermal conductivity through the relaxation time change due to the nanoparticles embedded using Mathiessen rule [41]. They used the Mie theory for acoustic wave scattering to calculate the scattering cross-section of a single particle and thus the additional relaxation time due to single particle scattering. Their method is valid if there is no inelastic scattering inside the particle and the interface scattering must be specular [42]. This approach does not recover the bulk material properties of composites since the thermal conductivity of the nanoparticle material is not taken into account. Similar to the wave model of superlattices, Balandin and Lazarenkova [40] assumed that a new homogeneous material is formed and they calculated the new electron and phonon dispersion relation thus showing a reduction in the group velocity. This approach requires phonon coherence over several unit cells and does not apply to diffuse interface scattering as observed in previous studies on superlattices.

The motivation of the present work in this thesis is to develop a microscopic framework for thermal conductivity of nanocomposites in terms of phonon particle transport model. More specifically, we will establish the deterministic solution of the phonon Boltzmann equation to study the phonon transport in periodic two-dimensional (2-D) nanocomposites where nanowires are embedded in a matrix material, for the thermal conductivity both along and across the wire directions. Chapter 4 complements this chapter by studying the thermal conductivity of both periodic and random nanoparticle composites using a Monte Carlo simulation of the phonon transport. Both models will help to understand some basic physical phenomena that exist in nanocomposites and the approach might be extended to study electron transport in nanocomposites. Some fundamental questions will be addressed in the investigation, such as (a) how is phonon transport in nanocomposites different from that in macroscale composites, (b) what is the behavior of the size effect in nanowire-embedded composites, and (c) can nanocomposites have a lower effective thermal conductivity than a superlattice.

3.2 Theoretical Model

To establish the phonon particle transport model, the following assumptions are made: (1) The phonon wave effect can be excluded. (2) The frequency-dependent scattering rate in the bulk medium is approximated by an average phonon MFP. (3) The interface scattering is diffuse. The first assumption has already been addressed in the introduction and the second one in Chapter 2. Here we are elaborating on the last assumption, i.e., diffuse interface scattering.

The interface scattering between the nanowire and the host material is assumed to be diffuse. Ziman [41] proposed the following expression for estimating the interface specularity parameter p,

$$p = \exp\left(-\frac{16\pi^3\delta^2}{\lambda^2}\right) \tag{3-1}$$

where δ is the characteristic interface roughness and λ is the characteristic phonon wavelength. At room temperature, the characteristic phonon wavelength $\lambda = hv/k_BT$ is about 1 nm, where h is Planck's constant, k_B is the Boltzmann constant and v is the sound velocity in the material. From this equation even a one monolayer roughness $\delta \sim 0.3\,\text{nm}$ gives an interface specularity parameter $p=0$, and allows for a totally diffuse interface assumption.

3.2.1 Unit Cell and Periodic Boundary Condition for Transport Processes

If there are two species, nanocomposites can be in the form of nano-particles and nanowires of one materials specie embedded in another host matrix material, or mixtures of two different kinds of nanoparticles that are compacted, as shown in Fig. 3-1 [43]. My thesis work focuses on nanocomposites with nanoparticles or nanowires embedded in a host material as shown in Fig. 3-1(a).

It can be a daunting problem to model or simulate the transport properties of nanocomposites since the distribution of the nanoparticle size and location can vary a lot. To accurately model the transport, the simulation box shown in Fig. 3-1(a) should be as large as possible, or even the same size as the sample. The memory and computational time requirements for such a multiscale problem are very demanding. Simulation of the properties of a periodic structure often gives physical insights of materials even in their random form. In this approach, as shown in Fig. 3-1(c), the nanocomposite is shown as a repeating structure of the simulation box. Such a simulation box is also often called a unit cell. A unit cell might consist of one nanoparticle/nanowire or many nanoparticles and nanowires. If the unit cell consists of only one nanoparticle or one nanowire, the repeating structure is a simple stack of a periodic nanocomposite. If the unit cell consists of many nanoparticles and nanowires inside and the distribution inside the unit cell (simulation box) is random, the nanocomposite is then semi-periodic, i.e, long range periodic but random inside the unit cell.

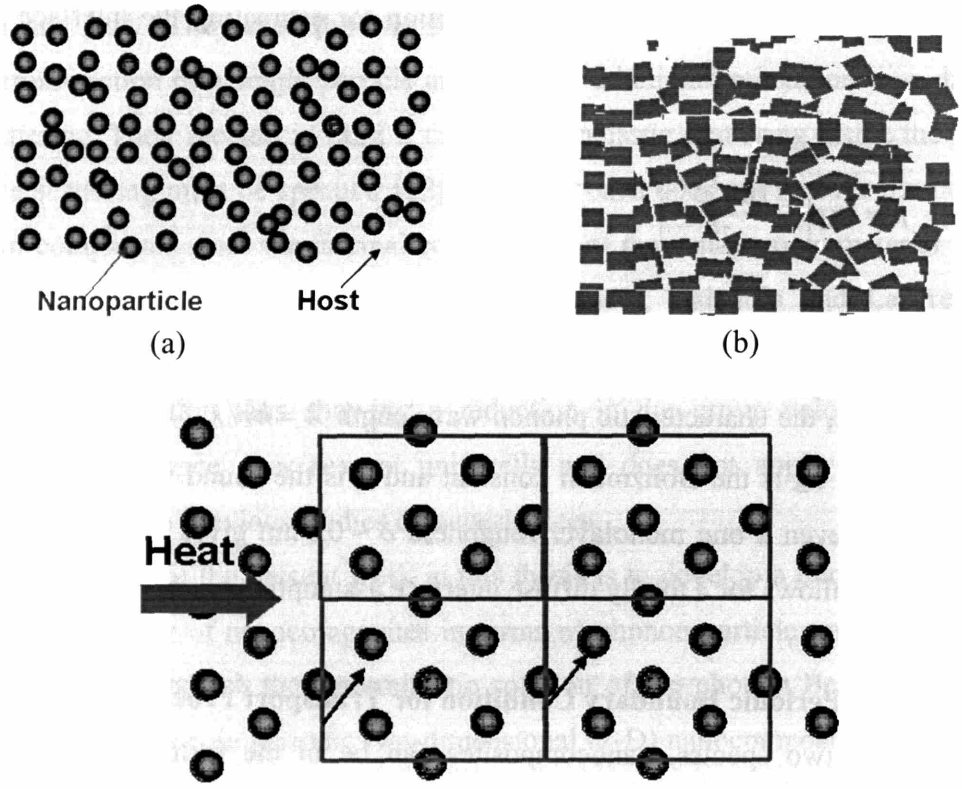

(a)

(b)

(c)

Figure 3-1. There are two forms of nanocomposites: (a) nano-particles or nanowires embedded in a host matrix material,or (b) mixtures of two different kinds of nanoparticles. (c) This thesis focuses on periodic nanocomposites where nanoparticles or nanowires are embedded periodically in a matrix material. The periodic nanocomposite can be viewed as a periodic stack of unit cells, shown as red squares.

Even to simulate the transport properties of periodic structures can be a challenge. The reason is that although the geometry is periodic, the distribution of the state properties such as temperature is not periodic since either a thermal or an electric field is applied in the transport direction. This is very different from studying state properties in solid state physics such as those using the Bloch theorem for finding electron states when a periodic potential is applied. If one does not pay careful attention to the boundary conditions, the transport properties obtained using the unit cell will not be the same as the composite, as shown in Fig. 3-1(a). The unit cell concept is actually often used to analyze transport properties of heterogeneous materials. For example, the constant wall heat flux and the constant-temperature boundary conditions are the two most often used boundary conditions for thermal conductivity modeling and simulation for periodic stacks when the Fourier law for heat conduction is applied [44]. However, neither of them would be able to resemble the transport properties of the structure.

It can be shown from the Fourier heat conduction equation that the heat transport in the unit cell represents the transport inside the whole structure when

$$\nabla T(\mathbf{r}+\mathbf{L}) = \nabla T(\mathbf{r}) \tag{3-2}$$

or

$$\mathbf{q}(\mathbf{r}+\mathbf{L}) = \mathbf{q}(\mathbf{r}) \tag{3-3}$$

where $\mathbf{r}$ is the vector describing any point inside a composite, $\mathbf{L}$ is the vector describing the periodic structure, and $\mathbf{q}$ is the directional heat flux in arbitrary $\hat{\mathbf{\Omega}}$ directions. For a rectangular unit cell as shown in Fig. 3-1(a) with heat flow imposed in th x direction (horizontal direction), the general condition of Eq.(2) or (3) results in such a set of boundary conditions:

$$q_x(0,y) = q_x(L_x,y) \tag{3-4}$$

$$q_y(x,0) = q_y(x,L_y) \tag{3-5}$$

In addition, to calculate the thermal conductivity, one needs to apply a constant temperature difference ΔT which is independent of y across the unit cell in the transport direction, i.e, in the x direction. The final results for the thermal conductivity will not depend on how large a ΔT that is applied. This boundary condition is stricter than constant wall heat flux and the constant-temperature boundary conditions.

When the Boltzmann equation is used to analyze the thermal conductivity of periodic composites, one would physically argue that Eq. (3-3) must be valid, but Eq. (3-2) cannot be established since a temperature gradient cannot be established. However, we need boundary conditions for calculating the intensity. In the following, we provide a physical argument leading to justification of the periodic boundary condition.

When the Boltzmann equation is used, the frequency-dependent phonon radiation intensity in the $\hat{\mathbf{\Omega}}$ direction is defined over all of space with a 4π solid angle, as

$$I_\omega\left(\mathbf{r},\hat{\mathbf{\Omega}}\right)=v_\omega \hbar\omega f\left(\mathbf{r},\hat{\mathbf{\Omega}}\right)D(\omega)/4\pi. \tag{3-6}$$

However, we cannot simply specify that $I_\omega\left(\mathbf{r},\hat{\mathbf{\Omega}}\right)=I_\omega\left(\mathbf{r}+\mathbf{L},\hat{\mathbf{\Omega}}\right)$ since $f\left(\mathbf{r},\hat{\mathbf{\Omega}}\right)$ is not equal to $f\left(\mathbf{r}+\mathbf{L},\hat{\mathbf{\Omega}}\right)$ due to the temperature field (or temperature difference) applied on the composite structure where the difference in the equilibrium distribution f_0 can be large. On the other hand, we can define a frequency-dependent directional heat flux $\mathbf{q}_\omega(\mathbf{r})$ in $\hat{\mathbf{\Omega}}$ direction, i.e., $q_\omega\left(\mathbf{r},\hat{\mathbf{\Omega}}\right)$, which is defined in over a 2π solid angle that is related to the frequency-dependent phonon intensity which is defined over a 4π solid angle as

$$q_\omega\left(\mathbf{r},\hat{\mathbf{\Omega}}\right)=I_\omega\left(\mathbf{r},\hat{\mathbf{\Omega}}\right)-I_\omega\left(\mathbf{r},-\hat{\mathbf{\Omega}}\right) \tag{3-7}$$

As discussed in Chapter 2, the nature of the Boltzmann transport equation requires that the boundary condition specify the intensity pointing inward towards the simulation domain direction at all the boundaries. Thus Eq.(3-7) would not be able to close the model based on the Boltzmann equation since it does not specify the intensity, and covers only a 2π solid angle. Noticing that $I_{0\omega}(\mathbf{r})$ is isotropic, one can write Eq. (3-7) as

$$q_\omega\left(\mathbf{r},\hat{\mathbf{\Omega}}\right)=[I_\omega\left(\mathbf{r},\hat{\mathbf{\Omega}}\right)-I_{0\omega}(\mathbf{r})]-[I_\omega\left(\mathbf{r},-\hat{\mathbf{\Omega}}\right)-I_{0\omega}(\mathbf{r})]\equiv q_\omega^+\left(\mathbf{r},\hat{\mathbf{\Omega}}\right)-q_\omega^-\left(\mathbf{r},\hat{\mathbf{\Omega}}\right) \tag{3-8}$$

Then we are able to specify the intensity over the full 4π solid angles, and then one should specify $q_\omega^+(\mathbf{r},\hat{\mathbf{\Omega}}) \equiv I_\omega(\mathbf{r},\hat{\mathbf{\Omega}}) - I_{0\omega}(\mathbf{r})$ for the 2π solid angle and $q_\omega^-(\mathbf{r},\hat{\mathbf{\Omega}}) \equiv I_\omega(\mathbf{r},-\hat{\mathbf{\Omega}}) - I_{0\omega}(\mathbf{r})$ for the other 2π solid angle. Comparing this expression to Eq. (3-3) for diffusive heat transport, the periodic condition for Boltzmann transport should be

$$I_\omega(\mathbf{r},\hat{\mathbf{\Omega}}) - I_{0\omega}(\mathbf{r}) = I_\omega(\mathbf{r}+\mathbf{L},\hat{\mathbf{\Omega}}) - I_{0\omega}(\mathbf{r}+\mathbf{L}) \tag{3-9}$$

which can represent the whole structure, where $I_{0\omega}(\mathbf{r}+\mathbf{L})$ and $I_{0\omega}(\mathbf{r})$ depend solely on the local temperature. Thus Eq.(3-9) means that the deviation of the phonon intensity at any point in any direction is periodic. Eq. (3-9) provides the basis for setting up the periodic boundary conditions when using the Boltzmann transport equation.

3.2.2 Transport across the wire direction

We first focus our work on the phonon transport in nanowire-embedded composites when the heat-flow direction is perpendicular to the wire axis. As shown in Fig. 3-2 (a), there is no heat flow along the wire axis. Thus the problem is simplified to a two-dimensional problem although the nature of the phonon transport is three-dimensional in nature, as shown in Fig. 3-2(c). The unit cell to be simulated is shown in Fig. 3-2(b). The details about the interface and boundary conditions will be presented in s later section. To make comparisons, we also calculated the cross-plane thermal conductivity of a simple one-dimensional Si-Ge layered structure, which is often called a superlattice when the thickness of each layer is tens of nanometers, as shown in Fig. 3-2(d).

For each material phase, the 2-D phonon BTE under the single mode relaxation time approximation can be written similarly to Eq. (2-6) as,

$$\sin\theta\cos\phi\frac{\partial I_i}{\partial y} + \cos\theta\frac{\partial I_i}{\partial x} = -\frac{I_i - I_{oi}}{\Lambda_i} \tag{3-10}$$

where θ and ϕ , as shown in Fig. 3-2(c) are the polar and the azimuthal angles, respectively, and Λ_i is the average phonon MFP. I_{oi} is determined by the Bose-Einstein distribution of phonons and depends on the local equilibrium temperature.

Boundary Conditions. As shown in Fig. 3-2(b), heat is forced to flow in the x-direction. The symmetry in the geometry and the physics of periodic transport renders that the specularly reflected boundary conditions should be enforced at the $y=0$ and $y=L_{Ge}$ boundaries,

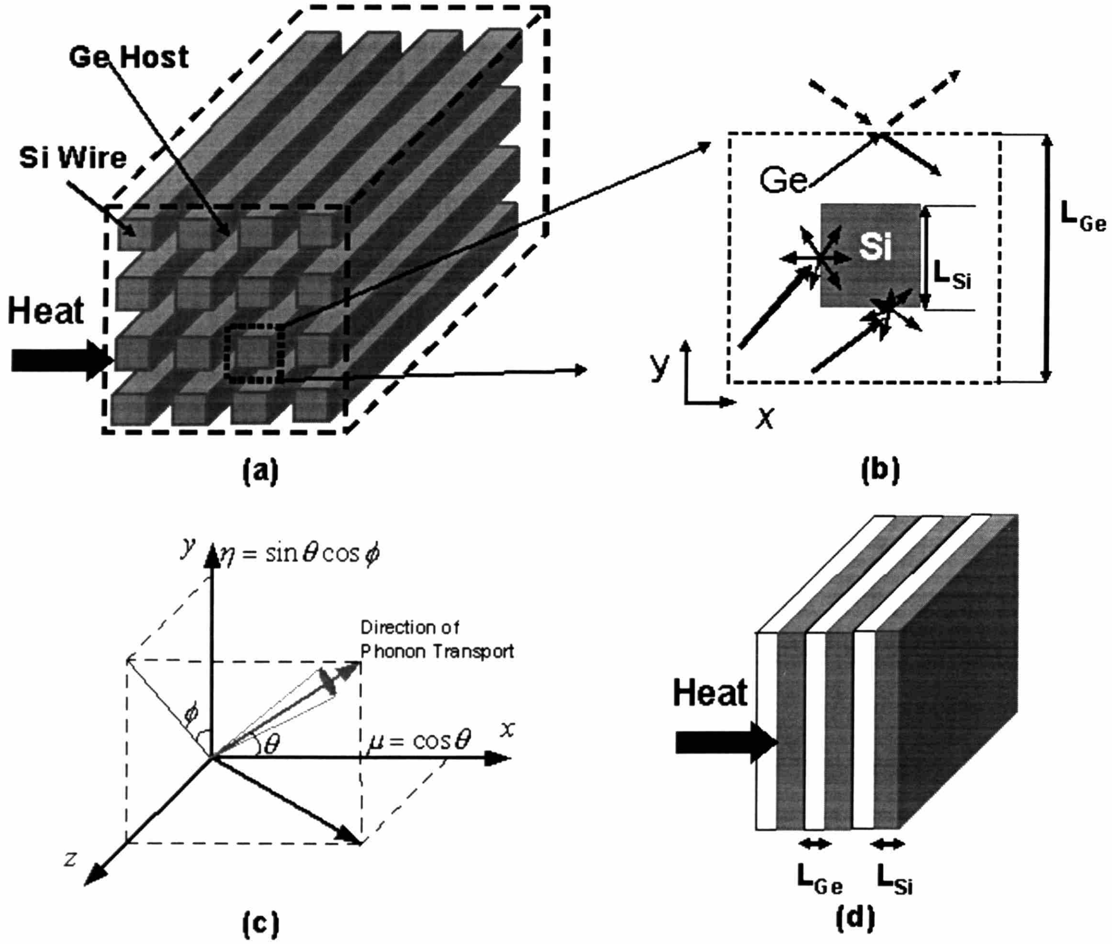

Figure 3-2. (a) Heat flow across a periodic 2-D composite with silicon wires embedded in the germanium host, (b) the unit cell to be simulated, (c) local coordinates used in the phonon Boltzmann equation simulation, (d) heat flow across a 1-D Si-Ge layered structure (superlattice).

$$I(x,L_{Ge},\theta,\phi)=I(x,L_{Ge},\theta,\pi-\phi) \tag{3-11}$$

$$I(x,0,\theta,\phi)=I(x,0,\theta,\pi-\phi). \tag{3-12}$$

In the x-direction, we can now straightforwardly write the boundary condition from Eq. (3-9) as

$$I(L_{Ge},y,\theta,\phi)-I_0(L_{Ge},y)=I(0,y,\theta,\phi)-I_0(0,y) \tag{3-13}$$

The physical meaning of this equation is that the distortion of the phonon intensity in each direction at each point *(0,y)* at the *x=0* boundary is the same as the distortion in the corresponding direction at the corresponding point *(L_{Ge},y)* at the *x=L_{Ge}* boundary.

With these boundary conditions shown in (3-11) to (3-13), the phonon transport of the whole structure can be represented by that in the unit cell due to the periodicity of the problem as formulated. Again the temperature difference across the unit cell in the x-direction should be independent of y. for a rectangular unit cell when the temperature difference is applied in the normal direction, that is:

$$I_o(0,y)-I_o(L_{Ge},y)=\frac{C_1v_1[T(0,y)-T(L_{Ge},y)]}{4\pi}=\text{constant}. \tag{3-14}$$

In our simulation, we superimposed $T(0,y)-T(L_{Ge},y)=1\,\text{K}$ on the above equation. If we do not superimpose such a temperature difference onto the program, Eq. (3-13) will automatically converged to a constant temperature difference $T(0,y)-T(L_{Ge},y)$. The converged value will vary with the simulated structure. But the final results of the thermal conductivity value will not depend on whether the temperature difference is superimposed. However, the calculation is much faster when a temperature difference value is superimposed. We should note that superimposing a temperature difference across the unit cell is physically different from superimposing a temperature (either an emitted or Fourier-limit temperature) at each boundary, which was done in most of the current literature.

Interface Conditions. Determining the phonon reflectivity and transmissivity at an interface is difficult as in the treatment of the classical thermal boundary resistance problem [45-47]. One rather crude model is called the diffuse mismatch model [47] which assumes that phonons emerging from the interface do not really bear any relationship the origin of the phonon, i.e., one cannot tell which side the phonons come from. This assumption implies that

$$T_{d21} = R_{d12} = 1 - T_{d12}, \tag{3-15}$$

where T_{d21} is the phonon transmissivity from medium 2 to medium 1, and R_{d12} is the phonon reflectivity in medium 1 at the interface between medium 1 and 2. In the above, the second equation comes from the energy conservation identity $R_{d12} + T_{d12} = 1$. Dames and Chen [23] obtained the following equation for T_{d12}, which is expected to be valid over a wide temperature range:

$$T_{d12}(T) = \frac{U_2 v_2}{U_1(T) v_1 + U_2(T) v_2} \tag{3-16}$$

where U is the volumetric internal energy, v_2 and v_2 is the average phonon group velocity in material 1 and 2, respectively.

With a given phonon transmissivity and reflectivity at interfaces, we can write down the phonon intensity at the interfaces. As an example, the phonon intensity for $0 < \theta < \frac{\pi}{2}$ ($\mu > 0$) at the (x=$\frac{L_{Ge} - L_{Si}}{2}$, $\frac{L_{Ge} - L_{Si}}{2} \le y \le \frac{L_{Ge} + L_{Si}}{2}$) interface can be written from the energy balance equation.

$$\int_0^{2\pi}\int_0^{\pi/2} I(\frac{L_{Ge} - L_{Si}}{2}, y, \theta, \phi)\cos\theta \cdot \sin\theta d\theta d\phi = -R_{d21}\int_0^{2\pi}\int_{\pi/2}^{\pi} I(\frac{L_{Ge} - L_{Si}}{2}, y, \theta, \phi)\cos\theta \cdot \sin\theta d\theta d\phi$$

$$+ T_{d12}\int_0^{2\pi}\int_0^{\pi/2} I(\frac{L_{Ge} - L_{Si}}{2}, y, \theta, \phi)\cos\theta \cdot \sin\theta d\theta d\phi \tag{3-17}$$

Because the phonons are scattered diffusely at interfaces, the phonons leaving an interface are isotropically distributed, and Eq. (3-17) can be written as

$$I\left(\frac{L_{Ge}-L_{Si}}{2},y,\theta,\phi\right)=-\frac{R_{d21}}{\pi}\int_0^{2\pi}\int_{\pi/2}^{\pi}I\left(\frac{L_{Ge}-L_{Si}}{2},y,\theta,\phi\right)\cos\theta\cdot\sin\theta d\theta d\phi$$

$$+\frac{T_{d12}}{\pi}\int_0^{2\pi}\int_0^{\pi/2}I\left(\frac{L_{Ge}-L_{Si}}{2},y,\theta,\phi\right)\cos\theta\cdot\sin\theta d\theta d\phi,\quad \text{for } 0<\theta<\frac{\pi}{2} \qquad (3\text{-}18)$$

The equations for phonons leaving for $\frac{\pi}{2}<\theta<\pi$ and at other interfaces can be similarly written.

Numerical Simulation and Effective Thermal Conductivity. Although at thenanoscale, the temperature cannot be defined as a measure of equilibrium, and so we can use an effective temperature to reflect the local energy density inside the medium. Assuming a constant specific heat over a wide temperature range, we can write an effective temperature as

$$T(x,y)=\frac{4\pi I_0(x,y)}{C|v|}=\frac{1}{C|v|}\sum_n\sum_m I(x,y,\mu_n,\varphi_m)w_n w'_m \qquad (3\text{-}19)$$

The heat fluxes $q_x(x,y)$ and $q_y(x,y)$ at every point can be accordingly written as:

$$q_x(x,y)=\sum_m\sum_n I(x,y,\mu_n,\varphi_m)\mu_n w_n w'_m \qquad (3\text{-}20)$$

$$q_y(x,y)=\sum_m\sum_n I(x,y,\mu_n,\varphi_m)\sqrt{1-\mu_n^2}\cos\varphi_m\cdot w_n w'_m \qquad (3\text{-}21)$$

where q_x and q_y are heat flux in the x- and y- directions respectively. After the local effective temperature distribution and heat flux are obtained, the thermal conductivity calculation is straightforward, taking advantage of the unit cell concept. The surface heat flux in the x-direction can be calculated as

$$Q_x(x)=L_Z\int_0^{L_{Ge}}q_x(x,y)dy \qquad (3\text{-}22)$$

where L_z is the unit length in the z-direction. Eqs. (3-11) and (3-12), i.e., the specular reflected boundary conditions enforced at $y=0$ and $y=L_{Ge}$ boundaries have ensured $Q_x(x)$=constant. The average energy density (average temperature) at each y-z plane along the x-direction can be written as:

$$\bar{T}(x)=\frac{1}{L_{Ge}}\int_0^{L_{Ge}} T(x,y)dy\,. \tag{3-23}$$

Therefore the effective thermal conductivity k of the composite can be obtained as:

$$k=\frac{Q_x}{L_z(\bar{T}(L_{Ge})-\bar{T}(0))} \tag{3-24}$$

from

$$Q_x=k*(L_zL_{Ge})*\frac{(\bar{T}(L_{Ge})-\bar{T}(0))}{L_{Ge}} \tag{3-25}$$

The following dimensionless parameters have been introduced to present results of temperature and heat flux distributions:

$$q^*=\frac{q}{C_1\mathrm{v}_1},\ Q_x^*=\frac{Q_x}{L_{Ge}L_ZC_1v_1},\quad x^*=\frac{x}{L_{Ge}},\quad y^*=\frac{y}{L_{Ge}} \tag{3-26}$$

2.3 Transport along the Wire Direction

In Fig. 3-3(a), a temperature gradient is applied along the axial direction (z-direction) of a periodic two dimensional nanocomposite with tubular nanowire inclusions. Since the transport is periodic in both the x and y directions, the transport inside the nanocomposites can be represented by that in the small unit cell shown in Fig. 3-3(b) applying the totally specular phonon reflection boundary conditions along the x and y boundaries. However simulation of phonon transport in a 3-D unit cell shown in Fig. 3-3(b) is still a big challenge that involves the use of both Cartesian and cylindrical coordinates. As an approximation, we further convert the outer surface of the square unit cell into a circle, i.e., to approximate a square unit cell cross-section as a circular cross-section, as is often used to study fluid flow problems [48,49]. The problem then becomes one of phonon transport in core-shell cylindrical structures, as shown in Fig. 3-3(c). This approximation results in a 10% error. Figure 3-3(c) shows the generic phonon transport model we developed for core-shell nanostructures, which consist of a tubular core layer and a shell layer. Here we use the following notations, r_0 is the inner radius of the core layer, r_1 is the outer radius of the core layer, and r_2 is the outer radius of the shell. We assume partially diffuse and partially specular surface scattering at the inner surface of the core layer and totally specular reflection at the outer surface of the shell layer, to be consistent with what occurs at the outer surface of the unit cell shown in Fig. 3-3(b), i.e., to represent the phonon transport in nanocomposites. The specularity parameter at the inner surface of the core layer and at the outer surface of the shell layer is represented by p_1 and p_2, respectively, where p (=p_1 or p_2) =0 corresponds to diffuse scattering and p=1 corresponds to specular scattering at the surface. This generic model can be used to simulate a variety of nanocomposites by changing some of the input parameters. For example, when the inner radius of the tubular core layer is r_0=0 and the interface specularity is p_1=1 at r_0=0, the structure represents periodic two-dimensional composites with simple wire inclusions as shown in Fig. 3-3(d). When the same material is used for the core and the shell layers, the interface between the core and shell layers disappears and the interface scattering at r_1 dies out, the model then represents the phonon transport inside a nanoporous medium with cylindrical pores along the pore direction as shown in Fig. 3-3(e).

In terms of the total phonon intensity *I*, the 2-D phonon Boltzmann equation under the single mode relaxation time approximation in cylindrical coordinates can be written as,

$$\frac{\mu}{r}\frac{\partial}{\partial r}(rI_i)-\frac{1}{r}\frac{\partial}{\partial \phi}(\eta I_i)+\zeta\frac{\partial I_i}{\partial z}=-\frac{I_i-I_{oi}}{\Lambda_i} \tag{3-27}$$

where the subscript *i* (=1,2) denotes the properties of the core and shell material, and Λ_i is the average phonon MFP. We also define μ, η, and ζ as the direction cosines:

$$\mu=\sin\theta\cos\phi,\quad \eta=\sin\theta\sin\phi,\quad \zeta=\cos\theta \tag{3-28}$$

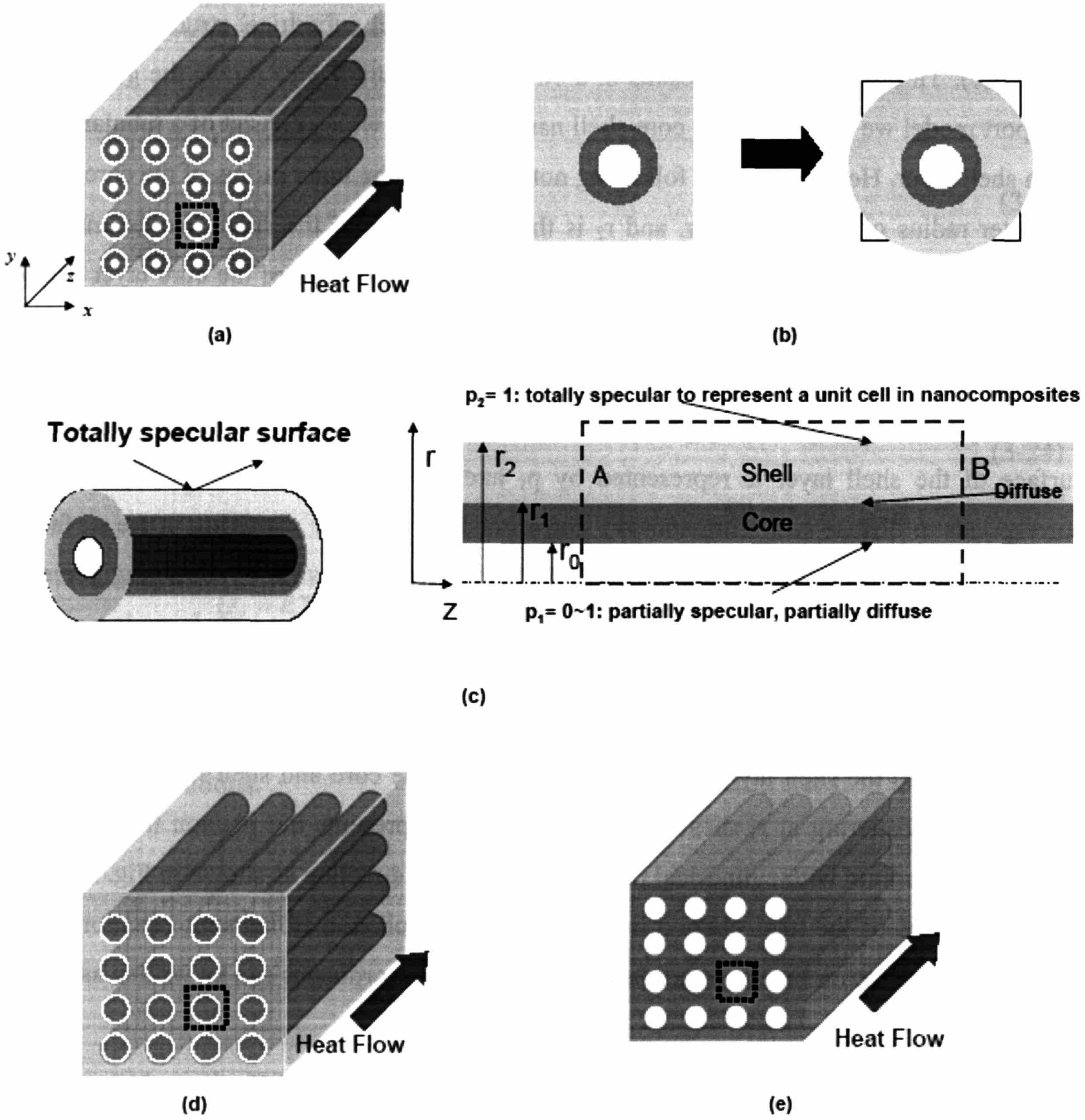

Figure 3-3. (a). A periodic two dimensional nanocomposite (composite with tubular nanowire inclusions), (b) cross-sectional view of a unit cell: a square unit cell cross-section is approximated as a circular cross-section of equal area, (c) by the approximation in (b), the transport in nanocomposites becomes phonon transport in core-shell cylindrical structures, (d) periodic silicon nanowire composites, (e) cylindrical nanoporous silicon material.

where θ and ϕ are the polar and azimuthal angles, respectively, as shown in Fig. 3-4. In the phonon Boltzmann transport equation [Eq. (3-27)], there are two coordinate systems [shown in Fig. 3-4]: spatial coordinates (r, ϕ_c and z) and directional coordinates (θ and ϕ) for the transport, which correspond to the movement of carriers in spatial and momentum space. As a phonon travels through a curved geometry, such as in cylindrical coordinates, the propagating direction is constantly varying, even though the phonon does not physically change its direction. This is why an additional term, the second term of the left hand side in Eq. (3-27), exists. Similary, we extend the previous work in Cartesian coordinates to cylindrical coordinates. The method separately discretizes the integration points in $\zeta = \cos\theta$ (the angle θ) and in the angle ϕ using the Gauss-Legendre quadratures. To obtain high accuracy, μ is discretized into 120 points from -1 to 1 and ϕ is discretized into 24 points for 0 to π (not 0 to 2π due to symmetry).

Following the conventional artifice of Carlson and Lathrop [50] and Lewis and Miller [51] which maintain phonon radiative energy conservation and permit minimal directional coupling, the angular derivative term can be written as follows:

$$\frac{\partial}{\partial\phi}(\eta^{nm} I_i^{nm}) = \frac{\alpha_{n,m+1/2} I_i^{n,m+1/2} - \alpha_{n,m-1/2} I_i^{n,m-1/2}}{w_n w'_m} \qquad (3\text{-}29)$$

where $w_n w'_m$ is are weights and $\alpha_{n,m\pm 1/2}$ are the coefficients for the angular derivative term determined from the non-divergent flow condition following the recursive equation

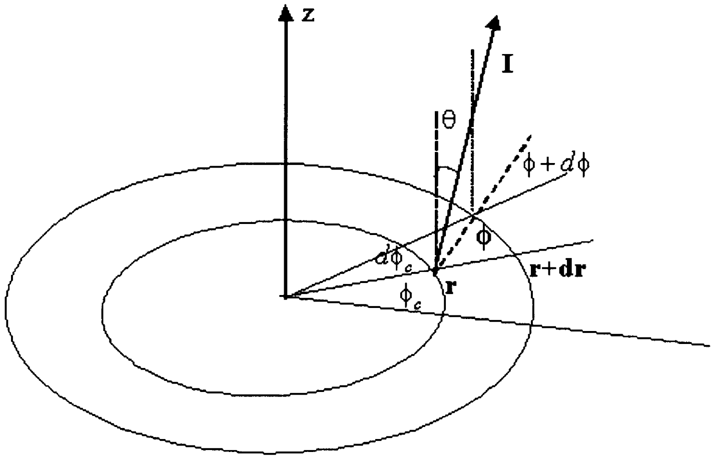

Figure 3-4. Phonon transport in cylindrical coordinates.

$$\alpha_{n,m+1/2} - \alpha_{n,m-1/2} = (w_n w'_m)\mu^{n,m} \tag{3-30}$$

For this work, we are only interested in the size effect occurring in the radial direction, not in the wire axis direction. However, because heat flows along the axial direction, the simulation requires choosing a proper length and setting the corresponding boundary conditions at the two ends along the transport direction. When heat is forced to flow in the axial direction, the temperature is different at the two ends. However, simply assuming a temperature difference at the two ends might induce an artificial size effect in the axial direction. To get rid of the artificial size effect in the axial direction, the periodic boundary condition on the phonon distribution deviation proposed in section 2.1 is used. For transport along the axial direction, the periodicity is arbitrary. So we can choose an arbitrary length L_Z and use the periodic boundary condition to obtain thermal conductivity values that are independent of L_Z. If the boundary conditions at the two ends are assumed as the emitted temperature condition [52], one often needs to simulate a domain more than 3 times longer than the phonon mean free path, which can be many times longer than the size in the radial direction. With the proposed boundary condition, the simulation domain length can be adjusted according to the size of the structure in the radial direction. We also note that the nature of the Boltzmann equation requires iterations to obtain convergent results with the boundary conditions we have defined.

As in previous work, a non-uniform grid system and the step scheme is used for spatial discretization to accurately capture the physics of the transport phenomena and to minimize the calculation time. The step scheme is used for spatial discretization. The equation is solved by iteration over the value of the equivalent equilibrium intensity $I_{0i}(r,z) = \frac{2}{4\pi}\sum_m \sum_n I_i(r,z,\zeta_n,\phi_m)w_n w'_m$. Assuming a constant specific heat over a wide temperature range, we can write the effective temperature, which is a measure of the local energy density inside the medium, as

$$T(r,z) = \frac{4\pi I_0(r,z)}{C_i|v_i|}. \tag{3-31}$$

The heat flux along the axial direction at every point can be accordingly written as:

$$q_z(r,z) = \sum_m \sum_n I(x,y,\zeta_n,\phi_m)\zeta_n w_n w'_m . \qquad (3\text{-}32)$$

The surface heat flux in the axial direction can be calculated as

$$Q_z(z) = \int_0^{r_2} q_z(r,z) 2\pi r dr . \qquad (3\text{-}33)$$

When the simulation is converged, then $Q_z(z)$=constant. After a local effective temperature distribution and heat flux are obtained, the thermal conductivity calculation is straightforward. The effective thermal conductivity k of the core-shell structure can be obtained as:

$$k = \frac{Q_z L_Z}{\pi r_2^2 \left[T(r,L_Z) - T(r,0)\right]} \qquad (3\text{-}34)$$

3.3 Results and Discussions

3.3.1 Transport across the Wire Direction

A. Nonequilibrium Temperature and Heat Flux Distribution

Figure 3-5 (a) and (c) show the effective temperature distribution in the composite structures with a silicon wire dimension of L_{Si} =268 nm and L_{Si}=10 nm, respectively. The atomic percentages are 20% for Si and 80% for Ge. Simple calculation gives the geometric ratio $\frac{L_{Ge}}{L_{Si}} = 2.35$. The choosing of L_{Si} =268 nm is based on the fact that the MFP value is around 268 nm as calculated from the silicon phonon dispersion curve [17]. Figure 3-5(a) is very close to the temperature we expect in macroscale composites with an interface thermal resistance. Therefore, for a wire dimension larger than 268 nm, the effective temperature distribution is expected to be similar to that plotted in Fig. 3-5(a). Comparison between Fig. 3-5(a) and (c) shows that the temperature or energy density distribution at the nanoscale in periodic 2-D composites can be very different from that at macroscale due to the ballistic nature of phonons. To better understand the effect of and interface thermal resistance, we plot the temperature distribution along the x direction at certain fixed y positions of the two structures in Fig. 3-5(b) and (d). Apparent temperature jumps at the wire-host material interfaces are clearly shown in Fig. 3-5(b) & (d). There are also temperature jumps along the y direction as indicated in Fig. 3-5(a) &(c). The larger the wire size, the lower the temperature jump relative to the total temperature difference across the interface, and thus the lower the contribution of the interface resistance to the effective thermal resistance of the composite. When the nanowire dimension is much smaller than the phonon MFP, say L_{Si}=10 nm, the temperature gradient along the x direction can be negative in some local regions. The heat fluxes in the x-direction, however, are always positive as shown in Fig. 3-6 (a) and (b). This phenomenon has not been observed before in macroscale composites and cannot be predicted by Fourier heat conduction-based theories. Another question that one may raise is whether the results shown in Fig. 3-5(c) and (d) violate the thermodynamic 2nd law because the temperature inside the cell is larger than the cell boundary. To answer this question, we should first remember, as pointed out before, that the temperature as defined is not the same as the case of thermal equilibrium or local thermal equilibrium. When ballistic transport dominates, no local thermal equilibrium can be established and the calculated temperature represents the local energy density. Figure 3-7(a) and 3-7(b) illustrate the mechanisms of the observation in Fig. 3-5. When L_{Si} is much smaller than the phonon MFP, the internal scattering in the medium (both for the host material and the wire) is negligible. We further assume that the phonon reflectivity is unity at the wire and host material interface. Then the scenario can be simplified as thermal radiation in vacuum with opaque wire inclusions (host material – vacuum, interface – solid wall, wire- opaque solid body). Referring to Fig. 3-7(a), we are interested in knowing the temperature distribution of A-F points when the heat is forced to flow in the x-direction. We can qualitatively call the left half of the region shown as the "hot" region and the right half as the "cold" region. As shown in the figure, points D and F "see" the hot region and points A and C "see" the cold region. Thus points D and F locally receive higher energy phonons and have a higher effective temperature than points A and C. Moving from point A to F (or from C to D), more hot area is seen than cold area. Thus the effective temperature increases. Comparing to D and F, point E has a lower temperature due to a small view factor from the hot region. Similarly point B has a higher effective temperature than A and C. Figure 3-5 shows the temperature distribution only in one unit cell. To visualize the temperature distribution, one needs to stitch together several periods of figure 3-5. Figure 3-7(b) shows the temperature distribution along x at several y points over three periods. The energy over those regions with even higher temperatures than the unit cell boundary comes from the much higher temperature region in their previous cells. The results do not violate the thermodynamic 2nd law if one view the nonequilibrium phonon transport through thermal radiation analogy.

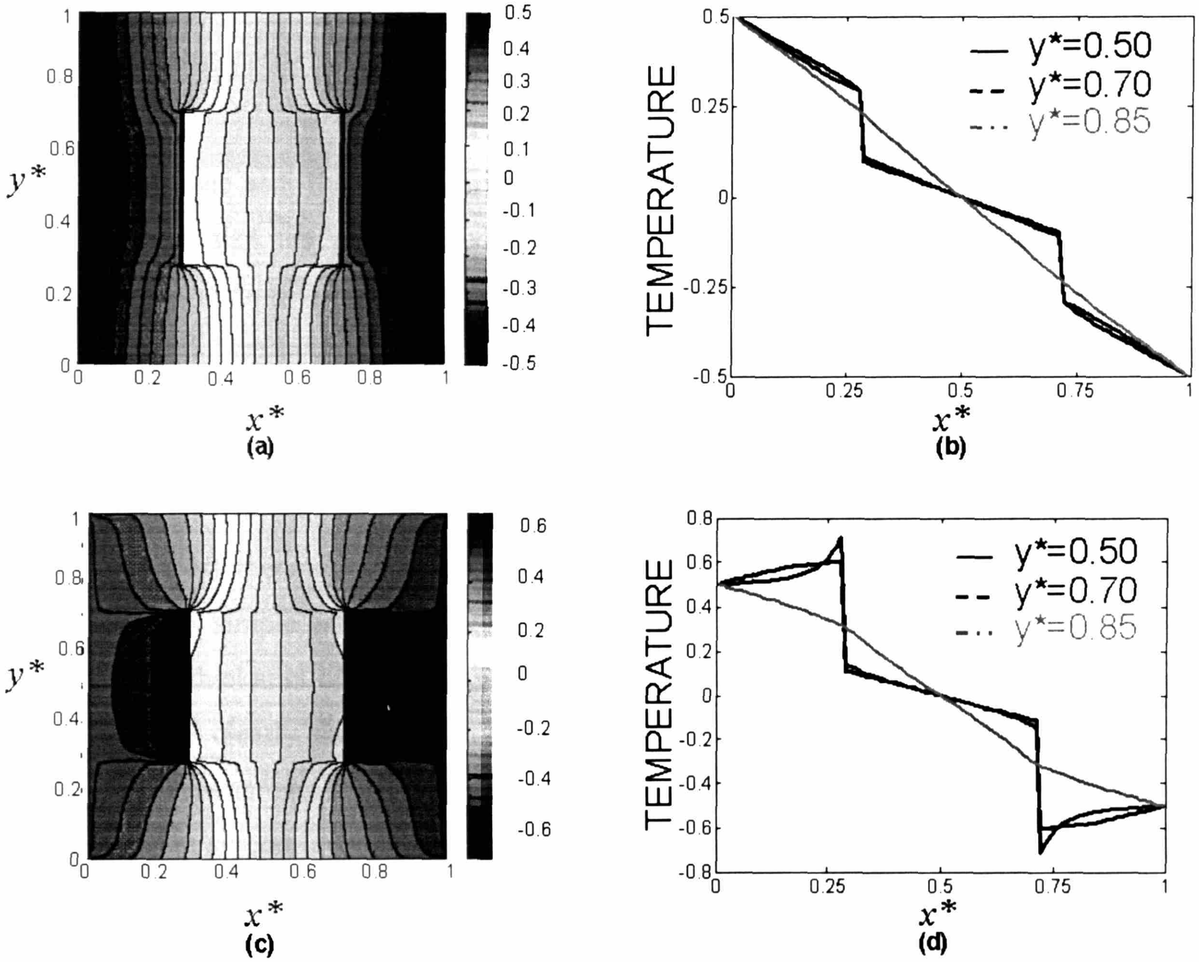

Figure 3-5. Effective temperature ($T-T_{ref}$) distribution in the unit cell of $Si_{0.2}$-$Ge_{0.8}$ composites with $T(0,y)$ - $T(L_{Ge},y)$ = 1 K applied for different wire dimensions: (a) temperature contour for L_{Si} =268nm, (b) the temperature distribution along x^* at $y^* = 0.5$, $y^* = 0.7$ and $y^* = 0.85$ for L_{Si} =268nm, (c) temperature contour for L_{Si} =10nm, (d) the temperature distribution along x^* at $y^* = 0.5$, $y^* = 0.7$ and $y^* = 0.85$ for a L_{Si} =10 nm. The temperature discontinuity at the interface is clearly shown. The temperature distribution in a L_{Si} =10 nm nanocomposite is very different from macroscale composites due to ballistic phonon transport at the nanoscale and these effects cannot be captured by Fourier heat conduction theory.

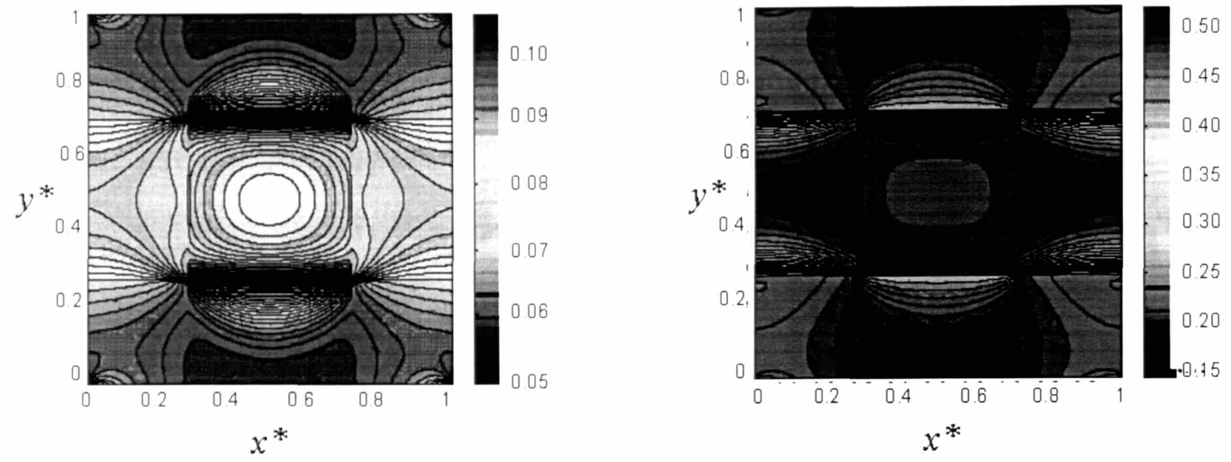

(a) (b)

Figure 3-6. The dimensionless heat flux distribution in the x-direction q_x*: (a) L_{Si} =268nm composite, and (b) L_{Si} =10 nm composite. These results show that the x-directional heat flux is always positive even in the localized negative temperature gradient region shown in Figure 3-5.

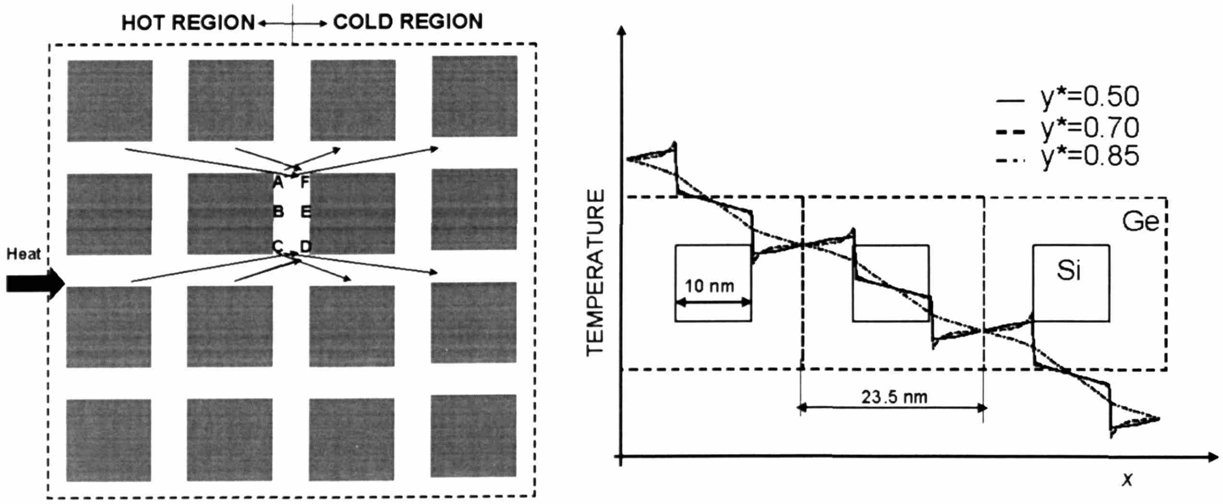

(a) (b)

Figure 3-7. (a) Illustration to show the mechanisms of negative temperature gradient in the localized regions using the thermal radiation analogy. (b) the temperature distribution along x^* at $y^* = 0.5$, $y^* = 0.7$ and $y^* = 0.85$ for L_{Si} =10 nm over three periods.

B. Effect of Wire Dimension

To calculate the effective thermal conductivity of composites, the surface heat flux and the average temperature (average energy density) at each y-z plane along the x direction is calculated. As an example, Fig. 3-8 show the dimensionless average energy density distribution along the x direction in a $Si_{0.2}$-$Ge_{0.8}$ composite with a silicon wire dimension of L_{Si}=268 nm and of L_{Si}=10 nm respectively. The dimensionless surface heat flux is conserved to $Q_x^*(x) = 0.088$ for a L_{Si}=268 nm composite and $Q_x^*(x) = 0.037$ for a L_{Si}=10 nm composite. Again, the surface heat flux is conserved and a temperature jump appears at the interface. The smaller the wire size, the larger the average temperature jump and thus the larger is the interface resistance contribution to the effective thermal resistance of the composite. We can expect that when the wire dimension is 2-3 times or even larger than the silicon MFP, the contribution of the interface thermal resistance will be negligible and the results will recover the Fourier limit. Figure 3-9 shows the thermal conductivity of $Si_{0.2}$-$Ge_{0.8}$ composites as a function of the silicon wire dimension. To make a comparison, we include the results of the cross-plane (perpendicular to the interfaces) thermal conductivity of a simple one-dimensional Si-Ge layered structure (superlattice). A simple calculation shows that the thickness of the germanium layer should be 4.52 times the thickness of silicon layer in 1-D stacks with a germanium atomic percentage of 80%. Figure 3-9 clearly shows that at a constant volumetric fraction (or atomic percentage), the smaller the characteristic length of silicon (the silicon wire dimension in composites and the thickness of the silicon layer in superlattices), the smaller the thermal conductivity. The simple 1-D layered structure has a lower thermal conductivity than periodic nanowire composites at this atomic percentage. We point out that the thermal conductivity of superlattices calculated here is lower than the experimental data because the interface scattering in superlattices may not fall into totally the diffuse scattering limit [17, 19]. The comparison shown in this chapter using totally diffuse phonon interface scattering is just for theoretical consistency.

C. Effect of Atomic Percentage

Some other questions of interests are: (1) can the thermal conductivity of nanowire composites be lower than that of simple 1-D stacks? (2) How the thermal conductivity changes with the atomic percentage? Figure 3-10 shows the thermal conductivity of Si_{1-x}-Ge_x composites as a function of atomic percentage x of germanium for wire dimensions L_{Si} of 50nm and 10 nm,

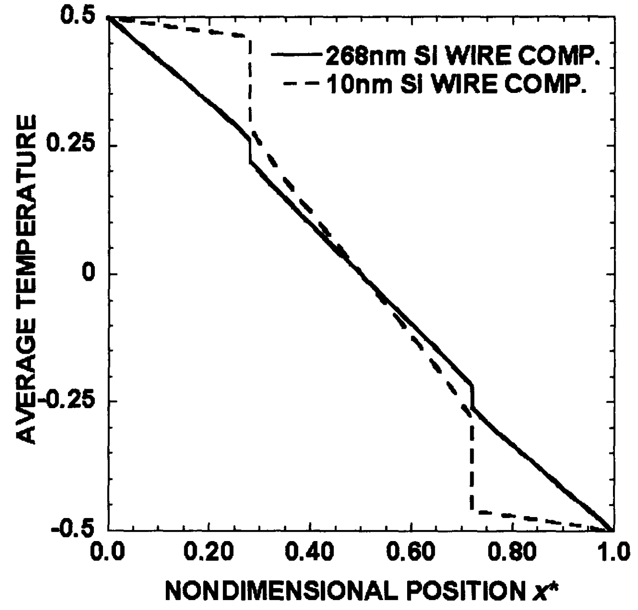

Figure 3-8. The dimensionless average temperature distribution along the x direction in a $Si_{0.2}$-$Ge_{0.8}$ composite with a silicon wire dimension of L_{Si}=268 nm and L_{Si}=10 nm, respectively.

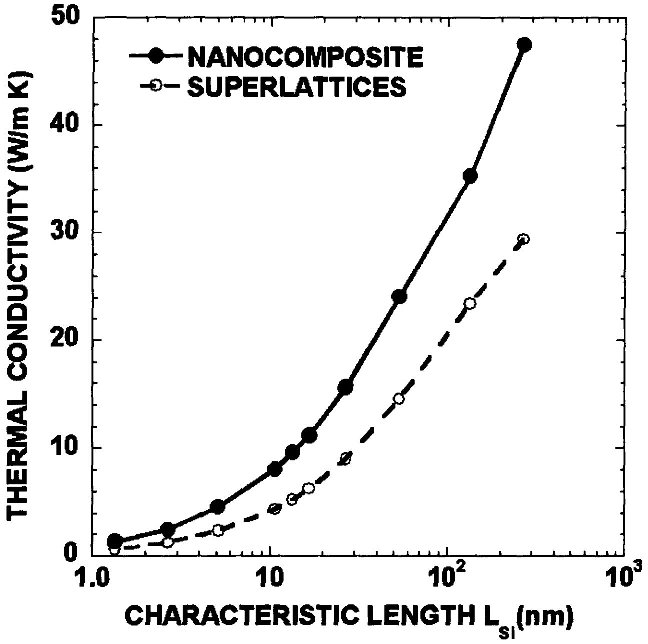

Figure 3-9. The thermal conductivity of $Si_{0.2}$-$Ge_{0.8}$ composites as a function of the silicon wire dimension or layer thickness. The smaller the characteristic length of silicon (the silicon wire dimension in composites and the thickness of the silicon layer in superlattices), the smaller is the thermal conductivity.

respectively. By changing the atomic percentage, the geometric ratio of the unit cell, i.e., the dimension of germanium is changed in the numerical simulation. The figure shows that for a fixed silicon wire dimension, the lower the atomic percentage of germanium, the lower is the thermal conductivity of the nanocomposites. This is very different from macroscale composites and nanoparticle-filled polymers, in which the thermal conductivity of the composites increases with the decreasing volumetric fraction of the low thermal conductivity component. This is caused by the ballistic transport of phonons in both the host material and the nanowires, and the interface resistance between the host material and the nanowires. In polymer nanocomposites, the thermal conductivity of the host polymer is usually very low and the thermal transport in polymers is diffusive. Thus the thermal conductivity of polymer nanocomposites increases with the volumetric fraction of high thermal conductivity nanoparticle fillers. Figure 3-10 also shows that the thermal conductivity of the periodic 2-D nanocomposites is lower than that of superlattice with a corresponding characteristic length when the atomic percentage x of germanium is lower than 35%. A simple calculation shows that the geometric ratio $\frac{L_{Ge}}{L_{Si}}$ is around 1.182 when x=0.35. For a simple 1-D layered structure as shown in Fig. 3-11(a), phonons experience cross-plane interface scattering in all the cross-sectional area z-y when the heat is forced to flow in the x-direction. Comparing Fig. 3-11 (a) and (b), we know that phonons can flow through a fraction of the $\frac{L_{Ge}-L_{Si}}{L_{Ge}}$ open area without experiencing cross-plane interface scattering. However, phonons must experience an additional fraction of $\frac{L_{Si}}{L_{Ge}}$ interface scattering parallel to the heat flow direction (in-plane scattering). When the thermal conductivity of a simple 1-D layered structure is the same as that of periodic 2-D nanocomposites at x=0.35, we can approximately infer that a fraction of the $\frac{L_{Si}}{L_{Ge}}$ in-plane interface scattering is equivalent to a fraction of the $\frac{L_{Ge}-L_{Si}}{L_{Ge}}$ cross-interface scattering. In other words, the efficiency of cross-interface scattering to reduce the thermal conductivity is around 5 times as effective as the scattering parallel to the interface. This result is consistent with previous experiments and modeling of the in-plane and cross-plane thermal conductivity of superlattices [17, 19]. It also suggests that anisotropic nanocomposites might be more effective for reducing thermal conductivity of nanocomposites.

D. Comparison with EMA

As stated in the introduction, most past studies on the thermal conductivity of nanocomposites were based on the Fourier diffusion theory together with consideration of the thermal boundary resistance. To examine the validity of such an approach, we compare the effective thermal conductivity obtained from the Boltzmann equation with that of the effective medium approach (EMA) developed by Nan et al [31], which gives the anisotropic effective thermal conductivity values of nanowire composites as:

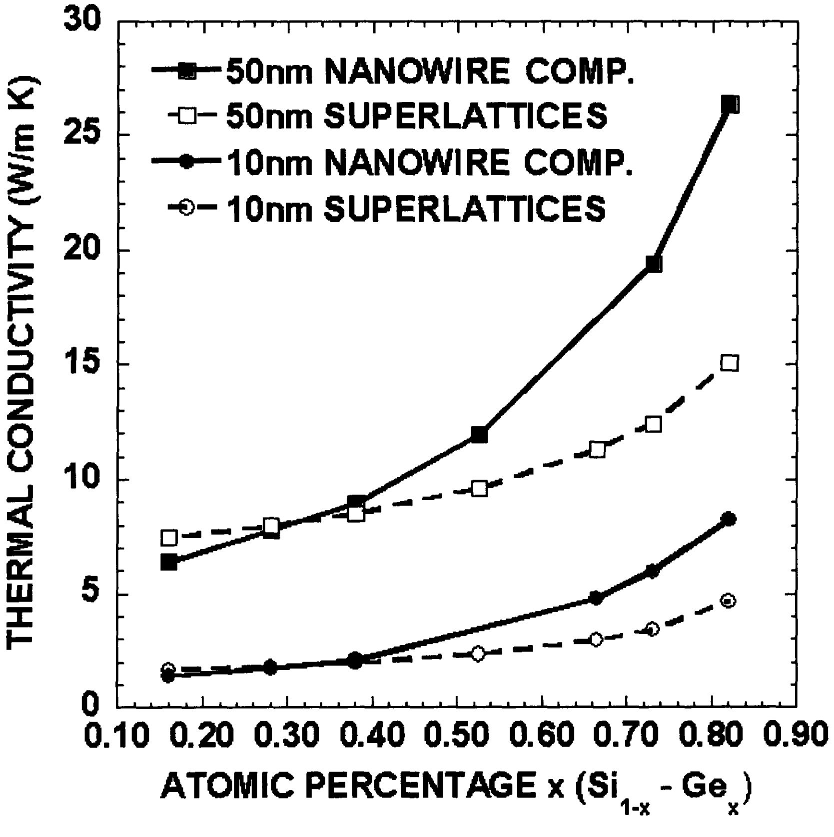

Figure 3-10. The thermal conductivity of Si_{1-x}-Ge_x composites as a function of atomic percentage x of germanium. For a fixed silicon wire dimension, the lower the atomic percentage of germanium, the lower is the thermal conductivity of the nanocomposites. The result is very different from the bulk material due to the ballistic nature of phonon transport at the nanoscale and the interface effect.

$$k_{11} = k_{22} = k_m \frac{k_P(1+\alpha) + k_m + \Phi_P[k_P(1-\alpha) - k_m]}{k_P(1+\alpha) + k_m - \Phi_P[k_P(1-\alpha) - k_m]} \tag{3-35}$$

$$k_{33} = (1 - \Phi_P)k_m + \Phi_P k_P \tag{3-36}$$

where k_{11} and k_{22} are the effective composite thermal conductivity across the wire axis direction and k_{33} is the effective thermal conductivity in the longitudinal direction, k_m is the thermal conductivity of the host material, k_P is the bulk thermal conductivity of the nanowire inclusion materials, Φ_P the volume fraction of nanowire inclusion, α is a dimensionless parameter defined as $a=a_k/a_P$ for nanowire composites. a_P is the radius of nanowire inclusions, and $a_k = Rk_m$, where R is the interface thermal resistance which can be calculated as [19]

$$R = \frac{4}{T_{d12}U_1 v_1} \approx \frac{4(U_1 v_1 + U_2 v_2)}{U_1 v_1 U_2 v_2} \tag{3-37}$$

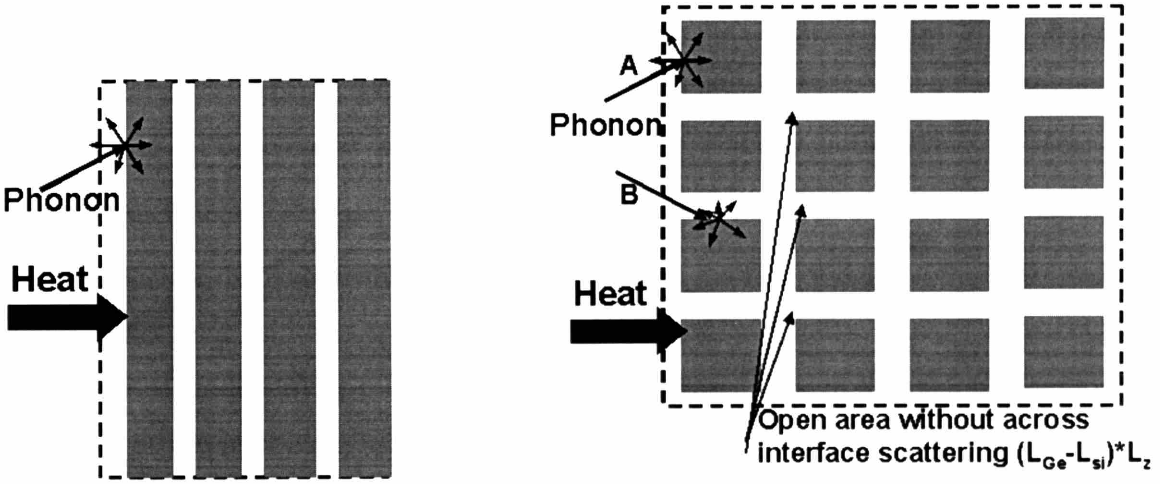

(a) (b)

Figure 3-11. Illustration to show that phonons experience less cross-interface scattering in periodic 2-D composites (b) than that in 1-D layered structures (a) but they experience additional scattering parallel to the interface. The efficiency of cross-interface scattering to reduce the thermal conductivity is around 5 times as effective as scattering parallel to the interface.

We compare k_{11}, the thermal conductivity perpendicular to the wire axis, with our phonon BTE simulation results. As our phonon BTE simulation was done for square wire inclusions, an effective diameter $D = 2a_p = 4A_C / P$ is used, where A_C is the cross-sectional area and P is the perimeter of the cross-section, to convert the square geometry into a circular geometry. Figure 3-12 compares the thermal conductivity in nanowire composites perpendicular to the wire axis obtained from the phonon Boltzmann equation simulation and the effective medium approximation (EMA). As we can see, the effective medium approach based on incorporating the thermal boundary resistance into the solutions of the Fourier heat conduction law leads to erroneous results that underpredict the size effects.

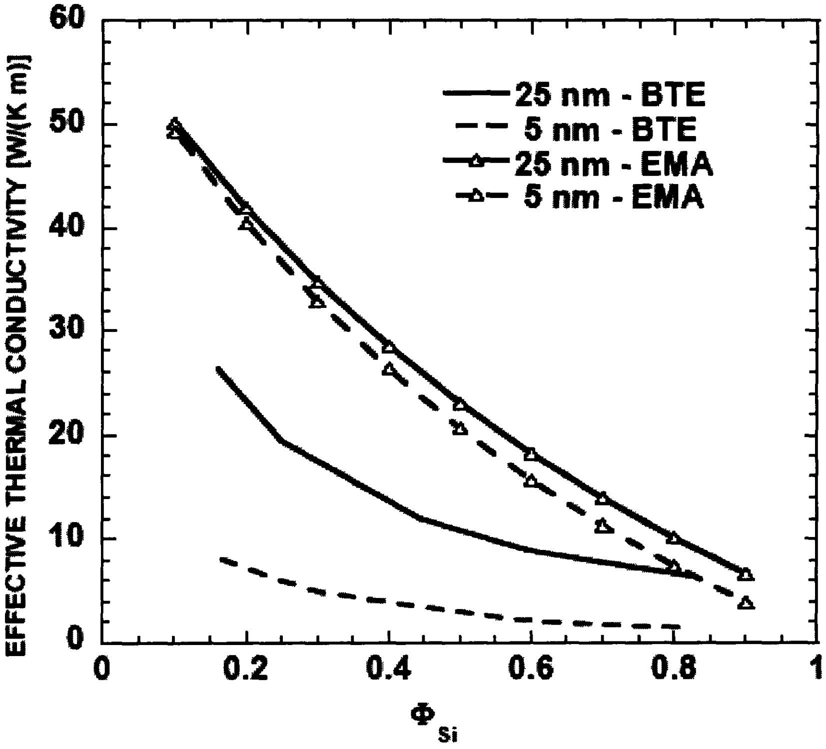

Figure 3-12. Comparison of the thermal conductivity of nanowire composites in the direction perpendicular to wire axial direction obtained from a phonon Boltzmann equation simulation and from the effective medium approximation (EMA) based on the Fourier law and the thermal boundary resistance, demonstrating that the EMA underpredicts size effects.

3.3.2 Transport along the Wire Direction

Figure 3-13 shows results for the thermal conductivity of a silicon-germanium nanocomposite which consists of a germanium matrix with silicon wire inclusions (as shown in Fig. 3-3(d)) as a function of the silicon wire radius and the volumetric ratio of Si, $\Phi_{Si} = \frac{r_1^2}{r_2^2}$, which can be related to the atomic ratio γ_{Si} through $\gamma_{Si} = \frac{\Phi_{Si}}{\Phi_{Si} + (1-\Phi_{Si})a_{si}/a_{Ge}}$, where a is the lattice constant. In a bulk Si-Ge composite, the effective thermal conductivity increases linearly as the cross-sectional area or volumetric ratio of Si (Φ_{Si}) increases, since Si has a much higher thermal conductivity than Ge. For Si-Ge nanocomposites, the effective thermal conductivity decreases as the radius of the wire inclusion decreases due to the relative increase in interface scattering area per unit volume. When the radius of the wire inclusion is larger than 500 nm, the effective thermal conductivity asymptotically approaches that of macroscale composites. This means that the interface scattering is negligible compared to the internal thermal resistance in Si wires and in the Ge matrix, and that the effective value for the thermal conductivity can be predicted by the Fourier law. For nanowire composites with an embedded wire radius less than 150nm, there exists a minimum thermal conductivity as the volumetric ratio of Si changes. The trend is similar as those predicted for core-shell Si-Ge nanowires [53]. When the volumetric ratio of Si (Φ_{Si}) in the composites is large, the effective thermal conductivity has the same trend as that of the macroscale composite. When the volumetric ratio of Si (Φ_{Si}) in the composites is small, the effective thermal conductivity increases as the fraction of the low thermal conductivity component increases, which is contrary to the behavior of bulk composites. This is because the effective thermal conductivity of the Si wire k_{eSi} is decreased to well below the bulk Ge thermal conductivity due to interface scattering. The effective thermal conductivity of the Ge matrix k_{eGe} increases as $(r_2-r_1)/r_1$ increases, since the scattering surface per unit volume of Ge decreases. The effective thermal conductivity of the core-shell structure can be written as $[k_{eSi}^* r_1^2 + k_{eGe}^*(r_2^2 - r_1^2)]/r_2^2$, thus accounting for the existence of a minimum value.

Apparently, Eq. (3-36) shows that the EMA model does not consider size the effect of effect on the thermal conductivity for nanowire composites in the longitudinal direction, i.e., when the temperature gradient is applied along the wire axis direction. Such a result is clearly contrary to the solution of the Boltzmann equation presented here that shows a strong size dependence.

The same code can be used to simulate the thermal conductivity of a nanoporous medium. Figure 3-14 shows results for the thermal conductivity of porous silicon along the cylindrical pore direction (as shown in Fig. 3-3(e)). Here r_0 is the pore radius and the shell thickness (r_2-r_0) is determined by the porosity as $\Phi_o = \frac{r_0^2}{r_2^2}$. For simplicity, only the results assuming diffuse surface scattering at the pore surface are reported. For macroscale porous materials, the effective thermal conductivity decreases linearly as the porosity increases. When the pore radius is less than 2-3 times the phonon mean free path in the silicon matrix, the effective thermal conductivity is not only a function of porosity, but also a function of pore radius. For composites with the same porosity, the effective thermal conductivity decreases as the pore radius decrease since the scattering area per unit volume increases. The implication of this study is that nanopores can possibly be used to further reduce the thermal conductivity of nanowire composites. In a recent report, Zhao et al. showed that the effective thermal conductivity is further reduced and thus the thermoelectric figure of merit ZT is increased in a Bi_2Te_3 composite with tubular Bi_2Te_3 nanowire inclusions [10].

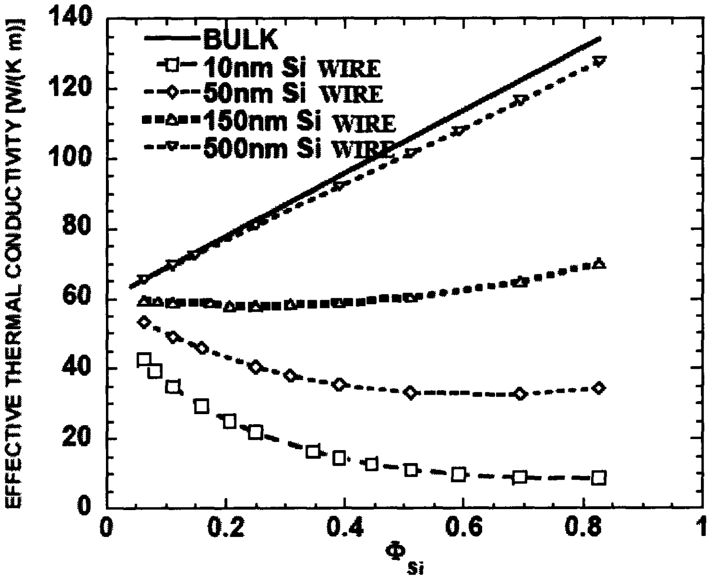

Figure 3-13. Thermal conductivity of the silicon-germanium nanocomposite which comprises of a germanium matrix with silicon wire inclusions as a function of the silicon wire radius and the volumetric ratio.

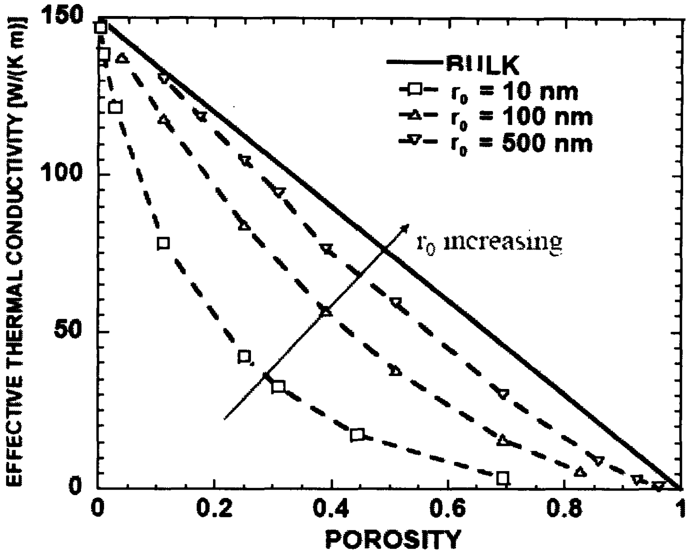

Figure 3-14. Thermal conductivity of porous silicon along the cylindrical pore direction as a function of the pore radius and porosity.

The model has also been used to study the thermal conductivity of tubular nanowire composites as shown in Fig. 3-3 (a). Again the results shown here assume a totally diffuse surface scattering at the pore surface. The effective thermal conductivity of tubular nanowire composites is a function of the pore radius inside the tubular silicon wire r_0, the outer radius of the silicon shell r_1 (the silicon shell thickness is defined as r_1-r_0), and the volumetric ratio of silicon $\Phi_{Si} = (r_1^2 - r_0^2)/(r_2^2 - r_0^2)$ in the composites. Figure 3-15 shows the effect of the silicon core layer thickness of the tubular silicon wire inclusions on the effective thermal conductivity of the nanocomposites. From Fig. 3-15, the effective thermal conductivity is smaller when the Si core layer thickness is thinner for the same volumetric ratio of Si and same inner pore radius. A smaller Si shell thickness means a smaller Ge shell thickness. This gives a smaller effective thermal conductivity for both the Si and Ge layers and thus a smaller effective thermal conductivity of the nanocomposites. Comparison of Fig. 3-15(a) and (b) shows that the effective thermal conductivity of the composites decreases as the radius of the inner pores increases for fixed Si shell thickness and volumetric ratio of Si due to the increase of surface scattering area per unit volume.

Figure 3-16 shows that the tubular Si nanowire composite has a lower solid thermal conductivity than that of simple nanowire composite due to the additional surface scattering introduced through the inner pore surface. Here the solid thermal conductivity k_S is defined as $k_S = \frac{QL}{A_S \Delta T}$, where Q is the heat flux, L is the length of the simulation domain along the direction where the temperature difference ΔT is applied, and A_S is the solid part of the cross-sectional area $A_S = \pi(r_2^2 - r_0^2)$. For comparison, the Si wire radius (or outer shell radius of the tubular nanowire) is fixed. Figure 3-16 also shows that the solid thermal conductivity decreases as the pore radius increases due to the increased surface scattering per unit volume.

3.4. Conclusions

We studied theoretically the phonon thermal conductivity of periodic two-dimensional nanocomposites with nanowires embedded in a host semiconductor material, both across and along the wire direction, using the deterministic solution of the phonon Botlzmann equation. Special attention has been paid to cell-cell interaction using periodic boundary conditions. The simulation shows that the temperature profiles in nanowire composites for transport across the wire direction are very different from those in conventional composites, due to ballistic phonon transport at the nanoscale. Such temperature profiles cannot be captured by existing models in the literature. The results show that the effective thermal conductivity changes not only with the volumetric fraction of the constituents but also with the radius of the nanowire, pore, and tubular nanowire inclusions due to the nature of the ballistic phonon transport. These results are in contradiction with the existing theory on the thermal conductivity of composites, which lead to effective transport properties depending only on the volume fraction but independent of size. The smaller the wire/pore diameter, the smaller is the thermal conductivity of periodic two-dimensional nanocomposites for a given volumetric fraction. Composites with tubular nanowire inclusions have both a lower effective and solid thermal conductivity than simple nanowire composites due to the introduction of surface scattering through the pores. We also show that the effective medium approach based on incorporating the thermal boundary resistance into the solution based on the Fourier heat conduction law leads to erroneous results that underpredict the size effects. Results of this study can be used to direct the development of both high efficiency thermoelectric materials and thermal interface materials with high thermal conductivity particle or wire inclusions.

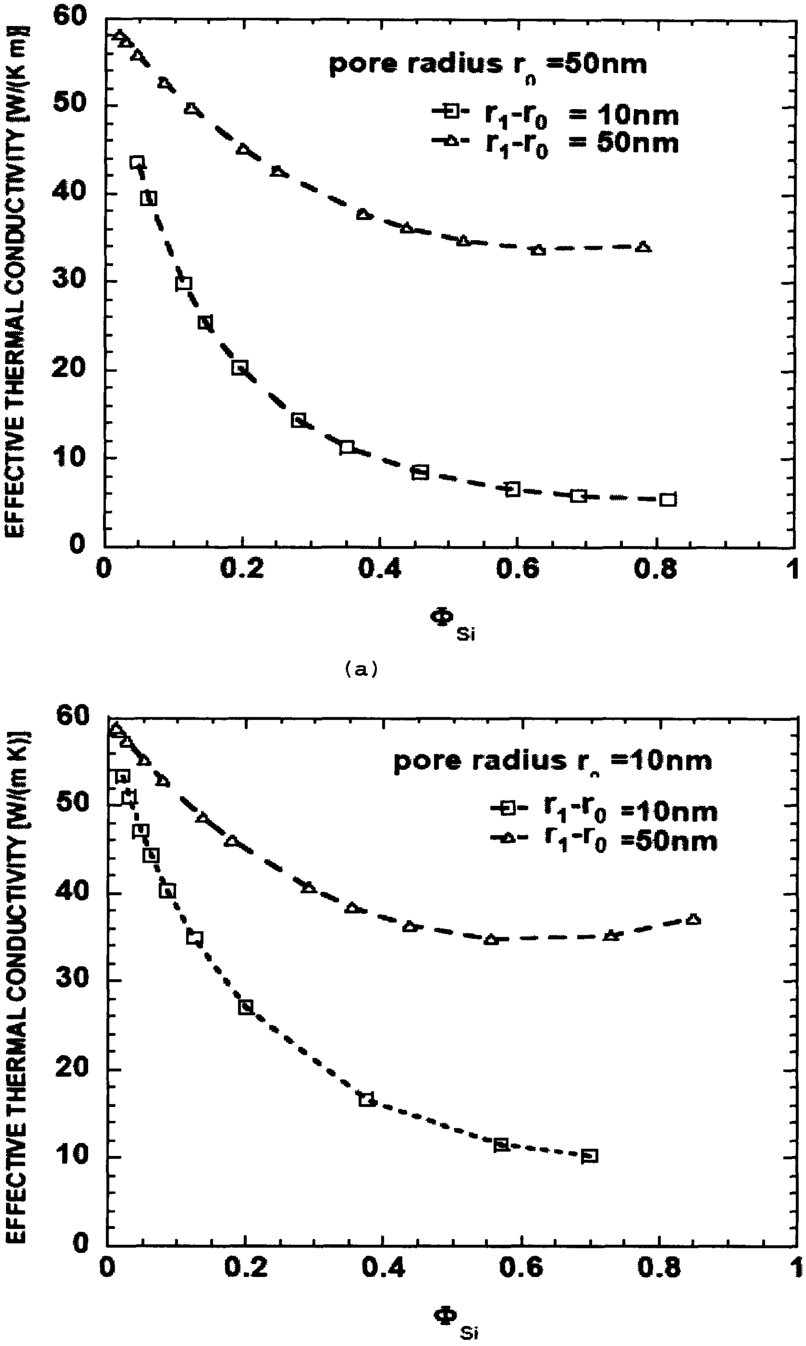

(a)

(b)

Figure 3-15. The effect of the silicon core layer thickness and the pore size of tubular silicon wire inclusions on the effective thermal conductivity of the nanocomposites: (a) 50nm pore radius, (b) 10nm pore radius.

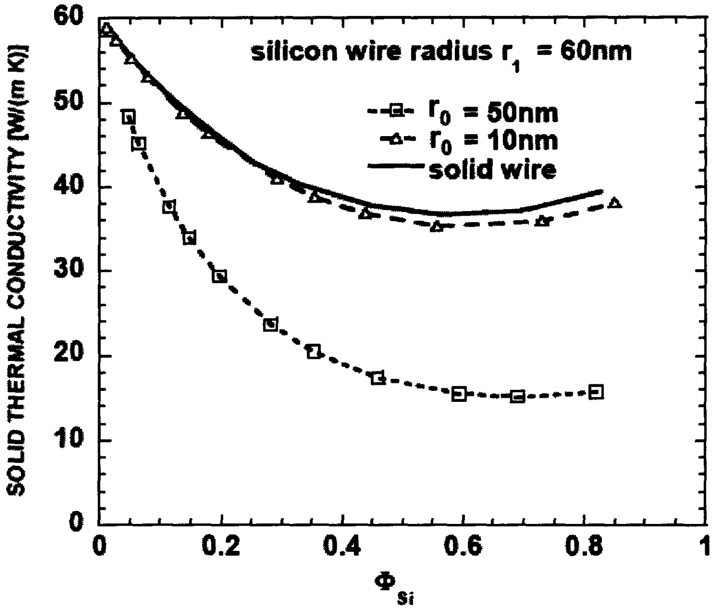

Figure 3-16. The solid thermal conductivity of the composites decreases as the pore radius increases due to the increasing surface scattering per unit volume.

3.5 References

1. H.J. Golsmid, Thermoelectric Refrigeration (Plenum Press, New York, 1964).
2. T.M. Tritt, Ed., Semiconductor and Semimetals **69-71**, (2001).
3. M.S. Dresselhaus, Y.M. Lin, S.B. Cronin, O. Rabin, M.R. Black, G. Dresselhaus, and T. Koga, Semiconductors and Semimetals **71**, 1 (2001).
4. G. Chen, Semiconductors and Semimetals **71**, 2003 (2001).
5. R. Venkatasubramanian, Semiconductors and Semimetals **71**, 175 (2001).
6. T.C. Harman, P.J. Taylor, M.P. Walsh, and B. E. LaForge, Science **297**, 2229 (2002).
7. R. Venkatasubramanian, E. Silvona, T. Colpitts, and B. O'Quinn, Nature **413**, 597 (2001).
8. R.G. Yang, and G. Chen, Material Integration, Sep. 2005 issue, in Press.
9. K.F. Hsu, S. Loo, F. Guo, W. Chen, J.S. Dyck, C. Uher, T.P. Hogan, E.K. Polychroniadis, and M.G. Kanatzidis, Science **303**, 819 (2004).
10. X.B. Zhao, X.H. Ji, Y.H. Zhang, et al, Appl. Phys. Lett. **86**, 062111 (2005).

11 G. Chen, D. Borca-Tasciuc, and R.G. Yang, in Encyclopedia of Nanoscience and Nanotechnology, Eds. H.S. Nalwa, Vol. **7**, pp.429-459, (American Scientific Publishers, Stevenson Ranch, CA, 2004).

12. B. Yang, and G. Chen, Phys. Rev. B **67**, 195311 (2003).

13. P. Hyldgaard and G.D. Mahan, Phys. Rev. B **56**, 10754 (1997).

14. S. Tamura, Y. Tanaka, and H.J. Maris, Phys. Rev. B **60**, 2627 (1999).

15. W.E. Bies, R.J. Radtke, and H. Ehrenreich, J. Appl. Phys. **88**, 1498 (2000).

16. B. Yang and G. Chen, Microscale Thermophys. Eng. **5**, 107 (2001).

17. G. Chen, ASME J. of Heat Trans. **119**, 220 (1997).

18. G. Chen and M. Neagu, Appl. Phys. Lett. **71**, 2761 (1997).

19. G. Chen, Phys. Rev. B **57**, 14958 (1998).

20. P. Hyldgaard and G.D. Mahan, Thermal Conductivity **23**, 172 (1996).

21 M.V. Simkin and G.D. Mahan, Phys. Rev. Lett. 84, 927 (2000).

22 B. Daly, H. Maris, K. Imamura, and S. Tamura, Phys. Rev. B 66, 024301 (2002).

23 C. Dames and G. Chen, J. Appl. Phys. **95**, 682 (2004).

24.G. Chen, Semiconductors and Semimetals **71**, 203 (2001).

25. R.G. Yang, and G. Chen, Phys. Rev. B **69**, 195316 (2004).

26. G.W. Milton, The Theory of Composites (Cambridge University Press, New York, 2002).

27. P.L. Kapitza, J. Phys. **4**, 181 (1941); for a review on thermal boundary resistance, see Ref. 47.

28. D.P.H. Hasselman and L.F. Johnson, J. Compos. Mater. **21**, 508 (1987).

29. Y. Benvensite, J. Appl. Phys. **61**, 2840 (1987); Y. Benvensite and T. Miloh, J. Appl. Phys. **69**, 1337 (1991).

30. A.G. Every, Y. Tzou, D.P.H. Hasselman, and R. Raj, Acta. Metall. Mater. **40**, 123 (1992).

31. C.-W. Nan, R. Birringer, D.R. Clarke, and H. Gleiter, J. Appl. Phys. **81**, 6692 (1997).

32. C.-W. Nan, and F.S. Jin, Phys. Rev. B **48**, 8578 (1993); C.-W. Nan, J. Appl. Phys. **76**, 1155 (1994)

33. P.A. Smith and S. Torquato, J. Appl. Phys. **65**, 893 (1989); S. Torquato and M.D. Rintoul, Phys. Rev. Lett. **75**, 4067 (1995).

34. R. Lipton and B. Vernescu, J. Appl. Phys. **79**, 8964 (1996).

35. See for example M. Jiang, I. Jasiuk, M. Ostoja-Starzewski, Computational Material Science **25**, 329 (2002); F.W. Jones and F. Pascal, Geophys. **60**, 1038 (1995).
36. S. Graham and D.L. McDowell, ASME J. Heat Transfer **125**, 389 (2003).
37. K. Ramani, and A. Vaidyanathan, J. Compos.Mater. **29**, 1725 (1995).
38. M. R. Islam, and A. Pramila, J. Compos. Mater. **33**, 1699 (1999).
39. A. Khitun, A. Balandini, and J.L. Liu, and K.L. Wang, J. Appl. Phys. **88**, 696 (2000); Superlattices and Microstructures **30**, 1 (2001); A. Khitun, K.L. Wang, and G. Chen, Nanotech. **11**, 327 (2000); J.L. Liu, et al., Phys. Rev. B **67**, 165333 (2003).
40. O.L. Lazarenkova, and A. A. Balandin, J. Appl. Phys. **89**, 5509 (2001); Phys. Rev. B **66,** 245319 (2002); A.A. Balandin, and O.L. Lazarenkova, Appl. Phys. Lett. **82,** 415, (2003).
41. J.M. Ziman, Electrons and Phonons (Oxford University Press, London, 1985).
42. R. Prasher, Appl. Phys. Lett. **83**, 48 (2003); ASME J. Heat Tranf. **125**, 1156 (2003).
43. M.S. Jeng, R.G. Yang, and G. Chen, Phys. Rev. B, submitted (2005).
44. M. Kaviany, Principles of Heat Transfer in Porous Media, 2ed, (Springer-Verlag, New York, 1999).
45. R.M. Costescu, M.A. Wall, and D.G. Cahill, Phys. Rev. B **67**, 054302 (2003).
46. D. G. Cahill, W. K. Ford, K. E. Goodson, G. D. Mahan, A. Majumdar, H. J. Maris, R. Merlin, and S. R. Phillpot, J. Appl. Phys. **93**, 793 (2003).
47. E.T. Swartz and R.O. Pohl, Rev. Mod. Phys. **61**, 605 (1989).
48. J.A. Fay, Introduction to Fluid Mechanics (MIT Press, Cambridge, MA, 1994).
49 J.H. Lienhard, and J.H. Lienhard, A Heat Transfer Textbook, http://web.mit.edu/lienhard/www/ahtt.html (2005).
50. H. Greenspan, C.N. Kelber, D. Okrent, editors, Computing Methods in Reator Physics (Gorden and Breach, London, 1967).
51. E.E. Lewis, and W.F. Miller, Computational Method of Neutron Transport, pp. 156-207 (Wiley, New York, 1984).
52. R.G. Yang, G. Chen, M. Laroche, and Y. Taur, ASME J. Heat Transf. **127**, 298 (2005).
53. R.G. Yang, G. Chen, M.S. Dresselhaus, Nano Letters **5,** 1111 (2005).

Chapter 4. Monte Carlo Simulation for Phonon Transport and Thermal Conductivity in Nanoparticle Composites

Though very much doable, extending the 2-D BTE simulation described in Chapters 2 and 3 to phonon transport in complex three-dimensional (3-D) spatial coordinates is very tedious, owing to the complexity of tracking phonon transport deterministically. In this chapter we present a Monte Carlo (MC) simulation scheme to study the phonon transport and thermal conductivity of nanoparticle composites, where nanoparticles are embedded in a matrix material. Special attention has been paid to the implementation of periodic boundary condition in Monte Carlo simulation. The scheme is then applied to study the thermal conductivity of silicon-germanium (Si-Ge) nanocomposites. The Monte Carlo simulation is first validated by successfully reproducing the results of two dimensional nanocomposites where silicon nanoparticles are embedded in a germanium matrix using the deterministic solution of the phonon Boltzmann transport equation and the experimental thermal conductivity of bulk germanium, and then the validated simulation method was used to study (three dimensional) nanoparticle composites, where Si nanoparticles are embedded in a Ge host. The size effects of phonon transport in nanoparticle composites are studied. It is found that randomly distributed nanoparticles in nanocomposites renders the thermal conductivity values close to that of periodic aligned patterns. We show that the interfacial area per unit volume (interface density) is a useful parameter to correlate the size effect of thermal conductivity in nanocomposites.

4.1 Introduction

The simulation results of the thermal conductivity in two-dimensional nanowire composites in chapter 3 show great promise to scale up the physics responsible for the reported high ZT in superlattices into mass-producible cost-effective high efficiency thermoelectric nanocomposites, where phonon thermal conductivity reduction is a blessing for the enhancement of the thermoelectric figure of merit. Thermoelectric nanocomposites have indeed become a promising direction for thermoelectric community. A few groups have practiced making various nanocomposites with both nanowire and nanoparticle inclusions in a matrix host [1, 2] or just a compact mixture of nanoparticles [3]. Among them some groups have reported very encouraging reductions in the thermal conductivity and consequently encouraging ZT enhancement.

In this chapter, we aim to study the phonon transport in three-dimensional nanocomposites, where nanoparticles are embedded in a matrix material. Though very much doable, extending the deterministic solution of the 2-D phonon BTE to phonon transport in complex three-dimensional (3-D) spatial coordinates is very tedious, owing to the complexity in tracking phonon transport deterministically. In addition, it is almost impossible for one to track phonon transport in a random nanocomposite in a deterministic way. Thus, we resort our efforts to the Monte Carlo (MC) simulation.

The Monte Carlo simulation solves the Boltzmann transport equation in a statistical framework, and has been widely used to simulate the radiative transfer equation and the Boltzmann equation for electrons and holes in semiconductors [4-9]. Only few reports of using the Monte Carlo technique for phonon transport have been published in the past. Peterson employed the Monte Carlo method to simulate phonon transport in a confined space [10] while Klitsner et al. [11] performed Monte Carlo simulations to obtain the temperature distribution in a crystal. Mazumder and Majumdar considered phonon dispersion as well as various phonon scattering mechanisms to study heat transport in complex geometries and to predict their thermal conductivities [12].

This work builds upon previous studies on the phonon transport in nanoscale structures and is the first attempt to use Monte Carlo methods to study phonon transport in complex three-dimensional nanostructructures, i.e., nanocomposites. The objective is to present an algorithm for studying phonon transport in nanocomposites using Monte Carlo simulation with special attention paid to the implementation of periodic boundary conditions and to study the size effect of the thermal conductivity in nanoparticle composites.

4.2 Monte Carlo Simulation

In a Monte Carlo solution technique, phonons are drawn and distributed inside the computational domain initially. These phonons are given velocity and direction, which correspond to wavevectors in the phonon dispersion relation, and are allowed to move freely. As the phonons move, they engage in various "intrinsic-scattering" events, such as phonon-phonon scattering, phonon-impurity scattering and phonon-dislocation scattering, and encounter interfaces and boundaries, mimicking the particle picture of phonon transport. If there is a large enough number of phonons and if the average time is long enough, the averaged transport quantities based on the phonon ensemble should approach the deterministic solution of the phonon Boltzmann equation. The initial selection of phonon positions and directions as well as the subsequent phonon movement must obey the physical laws that determine phonon properties and define phonon dynamics. Though a more comprehensive Monte Carlo simulation technique which accounts for phonon dispersion and polarization for scattering events has been presented before [12], as a first attempt to tackle the 3-D phonon transport problem in nanocomposites, we take a simplified gray media approach which assumes that the frequency-dependent scattering rate in the bulk medium can be approximated by an average phonon mean free path (MFP). As justified in chapter 2 and similar to the assumptions made in chapter 2 and chapter 3, another assumption has been made is that the phonon wave effect can be excluded. Temperature dependent average phonon properties are used including average phonon frequency, average phonon group velocity and average phonon mean free path as obtained in chapter 2 is used. In the program, a look-up table relating temperature, energy density and all the other average properties shown in chapter 2 is established before doing the calculation. In the Monte Carlo simulation, phonons are divided into phonon bundles, and the averaged phonon properties are assigned to the phonon bundles during the simulation. The properties of a phonon bundle do not change while it travels, until it encounters scattering events, either by interface scattering or "intrinsic-phonon" scattering. The number of phonons in a phonon bundle is pre-determined before the simulation, by considering the computational time and memory requirements.

In the following sections, we present the details of implementing the gray media Monte Carlo technique for solving the phonon transport problem in nanocomposites.

4.2.1 Computational Domain and Boundary Conditions

The challenge is to simulate the phonon transport in the whole composite structure, as shown in Figure 4-1(a), with Si nanoparticle embedded in a Ge matrix. The memory and computational time requirements for such a multiscale problem are demanding. Our approach is to apply periodic boundary conditions to a chosen unit cell. A rectangular parallelepiped in the composite material is taken as the computational domain, which is called a unit cell, as shown in Fig. 4-1(b). With the periodic boundary conditions we applied, shown in detail below, the phonon transport in the unit cell represents the phonon transport inside a composite made by repeating the unit cell. The heat is forced to flow in the x-direction. The transport in both the y-direction and the z-direction are periodic and thus the specularly reflected phonon boundary conditions can be enforced at these boundaries due to their symmetry. However in x-direction, although the geometry is periodic, the transport is not periodic since the temperature is not periodic. To address this problem for the deterministic BTE solution, the periodic boundary condition on the deviation of the distribution function was proposed in Chapter 3. The periodic boundary conditions are implemented in MC simulation as follows. For specular reflection boundaries at $y=0$, $y=L_y$, z=0, and z=L_z, the phonon bundles experience a mirror reflection when they hit these boundaries, without losing any momentum or energy. The implementation of the periodic boundary condition in the x direction needs more elaboration. First, a certain number of phonon bundles are emitted from the boundaries during each time step so that the net heat flow (phonon energy flow) across the boundaries x=0 and x=L_x are identical and equal to a prescribed value. The number of phonon bundles N_{emit} at each boundary emitted into the computational domain in each time step is calculated by,

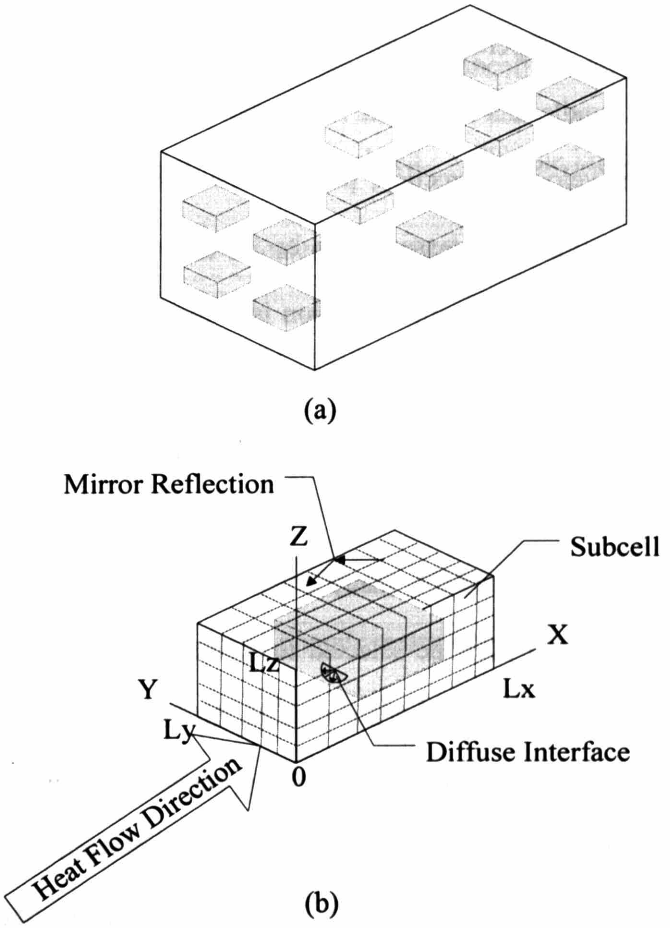

Figure 4-1. (a) Periodic nanocomposite with cubic silicon nanoparticles dispersed periodically in a germanium matrix. (b) With the periodic boundary condition dictated in section 4.2.1, the Monte Carlo simulation of phonon transport in the computational domain (unit cell) represents phonon transport in the whole structure shown in Fig. 4-1(a). The unit cell (computational domain) is further divided into subcells.

$$N_{emit} = \frac{(\pm Q + S \cdot \sum_{n} \hbar\omega_{n,absorb})}{\hbar\omega_{emit} \cdot S} \tag{4-1}$$

where Q is the prescribed heat flow, whose sign depends on the boundary emission direction, S the scaling factor representing the number of phonons contained in each bundle, $S \cdot \sum \hbar\omega_{n,absorb}$ the total phonon energy leaving the computation domain, and ω_{emit} the average phonon frequency corresponding to the local boundary temperature, which is obtained by extrapolating the temperature profile inside the computational domain to the boundary. When a phonon bundle hits one of the x boundaries, it is considered to be leaving that boundary. The pattern (velocity, direction, position, and the remaining flight time) of phonon emission at one x boundary is assumed to be the same as the pattern of phonon leaving the opposite x boundary. This implementation is realized by maintaining a pool of leaving phonons, recording their velocity, direction, position and flight time, and determining the properties of each emission phonon by randomly drawing from the pool. The pool is refreshed after each time step.

The unit cell is further divided into many grids, or "subcells", as shown in Fig. 4-1 (b). The dimension of the subcell must be selected to maintain a balance between spatial resolution and computation time. The larger the subcells, the more phonon phonons each subcell would enclose, and the better the accuracy of each subcell temperature estimate, but the poorer the resolution of temperature mapping within the unit cell due to the small number of temperature points. The smaller the subcells, the more subcells within the unit cell, and the higher the resolution of the temperature mapping within the unit cell, but the poorer the accuracy of each temperature point because of the lower phonon count within each subcell. In this work, the smallest subcell dimension that can generate stable results was found to be around 1nm.

At the end of each time step, the temperature of each subcell is assigned based on the total phonon energy it contains at this stage of each time step, i.e. just after all phonons have moved and scattered:

$$S \times \frac{\left(\sum \hbar\omega\right)_{Cell}}{V} = \sum_{p=1}^{3} \int \frac{\hbar\omega D(\omega)}{\exp\left(\frac{\hbar\omega}{k_b T_{Cell}}\right) - 1} d\omega \tag{4-2}$$

where $\left(\sum \hbar\omega\right)_{Cell}$ is the total phonon energy the subcell contains, V is the volume of the subcell, and T_{cell} is the temperature of the subcell. With the known temperature T_{cell}, all the averaged phonon properties can be calculated and then assigned to phonon bundles emitting from this local subcell.

4.2.2 Phonon Scattering

The dominant scattering event in nanocomposites is particle-host interface scattering. Similar to chapter 3 the phonon scattering at the particle-host matrix interface (Si-Ge) interface is assumed to be diffuse. In the Monte Carlo scheme, when a phonon hits an interface, a random number between zero and unity is drawn and compared with the transmissivity. If the random number is larger than the transmissivity, the phonon is transmitted. Otherwise, it is reflected. To comply with the concept of diffuse interface, the phonon direction vector is reset after encountering an interface, either transmitted or reflected, and is given by,

$$\hat{s}_r = \sin\theta\cos\psi\hat{t}_1 + \sin\theta\sin\psi\hat{t}_2 + \cos\theta\hat{n} \tag{4-3}$$

where $\sin^2\theta = R_1$, $\Psi = 2\pi R_2$, and $0 \leq R_1 \leq 1$ and $0 \leq R_2 \leq 1$ are independent random numbers, $\hat{n}$ the unit surface normal vector at the point of collision, and $\hat{t}_1$ and $\hat{t}_2$ the unit surface tangent vectors that are normal to each other. In order to maintain a continuum of energy density, a transmitted phonon is represented by a new phonon that assumes local properties (velocity, frequency and MFP) and travels along the new direction that is randomly determined as explained above until finishing the remaining time in the current time step. Because the frequencies at the two sides of the interface are generally different, the phonon energy is not conserved. This is remedied by monitoring the energy deficiency (or surplus) at each side of the interface. When the cumulated energy difference exceeds a certain amount, a new phonon is emitted from the interface (or the current phonon is absorbed). This treatment leads to conservation of energy in the interface scattering process.

In addition to phonon-interface scattering, phonons engage in various "intrinsic-scattering" events, such as phonon-impurities, phonon-dislocation, and phonon-phonon scattering, as they move inside a crystalline material. . Though it is possible to trace the detailed scattering events using the Monte Carlo simulation, many of the scattering mechanisms are not well understood and existing models are sometimes questionable in addition to the tremendous computational time and memory requirements that are needed. As a simplified approach, we calculate the scattering probability of a phonon by a lumped MFP,

$$P_S = 1 - \exp(-\mathrm{v}_{avg} \cdot \Delta t / \Lambda) \qquad (4\text{-}4)$$

where Λ is the lumped MFP as calculated in chapter 2, v_{avg} is the phonon group velocity and Δt the time step. The assumption is that the "intrinsic-scattering" events happen similarly in the bulk material as that in nanocomposites. This assumption is valid for most of cases since the modification of the phonon dispersion relation is not important due to the short wavelength of the dominant heat transport phonons which is around 1nm. In the current simulation, each phonon is treated for intrinsic phonon scattering at the end of each time step. A random number is drawn and compared to P_S. The phonon undergoes a scattering event when the random number is less than P_S. The scattered phonon then assumes local properties of velocity and frequency. The scattered phonon direction is assumed to be isotropic and the direction vector is given by,

$$\hat{s} = \sin\theta \cdot \cos\psi\hat{i} + \sin\theta \cdot \sin\psi\hat{j} + \cos\theta\hat{k} \tag{4-5}$$

where $\cos\theta = 2R_1 - 1$, $\Psi = 2\pi R_2$, and $0 \leq R_1 \leq 1$ and $0 \leq R_2 \leq 1$ are independent random numbers. The phonon energy is again not conserved since the phonon frequencies before and after scattering are usually different. The remedy is similar to that used for interface scattering. The energy difference of each subcell resulting from scattering is monitored, and when the difference exceeds a certain amount, a new phonon is generated (or an existing phonon is destroyed). Energy conservation is therefore maintained at the subcell level. Note that the isotropic resetting of the phonon direction in the above scheme tends to restore local equilibrium. This physical model is similar to all the relaxation time-based phonon BTE simulation that are done without considering the details of the momentum conservation of the intrinsic-phonon scattering events.

4.2.3 Process Flow

Figure 4-2 shows the schematic process flow of the Monte Carlo simulation algorithm. The Monte Carlo simulation starts with the initialization step, where phonons are created within the unit cell and at a given frequency, velocity, and direction to represent the initial temperature condition within the unit cell. The initial temperature inside the unit cell is assumed to be uniform. After the initialization step, phonons experience the moving (energy transport) and scattering (energy exchange) in each time step. The phonon bundles move one-by-one in straight lines for a prescribed time step and then scatter at the interfaces. The properties of the phonons that leave the unit cell are monitored and stored. The next step is phonon emission at the x boundaries using the stored phonon pattern, as explained in section 4.2.1. The total number of emitted phonons is determined by a constant heat flow boundary condition. After moving (transport) and emission, the three-dimensional temperature profile of the unit cell is obtained by tallying the internal energy of each subcell. The average phonon properties are then calculated accordingly. Based on the local temperature and mean free path values thus obtained, the phonons then undergo "intrinsic phonon" scattering. This step marks the end of a single time step, and the next time loop starts again from the start of the next moving (transport) step.

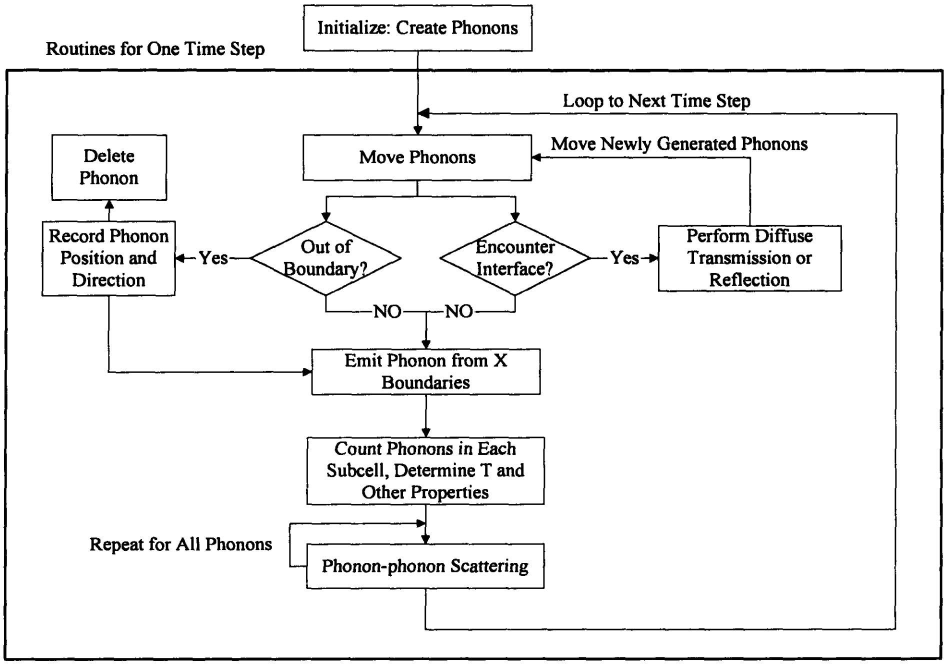

Figure 4-2. The schematic process flow of the Monte Carlo simulation algorithm. The Monte Carlo simulation starts with the initialization step. After the initialization step, phonons experience moving (transport) and scattering in each time step.

4.2.4 Convergence and Accuracy

The Monte Carlo technique is a statistical method, whose accuracy depends largely on the phonon bundle number and the time employed in the calculation. After some initial trials, we adopted a bundle number such that there are on average more than 50 phonon bundles in each subcell. The time step is selected such that within each time step a phonon travels a distance on the order of the magnitude of the subcell dimension. For example, if the subcell dimension is 1 nm, with a phonon group velocity on the order of 10^3m/s, the appropriate time step would be 10^{-12} second. The simulations usually attain converged thermal conductivity results after 1000 time steps. A typical trend for the calculated thermal conductivity with respect to the calculation time is shown in Fig. 4-3. The error after 1ns, equivalent to 1000 time steps, is within 3% of the final value, while the error after 10ns is within 0.1% of the final value. Note that due to the statistical nature of the Monte Carlo method, the results still exhibit variations, although insignificant, even after a 120ns calculation. In this study, a calculation time of at least 10ns, which normally corresponds to 10^4 time steps, is applied to all cases for calculating the thermal conductivity. The results of the last 500 time steps are further averaged to give a representative thermal conductivity value.

4.3 Results and Discussions

To validate our Monte Carlo (MC) simulation methodology, we first simulate the phonon transport in bulk Ge material to compare the thermal conductivity obtained through the Monte Carlo simulation with the experimental data in the literature. Then we conducted a MC simulation for phonon transport in 2D nanowire composites and compare the results with those obtained through the deterministic solution of the phonon BTE. After the validation, the code is then used to simulate phonon transport in various 3D Si-Ge nanocomposites to study the size effect of the thermal conductivity of nanoparticle composites. Some of the fundamental questions critical for designing highly efficient thermoelectric nanocomposites are addressed, including (a) how the thermal conductivity changes with the size of the nanoparticles and their atomic composition, and (b) what is the effect of non-monosize particles and what is the effect of the distribution pattern of nanoparticles on the thermal conductivity reduction in nanoparticle composites. A comparison with the effective medium approach based on the Fourier heat conduction with the addition of interface thermal resistance is also given. In the end, we suggest using an interfacial area per unit volume (interface density) as a parameter to correlate the size effect of the thermal conductivity in nanocomposites.

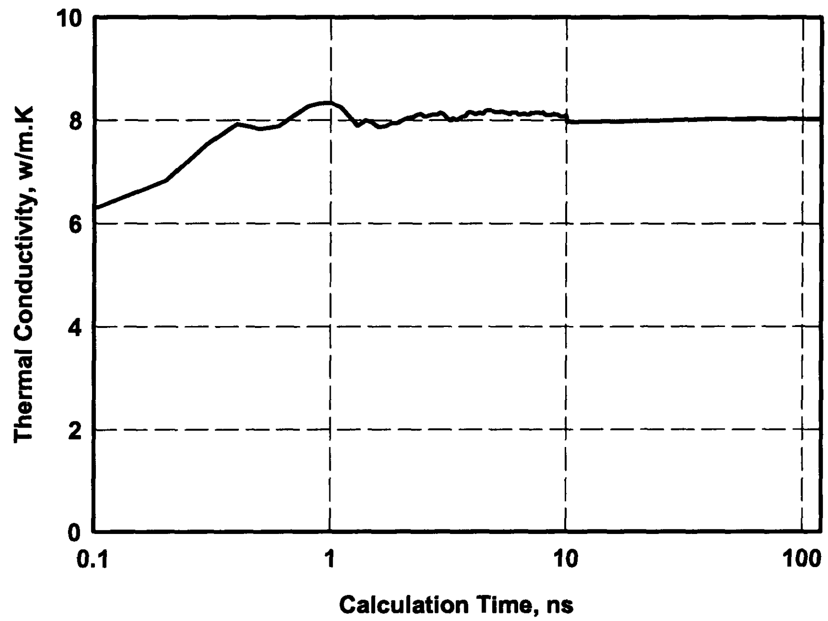

Figure 4-3. Typical variation of the thermal conductivity values with respect to the calculation time. The case shown is a 2D nanocomposite with 10nm Si nanowires embedded in a Ge host. The result converges after 10ns of simulation, corresponding to 10000 time steps, with a variation of less than 0.1% afterward.

4.3.1 Code Validation - Bulk and 2-D Simulation

Homogeneous bulk Ge material was simulated first, where the computational domain contains no particles and the only scattering mechanism is the intrinsic phonon scattering. Figure 4-4 shows the comparison of the thermal conductivity value from the gray-medium Monte-Carlo simulation conducted in this work with the experimental thermal conductivity value of a bulk germanium sample. The experimental Ge value is taken from Ref. [13]. The circular symbols indicate the results of simulating a solid bulk material without any particle inside. The triangle symbol represents the simulation of a "pseudo composite", when both the particle and the host material are Ge. When the two sides of the interface both have transmissivity values of one, the simulation should equal that of a solid bulk material without any particles. This pseudo composite simulation served to validate the Monte Carlo coding. The simulation results of the thermal conductivity of bulk Ge agree very well with the experimental data, as shown in Figure 4-4. The program was then used to study the thermal conductivity of 2D nanowire composites, which were previously studied by simulating phonon transport using the deterministic solution of the phonon BTE. To simulate phonon transport in 2-D nanowire composite, the particle in the unit cell, shown in Fig. 4-1(b) is extended to touch the z boundaries. Due to the specular reflection and periodic boundary conditions, this is equivalent to infinitely long nanowires (with a square cross-section) embedded in the host material, thus fully reproducing our previous two-dimensional case shown in chapter 3. The temperature distributions in the mid plane of the unit cell are taken for comparison with that obtained from the deterministic solution of 2-D phonon BTE. Figure 4-5 presents the temperature profiles of $Si_{0.2}$-$Ge_{0.8}$ nanocomposite consisting of 10nm X 10nm cross-section Si nanowires embedded in a Ge host material along the x direction for various y locations. Although the results by the Monte Carlo simulation exhibit a slight asymmetry, which is attributed to the statistical error associated with the Monte Carlo simulation method, the temperature profiles by the two simulations show very good agreement. Thermal conductivity values from the Monte Carlo simulation and those from of the deterministic Boltzmann transport equation solution also agree with each other, as shown in Figure 4-6, for 10nm and 50nm nanowires with heat flow in the cross-wire direction. Overall the difference on the thermal conductivity value is less than 8% for all the cases simulated. The above comparisons justify the phonon gray medium-based Monte Carlo simulation methodology adopted in this study and also validate the program coding.

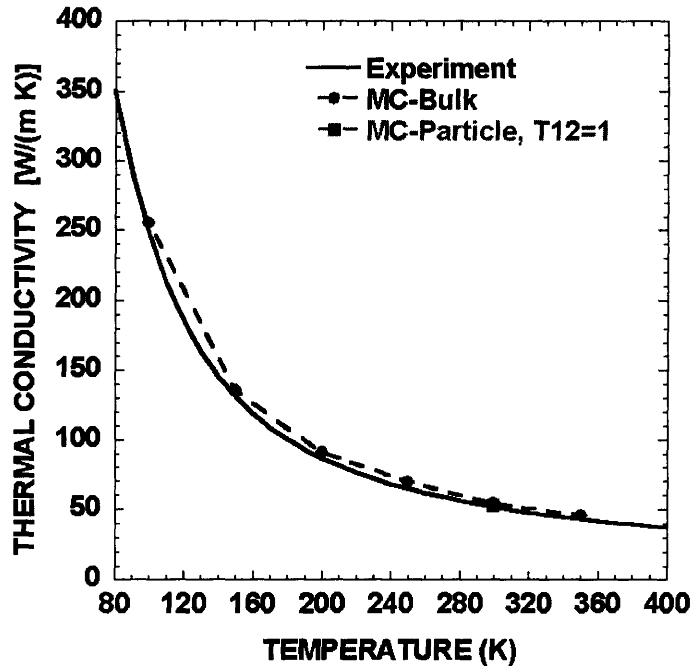

Figure 4-4. Comparison of the thermal conductivity value from the gray-medium Monte-Carlo simulation conducted in this work with the experimental thermal conductivity value of a bulk germanium sample. The experimental Ge value is taken from Ref. [35]. The circular symbols indicate the results of simulating a solid bulk material without any particle inside. The triangle symbol represents the simulation of a "pseudo composite", when both the particle and the host material are Ge. When the two sides of the interface both have transmissivity values of one, the simulation should equal that of a solid bulk material without any particles. This pseudo composite simulation served to validate the Monte Carlo coding.

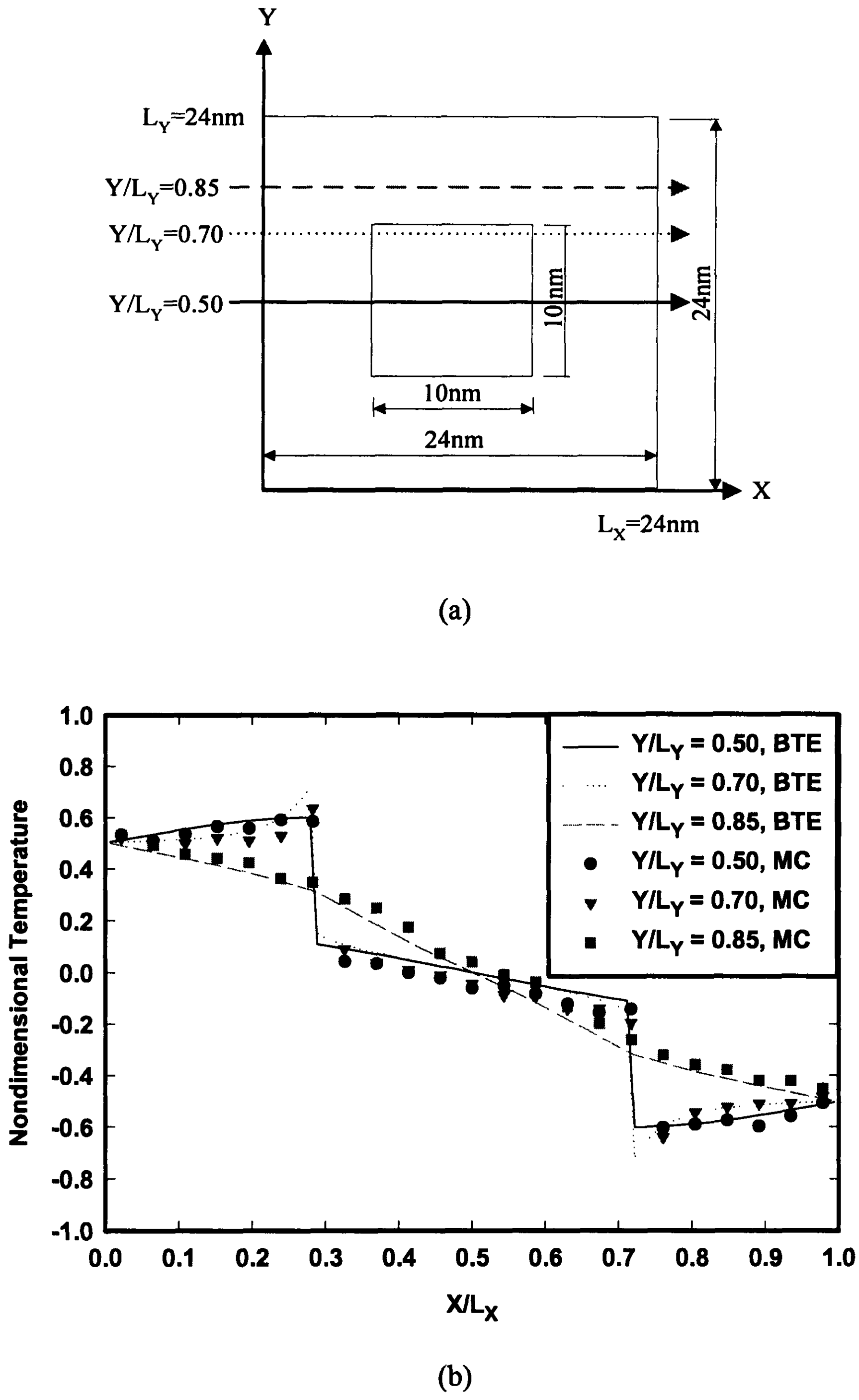

Figure 4-5. Comparison of the temperature (energy density) distributions inside a nanowire composite obtained, respectively, by the deterministic solution of the phonon Boltzmann transport equation and Monte Carlo method. (a) Geometric dimensions of the unit cell for a $Si_{0.2}$-$Ge_{0.8}$ nanowire composite with a 10nmx10nm nanowire inclusion with z along the wire direction, (b) temperature distribution along the x direction at various y positions assuming heat flows in the x-direction.

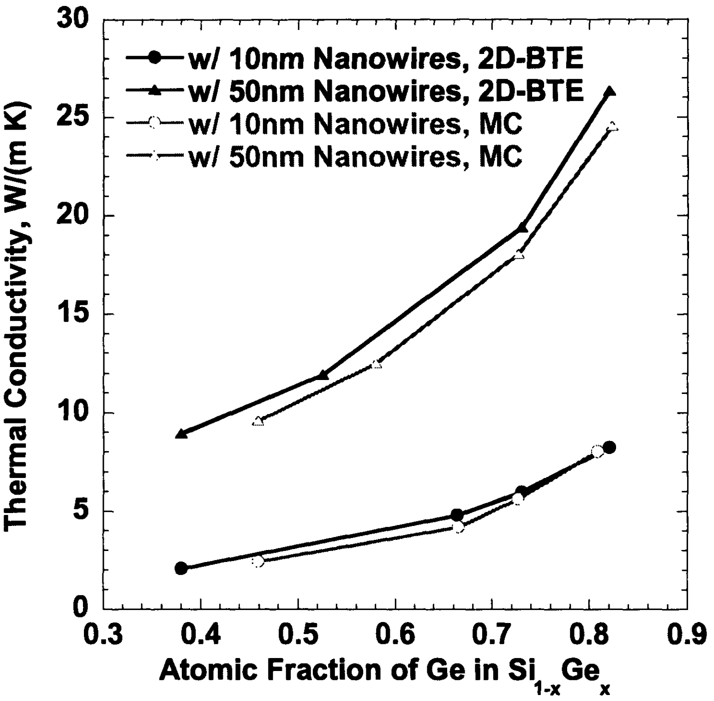

Figure 4-6. Comparison of thermal conductivity values for the 2D nanowire composites obtained by a Monte Carlo simulation and by a deterministic solution of the Boltzmann transport equation. The relative percentage deviation is less than 8%.

4.3.2 Three-Dimensional Periodic Structures

After verifying the Monte Carlo methodology, the program is used to simulate phonon transport in various nanocomposites with different cubic particle sizes and particle distributions. Figures 4-7(a) and 4-7(b) show the various cases for the nanoparticles with the mono-size particles distributed in aligned (a) and staggered (b) patterns in a periodic 3D nanoparticle composites. The staggered distribution resembles a face center cubic (FCC) structure, in the crystallographic terminology, with particles arranged in a pattern similar to the atomic pattern in an FCC crystal. Likewise, the aligned distribution resembles a simple cubic pattern. Figure 4-7(c) shows a random distribution regarding both size and position. All cubical particles shown in Fig. 4-7 are assumed to align with one of the cubic face parallel to the transport direction.

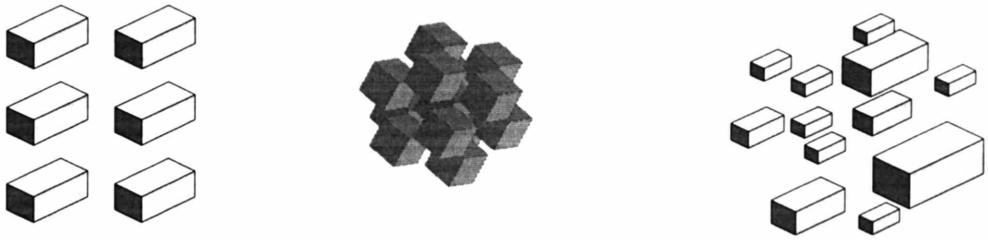

Aligned Pattern

Staggered fcc pattern

Random Distribution of Size and Position

(a) (b) (c)

Figure 4-7. Sketch of nanoparticle composites with silicon cubic nanoparticles distributed in an aligned pattern (a), in a staggered pattern (b), and randomly (c) in a germanium matrix for Monte Carlo simulation conducted in this work. Even in (c) the cubic nanoparticles are aligned in parallel to each other. The thermal conductivity calculated in this work are all in the direction normal to the cubic nanoparticles.

Figure 4-8 shows the two-dimensional temperature distribution in the mid plane of the unit cell for an aligned pattern. The Si particle has a size of 10nmx10nmx10nm and occupies a 3.7% volume fraction, the volume of Si particle divided by the total volume of the unit cell. Similar to the temperature profile shown in Figs. 4-5 for 2D nanowire composites, Figures 4-8 again show that the maximum temperature overshoot occurs at the nanoparticle - host lattice interface. The Monte Carlo simulation does not show the highest energy density (temperature) region occurring at the corner of the nanoparticle-host interface as those simulated by the deterministic BTE solution. The reason is due to the lower spatial resolution implemented in Monte Carlo simulation. As mentioned earlier, the requirement of having sufficient phonon bundles in each subcell largely limits the spatial resolution in Monte Carlo phonon simulation.

It is also worthwhile at this point to show the effectiveness of the periodic boundary conditions implemented in chapter 3, i.e., to verify that the phonon transport simulation in the unit cell can be used to represent the phonon transport in the whole nanocomposite and thus to deduce the effective thermal conductivity of the nanocomposites. Figure 4-9(a) shows the comparison of the heat flux at the hot (x=0) and cold (x=Lx) x boundaries in a periodic aligned nanoparticle composite, i.e., with one 10nm cubic particle inside a 14nm cubic unit cell. The periodicity in the local heat flux in the x-boundaries clearly demonstrated the unit cell with the periodic boundary condition has been effectively implemented in this work.

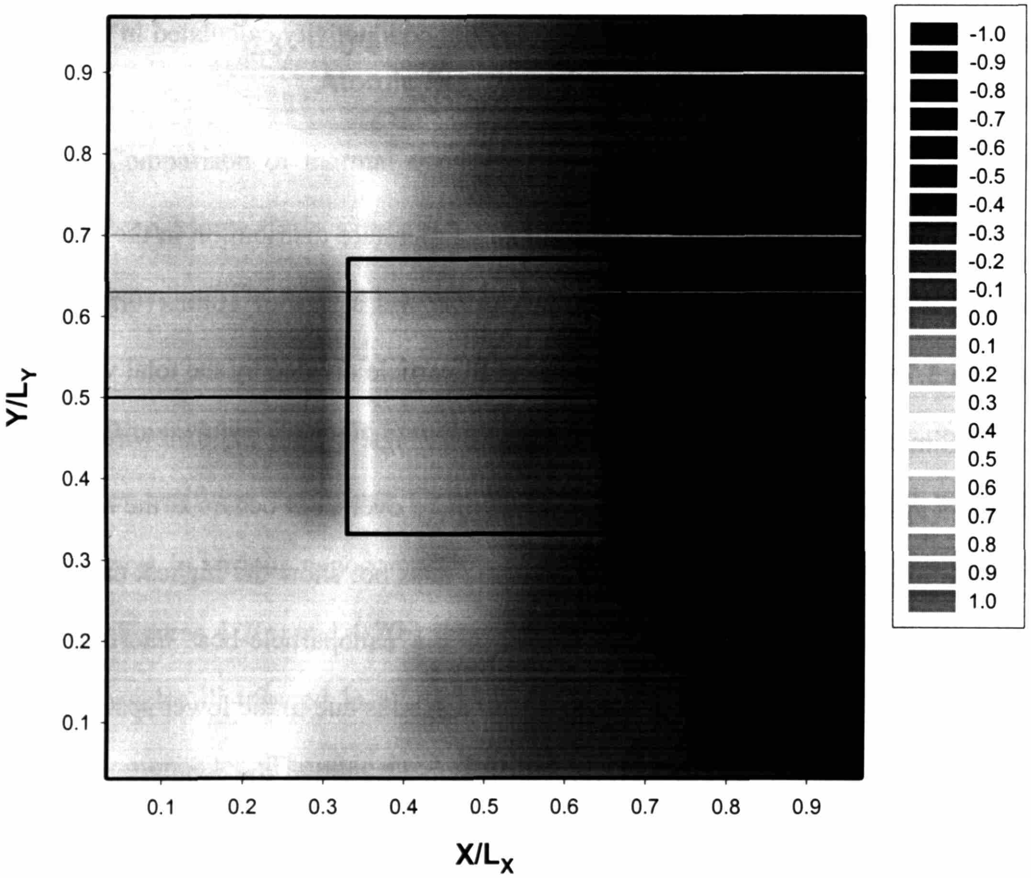

Figure 4-8. Temperature distribution inside an aligned periodic nanoparticle composite in the middle plane in the z-direction. The dimension of the nanoparticle is 10nm X 10nm X 10nm. The volume fraction of Si particles is 3.7%, corresponding to a $Si_{0.04}$-$Ge_{0.96}$ atomic composition.

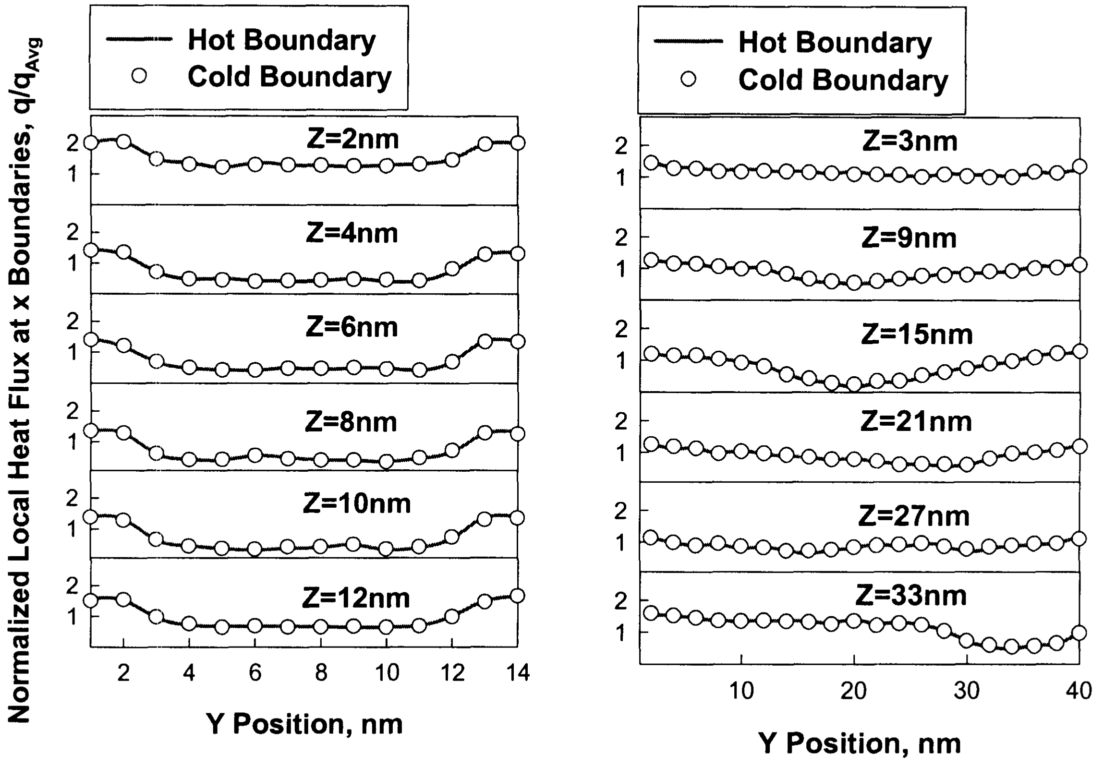

(a) (b)

Figure 4-9. Comparison of the heat flux at the hot (x=0) and cold ($x=L_X$) x boundaries in: (a) A periodic aligned nanoparticle composite, i.e., with one 10nm cubic particle inside a 14nm cubic unit cell; and (b) A random nanoparticle composite, i.e, with 10 nanoparticles, each of which is a 10nm cube randomly distributed inside a 40nmx40nmx40nm unit cell. The comparison demonstrates the periodicity of local heat flux in the x direction.

Figure 4-10 shows the size effect on the thermal conductivity of nanoparticle composites. The comparison of the thermal conductivity of the nanoparticle composites with 50nm silicon particles and 10nm silicon particles simply aligned in a germanium matrix and that of the SiGe alloy is presented in Fig. 4-10(a). The results show that the thermal conductivity decreases as the size of the nanoparticle decreases and the thermal conductivity of nanocomposites with 10nm particles can be even lower than that of the alloy value with the same constituents. This demonstrates that nanocomposites can be an effective approach to reduce the thermal conductivity and thus to develop high-efficiency thermoelectric materials.

Figure 4-10(b) shows the effect of the particle distribution on the thermal conductivity of nanocomposites with a 10nm Si particle in a Ge host material. For the same Si/Ge atomic ratio, the thermal conductivity of the random nanocomposites varies a little, but is very close to the thermal conductivity of periodic nanocomposites. The lowest thermal conductivity is achieved by well organizing the particles in a staggered pattern, where nanoparticles are distributed in a pattern similar to the atoms in the FCC crystal structure. This phenomenon is within our anticipation as staggered particles effectively block the pathway of ballistic transport and increase the chances of interface scattering. Also shown in Figure 4-10(b) are the thermal conductivity values of 2D nanocomposites consisting of 10nm Si nanowires in a Ge host. The difference between the thermal conductivity of the 2D nanocomposites (nanowire composites) and the 3D nanocomposites (nanoparticle composites) is mainly due to the interface area change at the same atomic ratio.

As stated earlier, most past studies on the thermal conductivity of nanocomposites were based on the Fourier diffusion theory together with consideration of the thermal boundary resistance. To examine the validity of such an approach, we compare the effective thermal conductivity obtained from the Monte Carlo simulation with that of the effective medium approach (EMA). The following EMA equation was developed by Nan et al. [14] for spherical particles.

$$\frac{k_e}{k_m} = \frac{k_P(1+2\alpha)+2k_m+2f[k_P(1-\alpha)-k_m]}{k_P(1+2\alpha)+2k_m-f[k_P(1-\alpha)-k_m]} \tag{4-6}$$

where k_e is the effective composite thermal conductivity, k_m is the host material thermal conductivity, k_P is the particle thermal conductivity, f is the volume fraction of nanoparticle inclusion, α is a dimensionless parameter defined as $\alpha = a_k/a_p$ for nanoparticle composites.

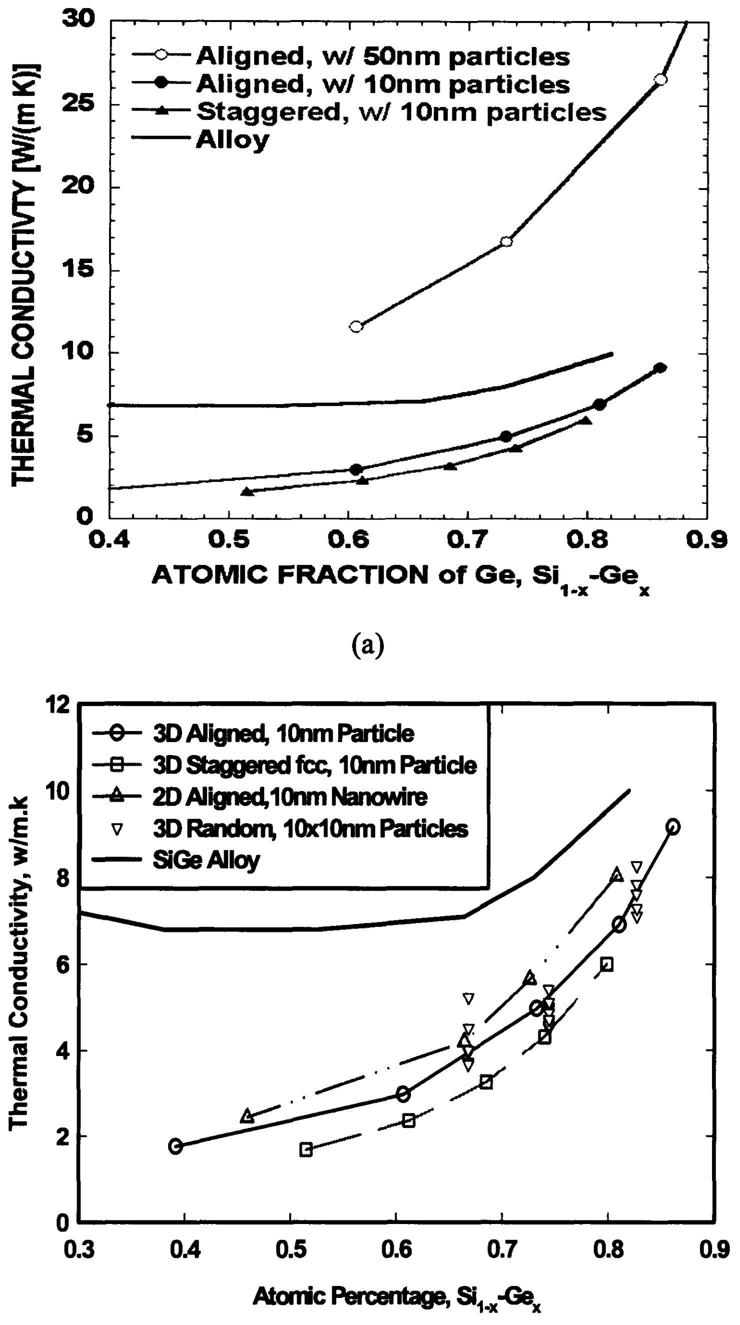

(a)

(b)

Figure 4-10. The effects of silicon nanoparticle size and distribution on the thermal conductivity of nanoparticle composites: (a) Comparison of the thermal conductivity of composites with 10nm and 50nm silicon cubic particles distributed in a simple periodic pattern in a germanium host and that of a Si-Ge alloy as a function of atomic composition. (b) The effect of the distribution pattern on the thermal conductivity of composites with 10nm silicon particle inclusions. Also shown in Figure 10(b) is the thermal conductivity of a Si-Ge alloy.

a_p is the radius of nanoparticle inclusions, and $a_k = Rk_m$, where R is the interface thermal resistance which can be calculated as [15]

$$R = \frac{4}{T_{d12}U_1 v_1} = \frac{4(U_1 v_1 + U_2 v_2)}{U_1 v_1 U_2 v_2} \tag{4-7}$$

Using the heat capacity and the sound velocity to calculate the interface thermal resistance shown in Eq. (4-7), we obtain $R=1.0*10^{-9}$ m^2K/W. Other parameters used in the calculation are k_m(Ge) = 51.7 W/(m K), k_p(Si) = 150 W/(m K), a_p = 5nm, 25nm and 100nm (for nanoparticle dimensions of 10nm, 50nm and 200nm). Strictly speaking, Eq.(4-6) is correct only for composites with spherical particle inclusions and the present Monte Carlo simulation is conducted for composites with cubic nanoparticle inclusions, but we expect that the difference of the true thermal conductivity values of nanocomposites between cubic and spherical nanoparticle inclusions should be very small. Figure 4-11 compares the thermal conductivity obtained from the Monte Carlo simulation and the effective medium approximation. As we can see, the effective medium approach based on incorporating the thermal boundary resistance into the solutions of the Fourier heat conduction law underpredicts the size effects for sizes of 50nm or lower. The EMA results do not predict a thermal conductivity value lower than bulk SiGe alloy in any case. This conclusion is further supported by recent experimental work, which shows that the thermal conductivity of Si-Ge nanocomposite is very close to that of the Monte Carlo simulation [16]

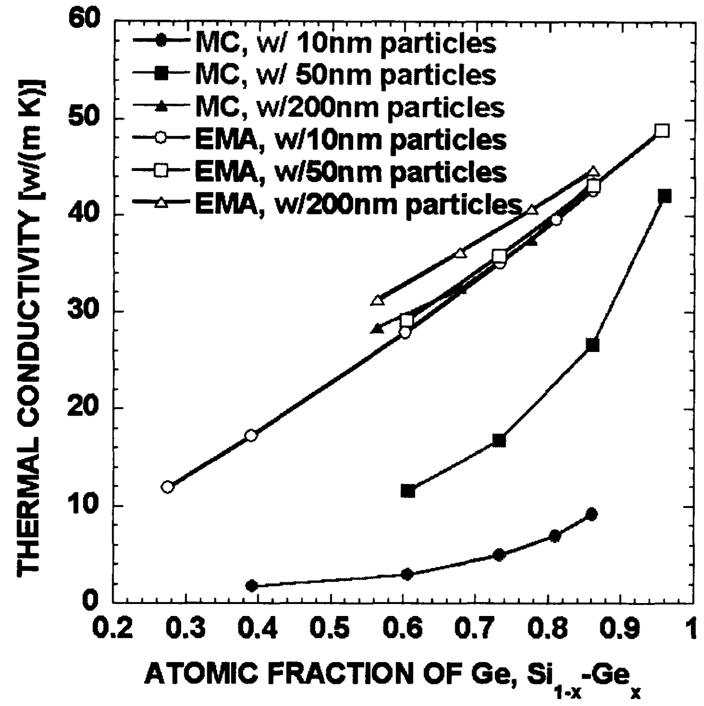

Figure 4-11. Thermal conductivity of nanoparticle composites predicted by the Monte Carlo simulation (MC) conducted in this work and that predicted by the effective medium approximation (EMA) proposed by Nan et al. in Ref. [14]. . The EMA based on incorporating the thermal boundary resistance into the solutions of the Fourier heat conduction law underpredicts the size effects.

4.3.3 Effects of Randomness

In a random distribution, the particles are distributed randomly with their positions determined by random numbers. Figures 4-8(c) also show further randomization on particle size in addition to random position distribution. However owing to the periodic boundary conditions addressed in Section 2.1, the computation is mathematically equal to simulating an infinite material consisting of repeating structures of the computational domain. In other words, the random distribution treated in this chapter represents a semi-random semi-periodic pattern (short range random and long range periodic pattern). This argument is solidified by the periodic heat flux shown in Fig. 4-9(b). Figure 4-9(b) shows that the periodicity of the heat flux is remarkably well preserved even in the random distribution case. Without a solid proof, we comment that if the computational domain (unit cell) is larger than a few phonon mean free paths (or contains enough particles), the simulation results should converge to the true value of the random nanocomposites. However, it requires a much larger computational time and memory since the problem is intrinsically a multiscale problem. We note that due to the computational power limit, the calculations have been performed only with cubic nanoparticles and the nanoparticles are aligned so that two of the surfaces of a nanoparticle are normal to the direction where a temperature difference is applied in the unit cell. Figure 4-10(b) and Fig. 4-12 show the thermal conductivity values of nanocomposites constituted of randomly distributed particles. In these figures, each data point for a random structure is the result of randomly distributing 10 particles in the computational domain. Since the process of distributing particles and selecting particle sizes is purely random and the computational domain is not large enough, the outcomes of the program after each run vary from one run to another. However, the spread of these random structure results sheds some light on the possible range of thermal conductivity reduction associated with a nanocomposite sample fabricated through a process like hot-pressing. Fig. 4-10(b) shows that the random distribution of particle positions generally results in thermal conductivity values very close or even lower than those of aligned distribution. However, a further randomness associated with particle sizes [distribution pattern shown in Fig. 4-8(c)] does not help reduce thermal conductivity, as shown in Fig. 4-12, which is shown by comparing the thermal conductivity values of aligned 50 nm particles and of random 10-100nm particles. The spread of the thermal conductivity value depends largely on the number of nanoparticles being simulated in a unit cell, which is limited by the computational power. The variation of the thermal conductivity of the random nanocomposites, as shown in Fig. 4-12, might due to the variation of the average size of the nanoparticles and thus the change of the total interfacial area in the random nanocomposites from one running case to another.

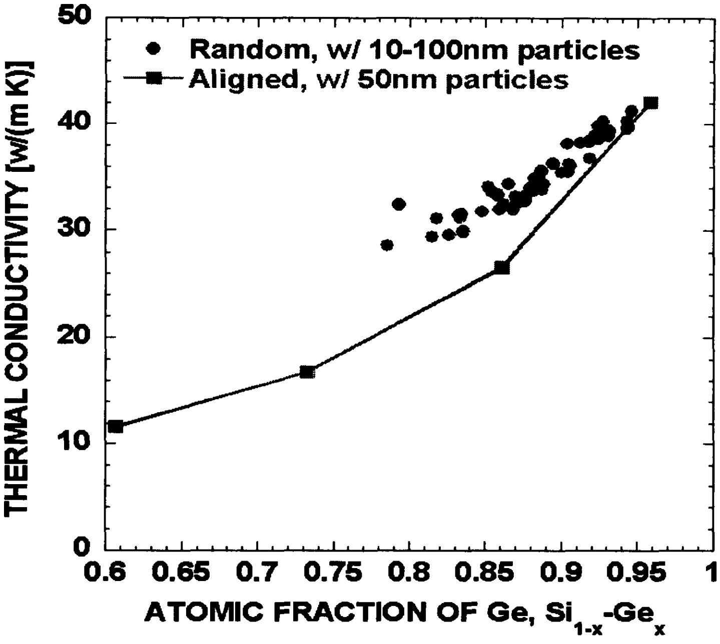

Figure 4-12. Comparison of the thermal conductivity of a periodically aligned nanocomposite with 50nm cubic silicon particles distributed in a germanium matrix and that of a random composite with silicon nanoparticles having a size range from 10 to 100nm distributed randomly in a germanium matrix as a function of germanium atomic composition.

4.3.4 Interfacial Area per Unit Volume (Interface Density)

Knowing that the phonon-interface scattering dominates the thermal conductivity reduction for nanocomposites, we propose using the interfacial area per unit volume (interface density) as a unifing parameter to replace the nanoparticle size and the atomic composition and to correlate the wide spread in the thermal conductivity data. Figure 4-13 show that the thermal conductivity data of nanoparticle composites follows a single curve nicely as a function of interfacial area per unit volume. The randomness either in particle size or position distribution causes slight fluctuations but is not a dominant factor for the reduction in the thermal conductivity. Also shown in Fig. 4-13 are the thermal conductivity values of 2D nanowire composites. Apparently, the effective thermal conductivity of 2D nanowire composites is lower than that of 3D nanoparticle composites for the same interface area per unit volume. The reason is that a 2D nanowire composite contains half of its interfacial area perpendicular to the applied temperature difference direction and the other half parallel to the applied temperature difference direction, while a 3D nanocomposite contains only one third of its interfacial area perpendicular to the applied temperature difference direction and the rest is parallel to the applied temperature difference direction. All the previous work show that interfaces which are perpendicular to the applied temperature direction are more efficient in scattering phonons and thus are more efficient in reducing the thermal conductivity [15]. This also suggests that one might try to use an effective interfacial area per unit volume (interface density) to correlate the thermal conductivity of nanocomposites with different shapes of nanowire/particle inclusions. The key for thermal conductivity reduction is to have high interface density where nanocomposites can have a much higher interface density than simple 1-D stacks such as superlattices. Thus nanocomposites benefits the enhancement of the thermoelectric figure of merit ZT in terms of reducing the thermal conductivity.

4.3.5 Temperature Dependent Thermal Conductivity (Comparison with Experiments)

The Monte Carlo code can be used to simulate temperature dependent thermal conductivity value of nanocomposites. Figure 4-14(a) shows the temperature-dependent thermal conductivity of nanoparticle composites. Boundary scattering results in a very different temperature dependence of the thermal conductivity of nanocomposites compared to their bulk counterpart where at high temperature the thermal conductivity is dominated by the Umklapp phonon-phonon scattering process. The thermal conductivity of Si-Ge nanocomposites with 10 nm particles in the germanium matrix is almost temperature independent. Figure 4-14 (b) shows the comparison of the simulated thermal conductivity with recent experimental results from Jet Propulsion Laboratory [16]. The "3run 2 HTB A" sample is a Si-Ge nanocomposite with 20-80 nm Si particles embedded in a Ge matrix. The

"SGMA05" sample is a ball-milled SiGe alloy nanocomposite with average particle size of 10nm. Although the "SMGA05" sample cannot be directly compared with the modeling since we did not consider the alloy scattering and the sample configuration is more like Fig. 3-1(b), both sets of experimental data clearly show that the size effect dominates the thermal conductivity reduction.

4.4 Conclusions

This chapter presents a phonon grey medium Monte Carlo scheme to simulate the phonon transport and thus to study the thermal conductivity in nanocomposites. Special attention has been paid to the implementation of periodic boundary conditions in the heat flow direction for the Monte Carlo simulation, which is essential to study the thermal conductivity of bulk composites with nanoparticle/nanowire inclusions – an intrinsic multiscale transport problem. With a simplified gray phonon approach, the simulation was able to duplicate our earlier results of deterministically solving the Boltzmann transport equation. The Monte Carlo simulation reveals the ballistic feature of phonon transport in nanocomposites, which is consistent with the deterministic solution of the phonon BTE. The size effects of phonon transport in nanoparticle composites were systematically studied and the results showed that the thermal conductivity of nanoparticle composites can be lower than the alloy value. Several other parameters that could influence the thermal conductivity were also investigated by the Monte Carlo simulation, including the distribution of the size and position of the Si nanoparticles. It was found that randomly distributed nanoparticles in nanocomposites rendered the thermal conductivity values close to that of periodically aligned patterns. On the other hand, a staggered distribution of nanoparticles could result in a slightly lower thermal conductivity for the same particle volume fraction. The thermal conductivity values calculated by this work qualitatively agree with recent experimental measurement in Si-Ge nanocomposites. This work also suggested using an interfacial area per unit volume (interface density) as a parameter to correlate the size effect of the thermal conductivity in nanocomposites. The key for the thermal conductivity reduction is to have a high interface density where nanoparticle composites can have a much higher interface density than th simple 1-D stacks, such as superlattices. Thus nanocomposites further benefit the enhancement of ZT in terms of thermal conductivity reduction.

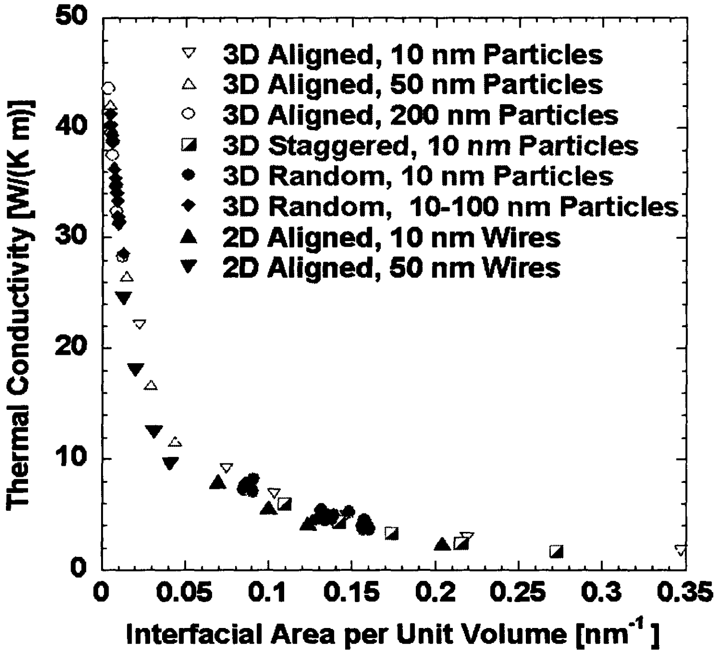

Figure 4-13. The thermal conductivity of nanoparticle composites as a function of the interfacial area per unit volume (interface density). The thermal conductivity data of nanoparticle composites falls on to a single curve nicely as a function of interfacial area per unit volume. The randomness either in particle size or position distribution causes slight fluctuations. However, these fluctuations are not a dominant factor for the reduction in the thermal conductivity. The effective thermal conductivity of 2-D nanowire composites is lower than that of 3-D nanoparticle composites for the same interface area per unit volume, since the effectiveness of interface scattering on the thermal conductivity reduction is different when the interface is perpendicular to the applied temperature difference direction and when the interface is parallel to the applied temperature difference direction.

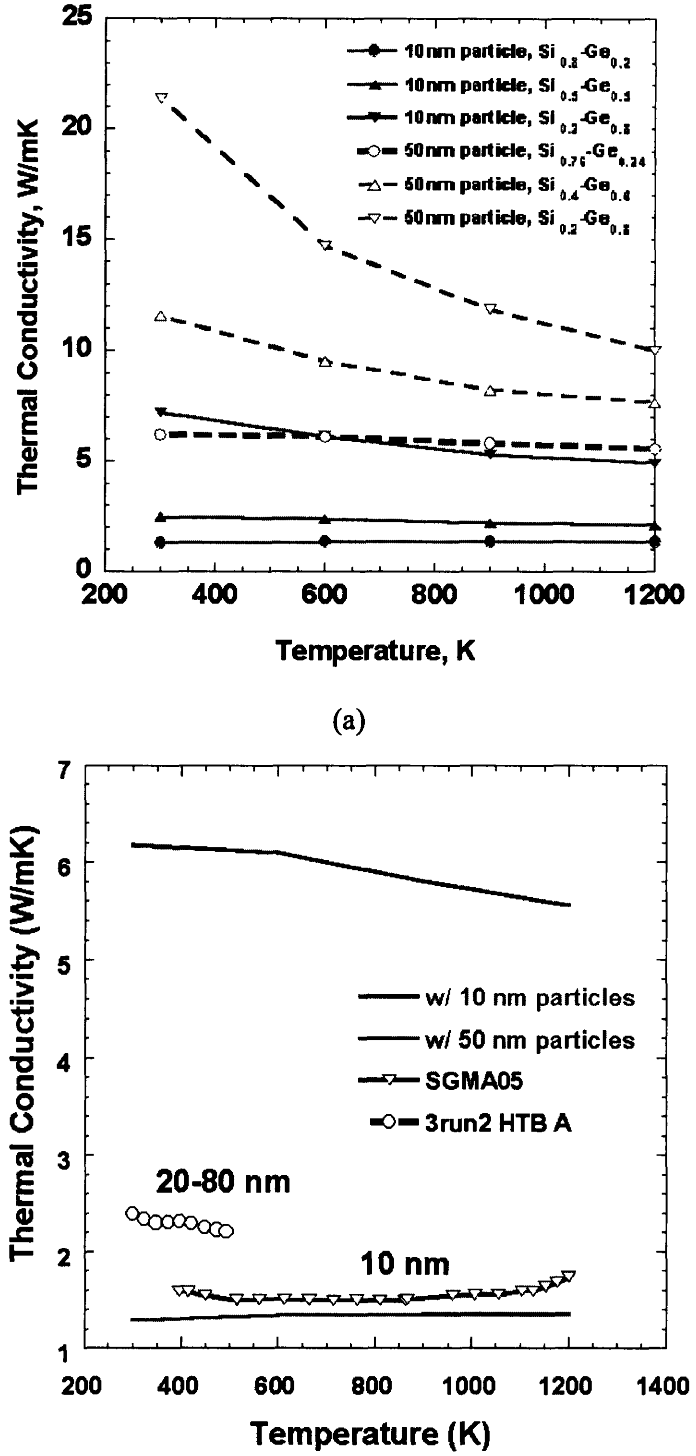

(a)

(b)

Figure 4-14. (a) The temperature-dependent thermal conductivity of nanoparticle composites. (b) Comparison of the simulated thermal conductivity with recent experimental results from Jet Propulsion Laboratory [16].

4.5 References

1. X.B. Zhao, X.H. Ji, Y.H. Zhang, et al, Appl. Phys. Lett. **86,** 062111 (2005). J.M. Zide, D.O. Klenov, S.Stemmer, et al., Appl. Phys. Lett. **87,** 112102 (2005)
2. H. Lee, et al., Proc. Int. 24th Int. Conf. Thermoelectrics, p.269 (IEEE Press, 2005)
3. J. Jiang, L.D. Chen, S.Q. Bai, and Q. Yao, J. Alloys and Compounds **390,** 208 (2005) H. Odahara, O. Yamashita, K. Satou, S. Tomiyoshi, J. Tani, H.Kido, J. Appl. Phys. **97,** 103722 (2005)
4. J. R. Howell, J. Heat Transf **120,** 547 (1998).
5. C. Moglestue, Comput. Methods Appl. Mech. Eng. **30,** 173 (1982).
6. C. Jacoboni and L. Reggiani, Rev. Mod. Phys. **55,** 645 (1983).
7. M.V. Fischetti and S.E. Laux, Phys. Rev. B **38,** 9721 (1988).
8. M.V. Fischetti and S.E. Laux, Phys. Rev. B **48,** 2244 (1993).
9. P. Lugli, P. Bordone, L. Reggiani, M. Rieger, P. Kocevar, and S. M. Goodnick, Phys. Rev. B **39,** 7852 (1989).
10. R.B. Peterson, Trans. ASME, J. Heat Transf. **16,** 815 (1994).
11. T. Klitsner, J.E. VanCleve, H.E. Fischer, and R.O. Pohl, Phy. Rev. B **38,** 7576 (1988).
12. S. Mazumder and A. Majumdar, Trans. ASME, J. Heat Transf. **123,** 749–759 (2001).
13. The temperature dependent thermal conductivity of bulk Si and Ge is available at http://www.ioffe.rssi.ru/SVA/NSM/Semicond/
14. C.-W. Nan, R. Birringer, D.R. Clarke, and H. Gleiter, J. Appl. Phys. **81,** 6692 (1997); C.-W. Nan, Z. Shi, and Y. Lin, Chem. Phys. Lett. **375,** 666 (2003)
15. G. Chen, Phys. Rev. B **57,** 14958 (1998).
16. M.S. Dresselhaus, G. Chen, Z.F. Ren, J.P. Fleurial, and P. Gogna, Second Annual Technical Report for NASA Contract NAS3-03108 (2005).

Chapter 5. Surface-Plasmon Enabled Nonequilibrium Thermoelectric Refrigerators and Power Generators

Thermoelectric energy conversion devices rely on electron transport for energy conversion, while phonon heat conduction is usually detrimental for the energy conversion efficiency. Higher energy conversion efficiency is possible if the electrons and phonons can be decoupled. This chapter proposes and investigates surface-plasmon coupled nonequilibrium thermoelectric devices. In such devices, the energy transport from the heat source of a power generator or from the cooling target of a refrigerator to the thermoelectric element is limited to electrons only through the coupling of surface-plasmons across a vacuum gap of the order of tens of nanometers. In the power generation mode, this method of thermal-energy coupling allows the creation of hot electrons in the thermoelectric element. In the refrigeration mode, cold electrons created in the thermoelectric element can be coupled to the cooling target through the surface-plasmons. Under certain conditions, these surface-plasmon coupled nonequilibrium thermoelectric devices perform significantly better than conventional thermoelectric devices based on the same materials.

5.1 Introduction

Direct energy conversion between heat and electricity using thermoelectric effects such as the Seebeck for power generation and the Peltier effect for refrigeration has been studied extensively [1, 2] . In a thermoelectric device, three competing processes occur simultaneously: the useful Peltier effect or Seebeck effect, the volumetric Joule heating, and the heat conduction from the hot end to the cold end. Device analysis shows that the performance of thermoelectric devices is determined by the materials figure of merit, $Z = S^2\sigma / k$, where S is the Seebeck coefficient, σ is the electrical conductivity, and k is the thermal conductivity. The thermal conductivity has contributions from both electrons and phonons. That is, $k = k_e + k_p$, where k_e and k_p are the electron and phonon thermal conductivities, respectively. Most research in thermoelectrics has focused on improving the figure of merit though reduction of the thermal conductivity using interfaces and quantum engineering on electron transport, and significantly progress has been made in these directions in the past decade [2-4]. In addition to the materials development, there are also new opportunities to create novel thermoelectric devices that can potentially outperform conventional thermoelectric devices. Different device configurations have been explored in the past. Past studies include the investigation of thermoelectric effects in pn junctions and minority carrier effects [5,6], multistage thermoelectric devices [7], and transient effects [8]. Recent examples are thermionic refrigeration and power generation based on single and multilayer structures [9,10].

In thermoelectric devices it is the electrons that do the useful energy conversion work and it isthe electron temperature that matters for energy conversion efficiency. Following the rationale of reducing the phonon thermal conductivity, if there is a way to impart energy to electrons only (as for example by cutting off the energy transport through phonons between the heat source or the cooling target and the thermoelectric element) while minimizing the energy coupling between electrons and phonons, it should be possible to obtain better performance in thermoelectric devices. Existing examples are the vacuum thermionic power generators [11] and electron tunneling refrigerators [12]. Electron thermionic emission, however, is limited by the work function of available materials, and electron tunneling requires extremely small gaps, of the order of several angstroms. An alternative way to decouple electrons and phonons is to explore thermal radiation between two surfaces, for example, using photons to transfer the energy from the heat source to electrons in the power generation unit. Along this line, the most apparent way of utilizing such an effect is to use a thermophotovoltaic converter [13] in which photovoltaic cells convert the energy of the photons emitted by a thermal source into useful electrical energy. Thermophotovoltaics, however, is limited to photons with energies above the bandgap. If radiation can create sufficient non-equilibrium conditions between electrons and phonons in a thermoelectric power generator or refrigerator, the performance of such devices can be significantly improved. It has been long recognized that nonequilbrium conditions between electrons and phonons in a thermoelectric element can be exploited to improve the thermoelectric energy conversion efficiency [14-18], but there exist no easy ways to create such nonequilibrium states between electrons and phonons to benefit from hot electrons for power generation or to benefit from cold electrons for refrigeration. Taking power generation as an example, to take advantage of nonequilibrium conditions between electrons and phonons, a small thermal radiation resistance is needed (1) to provide high energy flux to compensate for the electron energy loss to phonons and thus to create a nonequilibrium state between electrons and phonons (2) to reduce the temperature drop between the heat source and electrons in the thermoelectric element. The heat flux through the far-field thermal radiation is generally too small to create nonequilibrium conditions between electrons and phonons. Recent work on phonon-polariton coupling in the near-field shows that a heat flux as high as 10's or 100's W/cm^2 can be obtained when two half-spaces of a polar semiconductor (such as silicon carbide or boron nitride) are separated by a nanoscale vacuum gap for a temperature difference of 10's K between the two surfaces [19]. We anticipate that near-field energy transfer due to surface-plasmons will have a similar behavior with the additional advantage that only electrons (or plasmons) participate in the energy exchange.

In this chapter, we develop models to investigate the potential of surface-plasmon coupled nonequilibrium thermoelectric refrigerators and power generators. This chapter is organized as follows. In section 5.2, we develop models for surface-plasmon-coupled nonequilibrium thermoelectric devices, including a surface-plasmon energy transport model across a nanoscale vacuum gap and a nonequilibrium electron-phonon energy transport model in the thermoelectric device, followed by discussion of material property selection criteria. Section 5.3 presents the calculation results for refrigerators and power generators followed by a brief summary in section 5.4.

5.2 Theoretical Model

Figures 5-1(a) and 5-1(b) illustrate schematically a surface-plasmon coupled nonequilibrium thermoelectric refrigerator and power generator, respectively. A nanoscale vacuum is present to avoid the direct contact of heat source or cooling target from the thermoelectric element, thus cutting-off the heat flow through phonons between the heat source or the cooling target and the thermoelectric element. The vacuum gap should range from a few nanometers to a few tens of nanometers to ensure high radiative energy flux. The cooling target or heat source should support surface plasmon polaritons or be coated with a thin film of a material that can support surface plasmon polaritons. Similarly, the side of the thermoelectric element facing the cooling target or heat source should also be coated with a thin film of the same material. Having the same material on both sides of the vacuum gap gives the largest energy transfer due to surface plasmons. Also illustrated in the figure are the typical electron and phonon temperature distributions in the devices, which will be justified subsequently. We will first present the surface-plasmon energy transport model in section 5.2.1, and couple it to a nonequilibrium electron-phonon transport model for the whole device in section 5.2.2. We will also develop criteria for good device performance. Section 5.2.3 outlines the material property selection rules.

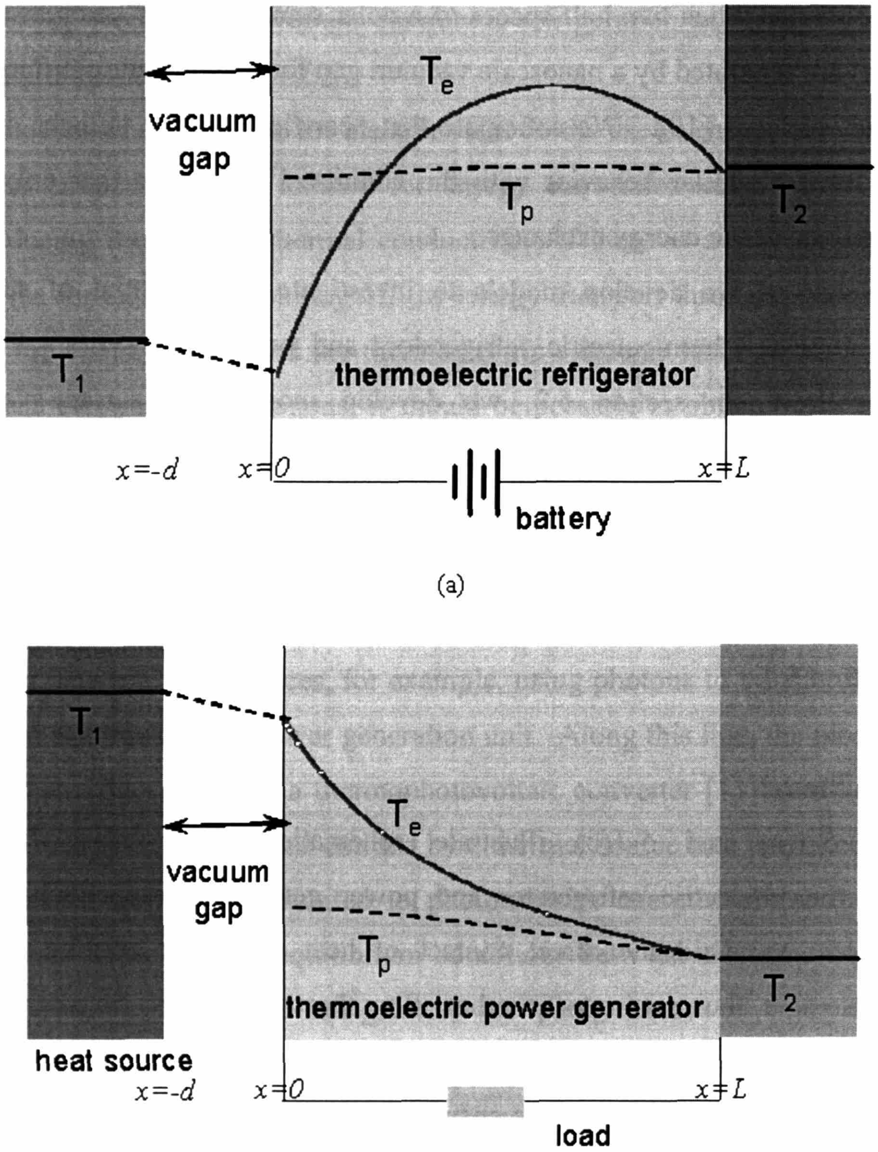

(a)

(b)

Figure 5-1. Schematic drawing of surface-plasmon coupled nonequilibrium thermoelectric devices: (a) refrigerator, and (b) power generator. A nanoscale vacuum gap is used to avoid the direct contact of the heat source or the cooling target with the thermoelectric device, and thus cut-off the heat flow through phonons between the heat source or the cooling target and the thermoelectric device.

5.2.1 Surface-plasmon Energy Transport Model

Radiative energy transfer between two surfaces separated by more than a few characteristic wavelengths, as given by Wien's displacement law, is too small to create significant non-equilibrium effects between electrons and phonons in the thermoelectric element for our proposed application. Tunneling of normal evanescent waves can give rise to an enhancement in the radiative energy transfer, with a maximum radiative flux proportional to n^2 times that of the blackbody flux in vacuum, where n is the material refractive inde [20,21]. Although the possibility of utilizing this enhancement for thermophotovoltaic energy conversion has been studied theoretically as well as experimentally [22,23], the increase in heat flux is still not sufficient for the current application. On the other hand, it has been found recently that excitation of electromagnetic surface waves, such as surface phonon-polaritons, can lead to an enhancement of radiative flux orders of magnitude higher than that of the blackbody limit [24]. The possibility of utilizing this effect for thermophotovoltaic energy conversion has been analyzed theoretically using materials that support surface phonon-polaritons [19]. Similar enhancement of the energy transfer can be achieved due to near-field coupling between surface plasmon polaritons, which involve electrons as opposed to phonons.

The radiative energy transfer between the heat source (or cooling target) and the thermoelectric element by surface plasmons is modeled following the same method used to model energy transfer between two half-spaces due to surface phonon-polaritons [19] using a combination of dyadic Green's function technique [25] and the fluctuation-dissipation theorem to characterize the spectral strength of the thermal sources [26]. Doped semiconductors with high electron or hole mobilities can support surface plasmon waves. An n-type semiconductor with the following dielectric function is assumed

$$\varepsilon(\omega)=\varepsilon_{\infty}-(\varepsilon_{DC}-\varepsilon_{\infty})\left(\frac{\omega_{TO}^2}{\omega^2-\omega_{TO}^2+i\omega\gamma_p}\right)-\frac{\omega_p^2}{\omega(\omega+i\gamma_e)} \tag{5-1}$$

The first term on the right hand side of Eq. (5-1) is due to atomic polarization, the second term is due to the optical phonons, and the third term is due to the conduction electrons. We choose parameters that are close to these of InSb, with $\varepsilon_\infty = 15.24$, $\varepsilon_{DC} = 17.76$, $\omega_{\mathrm{TO}} = 0.022$ eV , $\gamma_p = 3.56\times10^{-4}$ eV [27]. The plasma frequency is related to the doping by the relation

$$\omega_p^2 = \frac{ne^2}{m_{eff}\varepsilon_o} \tag{5-2}$$

where n is the electron concentration, m_{eff} is the effective mass of the electrons, and ε_o is the electrical permittivity of free space. The effect of doping on the radiative transfer is to vary the plasma frequency, ω_p, and the damping, γ_e. Though the entire device could be complicated, the heat source (or cooling target) and the thermoelectric element are modeled as two half-spaces that have the same plasmon frequency as shown in Fig. 5-2(a). For comparison, the spectral "absorptivity" of a 10 nm thin film of InSb adjacent to a half-space of InSb is shown in Fig. 5-3. The emitter is a half-space of InSb. Almost the entire energy incident on the thin film in the spectral range corresponding to transfer by plasmons is absorbed in this very thin layer. As long as the major part of the radiative energy transfer is due to surface plasmon polaritons, the exact configuration of the thermoelectric device can be approximated by that of two half-spaces separated by a vacuum layer since the penetration depth of surface plasmons is only around 10 nm. The spectral flux transfer between two half-spaces of InSb, with ω_p = 0.18 eV and γ_e = 5.33 meV, at 400 K and 390 K with a vacuum gap in-between them is shown in Fig. 5-4. The two peaks in the figure correspond to resonances due to surface waves. The smaller peak, which occurs around the surface phonon-polariton frequency, is due to the surface phonon polariton and the main peak, which occurs around the surface plasmon polariton frequency, is due to the surface plasmon of the conduction electrons. For our application, only radiative transfer by surface plasmons is desired. By doping InSb appropriately, the fraction of energy transfer due to phonons can be reduced. To do so, the surface plasmon polariton frequency would have to be sufficiently separated from the surface phonon polariton frequency. In addition, the optimum plasma frequency is also determined by the temperatures involved. Figure 5-5 shows the net energy transfer from one half-space at a constant temperature as a function of temperature difference between the two half-spaces. For comparison, the net energy transfer between two blackbodies, one of them at 500 K, is also shown in the same figure. The resonance effect of the surface plasmon results in an energy transfer 3-4 orders of magnitude higher than the far-field value. The net surface plasmon energy transfer is also a function of the distance between hot and cold surface (as shown in Fig. 5-4). The smaller the vacuum gap d, the larger is the energy transport flux with a given temperature difference. The total energy flux due to excitation of surface waves is proportional to $1/d^2$. In the rest of this chapter, a 10nm gap vacuum is assumed.

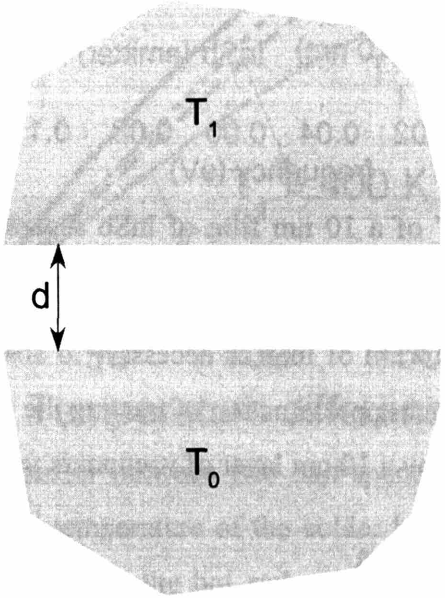

(a)

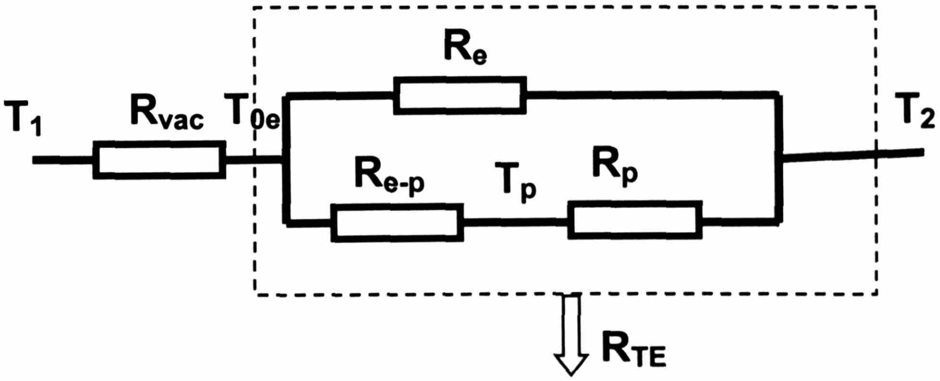

(b)

Figure 5-2. (a) Schematic of half-spaces of InSb separated by a vacuum gap of thickness d, (b) thermal resistance network of the surface-plasmon coupled nonequilibrium devices.

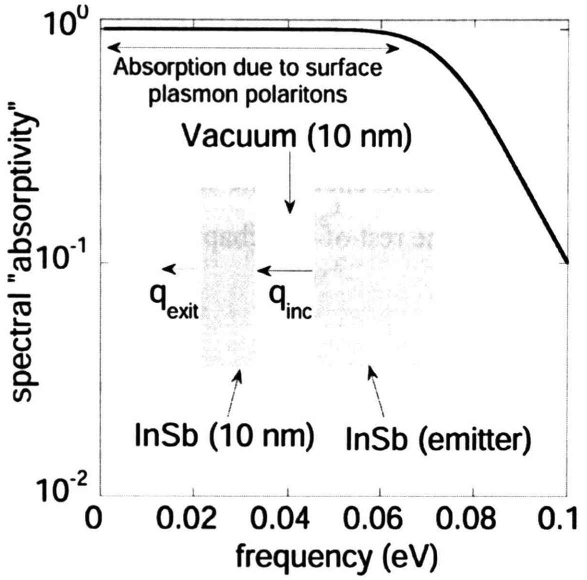

Figure 5-3. Spectral "absorptivity" of a 10 nm film of InSb separated from a InSb half space (emitter) by a 10 nm layer of vacuum. "Absorptivity" is defined as the ratio $(q_{inc} - q_{exit})/q_{inc}$. This figure shows that only 10 nm of InSb is necessary to absorb all the surface plasmon energy flux. It confirms that our approximation of treating the thermoelectric device as two half-spaces of InSb separated by a 10 nm layer of vacuum is valid.

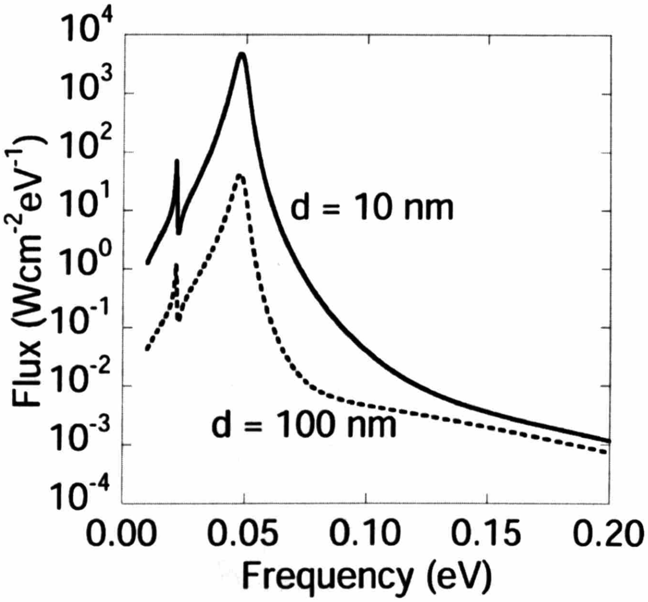

Figure 5-4. Spectral flux between two half-spaces of InSb separated by a vacuum gap of thickness d = 10 nm and d = 100 nm. The plasma frequency is assumed to be 0.18 eV. The smaller peak corresponds to resonance due to surface phonon polaritons and the bigger peak corresponds to resonance due to surface plasmon polaritons.

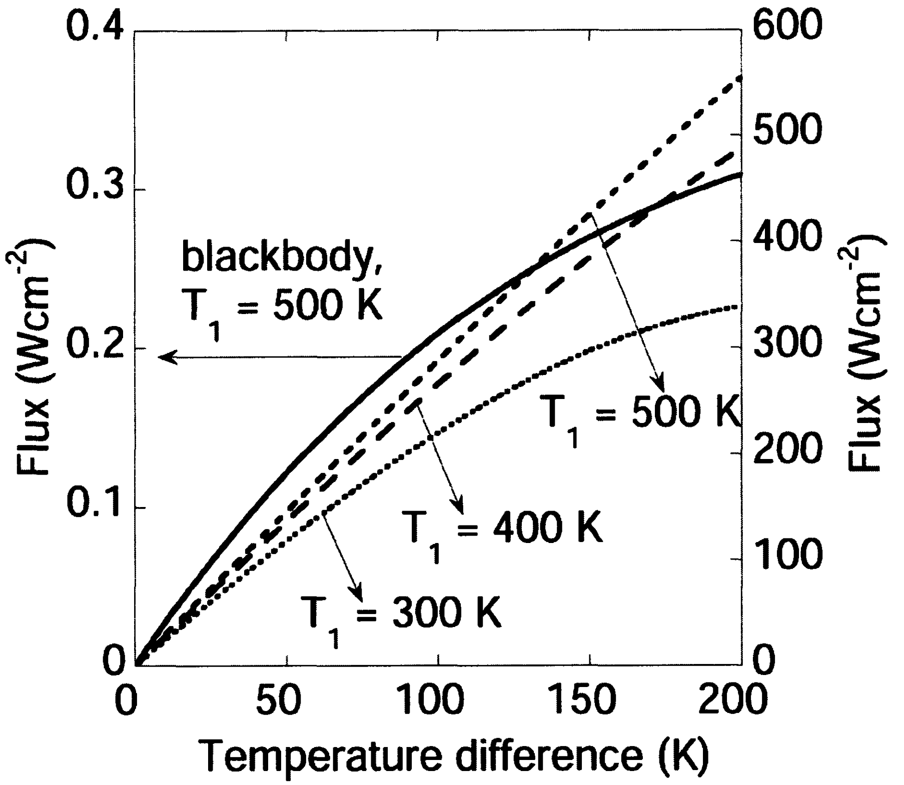

Figure 5-5. Total energy transfer between two half-spaces of InSb. The hotter half-space is maintained at T_1 and the temperature of the colder half-space is varied. The x-axis is the temperature difference between the hot and cold bodies. The blackbody energy transfer, with the hotter half-space maintained at 500 K, corresponds to the y-axis on the left. The other curves correspond to the y-axis on the right.

5.2.2 Surface-Plasmon Coupled Nonequilibrium Thermoelectric Devices

Standard thermoelectric device models assume that electrons and phonons are under local equilibrium. However, depending on the electron-phonon energy exchange rate and the rate of heat input, the electrons can be heated (or cooled) to a much higher (or lower) temperature than the phonons. Such a nonequilibrium electron-phonon effect, which is often called hot electron effect in high field electronics since electrical fields heat up electrons first, have been extensively studied for high field electronics [28, 29,30] and laser-material interactions where the electrons can be thrown out of equilibrium from lattice due to excitation by an ultra-short laser pulse [31,32]. A few papers have also dealt with nonequilibrium electron and phonon transport in thermoelectrics research [14-18]. We follow an established way to deal with such a nonequilbrium situation, the two-temperature model, which assumes that electron and phonons are in equilibrium with their respective subsystems and have their own temperature, and that the boundary conditions can be separately formulated. For this treatment to be valid, the electron-electron collisions which randomize the electron energy should be frequent enough, a condition usually satisfied if the electron concentration is 10^{16} cm^{-3} or higher, as is the case in good thermoelectric materials. We further restricted our analysis to monopolar (single carrier) semiconductors and assumed that there is no electron-hole pair generation and thus no additional recombination heat needs to be considered. We also neglected the temperature dependence of the thermal and thermoelectric properties (k_e, k_p, σ and S). Thus no Thompson effect is included in the model. Under these approximations, the governing transport equations for the electron and phonon subsystems in the thermoelectric element are:

$$k_e \frac{d^2 T_e}{dx^2} - G(T_e - T_p) + \frac{j^2}{\sigma} = 0 \tag{5-3}$$

$$k_p \frac{d^2 T_p}{dx^2} + G(T_e - T_p) = 0 \tag{5-4}$$

where T_e and T_p are the electron and phonon temperatures, respectively, j is the current density passed through the thermoelectric element, and G is the volumetric electron-phonon energy coupling constant, which can also be viewed as the cooling or heating rate of electrons due to their interaction with phonons. The first terms in Eqs. (5-3) and (5-4) are heat conduction terms due to electron carriers and phonon carriers, respectively, $G(T_e - T_p)$ describes the energy coupling or interaction between the electron and phonon subsystems, and $j^2\rho$ is the energy input to the electron subsystem due to Joule heating.

The general solutions for the electron and phonon temperatures are,

$$T_e(x) - T_p(x) = \theta_0 + \theta(x) \tag{5-5}$$

$$T_p(x) = -\frac{k_e}{k_e + k_p}\theta(x) - \frac{j^2}{2\sigma(k_e + k_p)}x^2 + C_3 x + C_4 \qquad (5\text{-}6)$$

where

$$\theta_o = \frac{j^2 k_p}{G\sigma(k_e + k_p)}, \quad \theta(x) = C_1 e^{mx} + C_2 e^{-mx} \qquad (5\text{-}7)$$

and

$$m^2 = \frac{G(k_e + k_p)}{k_e k_p} \qquad (5\text{-}8)$$

The above general solutions have been obtained before, together with different boundary conditions to determine the coefficients C_1 to C_4. The concept of coupling through surface plasmons requires us to establish new boundary conditions that are difficult to realize in conventional device configurations. If we look at the time scale, the characteristic time scale for creating a surface polariton mode is ω_p^{-1}, which in this case is ≈ 23 fs. The electron-electron scattering time is also around tens of femto-seconds. Finally, the characteristic time for energy transfer between electrons and phonons is given by the electron-phonon coupling constant, which can range from a pico-second to nano-seconds at low temperatures. Hence, this chapter assumes that the surface polaritons are regenerated almost instantaneously. The radiative energy due to surface polaritons is first transferred to the electrons, which form a subsystem at the electron temperature, and finally to the phonons, which form another subsystem at the phonon or lattice temperature, through electron-phonon coupling. This scale analysis justifies the boundary conditions established below for the nonequilibrium thermoelectric devices. Although the temperature profiles seem different in the surface plasmon thermoelectric refrigerators [Fig. 5-1(a)] and power generators [Fig. 5-1(b)], the boundary conditions for the control equations are actually similar.

At $x=L$, away from the plasmon coupling surfaces, we assume that the electrons and phonons are in equilibrium with each other at T_2. That is,

$$T_e = T_2 \text{ and } T_p = T_2 \qquad (5\text{-}9)$$

At $x=0$, the phonon subsystem is assumed to be isolated, i.e.

$$\frac{dT_p}{dx} = 0. \tag{5-10}$$

This assumption is used in most of the calculation results presented in this chapter except for Fig. 5-11 shown later, since the surface-plasmon energy transport calculation in Fig. 5-4 shows that less than 10% of total energy coupling between the surfaces is through phonons and this percentage can be further reduced by appropriate doping to control the separation between frequencies of the surface plasmon and surface phonon-polariton.

The boundary condition for the electron subsystem at $x=0$ can be written as

$$q = SjT_e \,|_{x=0} - k_e \frac{dT_e}{dx} \,|_{x=0} \tag{5-11}$$

The first term is the Peltier cooling term, which represents the heat absorbed from the hot surface of the power generator or cold surface of the refrigerator. The second term is the heat conducted by electrons.

It is through q in Eq. (5-11) that we couple the equations of the nonequilibrium electron-phonon transport model in thermoelectric devices to the surface-plasmon energy transport model across the vacuum. Because of this coupling, neither the heat flux nor the temperature at $x = 0$ (the interface between the vacuum and the thermoelectric element) are known variables. For power generators, the heat source temperature T_l at $x = -d$ is usually taken as the input for the efficiency calculation, where d is the size of the vacuum gap. For refrigerators, either the cooling target temperature T_l or the cooling power density is given for the performance calculation. Thus numerical iteration is inherently needed for the calculation of the temperature distribution. After the temperature inside the thermoelectric element is known, we can determine the performance of the whole device.

To evaluate the refrigerator performance, the temperature at the interface of the vacuum and thermoelectric element can be calculated for a given cooling load (cooling rate) at a cooling target temperature T_1. Then the energy expenditure p_{in} for cooling can be written as

$$p_{in} = Sj(T_2 - T_e|_{x=0}) + \frac{j^2 L}{\sigma} \tag{5-12}$$

The coefficient of performance (COP) ϕ is defined as

$$\phi = \frac{q}{p_{in}} \tag{5-13}$$

The minimum cooling target temperature is reached when q is set to zero.

For power generators, the power output depends on the external electrical load resistance R_L. Often the external resistance is written as $R_L = \mu R_{in} = \mu \frac{L}{\sigma A}$, where μ is the electrical resistance ratio, R_{in} is the electrical resistance of the thermoelectric element and A is the cross-section area of the thermoelectric element. Then the electric current density in the power generator can be written as

$$j = \frac{V_s}{R_{TOT} A} = \frac{S(T_e|_{x=0} - T_2)}{(\frac{L}{\sigma A} + R_L)A} = \frac{S\sigma(T_e|_{x=0} - T_2)}{L(1+\mu)} \tag{5-14}$$

The power output p_0 is thus,

$$p_0 = \frac{j^2 R_L}{A} = \frac{S^2 \sigma (T_e|_{x=0} - T_2)^2}{L} \frac{\mu}{(1+\mu)^2} = \frac{kZ(T_e|_{x=0} - T_2)^2}{L} \frac{\mu}{(1+\mu)^2} \tag{5-15}$$

The energy conversion efficiency η can be calculated as

$$\eta = \frac{p_0}{q} \tag{5-16}$$

We will also compare the COP and minimum temperature for refrigeration and the efficiency for power generation thus obtained with that of standard devices, for which the corresponding expressions are well documented [1].

We note that there are no simple equations for the performance evaluation of surface-plasmon coupled nonequilbrium thermoelectric devices. The numerical simulations are carried out to obtain various optimum values. Before presenting any numerical results, however, we will develop some criteria that serve as guidelines for device design and materials selection.

From the above discussion, we see that in the proposed devices, an additional temperature drop between the heating (cooling) source and the thermoelectric element develops across the vacuum gap. We define an effective thermal resistance for the vacuum gap, R_{vac}, due to the surface-plasmon energy transport, where $R_{vac} = \frac{T_1 - T_e |_{x=0}}{q}$. This resistance must be small such that most of the temperature drop happens in the thermoelectric element rather than the vacuum gap, i.e.,

$$R_{vac} << R_{TE} \tag{5-17}$$

where R_{TE} is the total thermal resistance of the thermoelectric element, which will be determined next.

For conventional thermoelectric devices (both a power generator and refrigerator), the thermal resistance is given by $\frac{L}{k}$. In the nonequilibrium thermoelectric devices, a first order analysis (neglecting the joule heating effect on thermal resistance model) gives the thermal resistance network as shown in Fig. 5-2(b). When the energy is coupled from the heat source or the cooling object to the interface between the vacuum and the thermoelectric element, it is transported through two channels in the thermoelectric element. One is through the electron subsystem and the other is through the electron-phonon interaction and then the phonon subsystem. The electron-phonon coupling thermal resistance can be written as

$$R_{e-p} = \frac{1}{GL_{e-p}} \tag{5-18}$$

where L_{e-p} is the length over which the electron and phonon subsystems have distinguishable temperatures. L_{e-p} is the thermoelectric element length or the electron cooling length, whichever is smaller. The electron cooling length l is defined as the distance required for electrons and phonons to reach equilibrium from the boundary where electrons is heated or cooled [15,17]

$$\frac{1}{l^2} = G\left[\frac{1}{k_e} + \frac{1}{k_p}\right] \tag{5-19}$$

The total thermal resistance of the thermoelectric element operating in nonequilibrium can be thus be approximated as,

$$R_{TE} = \left(\frac{1}{R_e} + \frac{1}{R_{e-p} + R_p}\right)^{-1} = \left[\left(\frac{1}{GL_{e-p}} + \frac{L}{k_p}\right)^{-1} + \frac{k_e}{L}\right]^{-1} \tag{5-20}$$

If $\frac{1}{GL_{e-p}}$ is much less than $\frac{L}{k_p}$, the nonequilibrium effect is not noticeable and Eq. (5-20) can be simplified to that of a conventional thermoelectric device, $\frac{L}{k}$. Thus, to have distinguishable benefit, R_{TE} must be larger than the thermal resistance of a conventional device, that is

$$R_{TE} > \frac{L}{k} \tag{5-21}$$

On the other hand, when $\frac{1}{GL_{e-p}} + \frac{L}{k_p} \to \infty$, the thermoelectric element can be viewed as an almost perfect one with thermal conductivity of k_e and a corresponding $Z = \frac{S^2\sigma}{k_e}$.

Thus one will apparently benefit from a nonequilibrium electron-phonon effect, if

$$\frac{1}{GL_{e-p}} + \frac{L}{k_p} > \frac{L}{k_e}. \tag{5-22}$$

Normally k_p is larger than k_e for thermoelectric materials. Then the criterion can be written as

$$\frac{1}{GL_{e-p}} > \frac{L}{k_e} \tag{5-23}$$

We note that in nanostructured thermoelectric materials, k_p is often reduced to the same order of magnitude as k_e [2]. In such a case, Eq. (5-22) should be used as a criterion.

In summary, a surface-plasmon enabled nonequilibrium thermoelectric device will have performance superior to a conventional one when:

1) $R_{vac} << R_{TE}$ to reduce the additional temperature drop due to surface-plasmon energy transfer. This criterion also explains why the coupling by conventional far field radiation or the tunneling of regular evanescent waves is not sufficient for the proposed device configurations.

2) $\frac{1}{GL_{e-p}} > \frac{L}{k_e}$ to have a distinguishable contribution from nonequilibrium electron-phonon temperatures. This means that materials with low electron-phonon coupling are desirable.

5.2.3 Material Property Selection

The efficiency of conventional thermoelectric devices is determined by *ZT*. Reviews of past and current research in thermoelectrics should be consulted for progress made [1,2,33]. Generally a good thermoelectric material has S~200 μV/K , and $\sigma \sim 10^5\ \Omega^{-1}\text{m}^{-1}$. For the proposed devices, the electron-phonon coupling constant G is of crucial importance, as well as the plasmon frequency. The electron-phonon interaction is an active research area due to its important role in solid state physics, notably as the process that determine the electrical resistance, superconductivity, and the equilibrium dynamics of hot electrons. More often, the electron-phonon energy exchange is represented by the electron energy relaxation time τ_e in the literature [28, 30,34-37]. Neglecting the electron kinetic energy, the electron-phonon coupling constant can be written as,

$$G = \frac{3nk_B}{2\tau_e} \tag{5-24}$$

Clearly, G is proportional to the doping concentration in Eq. (5-24) and is a very complicated function of both the electron and phonon temperatures rather than a constant, since τ_e depends on both the electron scattering mechanism and the electron degeneracy. References [35] and [36] summarize the theoretical form of τ_e for various scattering mechanisms and reference [38] for low dimensional systems. However, the theoretical value agrees only qualitatively with experimental results. A number of different techniques, including electrical transport (steady state) and optical methods (dynamics) have been used to study the electron energy relaxation [29,30,38]. Table 5-1 lists some experimental data for the energy relaxation time for various materials (after [29]). Clearly τ_e ranges from 0.1 ~ 10 ps at room temperature. At low temperatures, τ_e can be as long as tens nanoseconds. Depending on the optimum doping concentration for optimum ZT, G ranges from 10^9 to 10^{13} W/(m^3 K) in semiconductors. The optimum doping concentration for thermoelectric material varies from 10^{15} cm^{-3} or 10^{16} cm^{-3} for narrow bandgap materials (InSb [39], $Hg_{1-x}Cd_xTe$ [40]) to 10^{19} cm^{-3} or 10^{20} cm^{-3} for wide bandgap materials (SiGe alloys). Most good thermoelectric semiconductors have a G value around 10^{10} or 10^{12} W/(m^3 K) at their optimum ZT values. Metals have very high G, which is around $10^{16} \sim 10^{17}$ W/(m^3 K) [41].

In the Russian literature [14,15,17], the electron-phonon energy coupling constant is often given as an electron cooling length. The electron-phonon cooling lengths l vary from 100's nanometers to several microns at room temperature. However, this estimation does not give the details about the doping concentration dependence.

In our calculation, we used $S = 200\,\mu\mathrm{V\,K^{-1}}$, $\sigma = 10^5\,\Omega^{-1}\mathrm{m}^{-1}$ and $k = 2.0\,\mathrm{Wm^{-1}K^{-1}}$. G and k_e/k varies in different cases. With such material properties, the minimum temperature that the cold end of a conventional thermoelectric refrigerator can achieve is 241K at a zero cooling load and a hot side temperature of 300K. When this material is used to make a conventional thermoelectric power generator operating at 500K to 300K, the maximum efficiency is 7%.

Table 5-1. Experimental data of the energy relaxation time (after Reference [29]).

Material	Lattice Temperature (K)	Electron Temperature (K)	τ_e (10^{-12} sec)
Si	8	29	110.0
		107	24.0
		222	2.94
		505	0.5
	77	107	23.0
		222	2.6
		505	0.43
	300	330	2.6
		505	0.37
Ge	100	100	27.0
	150	150	10.0
	200	200	6.0
	300	300	6.0
		400	6.0
		640	9.7
		1500	19.0
InSb	4.2	5	2×10^5
		10	3×10^5
		15	4×10^5
	1.15	1-15	$2.35\text{-}3.3\times10^5$
	20	20	5×10^5
	25	25	1.3×10^5
	77	77	
		122	1.76
		192	2.46
		297	3.37
GaAs	50	50	17.3
	80	80	1.7
	77	150	0.35
		300	0.65
		700	0.82
		1000	1.02
	300	350	1.42
		500	1.28
		800	1.94
		1000	1.88

5.3 Results and Discussion

The model described in section 5.2 has an inherent assumption that the electrons and phonons are in good equilibrium with each other in the heat source or in the cooling target while maintaining their nonequilibrium state in the thermoelectric element. This assumption can be justified through careful design of the surface of the heat source or cooling target. We can think othat the heat source or cooling target are made of a very thin surface plasmon material (such as InSb), coated on a metal layer. The high electron-phonon coupling constant of a metal, which is usually around 4-5 orders of magnitude larger than that of semiconductors, ensures that the equilibrium between electrons and phonons in the metal underneath the material layer that supports surface plasmon. Then the thickness of the surface plasmon supporting material must satisfy two conditions: 1) The thickness should be large enough to support all the surface plasmon energy flux. As discussed in Fig. 5-3, it should be more than 10 nm. 2) The electron and phonon temperature drop inside the surface plasmon material layer should be small. Figure 5-6(a) shows the temperature drop in the surface plamson supporting layer under a cooling heat flux of q = 50W/cm^2. Fig. 5-6(a) shows the electron temperature drop (T_e-T_m) and phonon temperature drop (T_p-T_m) inside the surface plasmon supporting material layer, where T_m is the temperature at the surface of metal layer and surface plasmon material facing the vacuum. Figure 5-6(b) shows the temperature drop at the plasmon material surface as a function of the thickness of surface-plasmon material. The smaller the electron-phonon coupling constant, the larger the electron temperature drop. The temperature drop is less than 2.5 K if the thickness of the surface plasmon material is less than 1 μm. Thus we can assume that the electron temperature and phonon temperature are in equilibrium and they are the same as the cooling target or heat source temperature if the cooling target or heat source are coated with tens or several hundred nanometers of surface plasmon material with a thin metal layer underneath. In the rest, we present the calculation results for both the surface plasmon coupled nonequilibrium refrigerators and power generators.

5.3.1 Refrigerator

Figure 5-7 shows the variation of several characteristic temperatures as a function of the current density under a cooling load of 50 W/cm^2. In the figure, T_{0e} and T_{0p} are the electron and phonon temperatures at the cold end of the thermoelectric element (i.e., the interface between the

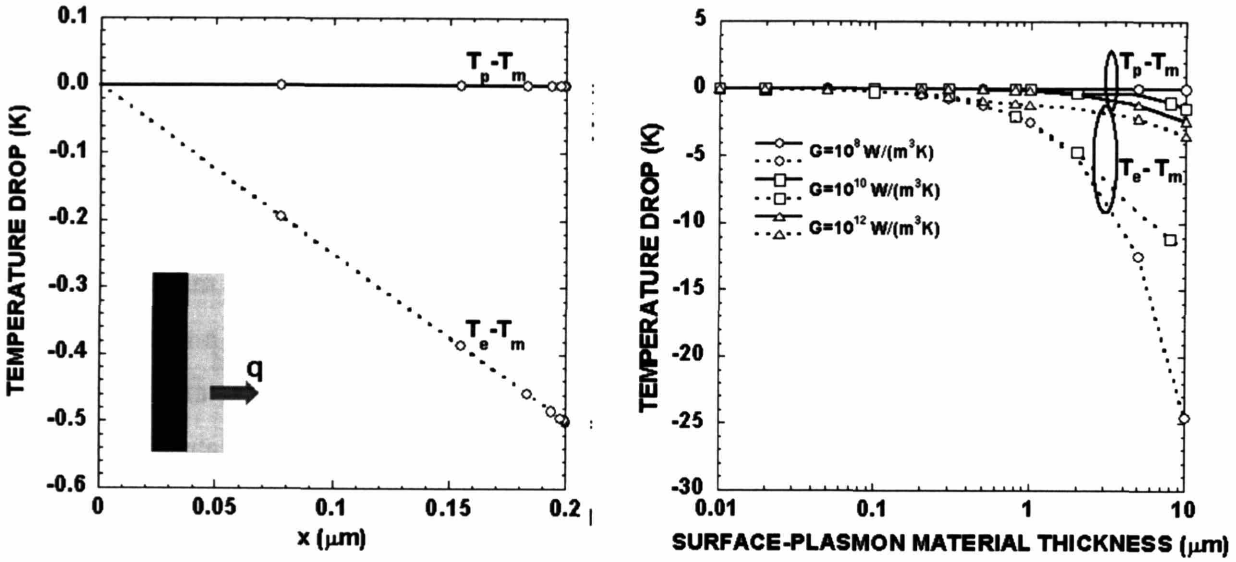

(a) (b)

Figure 5-6. The temperature drop in the surface plasmon supporting layer with a thin metal layer underneath under a cooling heat flux of q=50W/cm^2: (a) the electron (T_e-T_m) and phonon (T_p-T_m) temperature drop inside the surface plasmon supporting material layer, and (b) the temperature drop at the plasmon material surface as a function of the thickness of the surface-plasmon material.

vacuum gap and the thermoelectric element) respectively, and T_1 is the cooling target temperature. Two most distinctive features of this figure are: 1) The phonon temperature T_{0p} at the cold end is much higher than the electron temperature T_{0e}. The phonon temperature at the cold end can be even higher than the hot end temperature T_2 but the electrons at the cold end are still colder than T_2. This is because the Peltier effect cools the electrons first. 2) By using surface-plasmon coupling, the cooling target can reach as low a temperature as the electron temperature at the cold end. However, due to the additional thermal resistance or temperature drop at the vacuum side, the cooling target temperature T_1 is always higher than T_{0e} when there is an external cooling load. In this figure the cooling load is first calculated from the maximum cooling power density of a conventional thermoelectric refrigerator operating at $T_2 = 300$K and $T_1 = 250$K, which is $q = 50$W/cm^2 for a $L = 50\,\mu$m device. Then such a cooling load is applied to the surface-plasmon coupled device to calculate the temperature distribution inside the device and the cooling target temperature by sweeping the applied current. As shown in the figure, compared to the minimum temperature $T = 250$ K that the conventional refrigerator can reach at such a cooling load at its optimum current $j_{\mathrm{conv.opt.}}$, the surface-plasmon coupled nonequilibrium thermoelectric refrigerator can reach a much lower temperature. The minimum temperature with a cooling load of q = 50W/cm^2 surface-plasmon coupled nonequilibrium thermoelectric refrigerator can achieve is T_l = 201.63K, which corresponds to Z = 0.00547 K^{-1} or ZT_H = 1.641 (T_H=300K). If the cooling target is kept at T_l = 250K, a much smaller current than the conventional optimum current $j_{\mathrm{conv.opt.}}$ can be applied and thus a much higher COP, as large as 0.40, than the 0.092 of the conventional refrigerator can be achieved.

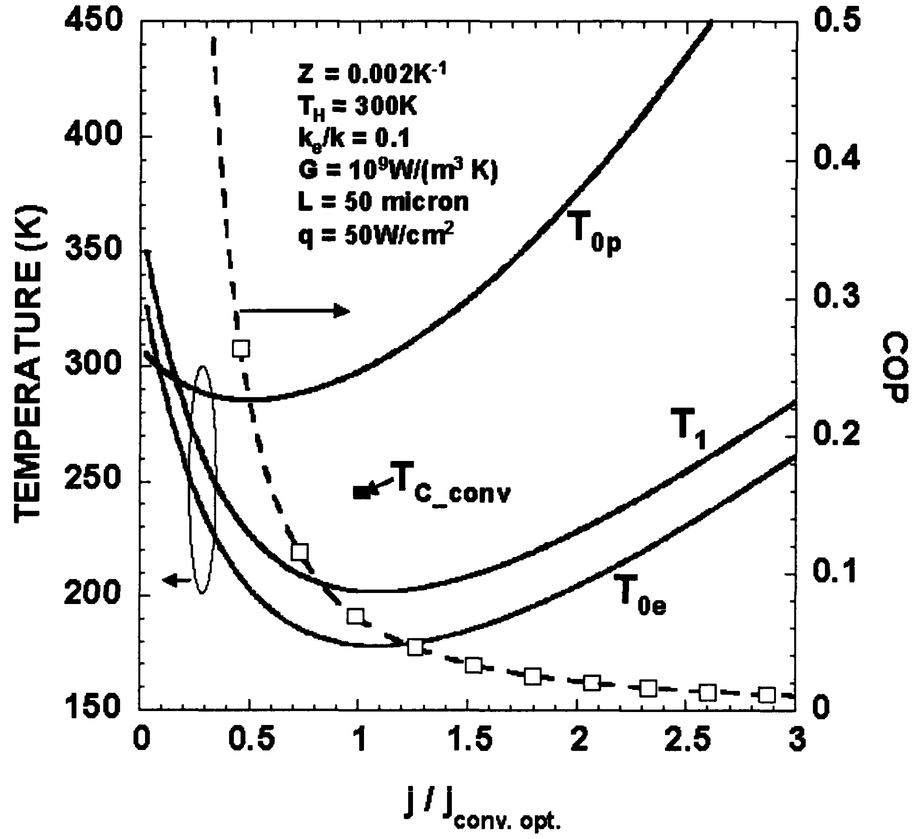

Figure 5-7. Typical temperature and COP change as a function of the applied current under a cooling load. T_{0e} and T_{0p} are the electron and phonon temperatures at the cold end of the thermoelectric element (i.e., the interface between the vacuum gap and the thermoelectric device) respectively, and T_l is the cooling target temperature. Comparing to the minimum temperature T=250 K to that which the conventional refrigerator can reach at such a cooling load at its optimum current density $j_{\mathrm{conv.opt.}}$, the surface-plasmon coupled nonequilibrium thermoelectric refrigerator can reach a much lower temperature.

When the cooling load is removed, a thermoelectric refrigerator achieves its minimum temperature if the optimum current is applied. In a surface-plasmon coupled nonequilibrium thermoelectric refrigerator, this means that the cooling target temperature (both electrons and phonons at the cooling target) achieves the same temperature as the cold end electron temperature of the thermoelectric element. Figure 5-8(a) shows the minimum temperature of the surface-plasmon coupled nonequilibrium thermoelectric refrigerator as a function of thethermoelectric element length for various G values. Apparently the shorter the thermoelectric element length and the smaller the coupling constant G, the lower the minimum temperature that can be reached. Interestingly, for the same $k_e / k = 0.1$, the minimum temperature can be grouped as a function of dimensionless parameter $\frac{GL^2}{k}$. Figure 5-8(b) shows the minimum temperature as a function of $\frac{GL^2}{k}$ for various k_e / k. For given values of Z and $\frac{GL^2}{k}$, the lower the k_e / k ratio,

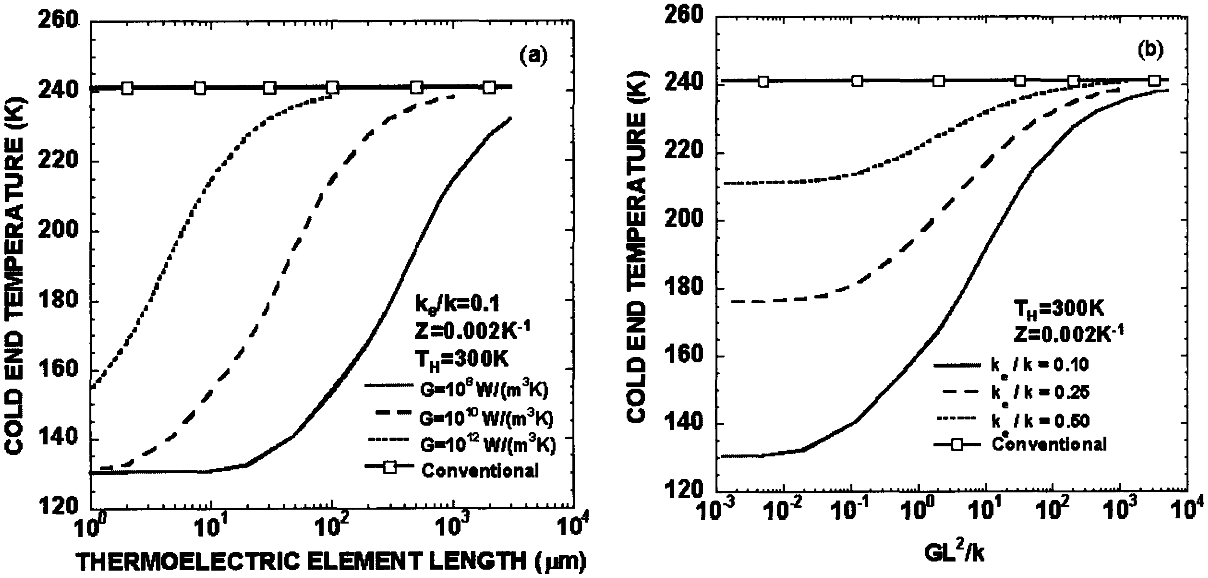

Figure 5-8. (a) The minimum cooling temperature of the surface-plasmon coupled nonequilibrium thermoelectric refrigerator as a function of thermoelectric element length for various G values. The shorter the thermoelectric element length and the smaller the coupling constant G, the lower the minimum temperature can be reached. (b) the minimum temperature as a function of $\frac{GL^2}{k}$ for various k_e / k.

the lower the minimum temperature, which means the phonon heat flux has been cut off more effectively. Figure 5-9 shows the temperature distribution inside a 50 μm nonequilibrium thermoelectric refrigerator when the minimum cold end temperature is reached. The smaller the electron phonon coupling constant *G*, the larger the temperature difference between electrons and phonons. For small *G* values [10^8 and 10^{10} W/(m^3 K)], the electron temperature near the hot end can be larger than the phonon temperature but electrons are much colder than phonons at the cold side.

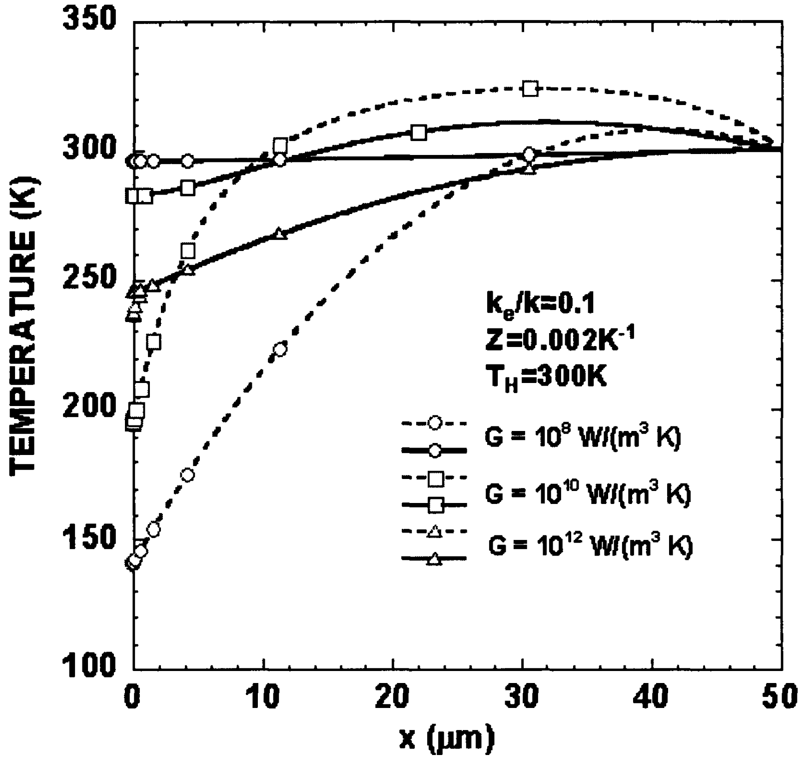

Figure 5-9. The temperature distribution inside a 50 μm surface-plasmon coupled nonequilibrium thermoelectric refrigerator when the minimum cold end temperature is reached (dashed lines – electron temperature, solid lines – phonon temperature) . The smaller is the electron phonon coupling constant G, the larger is the temperature difference between electrons and phonons.

Figure 5-10 shows the performance of a surface-plasmon coupled nonequilibrium thermoelectric refrigerator under a cooling load of 50 W/cm^2, which is the same as the maximum cooling power density of a L = 50 μm conventional thermoelectric refrigerator with $Z = 0.002\text{K}^{-1}$ operating at T_H = 300K and T_C = 250K. Figure 5-10(a) shows the cooling target temperature change with thermoelectric element length and the electron-phonon coupling constant. Also shown in the figure is the cooling target temperature for conventional thermoelectric refrigerators. Clearly, a much lower cooling target temperature can be obtained for a wide range of G and L combinations than the conventional device with the same given load. For a large G value, a smaller thermoelectric element length is necessary to take advantage of the nonequilibrium effect. Figure 5-10 (b) compares the COP of a surface-plasmon coupled nonequilibrium thermoelectric refrigerator with conventional thermoelectric refrigerator with the cooling target temperature at 250 K. Compared to the maximum COP = 0.092 for $Z = 0.002\text{K}^{-1}$ material in conventional thermoelectric refrigerator, which is independent of the thermoelectric element length, the COP of surface-plasmon coupled nonequilibrium thermoelectric refrigerators is a length dependent characteristic. For $G = 10^{12}$ W/(m^3 K) [large G value], the benefit from the nonequilbrium electron-phonon effect is much smaller than the degradation due to additional thermal resistance at the vacuum side. Thus, the COP is always smaller than the conventional thermoelectric refrigerator. However, for low G values, the COP of surface-plamson coupled nonequilibrium thermoelectric refrigerator can be much higher than the maximum of the conventional thermoelectric refrigerator.

As discussed in Section 5.2.2, there is small amount of energy flux due to the surface phonon polariton (the smaller peak in Fig. 5-4). The energy exchange through surface phonon polariton will degrade the performance calculated before since, in the case of refrigeration, the high phonon temperature in the thermoelectric element will cause a reverse flow of heat from the thermoelectric element to the cooling target. We have calculated the degradation caused due to this surface phonon polariton energy exchange. This is done by separating the energy exchange through surface plasmons and surface phonon polaritons. The boundary conditions (5-10) and (5-11) are changed accordingly. Figure 5-11 shows the cooling target temperature under a cooling load of 50 W/cm^2 with (dashed lines) and without (solid lines) consideration of the degradation. The degradation can be a few degrees for short thermoelectric elements. However, the overall performance is still much better than the conventional thermoelectric refrigerator.

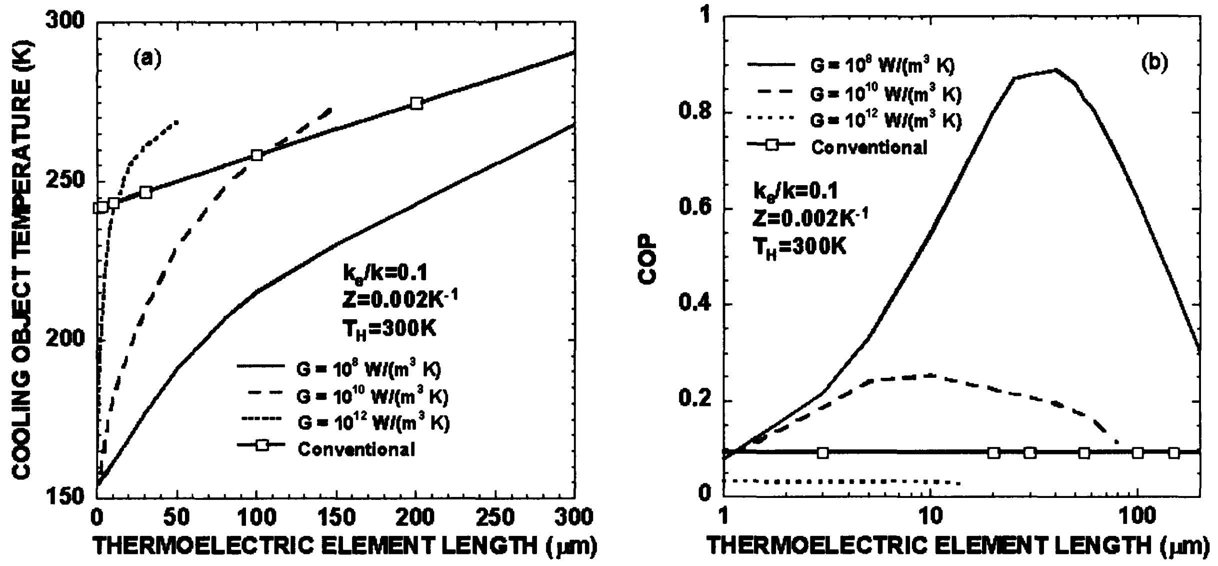

Figure 5-10. (a) The cooling target temperature changes with thermoelectric element length and the electron-phonon coupling constant under a load of q=50W/cm^2. (b) the COP of surface-plasmon coupled nonequilibrium thermoelectric refrigerator as a function of thermoelectric element length and electron-phonon coupling constant with the cooling target temperature at 250K.

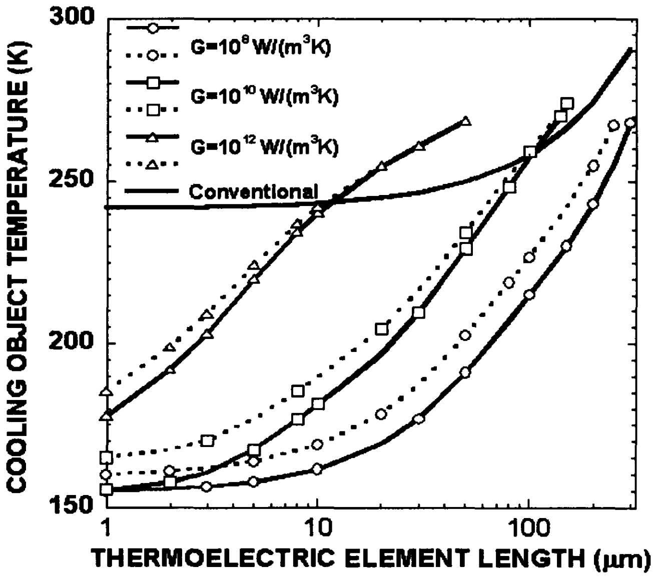

Figure 5-11. The cooling target temperature with and without consideration of the reverse energy flow due to surface phonon polaritons (dashed lines with symbols – without, solid lines with symbols – with) under a cooling load of 50W/cm^2. Though the surface phonon polariton degrades the cooling performance, the surface-plasmon coupled nonequilibrium devices have much better performance than conventional devices.

5.3.2 Power Generator

Figure 5-12 shows the typical change of the output power density and the energy conversion efficiency as a function of the ratio of the external and internal thermal resistances $\mu = R_L / R_{TE}$ operating with a heat source temperature at 500 K and the cold side temperature at 300 K. Compared to the conventional thermoelectric power generator, the surface-plasmon coupled device has a much higher energy conversion efficiency over a wide range of $\mu = R_L / R_{TE}$. The optimum efficiency is around 1.5 times the optimum of a conventional thermoelectric power generator for given parameters. However, the high efficiency comes with a decrease in the output energy density compared to the conventional thermoelectric power generator. The efficiency gain is more of interest than the loss of energy density since the device power density must match the external thermal management capabilities.

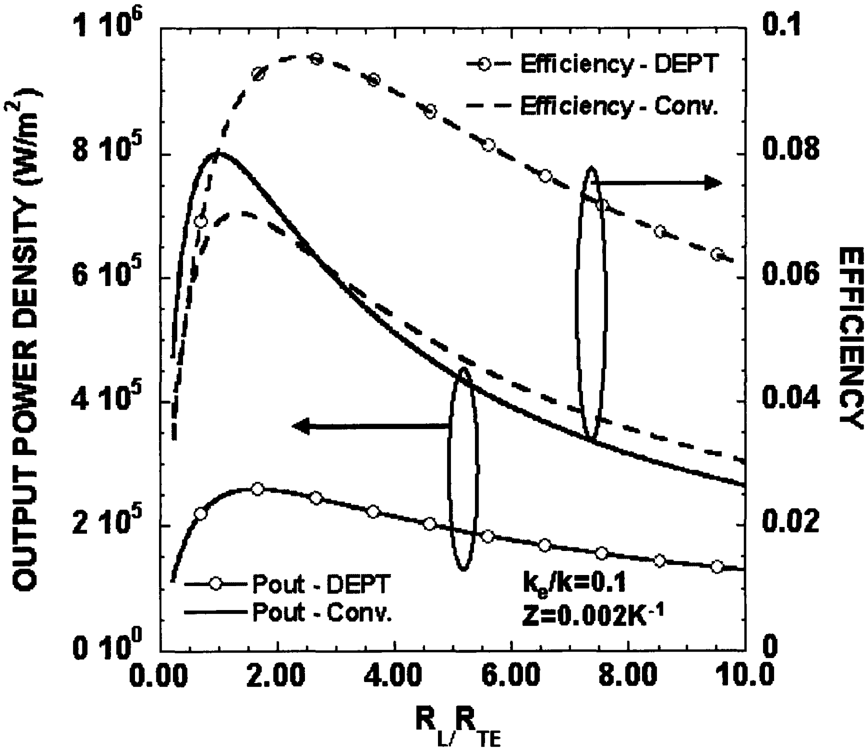

Figure 5-12. Typical change of the output power density and the energy conversion efficiency with the ratio of the external and internal thermal resistances $\mu = R_L / R_{TE}$. Compared to a conventional thermoelectric power generator, the surface-plasmon coupled nonequilbrium thermoelectric power generator has a much higher energy conversion efficiency over a wide range of $\mu = R_L / R_{TE}$.

Figure 5-13(a) shows the optimum efficiency as a function of thermoelectric element length for different electron-phonon coupling constants with k_e/k = 0.10 and Z = 0.002K^{-1} operating at T_1 = 500K and T_2 = 300K. For both G = 10^8 W/(m^3 K) and G = 10^9 W/(m^3 K), the efficiency of the surface-plasmon coupled device is higher than the conventional thermoelectric power generator due to the nonequilibrium electron-phonon effect. The longer the thermoelectric element, the less the benefit of the nonequilibrium effect and thus the less the energy conversion efficiency. For G = 10^{12} W/(m^3 K), the effective thermal resistance on the thermoelectric element side is small and so the performance is limited by the surface-plasmon energy transport. With longer thermoelectric elements, the relative thermal resistance of the vacuum decreases and thus the energy conversion efficiency increases. Figure 5-13(b) shows the corresponding electron temperature at the hot end of the thermoelectric element. Apparently, the longer the thermoelectric element, the higher is the electron temperature at the hot end due to the relatively larger thermal resistance of the thermoelectric element. Figure 5-13(c) shows the temperature distribution in a 50 μm surface-plasmon coupled nonequilibrium thermoelectric power generator when the heat source is maintained at 500K. Again, it shows that the relative temperature drop at the vacuum side is large for large G because the contribution of the nonequilibrium effect to the total thermal resistance of the thermoelectric device becomes small. It can also be seen that a small G results in a large temperature difference at the hot end.

Similar to refrigerator, the ratio of the electron thermal conductivity contribution to the total thermal conductivity k_e/k also plays an important role in the energy conversion efficiency. Figure 5-14 shows the energy conversion efficiency as a function of thermoelectric element length for different k_e/k. It is interesting to see that increasing k_e/k results in a change of the device from a nonequilibrium effect dominated regime (k_e/k =0.10) to a vacuum thermal resistance regime (k_e/k =0.50) and results in a conversion energy decrease.

Comparing the performance calculation of refrigerators and power generators, we expect that the nonequilbrium transport favors the realization of refrigerators than power generators due to: (1) at low temperatures, the electron-phonon coupling constant G is several orders smaller; (2) at low temperatures, the thermal wavelength is longer and thus the vacuum gap can be larger. Finally we note that our calculation results shown above are not optimized. Though ZT is a good indicator for the performance of conventional thermoelectric devices, it is only one of the determining factors of the performance of the surface plasmon nonequilibrium thermoelectric

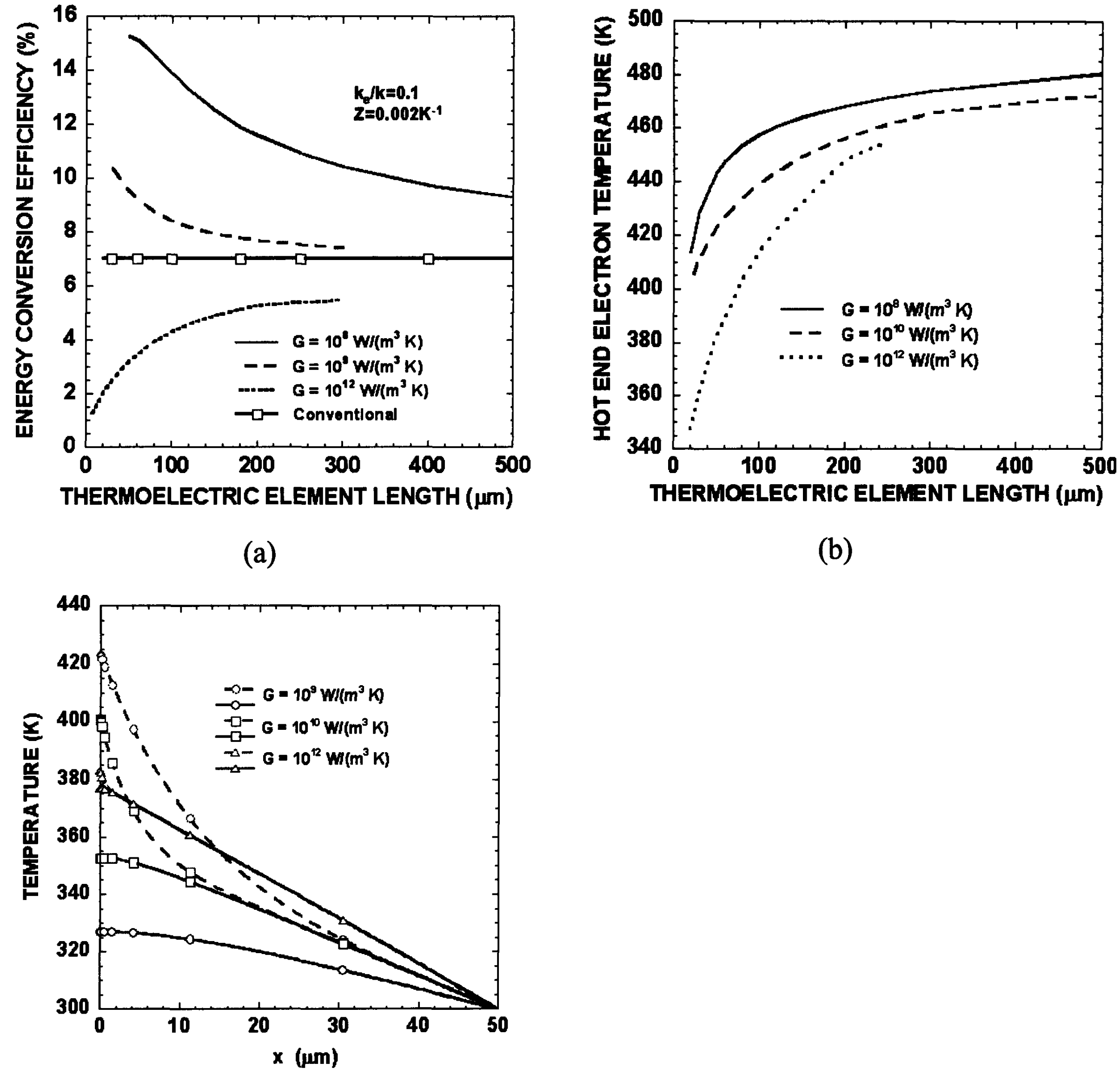

(a)

(b)

(c)

Figure 5-13. (a) the optimum energy conversion efficiency as a function of thermoelectric element length for different electron-phonon coupling constant with k_e/k=0.10 and Z=0.002K^{-1} operating at T_1=500K and T_2=300K, (b) the corresponding electron temperature at the hot end of the thermoelectric element. (c) the electron (dashed lines) and phonon (solid lines) temperature distributions in a 50 μm surface-plasmon coupled nonequilibrium thermoelectric power generator when the heat source is maintained at 500K.

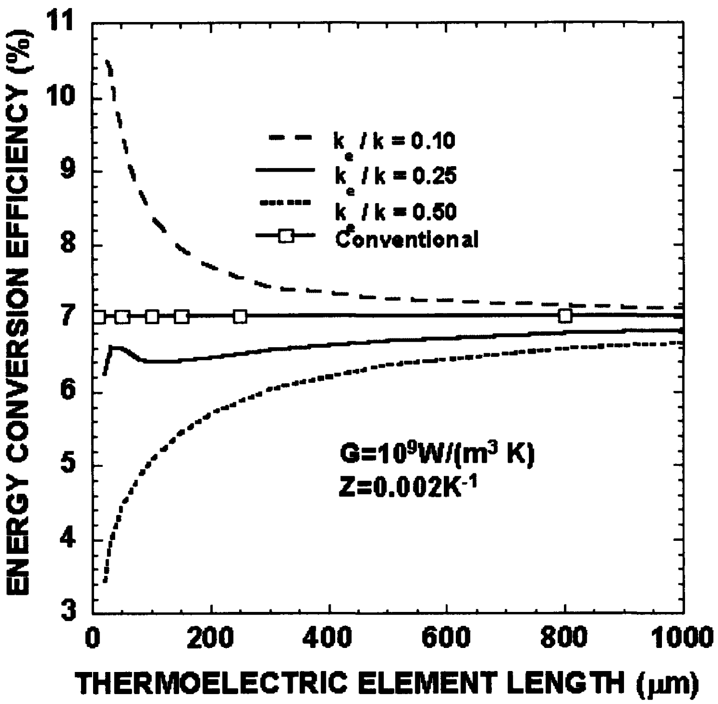

Figure 5-14. The energy conversion efficiency changes as a function of thermoelectric element length for different k_e/k.

devices. The optimum performance of such nonequilibrium devices is determined by the plasma frequency ω_p, and the damping γ_e, the electron-phonon coupling constant G, thermoelectric figure of merit ZT, and the contribution of the electrons to the total thermal conductivity, i.e., k_e/k. All these factors are strong functions of doping concentration and temperature. Optimization of such devices will be reported in the future.

5.4 Conclusions

This chapter conceptualizes and investigates the surface-plasmon coupled nonequilibrium thermoelectric devices. These devices use surface-plasmon coupling to limit the energy exchange between the heating source (or cooling target) and the thermoelectric element to electrons alone, while eliminating direct energy exchange between phonons. Models for refrigeration and power generation devices based on this concept are established, together with simplified criteria to guide the device design and materials selection. Our simulations show that these devices can lead to significant improvements in efficiency over conventional thermoelectric devices.

5.5 References

1. A.F. Ioffe, *Semiconductor Thermoelements and Thermoelectric Cooling* (Info-search, London, 1956); T.C. Harman and J.M. Honig, *Thermoelectric and Thermomagnetic Effects and Applications* (MacGraw-Hill, New York, 1967); H.J. Goldsmid, *Electronic Refrigeration* (Pion Ltd., London, 1986); D.M. Rowe, *CRC Handbook of Thermoelectrics* (CRC Press, Inc., 1995); G.S. Nolas, J.W. Sharp and H.J. Goldsmid, *Thermoelectrics: Basics Principles and New Materials Developments* (Springer-Verlag, Berlin, 2001).
2. Tritt, T.M. Ed., Semiconductors and Semimetals **69-71** (2001).
3. T.C. Harman, P.J. Taylor, M.P. Walsh, and B. E. LaForge, Science **297**, 2229 (2002).
4. R. Venkatasubramanian, E. Silvona, T. Colpitts, and B. O'Quinn, Nature **413**, 597 (2001).
5. J. Tauc, *Photo and Thermoelectric Effects in Semiconductors* (Pergamon Press, New York, 1962).
6. K. P. Pipe, R.J. Ram, and A. Shakouri, Phys. Rev. B **66**, 125316 (2002).
7. B.J. O'Brien, C.S. Wallace and K. Landecker, J. Appl. Phys. **27**, 820 (1956); P.W. Cowling and J.E. Sunderland, Energy Conversion **7**, 289 (1968); R.G. Yang, G. Chen, G.J. Snyder, and J.-P. Fleurial, J. Appl. Phys. **95**, 8226 (2004).
8. G.J. Snyder, J.-P. Fleurial, T. Caillat, R.G. Yang, and G. Chen, J. Appl. Phys. **92**, 1564 (2002); R.G. Yang, G. Chen, A.R. Kumar, G.J. Snyder, and J.-P. Fleurial, Energy Conversion and Management, in Press; and references therein.
9. A. Shakouri, and J.E. Bowers, Appl. Phys. Lett., **71**, 1234 (1997); G. D. Mahan and L. M Woods, Phys. Rev. Lett. **80**, 4016 (1998).
10. C.B. Vining and G.D. Mahan, J. Appl. Phys., 86, 6852 (1998).
11. G.N. Hatsopoulos, and J. Kaye, J. Appl. Phys. **29**, 1124 (1958).
12. F. N. Huffman, U.S. Patent No. 3169200 (1965); Y. Hishinuma, T.H. Geballe, B.Y. Moyzhes, T.W. Kenny, J. Appl. Phys. **94**, 4690 (2003); -, Appl. Phys. Lett. **78**, 2572 (2001).
13. T. J. Coutts, Renewable Sustainable Energy Rev. **3**, 77 (1999).
14. V.S. Zakordonests and G.N. Logvinov, Semiconductors **31**, 265 (1997); Yu G. Gurevich and G.N. Logvinoz, Sov. Phys. Semicond. **26**, 1091 (1992).
15. Y.G. Gurevich, O.L. Mashkevich, Phys. Rep. (Rev. Sec. Phys. Lett.) **181,** 327 (1989).

16. L.P. Bulat and V.G. Yatsyuk, Sov. Phys.-Semicond. **18**, 383 (1984); L.I. Anatychuk, L.P. Bulat, D.D. Nikirsa, and V.G. Yatsyuk, Sov. Phys.-Semicond. **21**, 206 (1987).
17. L.P. Bullat, Thermoelectricity under large temperature gradients, J. Themoelect. **4**, 3 (1997).
18. G. Chen and T. Zeng, Microscale Thermophyis. Eng. **5**, 71 (2001).
19. A. Narayanaswamy and G. Chen, Appl. Phys. Lett. **83**, 3544 (2003).
20. E. G. Cravalho, C. L. Tien, and R. P. Caren, ASME J. Heat Transf. **89**, 351 (1967).
21. D. Polder and M. Van Hove, Phys. Rev. B **4**, 3303 (1971).
22. M. D. Whale, *A fluctuational electrodynamic analysis of microscale radiative heat transfer and the design of microscale thermophotovoltaic devices*, Ph. D. thesis, (MIT, Cambridge, 1997).
23. R. S. DiMatteo, P. Greiff, S. L. Finberg, K. Young-Waithe, H. K. H. Choy, M. M. Masaki, and C. G. Fonstad, Appl. Phys. Lett. **79**, 1894 (2001).
24. R. Carminati and J.-J. Greffet, Phys. Rev. Lett. **82**, 1660 (1999).
25. L. Tsang, J. A. Kong, and K. H. Ding, *Scattering of Electromagnetic Waves* (Wiley, 2000).
26. S. M. Rytov, Y. A. Kravtsov, and V. I. Tatarski, *Principles of Statistical Radiophysics*, Vol. 3 (Springer, Berlin, 1987).
27. P. P. Paskov, J. Appl. Phys. **8**, 1890 (1997).
28. E.M. Conwell, *High Field Transport in Semiconductors* (Academic press, New York & London, 1967).
29. R.R. Alfano, Ed., *Semiconductor Probed by Ultrafast Laser Spectroscopy* (Academic Press, New York, 1984).
30. L. Challis, Ed., *Electron-Phonon Interactions in Low Dimensional Structure* (Oxford University Press, Oxford, 2003).
31. R. W. Schoenlein, W. Z. Lin, J. G. Fujimoto, and G. L. Easley, Phys. Rev. Lett. **58**, 1680 (1987).
32. T. Q. Qiu, and C. L. Tien, Trans. ASME, J. Heat Transf. **115**, 835 (1993).
33. C. Wood, Rep. Prog. Phys. **51**, 459 (1988).
34. J.M. Ziman, *Electrons and Phonons* (Clarendon, Oxford, 1960).
35. K. Seeger, *Semiconductor Physics*, 8th, (Springer, New York, 2002).
36. B.K. Ridley, *Quantum Processes in Semiconductors* (Oxford University Press, Oxford, 1999).

37. D.K. Ferry, *Semiconductor Transport* (Taylor & Francis, New York, 2000).
38. B.K. Ridley, Rep. Prog. Phys. **54**, 169 (1991).
39. R. Bower, R.W. Ure, J.E. Bauerle, and A.J. Cornish, J. App. Phys. 30, 930 (1959)
40. J.O. Sofo, G.D. Mahan, and J. Baars, J. Appl. Phys. **76**, 2249 (1994)
41. M.I. Kaganov, M.I. Lifshitz, and L.V. Tanatarov, Sov. Phys. JETP **4,** 173 (1957); J. Fujimoto, J.M. Liu, E.P. Ippen, N. Bloembergen, Phys. Rev. Lett. **53,** 1837 (1984); H.E. Elsayed-Al, T.B. Norris, M.A. Pessot, G.A. Mourou, Phys. Rev. Lett. **58,** 1212 (1987) ; P.B. Allen, Phys. Rev. Lett. **59**, 1460 (1987); R.H.M. Groeneveld, R. Sprik, A. Lagendijk, Phys. Rev. B **51**, 11433 (1995).

Chapter 6. Sub-picosecond Pump-and-probe Characterization of Thermal Transport at Nanoscale

As shown in all the current theoretical modeling and simulation work, it is extremely important to have a correct input of the phonon relaxation time or phonon mean free path and phonon reflectivity at interfaces for nanoscale heat conduction modeling and simulation programs such as Monte Carlo simulation or phonon BTE and BDE solvers. The phonon reflectivity at interfaces and the phonon relaxation time are clearly the most fundamental heat carrier properties for nanoscale heat conduction. No work has been done so far for phonon dynamics to extract these phonon properties. The closest studies are using the optical pump-and-probe (pump-probe) measurement to study thermal diffusivity and the interface thermal resistance. Optical pump-and-probe measurement uses ultrafast laser (with femtosecond or picosecond pulses) to construct a high temporal resolution temperature measurement system. The laser output from an ultrafast laser is split into two beams. A higher power beam is used to heat the sample, which is called the "pump" beam. A relatively low power "probe" beam measures the reflectivity change after ultrafast pump beam heating, from which the temperature information (cooling curve) of the sample is deduced by using the reflectivity-temperature correlation. Almost all pump-and-probe measurements use the heat diffusion equation to fit the cooling curve to get the thermal conductivity and interface resistance. However for the heat diffusion equation to be valid, this cooling time scale should be many times longer than the phonon relaxation time. So the fit would result in fundamental errors if the cooling delay time is not long enough. For example, the phonon relaxation time in silicon is around 100 ps, and the experimental delay time is often around several hundred picoseconds or 1-3 nanoseconds. We have indeed seen some reports in the literature that the extracted thermal conductivity is much smaller than its true thermal conductivity using such optical measurements. In this work, we set up the sub-picosecond pump-and-probe optical measurement facility, which would be a platform for future studies on the fundamentals of heat carriers. To explain the difference, a new two temperature model, the electron Fourier conduction and phonon Boltzmann transport model, is proposed to describe the energy transport process after ultrafast laser illumination on materials. The modeling results show the rationale and feasibility to extract the phonon reflectivity and relaxation time using the optical pump-and-probe measurement. In summary, this chapter reports the experimental setup, the modeling, and some preliminary experimental results with the data analysis still in progress.

6.1 Introduction

The availability of ultrafast lasers with picoseconds (ps) and femtosecond (fs) pulses has sparked considerable work in both fundamental and applied physics. There has been great interest in understanding the evolution of matter (primary solids, and more recently soft- and bio-materials) under highly nonequilibrium conditions induced by impulsive heating by a sub-ps laser pulse [1, 2]. The dynamics of the materials evolution, such as ultrafast phase transitions, thermal and non-thermal structural transformations and melting dynamics, under a high pulse intensity [3, 4, 5, 6], $\geq 10^{14}$ Wcm^{-2}, has been attracting significant attentions due to their immediate importance for the increasing application of ultrafast lasers in precision micromachining and materials processing [7, 8, 9]. Relatively low intensity experiments (~10Wcm^{-2}) have enabled substantial understanding of the electronic properties of solids exposed to nonequilibrium conditions and short time scales, mostly through time-resolved optical methods such as the pump-and-probe technique. A number of recent works have been done on the generation and propagation of coherent phonons using femtosecond lasers and thus probe their structure properties [10, 11]

In the optical pump and probe method, sub-ps time resolution is made possible by splitting the ultrafast laser with sub-ps pulse output into an intense heating pulse, i.e. a "pump" beam, and a weaker "probe" beam, and controlling the optical path length difference of the pump and probe beam through a mechanical delay stage. The length difference of the optical paths results in variable time delay between the pump and the probe beams. The pump beam is used to generate a temperature change at the sample surface. The decay of the temperature rise is measured by the reflected energy of the probe pulse series, where the probe takes a snapshot of the reflectance at a specific experimental time delay relative to the pump. When the reflectance is measured, the method is often called sub-ps transient thermoreflectance technique (TTR). If one is to measure the transmissivity change, the method is termed as sub-ps transient thermotransmission (TTT). The temporal resolution of the optical pump and probe method is on the order of the probe pulse duration. By localizing the energy deposition spatially and temporally, it is possible to monitor thermal changes in both the electron and phonon lattice systems with very high temporal resolution, thus allowing for observation of electron–phonon relaxation dynamics, interface thermal resistance, and thermal conductivity of nanostructures, especially superlattice and thin films [12,13,14, 15,16,17,18, 19, 20, 21, 22, 23, 24, 25].

Understanding the energy deposition and transport process in the material after ultrafast laser illumination is apparently of significant importance for both ultrafast laser applications in manufacturing and sensing abilities. As a general framework, it has been established that when a short laser pulse illuminates a sample, the electrons are driven into a highly nonequilibrium state different from the phonons or the lattice, since electrons absorb most of the photon energy. Within the electron subsystems, the timescale for energy exchange τ_{ee} is within 10^{-14} s. Thus electrons are in local thermal equilibrium and can be characterized by a single electron temperature value. Strongly coupled ions can also be described by a single temperature. The energy exchange between electrons and phonons (ions) is governed by the electron-phonon collisions. Although the electron-phonon collision time can be as short as electron-electron collision time, the energy transfer from the electrons to the lattice will last much longer than the thermalization time of electrons due to the large mass difference between electrons and phonons, typically of the order of a few to a few tens of picoseconds. This picture is well verified by experiments [12,13,14] and can be approximately described as a classical two-temperature nonequilibrium system, which was proposed by Ansimov [1]. Due to the relatively small electronic heat capacity, the electron temperature can be 2 to 3 orders of magnitude higher than that of lattice/phonons, sometimes even reaching several thousand of Kelvins above the equilibrium melting point. The thermalized electrons transport first ballistically and then diffusively while exchanging energy with phonons. The electron and phonon energy exchange is determined by the electron-phonon coupling factor. Lots of work has questioned whether the temperature concept can be used for the electron and phonon subsystems and whether the electron transport is diffusive at an ultrafast time scale. It has been well demonstrated that electron thermalization time in gold and in most of metals is faster than 10 fs [26,27], and thus the electron temperature concept should be valid when we are interested in time scales much larger than 10 fs. Attempts have been made to revise the heat diffusion model for electrons, including the use of hyperbolic heat conduction model for electrons [15, 28], electrohydrodynamics model, and the higher order or even full collision-integral solution of electron Boltzmann equation [29, 30]. The full solution of electron Boltzmann equation shows that the energy exchange between electrons and lattice can be well described by the two-temperature model, in spite of the nonequilibrium distribution function of the electron gas due to the ultrafast heating [30]. However, the energy exchange rate could be lower as demonstrated in experiment [31]. Very few works have looked into the phonon transport after ultrafast laser interaction [32, 33].

Naturally the initial investigations of ultrashort heating has mostly been performed on very thin metal layers, where minimizing of the electron heat diffusion is of practical interest, to measure the electron–phonon coupling factor for a variety of metals [12,13,14]. The scaling of nanoelectronic devices and the advent of optoelectronics is the primary driver for studying the electron-phonon coupling in semiconductor nanostructures in the past decade [34, 35]. The thermal transport experiment for measuring thermal diffusivity of thin films using an ultrafast pump and probe method was pioneered by Paddock and Eesley in 1986 [16, 17]. Several investigators have recently revisited this idea since the thermal properties of thin films and interface thermal resistance have become a topic of great interest to the nanoelectronics, optoelectronics and thermoelectrics communities. The most complete and systematic study on thermal interface resistance and thermal conductivity of nanostructures using sub-picoseconds optical pump and probe method was performed by Maris and co-workers [18,19,20,21]. Cahill built a system similar to Maris' and extended the study for thermal interface resistance for different materials combinations including solid-liquid interfaces [22, 36, 37, 38]. Reviews on current work on optical pump-and-probe method for thermal property measurement can be found in [23,24,25]

Figure 6.1 shows typical sample configurations for interface and thermal conductivity measurements using the ultrafast pump and probe method: (a) for measuring the thermal interface resistance and thermal conductivity of bulk substrate, (b) for measuring the thermal conductivity of thin film or superlattice nanostructures. A metallic layer with a thickness of ~10s nm is sputtered or evaporated on top of a thin film or a substrate for which we are interested in finding the thermal conductivity. Almost all ultrafast (sub–pico second and pico second) pump-and-probe measurements fitted the interface thermal resistance and thermal conductivity using the heat diffusion equation. There are a few problems with previously published models analyzing the experimental data. First of all, no one has looked into the detailed energy transport

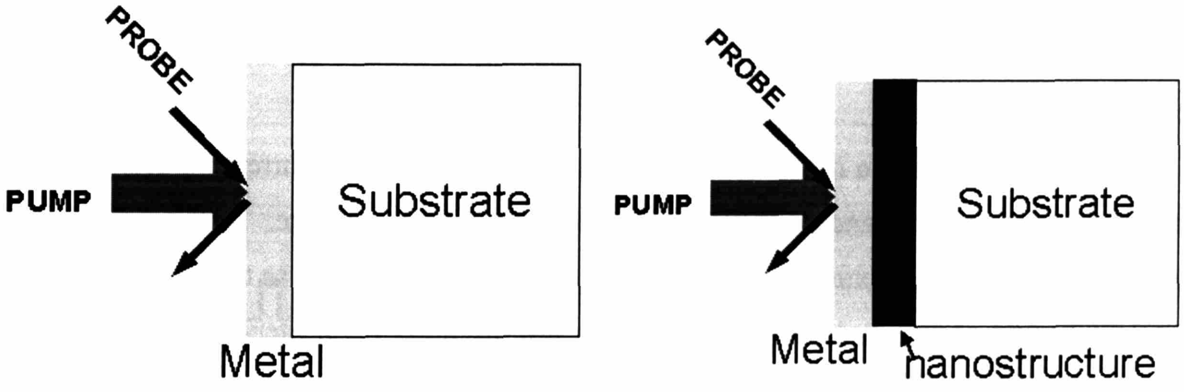

(a) (b)

Figure 6-1. Typical sample configurations for the ultrafast pump-probe method: (a) to measure the interface thermal resistance and the thermal conductivity of the substrate. (b) to measure the thermal conductivity of thin film and superlattice nanostructures.

processes in the metal. Most of the previous work neglected energy transport (thermal resistance) in the metal layer. Although the total thermal conductivity of a metal layer is usually ~100W/mK or above, the phonon or lattice thermal conductivity of the metal layer is often on the order of 5-10W/mK. A large temperature gradient can be built in the ultrashort time scale and thus the phonon transport dominates the thermal resistance for energy relaxation. The detail energy transport process might put the current data analysis technique in question. Secondly, all analysis so far is based on diffusion equations for both the film and the substrate. The criterion for the heat diffusion equation to be valid is that the time scale of interest should be many times longer than that of the carrier energy relaxation time. As stated earlier, the electron-electron energy relaxation time is often of the scale of tens of femtoseconds. Thus the conventional transport theory might be valid for electron energy transport. But the phonon relaxation time can be much longer than that of electrons. For example, in silicon the phonon relaxation time is a few hundred ps, so the data fitting would result in fundamental errors if the cooling time delay measurement is not long enough. Unfortunately, the experimental time delay is limited by the experimental setup itself, and is often on the order of nanoseconds. One reason is due to the repetition rate of femtosecond lasers. Most commonly used femtosecond laser systems have a pulse repetition rate of ~76 MHz which gives a time window of 13ns for detection. The other reason is that the travel distance associated with a long delay time would result in difficulty in overlapping the pump and probe beams on the sample. A 5 ns delay time corresponds to a round trip travel length of 75 cm for the probe beam.

The above discussion raises questions about the validity of the current models to extract the thermal boundary resistance and thermal conductivity of the substrate. At the same time, it suggests the possibility of extracting more fundamental parameters such as the phonon interface transmissivity and phonon relaxation time, which are the input parameters for nanoscale heat conduction models and simulators such as Monte Carlo simulations or phonon BTE and BDE solvers. The ability to characterize the phonon relaxation time and phonon reflectivity to the nanoscale transport characterization would be of similar importance as the thermal conductivity measurement is to bulk materials characterization today. Thus the task of this chapter is to establish a sub-ps pump-and-probe measurement system and to explore the possibility of using this measurement system as a new gateway to study nanoscale heat transfer problems by extracting the phonon relaxation time and phonon reflectivity at an interface. This chapter is organized as follows. Section 6.2 describes the ultrafast optical pump and probe system we built in the W.M. Roshenow Heat and Mass Transfer Lab. To better describe the energy transport process, section 6.3 proposes a new two temperature model, the electron Fourier conduction and phonon Boltzmann transport model, and studies the nonequilibrium electron-phonon transport under ultrafast laser illumination. The modeling results demonstrate the possibility of extracting the phonon relaxation time and the phonon reflectivity at an interface using the sub-ps pump-and-probe method. Section 6.4 reports some of the preliminary experimental results and the work in progress to improve our experimental system and to analyze the experimental results.

6.2 Pump-and-probe Experimental Setup and Data Acquisition.

Figure 6-2 is a schematic diagram of the pump–and-probe experimental setup constructed in the W.M. Rohsenow Heat and Mass Transfer Lab with the photo of the experimental system shown in Figure 6-3. The pulses from a Spectra-Physics Titanium:sapphire (Ti:Al_2O_3) Tsunami laser are generated at a 76 MHz repetition rate with a full width at half maximum FWHM of ~100 fs and are separated into two beams by a nonpolarizing beam splitter with an intensity ratio of ~ 9:1. The Ti:Sapphire laser is pumped by a 8W Spectra-Phsyics solid state laser and can be tuned to produce pulses through a range of photon wavelength from 800 nm to 1015 nm. The

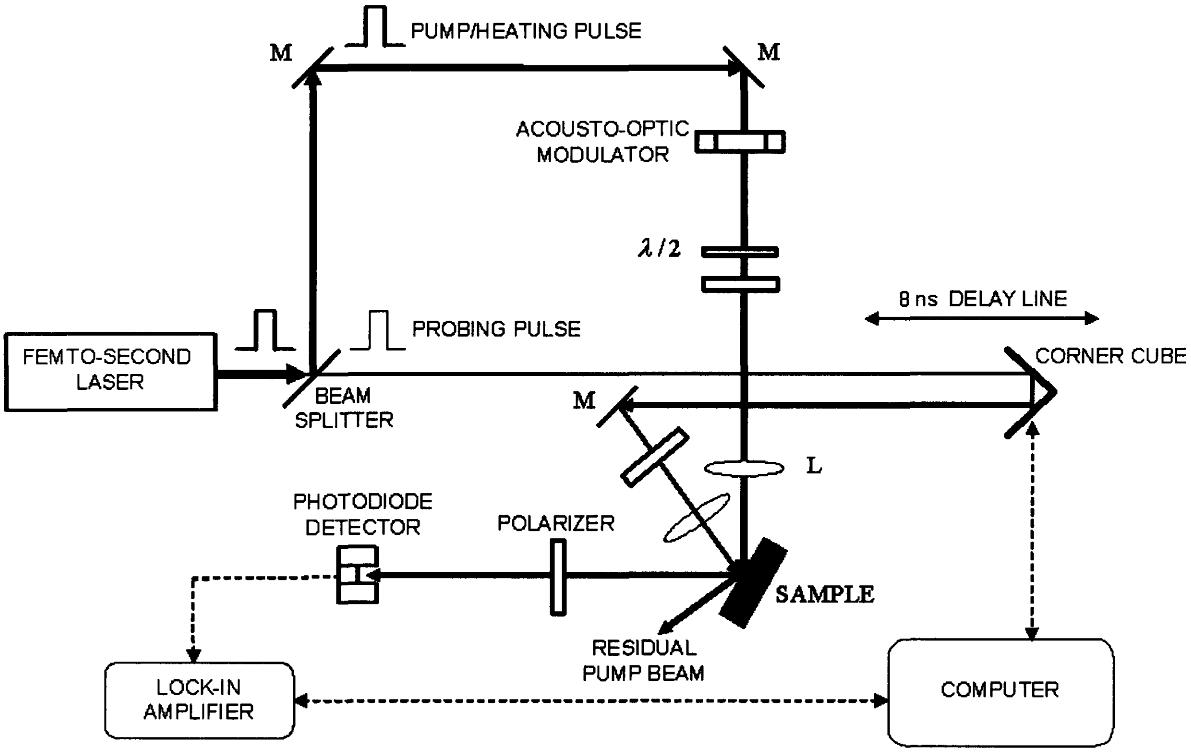

Figure 6-2. A schematic diagram of the pump-and-probe experimental setup constructed in the W.M. Rohsenow Heat and Mass Transfer Lab.

intense pump beam ~5 nJ/pulse is used as a heating source while the lower power probe beam is used to monitor the change of the reflectivity of the sample due to the ultrafast laser pumping of the material.

The pump beam passes through an acousto-optic modulator (AOM), creating a modulated pulse train at a prescribed frequency of 1 MHz regulated by a HP function generator. The pump beam reaching the sample surface creates the modulated heating required for transient thermoreflectance detection. After the AOM, the pump beam passes through a half waveplate and a polarizer. The polarizer is to control the polarization of the pump beam to be orthogonal to that of the probe beam's polarization and thus to aid in filtering of the scattered pump beam from the sample surface. The waveplate is to control the pumping power intensity. The pump beam is then focused down to a diameter of ~30 um at the sample surface. The pump beam is incident close to the normal direction upon the sample surface while the probe beam is incident at an angle of ~30° from the normal direction to the sample surface to minimize the scattered pump light to the detector. The energy deposited within the penetration depth of the sample creates the temperature rise that the probe beam monitors.

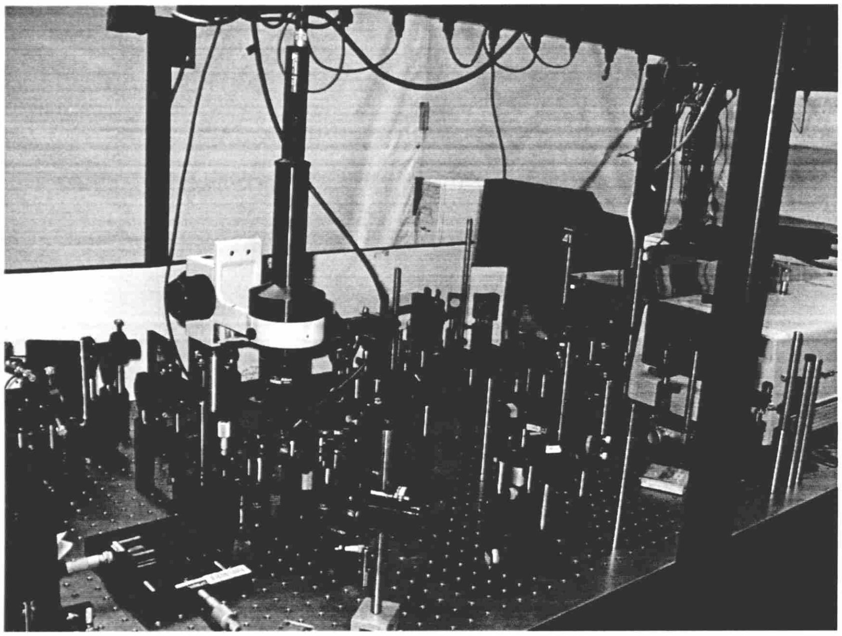

(a)

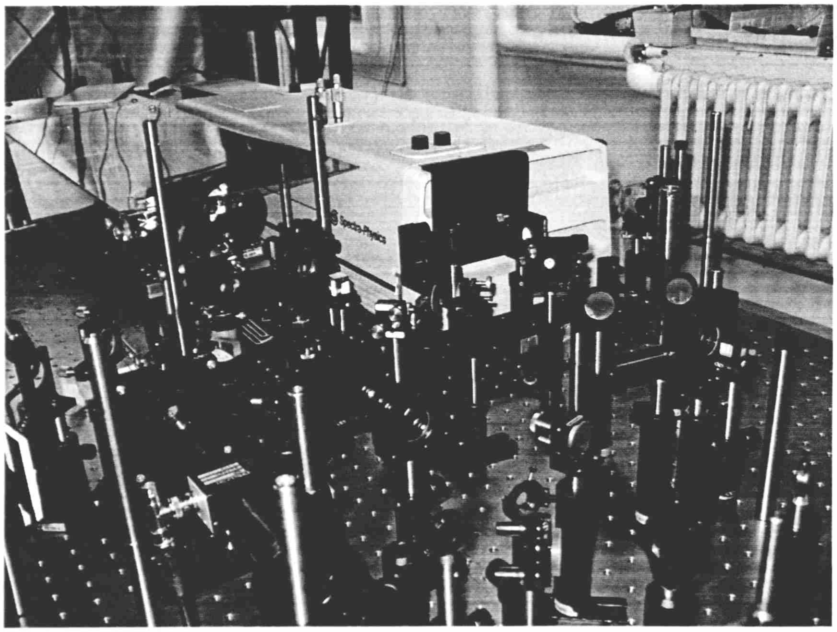

(b)

Figure 6-3. Photos of the sub-picoseconds pump-and-probe experimental system housing in the Rohsenow Heat and Mass Transfer Lab.

The probe beam passes through a retroreflector mounted on a delay stage, which has a step resolution of 1μm, used to vary the optical path length, allowing for measurement of the transient change in reflectance of the sample with a resolution on the order of the probe pulse duration, ~100 fs. The retroreflector directs the beam back at 180° from that of the input beam. As the stage is moved, the time at which the probe pulse hits the sample surface can be altered so that the probe pulses arrive at the sample surface before, during or after the arrival of the pump pulses. As the optical path length of the probe increases, an experimental time delay is created between the arrival of the pump and probe pulses. In practice, we used two retroreflectors on the delay stage and thus the light has two round trips on the stage as shown in Fig. 6-3, which results in a total of ~8 ns time delay using a 60cm delay stage. The probe beam is focused to ~ 20 μm at near 30° incidence in the center of the heated region by the pumping beam, assuring that the probe beam lies entirely within the heated region. The reflected probe beam is re-collimated using an identical lens and passes through an iris that helps block out scattered light from the pump beam. A polarizer with same polarization as the input probe beam but normal to the pumping beam is positioned before the detector to reduce the effect of the scattered pump light. Since the pump beam is modulated at 1 MHz, the photocurrent created by the detector is sent into the lock-in amplifier, which is also tuned to monitor the signal modulations at 1 MHz. A lock-in amplifier determines the magnitude and phase of the voltage signal at the modulation frequency of the AOM, say 1MHz.

Figure 6-4 helps to describe the signal detection mechanisms, especially the role of the photodiode and the lock-in amplifier (after Qiu [39]). The ~100fs heating pulses with a separation of 13 ns (at a pulse repetition rate of 76MHz but modulated at 1MHz by AOM), shown in Fig. 6-4 (a), are incident on the surface of the sample and create a temperature rise with each pulse as seen in Fig. 6-4(b). The period where there are no heating pulses results in a relaxation back to the initial temperature, T_0. The corresponding change in reflectivity of the sample is shown in Fig. 6-4(c). Assuming that the reflectivity is a linear function of temperature, the reflectivity will have same shape as the temperature profile. Fig. 6-4 (d) represents the probe beam intensity before reflecting off of the sample. After refection, the intensity of the probe is modulated according to the temperature of the sample surface as depicted in Fig. 6-4 (e). The probe photodiode has a rise time of ~ 30 ps, and therefore it sees the incoming pulses, of width 100 fs, as a smeared out pulse on the order of a few tens of picoseconds, as depicted in Fig. 6-4 (f). The photocurrent generated by the photodiode is passed through a band pass filter that selects only the phenomena occurring in a narrow band around 1 MHz. The resulting signal is a sine-like wave with an amplitude on the order of a few micro Volts, as shown in Fig. 6-4 (g). Figures 6-4 (a through g) represent the signal when the stage is positioned at one point shown in Fig. 6-4 (h). A typical temporal measurement curve which is also often called a cooling curve shown in Fig. 6-5 is constructed by moving the stage a small step which corresponding to a changing delay and measuring the amplitude and phase of the sine wave at that point by a lock-in amplifier.

A LabView® program has been developed to control the motion of the retroreflectors mounted on the delay stage and for data acquisition. The delay stage motion must be accurately coordinated with the recorded photodiode signal and laser power. The program works in a leap-frog fashion. First, a message is sent to the stage controller to begin the motion of the stage. Then, the program records a data point from the output (voltage and phase) of the lock-in amplifier. Movement of the delay stage corresponds to an experimental measurement in time, with an associated minimum time increment referred to as the ''time constant.'' This time constant is directly related to the velocity of the delay stage and is also limited by the delay in real time between acquiring data points. The effective time constant of the program between lock-in data points is 400 ms. The time constant of the lock-in amplifier was sent to sample the photocurrent of the photodiode every 100 ms. This sampling rate was found to be the optimum for the setup. Decreasing the time constant resulted in no change in the temporal profile of the scan, only more noise. Increasing the time constant too much resulted in data that did not accurately represent the cooling curve.

The delay stage can be moved in 1 micron intervals with a total travel of 60 cm. Since the beam is folded twice (two rounds) on the stage, a 1 micron displacement of the retroreflector in the stage results in a 13.3 fs time delay, and the maximum delay time is 8 ns. Apparently the temporal resolution is not limited by the delay stage but ultimately by the laser pulse itself, on the order of ~100 fs. The program allows the user to prescribe different time scale and resolution combinations for any particular measurement. This ensured the best temporal resolution possible of ~ 100 fs for fast transient just tens picoseconds after ultrafast laser interaction and fast scan to study slower phenomena happening on a longer time scale. A typical scan for an ~ 8ns delayed cooling curve takes approximately 20 minutes. Both the magnitude and phase of the signal measured by the lock-in amplifier are recorded at each experimental time step.

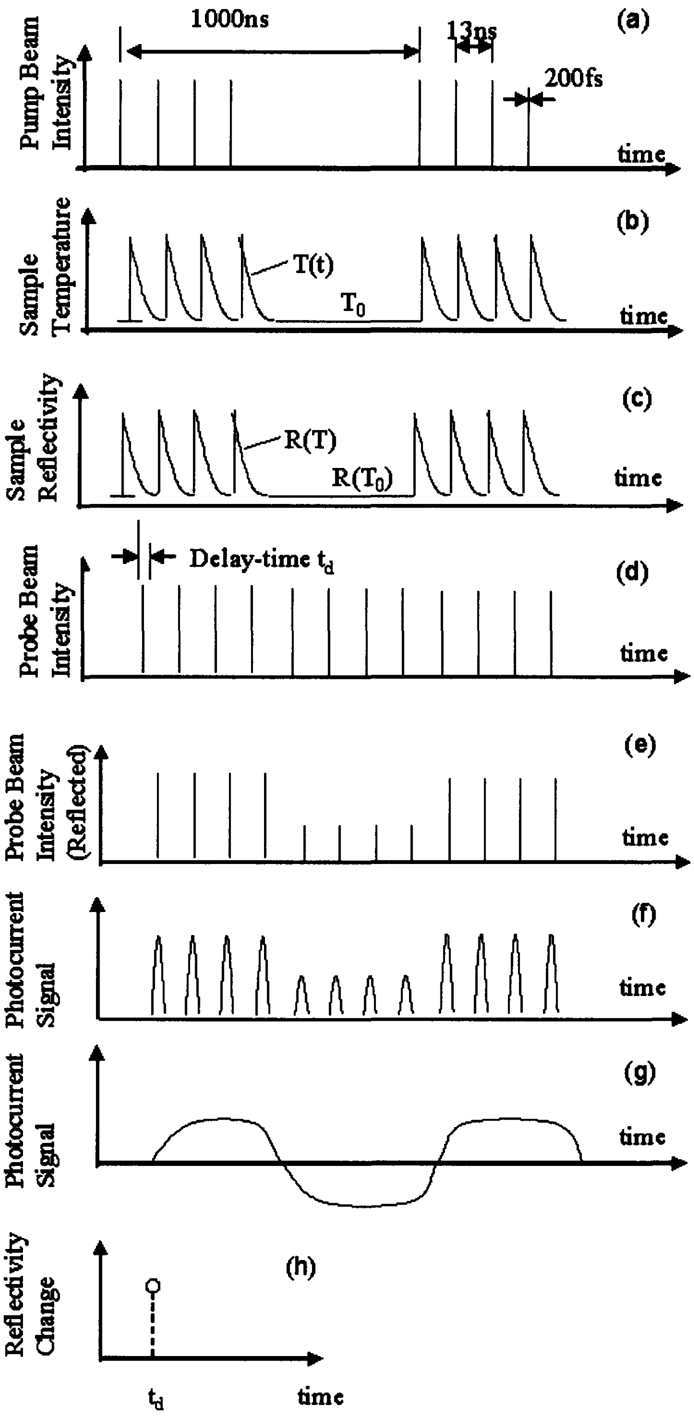

Figure 6-4. The signal detection mechanisms of the sub-ps pump-and-probe measurement.

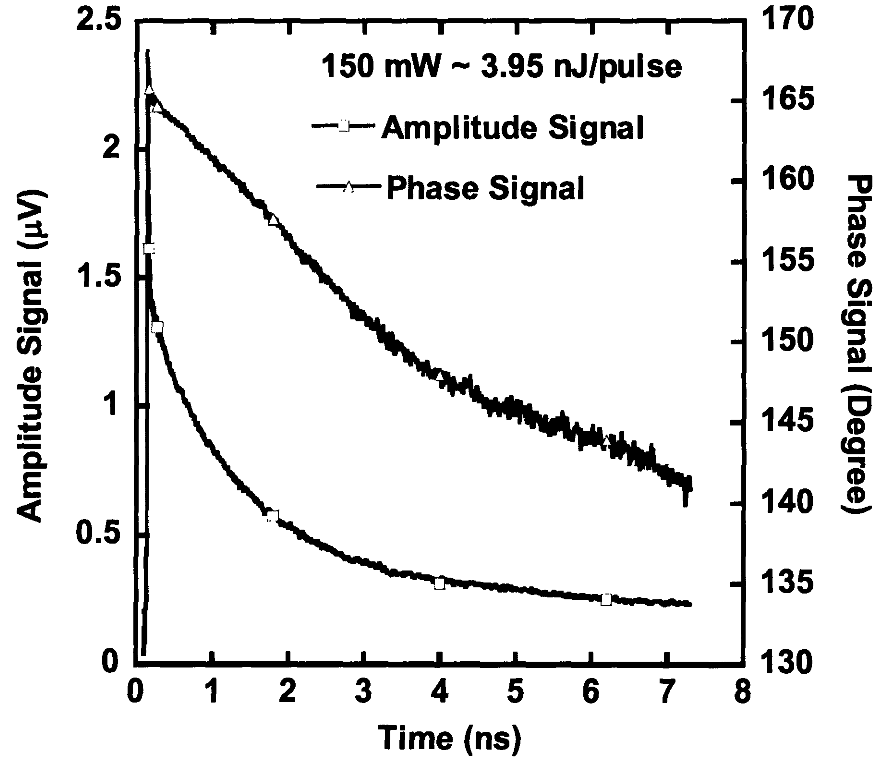

Figure 6-5. A typical temporal measurement curve which is constructed by moving the stage a small step and then measuring the amplitude and phase of the sine wave at that point, as described in Fig. 6-4.

6.3 Model Development

After the classical two temperature model [1], there are a variety of papers arguing that the electron would not follow simple heat diffusion theory [15,28,30,31]. Ideally one should solve the coupled electron and phonon Boltzmann transport equation to study the ultrafast transport process in laser-material interaction. However, replacing the Fourier heat conduction equation with the hyperbolic equation for electrons indeed does not give too much difference for the temperature prediction after ultrafast laser illumination on solids [39]. In addition, the recent solution of the Boltzmann equation seems to confirm that the Fourier law for heat conduction captures well the electron behavior but with temperature dependent electron properties [29, 30]. This is mainly due to the short mean free path of electrons, for example, which is around a few nanometers at room temperature. However it usually takes a much longer time for phonons to relax to their equilibrium state. The phonon relaxation time of semiconductors underneath the metal layer shown in Fig. 6-1 is usually much longer than the electron relaxation time. For example, it can be several 100ps in silicon. When the time scale is smaller than the phonon relaxation time, the phonon transport can be very different from the prediction by the Fourier law [40, 41]. The thermal conductivity prediction at high frequency can be much lower than that at low frequency. Volz [41] termed this phenomenon as thermal insulation at high frequencies. Thus we propose a coupled electron Fourier conduction – phonon Boltzmann transport model to describe the heat transfer in the model system shown in Fig. 6-6, essentially the same as Figure 6.1, under ultrafast laser heating. The idea is that phonon transport is under highly nonequilibrium condition while electron transport is close to local equilibrium and can be described by Fourier heat conduction theory with temperature dependent thermal properties.

An interesting point is that electrons dominate heat conduction in metals, whereas phonons dominate that in semiconductors and insulators. Hence, for heat transport to occur across metal–nonmetal interfaces, energy transfer must occur between electrons and phonons. This is a very fundamental problem that needs to be explored both theoretically and experimentally for understanding the interface phenomena [42]. There are two possible pathways, namely: (1) coupling between electrons of the metal and phonons of the nonmetal through anharmonic interactions at the metal–nonmetal interface [43,44], and (2) coupling between electrons and phonons within the metal, and then subsequently coupling between phonons of the metal and phonons of the nonmetal [42]. In this work, we assume that the energy coupling between a metal and a semiconductor is primary through phonon-phonon coupling.

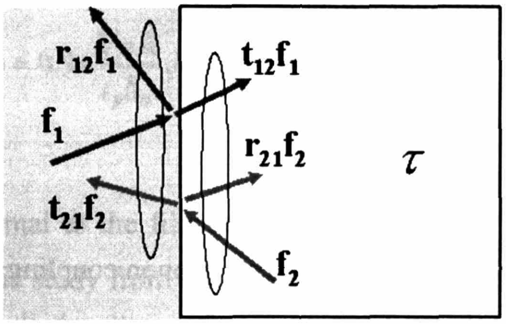

Figure 6-6. The fundamental transport process across a metal-semiconductor interface and the idea of the newly proposed model is to extract the interface phonon reflectivity and phonon relaxation time (τ) by fitting the experimental data of the pump-probe measurement rather than fitting the interface thermal resistance and the thermal conductivity of the substrate.

On the metal side, the photon energy is deposited in the electron subsystem and the electrons establish an equilibrium temperature T_e. Electrons relax their nonequilibrium energy through both the electron diffusive conduction and the relaxation of their energy to the phonon subsystem. Similar to Eq. (5-3), we can write the governing equation for the electron subsystem as,

$$\rho c_e \frac{dT_e}{dt} = \nabla(k_e \nabla T_e) - G(T_e - T_p) + S(\mathbf{r},t) \tag{6-1}$$

where $S(\mathbf{r},t)$ is the energy deposition rate from laser heating. We used the temperature dependent thermal properties for electron subsystems in metals since the electron temperature rise can be several hundred Kelvin (K) or larger under ultrafast laser interaction due to its low heat capacity. The temperature dependent properties can be found in Kittel [45]. The electron heat capacity is linearly related to the electron temperature as $c_e = c_e' T_e$, where c_e' is the electron heat capacity constant. The thermal conductivity depends on the ratio of the electron and lattice temperatures as $k_e = k_{eq}(T_L)T_e / T_L$, where $k_{eq}(T_L)$ is the equilibrium thermal conductivity at a lattice temperature T_L. The linear relationships for the heat capacity and electron thermal conductivity are valid for $T_e < T_F$, where T_F is the Fermi temperature.

Depending on the relaxation time of the phonons, the phonon subsystem might experience diffusive or ballistic transport. The transport equation can be described by the phonon BTE under relaxation time approximation as discussed in chapter 2,

$$\frac{\partial f}{\partial t} + \mathbf{v}_m \bullet \nabla_{\mathbf{r}} f = -\frac{f - f_{om}}{\tau_m} + f_g \tag{6-2}$$

where f_g is the phonon source term due to electron-phonon coupling and the subscript m denotes metal properties. Due to the short phonon mean free path which corresponds to a very short phonon relaxation time in metals [46], Eq. (6-2) can be written as a phonon thermal diffusion equation when necessary.

Equations (6-1) and (6-2) are the governing transport equations for the electron and phonon subsystems systems, respectively, and are coupled by the electron–phonon energy coupling factor, *G*. The electron-phonon coupling factor *G* is constant for small temperature changes above the Debye temperature. We note that the electron-phonon coupling factor G is usually measured or derived under the assumption that the phonon subsystem is in equilibrium. In our case, although we write a phonon Boltzmann equation for the phonon system, we expect phonon transport in a metal to be more diffusive-like. In addition, the temperature rise in the lattice temperature is usually only a few K, and thus we expect that nonequilibrium phonon transport will not significantly affect the electron-phonon coupling factor G.

On the semiconductor side, heat is primary transported by phonons. The transport is described by the phonon Boltzmann equation under the relaxation time approximation.

$$\frac{\partial f}{\partial t} + \mathbf{v}_s \bullet \nabla_{\mathbf{r}} f = -\frac{f - f_{os}}{\tau_s} \tag{6-3}$$

where the subscript s denotes the semiconductor properties.

Due to the slow speed of phonons in the semiconductor comparing to a much faster electron Fermi velocity in a metal and a larger pump spot size (~ 30 microns) compared to the phonon travel distance of a few microns within a few nanoseconds, one dimensional transport across the metal-semiconductor interface would be a reasonably good approximation.

The heat source term $S(\mathbf{r},t)$ representing a Gaussian temporal pulse shape with constant optical properties in Eq. (6-1) can be written as [47]

$$S(x,t) = 0.94\frac{1-R}{t_p \delta_\alpha} J \exp\left[-\frac{x}{\delta_\alpha} - 2.77\left(\frac{t}{t_p}\right)^2\right] \tag{6-4}$$

where x is the direction normal to the film surface, J is the laser fluence, t_p is the laser pulse width which is ~100 fs in this study from the Ti:Sapphire femtosecond laser system output, R is the reflectance of the film, and δ_α is the optical penetration depth. Changes in R are generally less than 0.1% for nonequilibrium heating, so for the purposes of modeling, R is taken to be constant in the source term.

Equations (6-1) to (6-4) complete the newly proposed electron Fourier conduction – phonon Boltzmann transport model for studying the ultrafast laser-material interaction when facilitated with appropriate initial and boundary conditions.

At the initial stage before the laser pulse arrives, we assume that both electrons and phonons in the metal and phonons in the semiconductor are maintained at an initial temperature T_0. At both x=0 and x=d, the adiabatic boundary condition is assumed for electrons. It is a reasonable boundary condition for electrons at x=d when the electron concentration is low in a semiconductor and where electrons on the metal side are confined due to the Schottky barrier, and the electron energy can be coupled from the metal to the semiconductor through electrons only. How much is the electron heat coupled to the environment at such a short time scale through both radiation and convection remains a question to explore? A widely accepted assumption is that the electron system is adiabatic at the front surface since the time scale of interest is very short, on the nanosecond scale. The phonon system is also assumed to be adiabatic at the front surface x=0 and at a constant temperature T_0 far inside the semiconductor.

Before moving on to the simulation results of the newly proposed model denoted as a nonequilibrium BTE model ("Non_Eq BTE" in the figures) in the rest of this chapter, I would like to emphasize the hierarchical relation between the new model and the classical heat diffusion models used for pump-and-probe experiments. Depending on which properties are targeted to be measured, the past works have been using two sets of models, as shown in Figure 6-7. One set of the model is the conventional two temperature models which assume that electrons and phonons are in nonequilibrium and phonons are in nonequilibrium and the phonon/lattice thermal transport is diffusive. This set of models is to be denoted as the nonequilibrium Fourier model ("Non_Eq Fourier" in the figures) in the rest of this chapter. If not considering the effect of substrate, the model consists simply of the first two equations in the model system. This model is often used to fit the nonequilibrium electron-phonon coupling factor G from experiments. The scanning time for the pump-and-probe method is often in the range of a few ps to tens of ps (short scan mode) since the electron-phonon thermalization time is on this order of magnitude. The other set of models is often used to fit the interface thermal resistance and the thermal conductivity of the layer underneath the metal layer, as done by Maris and co-workers [18,19,20,21,50], Cahill and co-workers [22,23], and Norris [25, 48]. This model is referred to as the Fourier model with lumped thermal mass (simply denoted as "Fourier" in

Figures) in the rest of this chapter. In this model, the whole metal layer is lumped into a thermal mass and assumed to be at one temperature and the heat is transported through the interface and then diffused into the layer underneath. In this case, the temperature cooling curve is often measured for more than 100ps to a few nanoseconds (long scan mode). Apparently both sets of models often used are heat diffusion models and are just subsets of the newly proposed model. In fact, there are very few works considering the effect of the substrate on the two temperature model.

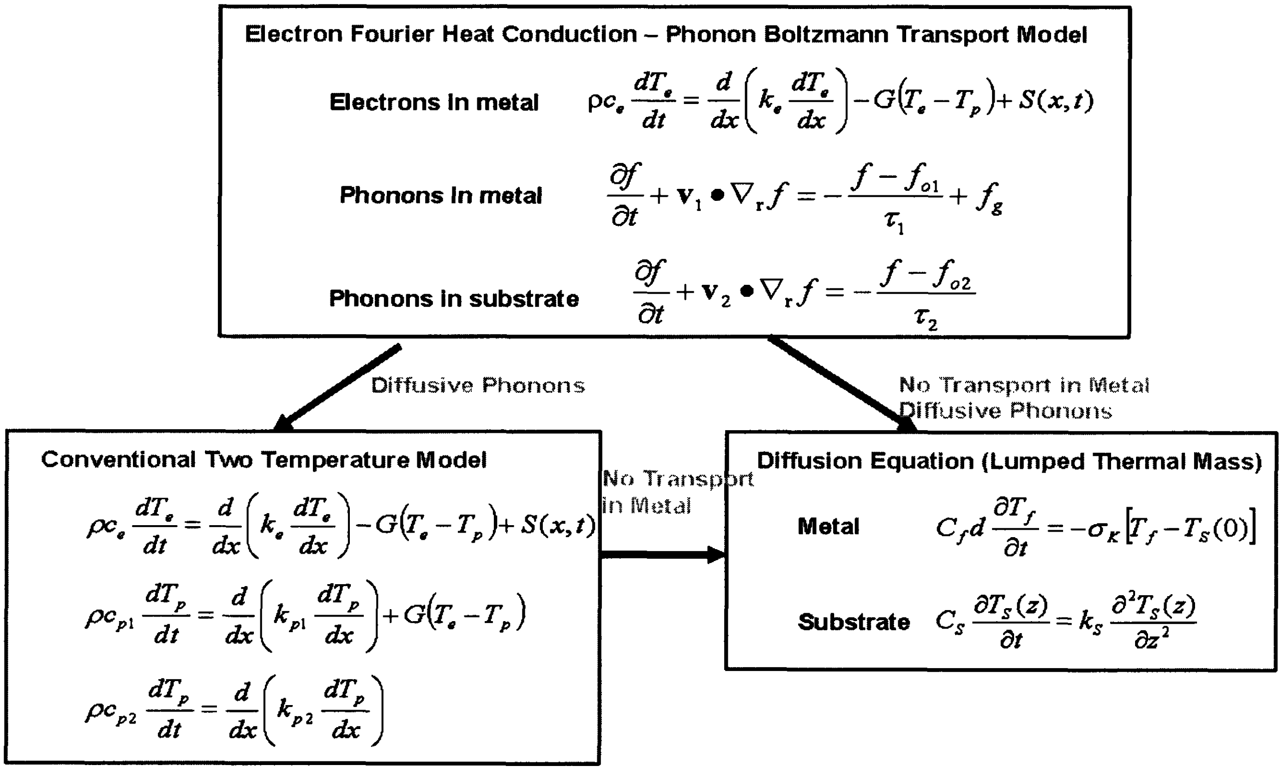

Figure 6-7. Model hierarchy for the description of the energy transport processes for ultrafast laser-material interactions. The conventional two temperature model which assumes that the electrons and phonons are in nonequilibrium and the phonon/lattice thermal transport is diffusive. This model is often used to fit the nonequilibrium electron-phonon coupling factor G from experiments. The other set of models that are often used to fit the interface thermal resistance and the thermal conductivity of the layer underneath the metal layer assumes that the metal layer is a lumped thermal mass. Both the conventional heat diffusion models are subsets of the newly proposed electron Fourier heat conduction and phonon Boltzmann transport model.

Now let's show the rationale whether we are able to extract the phonon relaxation time and the phonon reflectivity at an interface from the experimental system we are building and the experiments we are conducting. Most of the earlier work used a heat diffusion model to fit the experiments to get the interface thermal resistance and thermal conductivity of the layer underneath the metal layer, where there are two unknowns used to fit the experiment data after cooling for 50 ps to a few nanoseconds assuming that electrons and phonons are in equilibrium with each other after tens of picoseconds. Ideally, we would be able to optimally fit all the three parameters, electron-phonon coupling factor, phonon interface reflectivity, and phonon relaxation time in the substrate of our newly proposed electron Fourier conduction - phonon Boltzmann transport model from one temperature cooling curve starting from 0 ps (right after the laser heating). In practice, we can fit the parameters in two steps using the newly proposed model; the first step is to fit the electron-phonon coupling factor G for short scans (less than 50ps) where the effect of thermal transport through the interface and the substrate on the nonequilibrium process is negligible. Then by knowing G, we can fit the remaining two, the phonon reflectivity at an interface and the phonon relaxation time, using the newly proposed model in a similar fashion as done for the thermal conductivity and interface thermal resistance fitting using the heat diffusion models. As discussed earlier, the idea here is that the Boltzmann equation based model is valid at any time scale as short as picoseconds. Thus the fit for the fundamental transport properties (phonon reflectivity and relaxation time) should be much more accurate than usingthe heat diffusion equation for the interface thermal resistance and thermal conductivity where the scan time should be many times longer than the phonon mean free path for the heat diffusion equation to be valid and experiments sometimes can not afford such luxuriates. In addition, if we can extract the phonon relaxation time, we would be able to accurately recast the steady state thermal conductivity using a short time scale measurement. This is analogous to using the short scale MD simulation to extract bulk properties [49].

Before moving on to the experimental results, I would like to show some comparisons between these models and to emphasize the rationale of using the proposed model to fit the phonon reflectivity at an interface and the phonon relaxation time of the substrate. The model simulation is constructed for aluminum (Al) on a silicon (Si) sample, similar as the schematic shown in Fig. 6-6. As discussed earlier, we assume that energy coupling between metals and semiconductors is primarily through phonons. The phonon transmissivity is the parameter we need to fit from the experiments. To show the rationale, we used the diffuse mismatch model (DMM) for phonon transmissivity across metal–nonmetal interfaces in model calculations. Similarly DMM model has been applied to explain the metal and non-metal interface thermal resistance by Maris [50], Costescu et al [22], Majumdar and Reddy [42], and more recently Stevenson et al [48]. Thus we would expect the transmissivity used in the calculation could be reasonably close to the experiment results. The details of the diffuse mismatch model for phonon transport across an interface and finding the interface thermal resistance from the transmissivity for heat diffusion theory have been described in chapter 3.

Figure 6-8 shows the electron and phonon temperature rise at the front surface of the metal layer. For nonequilibrium models (Non_Eq Fourier and Non_Eq BTE), the temperature shown is the front surface temperature of the metal layer (the surface facing the incidence laser beam). T_m is the lumped average temperature of the metal layer for the Fourier model using a lumped surface layer. T_m is lower than the nonequilibrium front surface temperature since the lumped model assumes that the energy is immediately distributed over the whole metal layer, a superfast process. We can clearly see the nonequilibrium temperature distribution between electrons and phonons at a time scale of a few tens of ps as shown in Fig. 6-8(a). This timescale is much longer than the electron-phonon thermalization time if estimated simply from $\tau = c_e / G$ ~ 0.1ps for aluminum. In addition, we find that the difference between the nonequilibrium Fourier model and the nonequilibrium BTE model is negligible during this period. At longer times shown in Fig. 6-8(b) and (c), the temperature difference between the electrons and phonons is negligible although some temperature differences will always exist, since phonons are the only way to have cross-talk with the substrate. However the difference between the BTE and Fourier model becomes larger. The cooling process is slower for the nonequilibrium BTE model which results in a higher temporal temperature since the phonon transport is ballistic during the first few 100 picoseconds.

For accurate characterization of the temperature for a pump-and-probe measurement, one needs to establish a very accurate temperature – reflectance relation, which could be difficult to do especially when the laser – material interaction is nonequilibrium heating. Thus the absolute temperature rise is usually not used and the normalized signal is often used for the fitting procedure. The procedure is to find an optimized global fit to the whole temporal measurement of the reflectivity change curve (the cooling curve). To fit for thermal interface resistance and

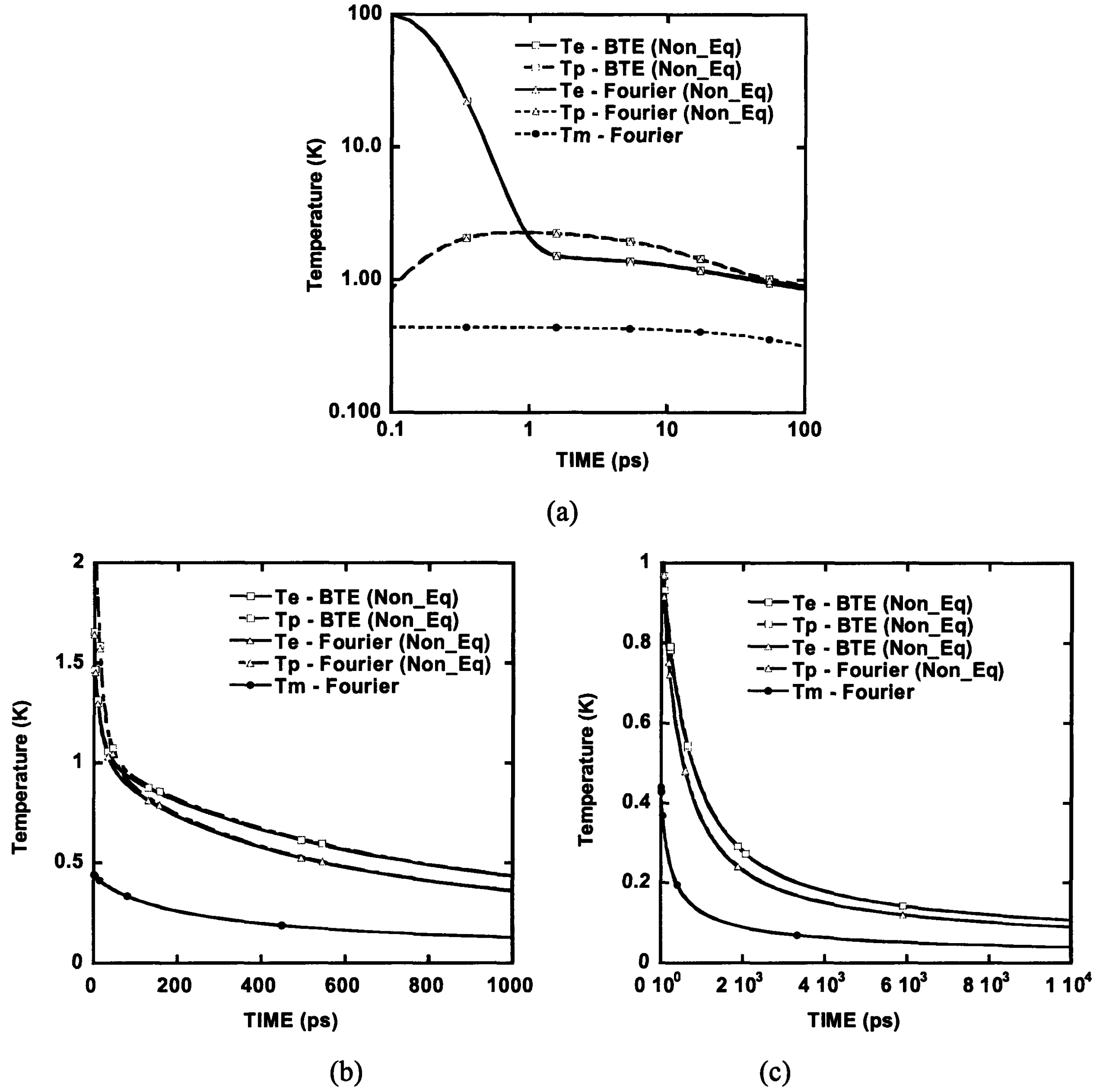

(a)

(b) (c)

Figure 6-8. The electron and phonon temperatures rise after femtoscond laser heating. For the nonequilibrium models, the temperature shown is the front surface temperature. Tm is the lumped average temperature of the metal layer for the lumped model often used for the thermal interface resistance measurement. (a) The electrons and phonons are in nonequilbrium conditions at a short time scale, ~ tens of ps, but the difference of the nonequilbrium Fourier model and the nonequilbrium BTE model is negligible. (b)&(c), the difference between the electron and phonon temperatures at the front surface at large timescales is negligible. The difference between the nonequilibrium Fourier model and the nonequilbrium BTE model clearly shows a much slower phonon ballistic transport process.

the thermal conductivity of the layer underneath, one usually uses the normalized signal after 50ps, which is assumed to be longer than the electron-phonon thermalization time, and thus having a minimal effect from the nonequilibrium electron-phonon heating. We expect that the phonon reflectivity and phonon relaxation time can be similarly fitted. Thus Figure 6-9(a) shows that the normalized temperature decay curve using different models from 50ps to 2000ps after femtoscond laser pumping, which is often the temporal range of the pump-and-probe experiment, where the temperature rise is normalized to that at 50ps. Compared to heat diffusion models, the temperature decays much slower for the nonequilibrium BTE model which would result in a much smaller thermal conductivity and larger thermal interface resistance if one is trying to fit the phonon BTE results with the Fourier results. Again this is expected. Figure 6-9(b) shows the temporal temperature decay normalized to the temperature at 1 ns. Here we find that the nonequilibrium Fourier results agrees very well with the nonequilibrium BTE results for long-time decay curve (cooling curve). This is because after many relaxation times, the transient Fourier transport becomes valid. The normalized temperature decay curve of the Fourier model with lumped thermal mass does not agree with the nonequilibrium models since in the beginning the lumped model neglects the thermal resistance in the metal that should be considered, a neglect of the thermal resistance results in too fast a process in the beginning.

Figure 6-10(a) shows the transient temperature distribution at different time scales (cooling process) at the interface region. At t = 0.7 ps, the electrons have a much higher temperature than the phonons. At t = 7 ps, the average electron and phonon temperatures are close to equilibrium in the metal layer. But at the front surface the phonon temperature can be higher than the electron temperature. This is because the the electron temperature is redistributed to equilibrium very quickly due to its high electron thermal conductivity. But the thermal energy is extracted by the phonons to the substrate, the phonons in the metal layer must establish a temperature gradient to conduct the heat through the interface and out to the semiconductor substrate. At a larger time scale, electron and phonon temperature is very close but the phonon temperature is still a little higher than the electron temperature at the front surface to establish the energy relaxation process. Figure 6-10(b) shows the normalized phonon temperature distribution close to the interface region, which is normalized to the front phonon temperature at that time instant. This figure shows the relative contribution of the thermal resistance in the metal layer and the interface thermal resistance to the overall thermal resistance for the energy relaxation from the metal surface deeply into the semiconductor interface. Apparently in the beginning stage, the dominant thermal resistance is in the metal layer and in the interface thermal resistance (<0.5-1ns) since the phonon thermal conductivity is only 5 W/m K and the phonon-phonon coupling is the only mechanism for energy relaxation through the interface even though the total thermal conductivity of the metal layer can be 200-300 W/m K. It also shows that the thermal resistance of the metal layer plays an important role even after 5 ns. This is again due to the low thermal conductivity of the phonon system although the electron temperature has already been re-distributed into equilibrium after a few tens of picoseconds.

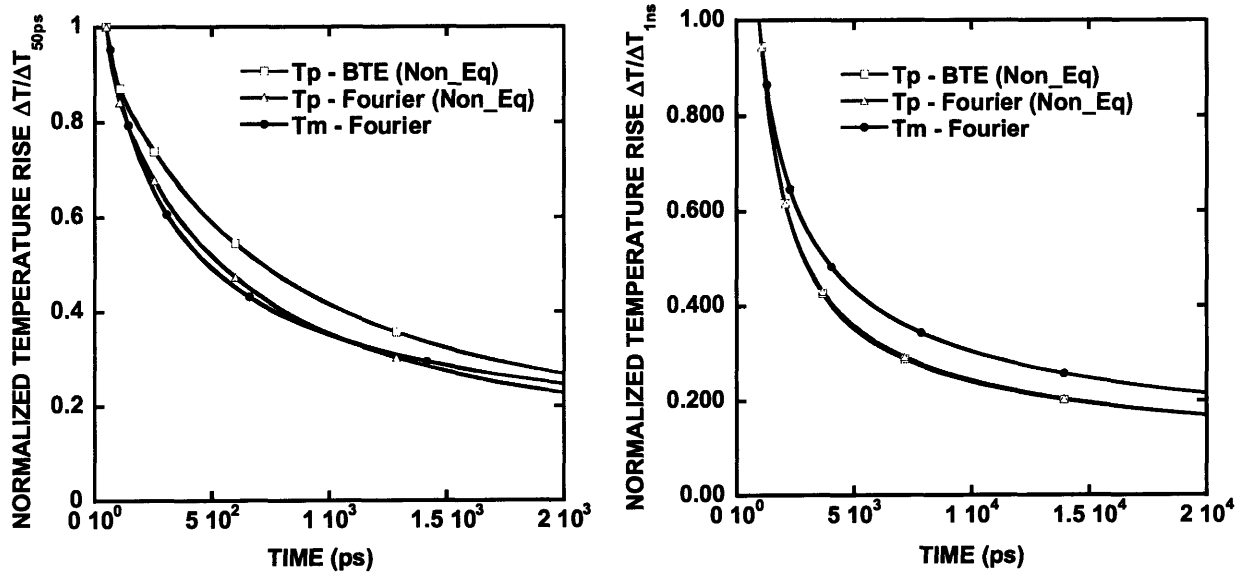

(a) (b)

Figure 6-9. The normalized temporal cooling curve. (a) The normalized temperature decay curve is different for the heat diffusion model and the nonequilibrium BTE model from 50ps to 2000ps, which is often the range of the pump-probe experiment. The temperature decays much more slowly for the phonon BTE model which would result in a much smaller thermal conductivity and a larger thermal interface resistance if one is trying to fit the phonon BTE results with the Fourier results. (b) If one fits the results with normalization to 1 ns and uses a much longer decay curve, say 10ns, one would find that the nonequilibrium Fourier results agrees very well with the nonequilibrium BTE results.

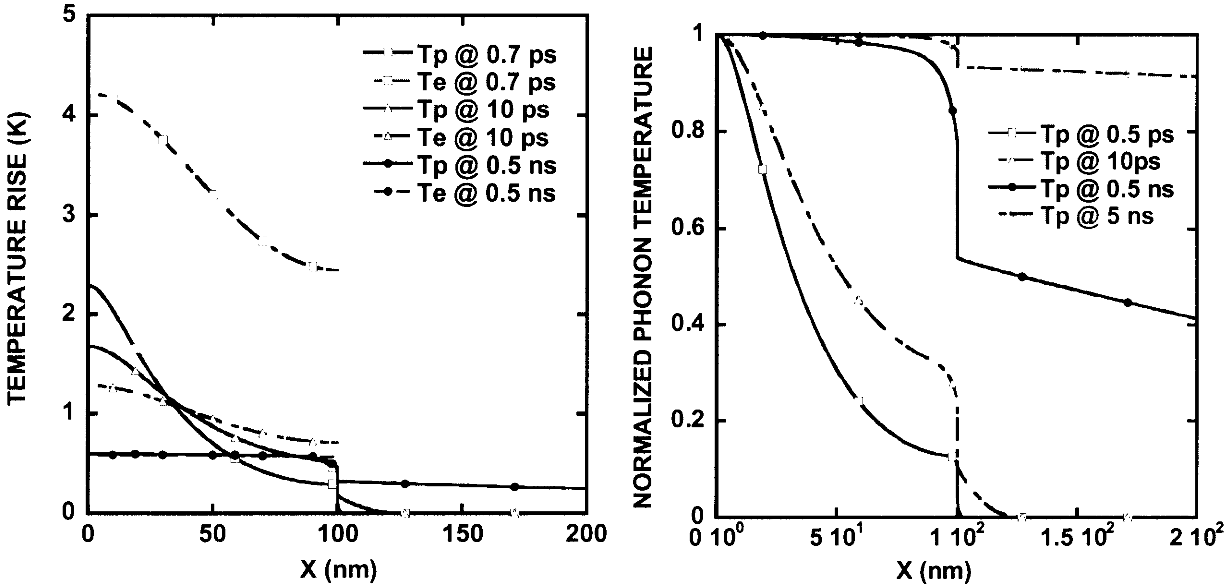

(a) (b)

Figure 6-10. (a) The distributions of the temperature rise close to the interface region at various transients. (b) The distributions of the normalized temperature distribution close to the interface regime. This figure shows the relative contribution of the thermal resistance in the metal layer and the interface thermal resistance to the overall thermal resistance for the energy relaxation from the metal surface deeply into the semiconductor interface.

The modeling results above clearly show that the transient energy transport process is different from the prediction of the heat diffusion theory since the heat diffusion theory is valid only after the time of interest is many times of the phonon relaxation time. This also shows the need and promise to extract phonon relaxation time and phonon reflectivity at an interface, which are the most fundamental properties for energy transport at the nanoscale. The modeling also shows that the phonon transport in the metal can be a dominant slow process for energy relaxation through metal-semiconductor interfaces.

6.4 Preliminary Experimental Results and Discussions

The experimental setup has been tested and is being used to characterize the phonon transport at the nanoscale. Here I would like to show some of the preliminary results for Al on a Si sample. Figure 6-11 shows the raw amplitude and phase signal of the lock-in output for a

100nm thick aluminum evaporated on top of a silicon sample under femtosecond laser illumination with different laser intensity. The amplitude signal in Fig. 6-11(a) shows that there is a spike in the first few picoseconds and later there is a slow exponential decaying process. The initial spike is due to the electron-phonon relaxation. This is more clearly shown in Fig. 6-11(b). The change of the reflectivity is due to both the electron temperature and phonon temperature rise. The peak of the signal occurs at around 6 ps. The electron-phonon energy exchange process occurs during a time period of about 40ps. After that, the electrons and phonons are close to equilibrium and the signal is dominated by the heat transport into the semiconductor. Figure 6-11(c) shows the raw phase signal. Figure 6-12 shows the amplitude signal normalized to their respective amplitude signals at 50ps at different laser intensities. The collapsing of the normalized signals with different laser fluencies at short time scales, as shown in Fig. 6-12 (a), demonstrates that the electron transport is thermalized [51] . In other words, the electron thermal conduction obeys the Fourier heat conduction theory.

We are in the process of analyzing the experimental data with the newly proposed model to extract the phonon relaxation time and the phonon reflectivity and comparing the results of this fitting procedure with the fitting for the thermal interface resistance and thermal conductivity. Here I would like to identify the several noise sources which are very important for interpreting the signal.

The first most obvious signal noise source is due to the scattered pump light. The scattered pump beam is occurring at the modulation frequency. Both the roughness of the sample surface and the intensity of the pump beam affect the scattered pump signal amplitude. In order to minimize this unwanted signal, the polarization of the probe beam is rotated by 90° relative to the pump so that a polarizer can be used to filter out most of the scattered pump beam. The incidence of the pump is close to normal to the sample surface and the probe beam is formed at a 30° angle. A pinhole is placed in front of the photodiode such that only the scattered pump light traveling in the same direction as the reflected probe reaches the detector.

Ideally the assumption that is often made is that the change in reflectivity measured by a probe light pulse originates entirely from the previous pump pulse. Thus the magnitude of the detected signal is a direct measure of the change in reflectance due to the nonequilibrium heating induced by a single ultrafast pulse. This is certainly a valid assumption if the energy deposited from each pulse has completely dissipated prior to the arrival of the next pulse. However, for

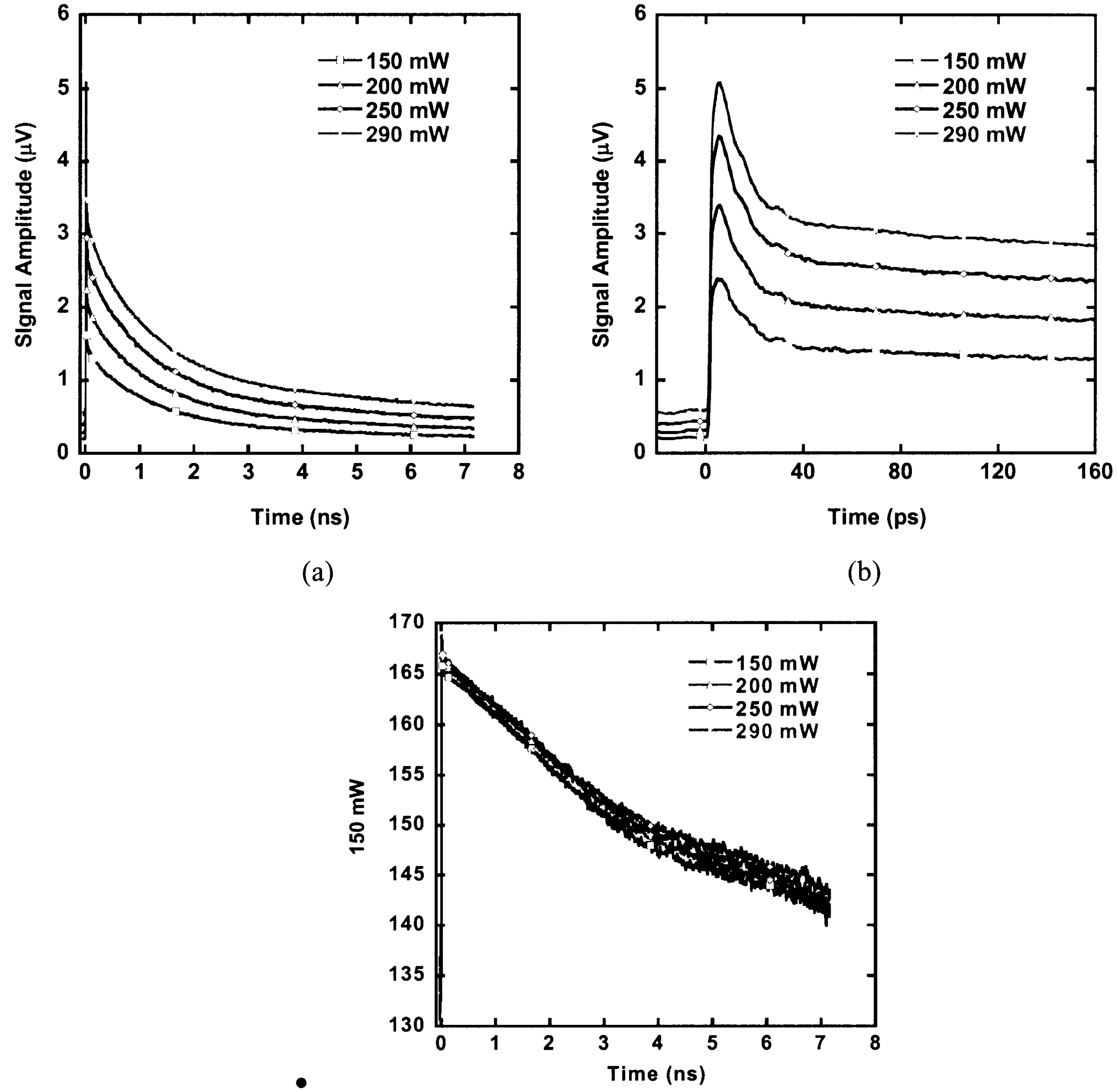

(a)

(b)

(c)

Figure 6-11. Raw experimental signals at different laser pumping intensities: (a) amplitude at a long time scale, ~ns, shows a fast peak in the beginning and a slow decaying process later, (b) The fast peak is an indication of the electron-phonon energy exchange that occurs during the ~ 10 ps time scale, (c) the raw phase signal.

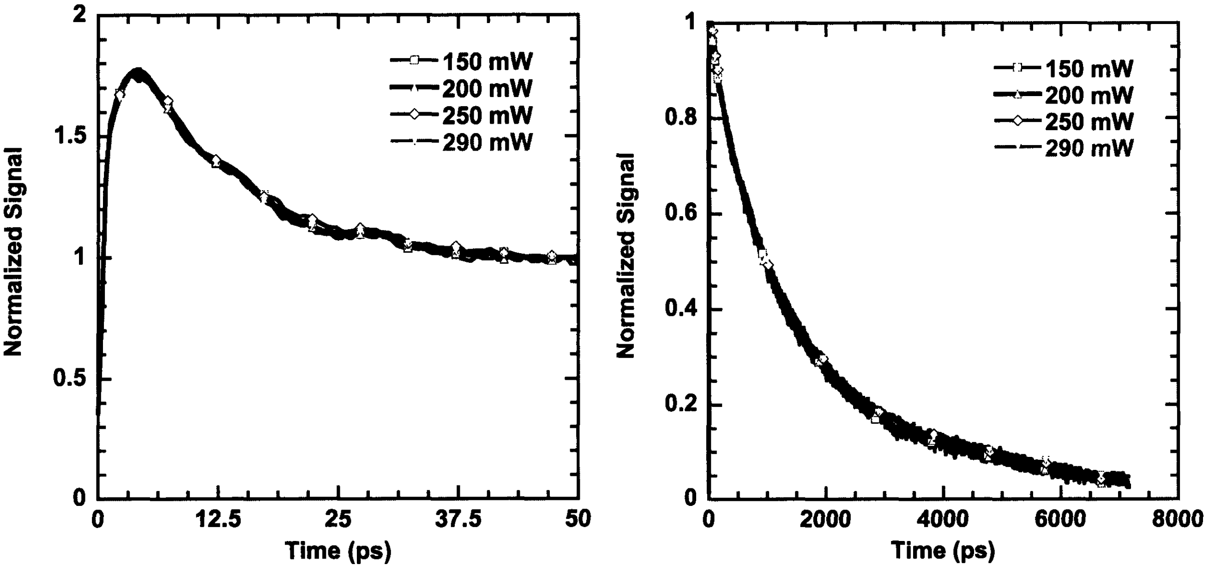

(a) (b)

Figure 6-12. The transient amplitude signal normalized to the amplitude of the signal at 50ps: (a) the fast peak is an indication of the electron-phonon energy exchange that occurs during the ~10 ps time scale, (b) the slow decaying process due to the energy transport through the interface and the substrate.

most of the cases in our experiments, the reflectivity change of the metallic thin film due to a single pump pulse does not fall to a negligible value by the time the next pump pulse arrives. There is a certain amount of residual heating that remains after each pump pulse. The amount of residual heating is a function of the incident fluence and the diffusion time constant of the sample system. Therefore it is necessary in the analysis to consider the contributions to $\Delta R(t)$ that come from previous pump pulses. Figure 6-13(a) depicts the time evolution of the reflectivity change measured in the experiment (after Capinski [52]). Time t=0 refers to the absorption of the first pump pulse after the laser is turned on. The time axis is in units of the time between pump pulses Δt_p. The cooling signal would be the first curve close to time zero if only a single pump pulse heats the sample. In reality, the next pulse heats the sample before the sample cools to its initial value. Thus the measured signal is a superposition of many pump pulses as shown in Fig. 6-13(a). Figure 6-13(b) shows a comparison of the single pulse signal and the measured signal when we normalized both signals to their own maxima. Clearly the measured signal due to the many pulse effect (slow decaying effect) would be much sharper than the signal expected from a single pulse. As a first step, Fig. 6-14 (a) and (b) compare the modeling of a single pulse signal with the experimental results by changing the phonon transmissivity at the interface and the phonon relaxation time. None of the reasonable data input would be able to capture the fast decaying measured signal. This plot clearly demonstrates the importance of a multi-pulse effect. We are now in the process of taking into account the multi-pulse effect in the data fitting process.

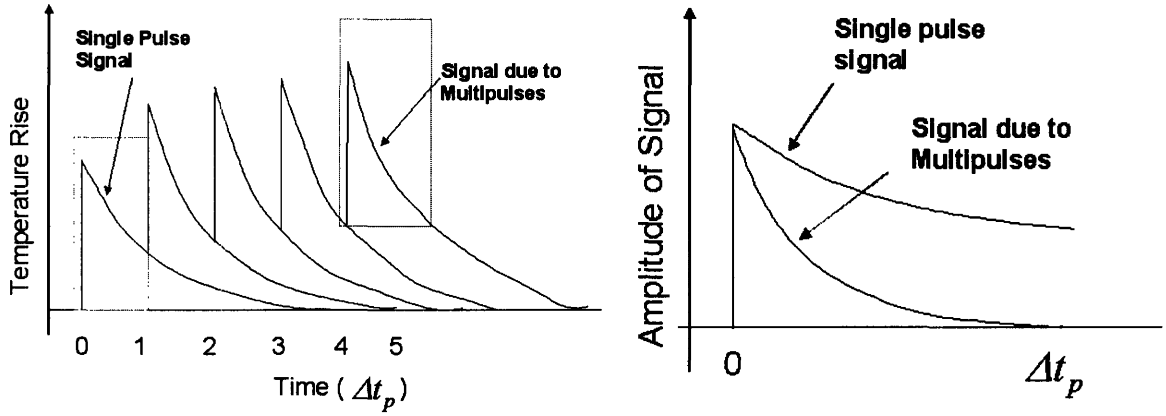

(a) (b)

Figure 6-13. (a) Time evolution of the reflectivity change measured in the experiment. Time t=0 refers to the absorption of the first pump pulse after the laser is turned on. The time axis is in units of the time between pump pulses. The measured signal is a superposition of many pump pulses. (b) A comparison of the single pulse signal and the measured signal when we normalized both signals to their own maxima.

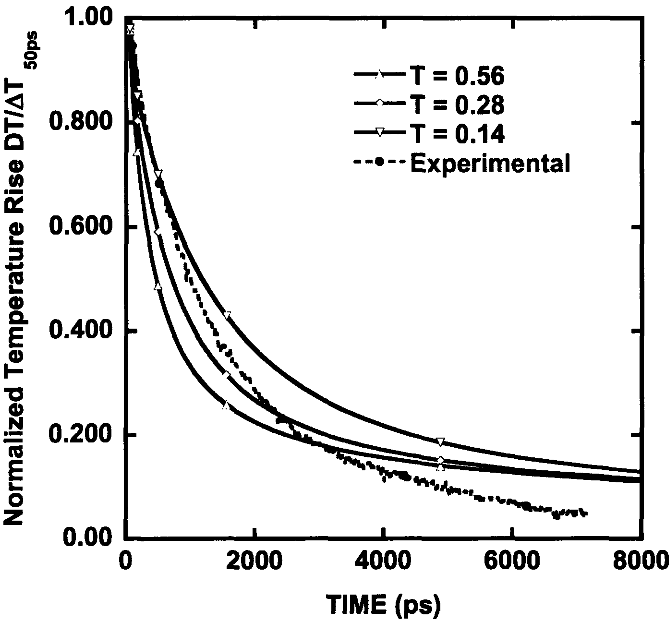

(a)

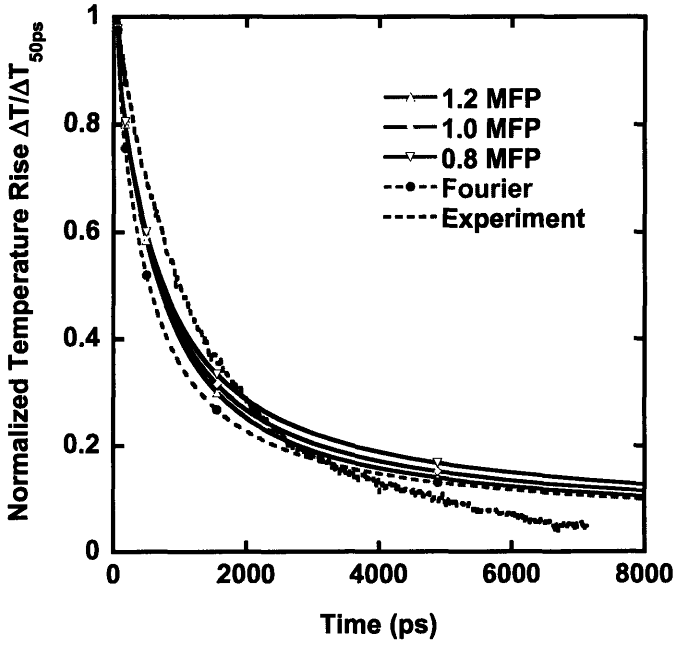

(b)

Figure 6-14. Comparison of single pulse modeling results with the experimental signal by changing (a) the phonon transmissivity at the interface and (b) the phonon relaxation time. None of the reasonable data input would be able to capture the fast decaying measured signal. This plot clearly demonstrates the importance of the multi-pulse effect.

6.5 Summary and Future Work

In this work, we set up the sub-picosecond pump-and-probe optical measurement system employing a Ti:Sapphire femtosecond laser system. The measurement system would be a platform for future studies on nanoscale heat transfer measurements. A new two temperature model - electron Fourier conduction & phonon Boltzmann transport model is proposed to describe the energy transport process under ultrafast laser-materials interaction. Calculations show that there are significant differences between heat diffusion and phonon transport at ultrafast time scale. This renders the rationale and the possibility to extract the phonon reflectivity at an interface and the phonon relaxation time from the sub-ps pump-and-probe measurements. We present preliminary measurement results. However more work is needed to analyze the signal, especially taking into account the multi-pulse effect, and to fully explore the powerfulness of the sub-ps pump-and-probe measurement system as a vehicle for characterization of nanoscale thermal transport. The following work is planned for the near future.

To eliminate the unwanted signal due to the scattered pump light reaching the photodetector and thus to increase the signal-noise ratio, we plan to employ the two color scheme for the pump-and-probe measurement system. In the two color scheme, a pump and probe light beams are at different frequencies (wavelengths) by employing second harmonic generation to double the frequency of one laser beam. The color filter placed before the detector will successfully decrease the noise level.

After this work, the sub-ps pump-and-probe measurement system is suggested to be used to study the following interesting problems: 1) Electron-phonon interactions in low dimensional systems which are known to play important roles in the determination of device performance and reliability. 2) Energy relaxation of a single particle in a medium which is a fundamental energy transport process relating to nanoparticle thermal therapy and nano fluids. 3) thermal energy transport across a variety of interfaces between different materials, for example, organic-inorganic, solid-liquid, metal/semiconductor- polymer, crystalline-amorphous materials, to name a few. 4) thermal transport in a polymer system which is closely related to polymer solar cells and OLEDs (Organic Light Emitting Diodes) and ultrafast laser processing of polymers.

6.6 References

1. S.I. Anisimov, B.L. Kapeliovic, and T.L. Perel'man, Sov. Phys. JETP **39**, 375 (1974).
2. R.W. Schoenlein, W.Z. Lin, J.G. fujimoto, and G.L. Eesley, Phys. Rev. Lett. **58**, 1680 (1987).
3. K. Sokolowski-Tinten, C. Blome, C. Dietrich, A. Tarasevichm, M. Horn Von Hoegen, D. von der Linde, A. Cavalleri, J. Squire, and M. Kammler, Phys. Rev. Lett. **87**, 225701 (2001).
4. C.V. Shank, R. Yen, and C. Hirlimann, Phys. Rev. Lett. **50**, 454 (1983).
5. B. Rethfeld, K. Sokolowski-Tinten, D. von der Linde, and S.I. Anisimov, Phys. Rev. B **65**, 092103 (2002).
6. S.I. Kudryashov, and V.I. Emel'yanov, JETP Lett. **73**, 551 (2001).
7. E.N. Glezer and E. Mazur, Appl. Phys. Lett. **71**, 882 (1997).
8. M.D. Perry, B.C. Stuart, P.S. Banks, D. Fiet, V. Yanovsky, and A.M, Ribernchuk, J. Appl. Phys. **85**, 6903 (1999).
9. R. Le, Harzic, N. Huot, E. Audouard, C. Jonin, P.Laporte, S. Valette, A. Fraczkiewics, and R. Fortunier, Appl. Pys. Lett. **80**, 3886 (2002).
10. T.K. Cheng, J. Vidal, H.J. Zeiger, G. Dresselhaus, M.S. Dresselhaus, and E.P. Ippen, Applied Physics Letter **59**, 1923 (1991).
11. M. Hase, K. Ishioka, M. Kitajima, et al., Applied Surface Science **197**, 710, (2002).
12. J.G. Fujimoto, J.M. Li, E.P. Ippen, and N. Bloembergen, Phys. Rev. Lett. **53**, 1837 (1984).
13. S.D. Brorson, A.Kazeroonian, J.S. Moodera, D.W. Face, T.K. Cheng, E.P. Ippen, M.S. Dresselhaus, and G. dresselhaus, Phys. Rev. Lett. **64**, 2172 (1990).
14. H.E. Elsayed-Ali, T.B. Norris, M.A. Pessot, and G.A. Mourou, Phys. Rev. Lett. **58**, 1212 (1987).
15. T.Q. Qiu, and C.L. Tien, Int. J. Heat Mass Transfer **35**, 719 (1994).
16. C.A. Paddock, and G.L. Eesley, J. Appl. Phys. **60**, 285 (1986).
17. B.M. Clemens, G.L. Eesley, C. Paddock, Phys. Rev. B **37**, 1085 (1988).
18. R.J. Stoner, and H.J. Maris, T.R. Anthony, and W.F. Banholzer, Phys. Rev. Lett. **68**, 1563 (1992).
19. C.J. Morath, H.J. Maris, J.J. Cuomo, D.L. Pappas, A. Grill, V.V. Patel, J.P. Doyle, and K.L. Saenger, J. Appl. Phys. **76**, 2636 (1994).
20. W.S. Capinski, and H.J. Maris, Rev. Sci. Instrumentation **67**, 2720 (1996).

21. W.S. Capinski, and H.J. Maris, T.Ruf, M. Cardona, K.Ploog, and D.S. Katzer, Phys. Rev. B **59**, 8105 (1999).
22. R.M. Costescu, W.A. Wall, and D.G. Cahill, Phys. Rev. B **67**, 054302 (2003).
23. D.G. Cahill, K. Goodson, A. Majumdar, ASME Journal of heat transfer **124**, 223 (2002)
24. D.G. Cahill, K. Goodson, and A. Majumdar, ASME J. Heat Transf. **124,** 223 (2002). Costescu, R.M., Wall, M,A., and Cahill, D.G., Phys. Rev. B **67**, 054302 (2003).
25 P.M. Norris, A.P. Caffrey, R.J. Stevenson, J.M. Klopf, J.T. Mcleskey, A.N. Smith, Rev. Sci. Instrum. **74**, 400 (2003).
26. C.-K. Sun, F. Vallee, L. Acioli, E.P. Ippen, and J.G. Fujimoto, Phys. Rev. B **48**, 12365 (1993)
27. W.S. Fann, R. Storz, H.W.K. Tom, and J. Bokor, Phys. Rev. Lett. **68**, 2834 (1992)
28. D.Y. Tzou, J.E. Beraun, and J.K. Chen, ASME Journal of Heat Transfer **124**, 284 (2002).
29 B. Huttner, J. Phys. Condens. Matter. **11**, 6757 (1999).
30. R. Rethfeld, A. Kaiser, M.Vicanek, and G. Simon, Phys. Rev. B **65**, 214303 (2002).
31. R.H.M. Groeneveld, R. Sprik, and A. Lagendijk, Phys. Rev. B **45**, 5079 (1992).
32. J. Xu, and X.W. Wang, Physica B **351**, 213 (2004)
33. R.G. Yang, X.Y. Chen, A. Schmidt, and G. Chen, "Pump-Probe Experimental Study of Phonon Reflectivity at an Interface and Phonon Relaxation Time (Nano2005-87064)," Proc. ASME 4th Integrated Nanosystems – Design, Synthesis, & Applications, UC-Berkeley, September 14-16, 2005.
34. R. Gupta, N. Balkan, and D.K. Ridley, Phys. Rev. B **46**, 7745 (1992).
35. B.K. Ridley, Report on Progress in Physics **54**, 169 (1991).
36. S.A. Putnam, and D.G. Cahill, Langmuir **21**, 5317 (2005).
37. Z.B. Ge, Y.J. Kang, T.A. Taton, P.V. Braun, D.G. Cahill, Nano Letters **5**, 531 (2005).
38. S.A. Putnam, D.G. Cahill, B.J. Ash, and L.S. Schadler, Journal of Applied Physics **94**, 6785 (2003).
39. T.Q. Qiu, Energy Deposition and Transport during High-Power and Short-Pulse Laser-Metal Interactions, Ph.D Thesis, University of California at Berkeley (1993).
40. F. Carlo, and G.D. Mahan, Journal of Applied Physics **66**, 4213-4217 (1989).
41. S.G. Volz, Phys. Rev. Lett. **87**, 074301 (2001).
42. A. Majumdar, and P. Reddy, Appl. Phys. Lett. **84**, 4768 (2004).

43. A. V. Sergeev, Phys. Rev. B **58**, R10199 (1998).

44. M. L. Huberman, and A. W. Overhauser, Phys. Rev. B **50**, 2865 (1994).

45. C. Kittel, Introduction to Solid State Physics, 7th ed, (Wiley, 1995)

46. P. Heino and E. Ristolainen, Microelectronic Journal **34**, 773 (2003). P. Heino, Phys. Rev. B **71**, 144302 (2005).

47. T.Q. Qiu, and C.L. Tien, Int. J. Heat Mass Transfer **37,** 2789–2797, 1994.

48. R. J. Stevens, A.N. Smith, and P.M. Norris, ASME J. Heat Transf. **127**, 315 (2005).

49 Volz and Gang MD for Bulk Silicon

50. R. J. Stoner, and H. J. Maris, Phys. Rev. B **48**, 16373 (1993).

51. C.K. Sun, F. Vallee, L.H. Acioli, E.P. Ippen, and J.G. Fuimoto, Physical Review B **50**, 15337 (1994)

52. W.S. Capinski, Thermal Conductivity of (GaAs)n/(AlAs)n Superlattices and Isotopically Enriched Si and GaAs, Ph.D Thesis, Brown University (1998).

Chapter 7. Summary and Recommendations

7.1 Summary and Conclusions

The research on nanoscale heat transfer has steadily been in rapid progress over the last two decades with applications in nanoelectronics, nanophotonics, energy conversion, thermal biology, and nano-manufacturing. This thesis contributes to the following aspects for the heat transfer, nanoelectronics, and thermoelectrics research communities:

1) It has been demonstrated in the last decade that the Boltzmannn equation is a valid and useful tool for studying the classical size effect of phonon transport at the nanoscale. The solution of the phonon BTE has been limited to a few simple geometrical configurations due to inherent difficulties and thus has limited consideration of the size and transient effects in multidimensional real engineering problems. Chapter 2 develops numerical solution strategies for the transient phonon BTE in multidimensional structures. Modeling the multidimensional heat conduction processes in most devices involving multiple length scale devices from the nanoscale to the macroscale is very challenging. Direct numerical solution of the phonon BTE is preferred, but it is usually slow. Approximate methods that are capable of capturing the major size effects but easier to implement are thus desirable. Chapter 2 also extends the ballistic-diffusive equations proposed earlier [1,2] to multidimensional problem with a nanoscale heat source term and we have performed numerical implementations of the transient ballistic-diffusive equations. The so-developed numerical simulation tools are applied to study heat transport surrounding nanoscale heat source, which mimics the heating issue in a nanoscale MOSFET structure. Simulation results show that the localized nanoscale heating in a nanoscale MOSFET can have a temperature rise several times larger than that predicted by the Fourier law. This has significant implications for the reliability of MOSFET devices. This work also demonstrates that the ballistic-diffusive equations and the numerical calculation strategies can be promising to be incorporated into commercial device simulators.

2) Nanostructure-based materials such as Bi_2Te_3/Sb_2Te_3 superlattices and PbTe/PbSeTe quantum dot superlattices have shown significant increases in *ZT* values compared to their bulk counterparts due mainly to the reduction of the phonon thermal conductivity in these structures

[3, 4]. Nanocomposites may realize a similar thermal conductivity reduction and provide a pathway to scale-up the nanoscale effects observed in superlattices to thermoelectric material in bulk form. The study on the thermal conductivity of nanocomposites has been rather scarce. In chapter 3 the deterministic solution of the phonon Boltzmann equation is established to study the thermal conductivity of 2-D nanocomposites where silicon nanowires are periodically aligned in a germanium matrix both along and across the nanowire directions. Though very much doable, extending the 2-D BTE simulation to phonon transport in complex three-dimensional (3-D) spatial coordinates is very tedious, owing to the complexity in tracking phonon transport deterministically in such a simulation algorithm. Chapter 4 presents an algorithm for studying phonon transport in nanoparticle composites using a Monte Carlo simulation with special attention paid to the implementation of periodic boundary conditions. The size effects of phonon transport in nanoparticle composites were studied and the results showed that the thermal conductivity of nanoparticle composites can be lower than that of the corresponding alloys and superlattices. The results also show that the key for the thermal conductivity reduction is a large interfacial area per unit volume (high interface density), where nanocomposites offer better results than superlattices. Results of this study can be used to direct the development of high efficiency advanced thermoelectric materials.

3) In thermoelectric devices it is the electrons that do the useful energy conversion work and the electron temperature that matters for energy conversion efficiency. Following the rationale of reducing the phonon thermal conductivity, if there is a way to impart energy to electrons only (by cutting off the energy transport through phonons between the heat source or the cooling target and the thermoelectric element) while minimizing the energy coupling between electrons and phonons, it is possible to obtain better performance of thermoelectric devices. In Chapter 5, we conceptualize and investigate the surface-plasmon coupled nonequilibrium thermoelectric devices. These devices use surface-plasmon coupling to limit the energy exchange between the heating source (or cooling target) and the thermoelectric element to electrons alone, while eliminating direct energy exchange between phonons. Models for refrigeration and power generation devices based on this concept are established, together with simplified criteria to guide the device design and materials selection. Our simulations show that these devices can lead to significant improvements in efficiency over conventional thermoelectric devices.

4) As shown in all the current theoretical modeling and simulation work, it is extremely important to have a correct phonon relaxation time or phonon mean free path as input parameters for any Monte Carlo or Boltzmann transport equation based simulations for nanoscale heat conduction problems. The phonon reflectivity at interfaces and the phonon relaxation time are clearly the most fundamental energy carrier properties for nanoscale heat conduction. No experimental work has been done so far to study the phonon dynamics and thus to extract these phonon properties. During this thesis work, we set up a sub-picosecond pump-probe optical measurement facility employing a Ti:Sapphire femtosecond laser. Chapter 6 studies the fundamentals of ultrafast laser-materials interaction and the possibilities of using the phonon Boltzmann equation to fit the experimental data and to extract the phonon reflectivity and relaxation time using the optical pump and probe measurement.

7.2 Recommendations for Future Directions

Nanoscale heat transfer has been “hot” over the past two decades. With the recent progress in nano materials synthesis and nanostructure fabrication, nanoscale heat transfer will remain “hot” in the future, playing a significant role in information technology, energy conversion technology, and bio-medical engineering. Solid contributions in both theory and experiments are desirable with the following as immediate needs and extensions:

1) Energy Transport across Interfaces

Nanotechnology enables material scientists to introduce nanostructured materials with a high density of controlled interfaces between constituent materials. Energy transport across interfaces often involves reflection and diffraction of energy carriers. When the constituent materials across an interface are dissimilar, the energy carriers can be very different, and thus coupling among different energy carriers, for example electrons and phonons, can be very important. How the energy is coupled and is transported across interfaces among different groups of energy carriers remains an open challenge. There are different kinds of interfaces of scientific and engineering interest, to name a few, superconductor /metal – insulator, organic-inorganic. Understanding the fundamentals of energy transport across interfaces is the key to the breakthrough of developing novel materials for high efficiency energy conversion and thermal management.

2) Full Dispersion Phonon Transport Simulation for Nanostructures

The current Boltzmann transport equation solver and Monte Carlo simulation assume phonon gray medium. More detailed simulations that can account for the complete dispersion relationships by considering the frequency or even wavevector dependent phonon propagation and phonon scattering can be introduced to refine the simulation results. With the size of nanostructures, for example, the size of the heat generation region and the thickness of thin films, approaching the wavelength of phonons, one might need a better way accounting for phonon wave characteristics in thermal transport, as some have done before for thermal transport in superlattices [5].

3) Coupled Electron and Phonon Transport Solver

Conventional two-temperature models and electrohydrodynamics models [6] only capture the nonequilibrium conditions between electrons and phonons to a certain extent. Accurate prediction of how heat is generated, how the heat is transported in nanostructures, and how the heat transport affects the electron performance calls for a more detailed coupled electron-phonon Boltzmann equation solver or Monte Carlo simulator. The simulation results of such a solver or simulator will help the device and circuit designers predicting device failure and will help to come up with a better design using a variety of new materials and new architectures. In addition, a better understanding of coupled electron and phonon transport is the key for advancing laser-materials processing and the performance prediction of nanoengineered energy conversion devices and technologies.

4) Transport Properties of Nanocomposites

Nanotechnology offers the opportunities to make nanocomposites with unveiling properties. Predicting transport properties of nanocomposites has been a challenge since most of the conventional formule can not be valid any more. The periodic transport simulation scheme developed in this thesis might be used for studying other transport properties, for example, the electrical conductivity, Seebeck coefficient and magnetoresistance, of nanocomposites. Simplified models taking into account the nanoscale transport physics that can give consistent results as those obtained through detailed simulations are highly desirable for fast turnaround and engineering applications. In addition, nanoengineering often results in the change of a variety of material properties simultaneously, some good and some bad. There is currently a need for better optimization strategiese for multifunctional nanocomposites.

5) Thermal Characterization and Thermal Imaging at Nanoscale

While the thermal conductivity of silicon thin films and nanowires, and carbon nanotubes have been recently characterized, no such data is yet available for a large volume of other interesting engineering materials. In addition, nanoengineered materials with superior properties might be found from some so-so conventional bulk materials due to the radical change of materials properties at the nanoscale. It is also good to keep in mind that conventional properties, such as the thermal conductivity, might not be the best way to characterize nanostructures. Carrier reflectivity and energy relaxation time might offer a better alternative for describing thermal transport in nanostructures. Sub-pico second pump-probe is expected to be an ideal tool to study interface thermal transport properties. A database on the phonon reflectivity and phonon relaxation time for nanoengineeringed materials might be as important as thermal conductivity database we have today for bulk materials. In addition, the sub-picosecond pump-probe method can be improved for high spatial resolution profiling thermal transport at ultrafast time transients.

7.3 References

1. G.Chen, Phys. Rev. Lett. **86**, 2297 (2001).
2. G. Chen, ASME J. Heat Transf. **124**, 320 (2002).
3. R. Venkatasubramanian, E. Silvona, T. Colpitts, and B. O'Quinn, Nature **413**, 597 (2001).
4. T. C. Harman, P.J. Taylor, M.P. Walsh, and B. E. LaForge, Science **297**, 2229 (2002).
5. B. Yang and G. Chen, Physical Review B **67**, 195311 (2002).
6. M. Lundstrom, Fundamentals of Carrier Transport, 2nd ed, Cambridge University Press, 2000).